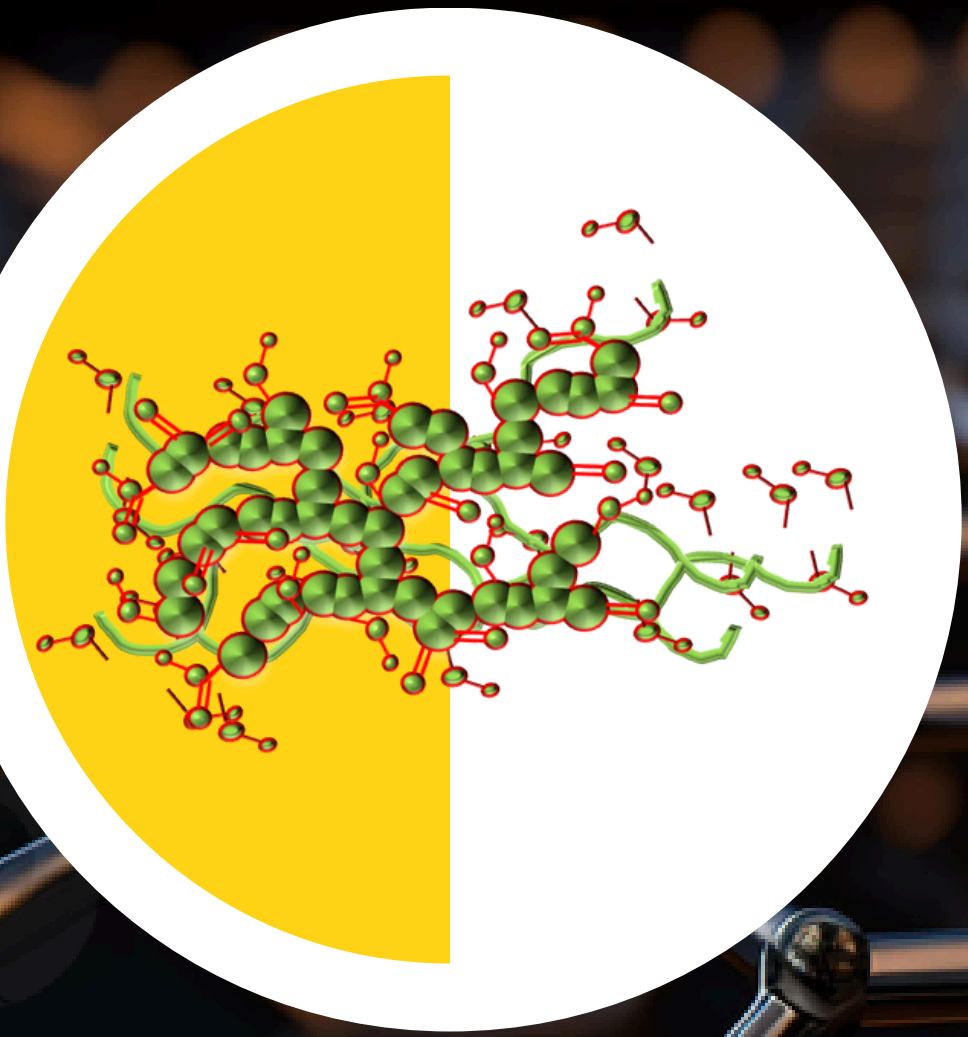

TUNING OF NEGATIVE PERMITTIVITY AND X-BAND MICROWAVE ABSORPTION IN PVA - NANOSTRUCTURED CARBON METACOMPOSITES

Swetha P
Dept. of Nanoscience and Technology
University of Calicut

TUNING OF NEGATIVE PERMITTIVITY AND X-BAND MICROWAVE ABSORPTION IN PVA - NANOSTRUCTURED CARBON METACOMPOSITES

Thesis

Submitted to the Faculty of Science University of Calicut in Partial Fulfilment of the Requirements for the Degree of

Doctor of Philosophy

By

Swetha P

Under the Guidance of

Dr. Sindhu S

Department of Nanoscience and Technology

University of Calicut

Kerala-673635

June - 2024

UNIVERSITY OF CALICUT
Department of Nanoscience & Technology

Calicut University P.O.,
Kerala, 673635, INDIA
0494 2407373, 2407374
Email: sindhus@uoc.ac.in
Website: https://nanotechnology.uoc.ac.in

Dr. Sindhu S
Professor & Head

CERTIFICATE

This is to certify that the thesis entitled ***"Tuning of Negative Permittivity and X-band Microwave Absorption in PVA - Nanostructured Carbon Metacomposites***" is a bona-fide record of research work carried out by Smt. Swetha P. under my supervision in partial fulfilment of the requirements for the award of the degree of Doctor of Philosophy in Physics, under the faculty of science, University of Calicut, Kerala. The contents of the thesis have been checked for plagiarism using the software iThenticate and the similarity index falls under the permissible limit. I further certify that the thesis or part has not previously formed the basis for the award of any degree, diploma or associateship of any other University or Institute. I also certify that the suggestions recommended by the adjudicators have been incorporated in the thesis and the content in the thesis and the soft copy are one and the same.

Dr. Sindhu S., Professor
(Supervising Guide)
Department of Nanoscience and Technology
University of Calicut

DECLARATION

I hereby declare that the work presented in the thesis entitled **"Tuning of Negative Permittivity and X-band Microwave Absorption in PVA - Nanostructured Carbon Metacomposites"** is based on the original work done by me under the guidance of Dr. Sindhu S, Professor and Head, Department of Nanoscience and Technology, University of Calicut and has not been included in any other thesis submitted previously for the award of any degree. The contents of the thesis are undergone plagiarism check using ithenticate software at C.H.M.K. Library, University of Calicut, and the similarity index found within the permissible limit. I also declare that the thesis is free from AI generated contents.

Swetha. P

University of Calicut Swetha P.

20/06/2024

THIS THESIS IS DEDICATED TO MY KIDS, AMMA AND MY BETTER HALF FOR THEIR CONSTANT LOVE AND SUPPORT

ACKNOWLEDGMENT

First and foremost, I would like to thank almighty God for giving me strength, knowledge, ability and opportunity to undertake this research journey and to preserve and complete it satisfactorily. Without His blessings, this achievement would not have been possible.

I would like to express my deepest gratitude to my supervisor, **Dr. Sindhu S**, Professor, Department of Nanoscience and Technology, University of Calicut, for their invaluable guidance, support and encouragement throughout my research. Their profound knowledge and experience helped me throughout this research period. I always thankfully remember my guide for considering me as a Research Scholar at the age of thirty. Thank you miss for your immense support throughout my research period.

I also thankfully remember **Dr. Kishore Sridharan**, UGC Assistant Professor, Department of Nanoscience and Technology, University of Calicut, for their invaluable support and guidance during my research period. I also express my gratitude to **Dr. Mohamed Shahin Thayyil,** Department of Physics, University of Calicut for providing the instrument throughout my research. I also remember the office staff, all other non – teaching staff and librarian at this moment with great gratitude. I thank my colleagues Dr. Nazeer A.P, Dr. Vinod K.T, Dr. Jijil C P, and Dr. Shameel for their support and valuable information's. I also thank all colleagues from Devamatha College especially Dr. Jincemon Cyriac, Dr. Tina Sebastian, Dr. Saji Augustine Mr. Vishnu pran and my students Roselin George and Dr. Adon Jose etc. for their motivation to doing Research. I also thank Dr. Sreed sharma K, for his support throughout the research.

Support from my dear friends who made the lab atmosphere charming and lively space to work with is to be mentioned separately. I remember everyone including Amrutha Raveendran,

Neethumol S V, Deepa Suresh, Aswini R, Dr.Jyothilakshmi V P, Nishanth, Anjitha, Athira, Elza, Rival Jose, Sreeraj, Abid, Akshay, Hasna, Shijina and also remember Binesh M, Ashifa M S, Faheema, Sravan, Reeja teacher from Department of Physics, University of Calicut.

I am also grateful to my department, Department of Nanoscience and Technology, University of Calicut for providing necessary resources and facilities to conduct my research. I also acknowledge University of Calicut for providing fund and facilities for doing research. I also express my gratitude to Indian Institute of Technology, Palakkad for providing facility for doing my Research.

Lastly, I would like to thank my family for their unwavering support, patience, and encouragement throughout my academic journey. Their belief in me has been a constant source of motivation and strength. I thankfully remember my Parents **Smt. Renuka N**, and **Mr. Narayanan P,** your sacrifices, guidance, and wisdom have shaped me into the person I am today. I owe my accomplishments to the values you instilled in me and the lessons you taught me. Your patience and understanding during the long hours of study and research have been invaluable. and also remember my in-laws **Mr. Kesavanunny** and **Smt. Sumathi**. I also remember my siblings **Dr. Shilpa P** and **Mr. Sarath Sankar** for their love and support. I would like to express my deepest gratitude to my beloved husband, **Mr. Rakesh P**, for his unwavering support, patience, and encouragement throughout the course of my research and thesis writing. His love and belief in me have been a constant source of strength and motivation. Thank you for understanding the long hours and the sacrifices made during this journey. Your emotional support and practical assistance have been invaluable, and I could not have accomplished this without you by my side. Finally, to my kids **Sivada** and **Tanusree**, your unwavering love, patience, and support have been the cornerstone of my journey. I dedicate this achievement to you, my precious ones. I thank each and every one who helped me in this Research journey.

Swetha P.

CONTENTS

LIST OF FIGURES AND SCHEMES

LIST OF TABLES

ABBEREVIATIONS

SI. No.	Full Form	Abbreviations
1.	Electromagnetic	EM
2.	Double positive	DPS
3.	Epsilon negative	ENG
4.	Mu negative	MNG
5.	Double negative	DNG
6.	Polyvinyl alcohol	PVA
7.	Carbon black	CB
8.	Multiwalled carbon nanotube	MWCNT
9.	Graphite flakes	GF
10.	Barium titanate	BT
11.	Titanium nitride	TiN
12.	Electromagnetic Interference	EMI
13.	X – Ray Diffraction	XRD
14.	Field emission Scanning electron microscopy	FE-SEM
15.	Transmission electron microscopy	TEM
16.	Fourier transform infrared spectroscopy	FTIR
17.	Thermogravimetric analysis	TGA
18.	Broadband dielectric spectroscopy	BDS
19.	Vector network analyzer	VNA
20.	Shielding effectiveness	SE

21.	Shielding effectiveness by reflection	SE_R
22.	Shielding effectiveness by absorption	SE_A
23.	Total Shielding effectiveness	SE_T
24.	Reflection	R
25.	Absorption	A
26.	Transmission	T
27.	Shielding efficiency in percentage	SE (%)
28.	Decibel	dB
29.	Scattering parameters	S
30.	High resolution TEM	HRTEM
31.	Selected area electron diffraction	SAED
32.	Sodium dodecyl sulphate	SDS

SYMBOLS

SL. No.	Symbols	Meaning
1.	ε^*	Complex permittivity
2.	ε'	Real part of permittivity
3.	$\varepsilon^{"}$	Imaginary part of permittivity
4.	ω	Angular frequency
5.	E	Electric field vector
6.	H	Magnetic field vector
7.	μ	Magnetic permeability
8.	Γ	Damping constant
9.	ω_p	Plasma frequency
10.	ω_0	Characteristics frequency
11.	f	Frequency
12.	S_{11} & S_{22}	Forward and Backward reflection coefficient
13.	S_{12} & S_{21}	Forward and backward transmission coefficient

LIST OF PUBLICATIONS

1. **Swetha P**., Aswini R., Binesh M., Muhammed Shahin T.H., Kishore Sridharan, Sindhu Swaminathan, Cost efficient fabrication of flexible polymer metacomposites: Impact of carbon in achieving tunable negative permittivity at low radio frequency range, Materials Today Communications, Volume 34,2023,105287 – Impact factor – 3.8

2. **Swetha P**, Dharsana M. Vidyadharan, Kishore Sridharan, Mohamed Shahin T. H, Binesh M, Sindhu Swaminathan, Investigation of negative permittivity in $BaTiO_3$/TiN metacomposites at the radio frequency region, Materials Chemistry and Physics, Volume 317,2024, 129156 – Impact factor – 4.6

3. **Swetha P**, Sindhu Swaminathan, Kishore Sridharan, *Mohamed Shahin T. H., Faheema S.,* Modified Negative Permittivity and X-band Microwave Absorption in Polyvinyl Alcohol–MWCNT Metacomposites, composite communications, volume 52, 2024, 102161, Impact factor – 6.5

4. **Swetha P,** Sindhu Swaminathan, Kishore Sridharan, Ashifa. M.S, *Mohamed Shahin T. H.,* Flexible PVA-graphite metacomposites with variable negative permittivity for electromagnetic interference shielding applications, Communicated.

CONFERENCE PRESENTATIONS

1. Attended and presented a paper (Oral), International conference on advanced materials "Tuning of Negative permittivity in $BaTiO_3$-TiN metacomposites", Devamatha College, Kuravilangad, 3-4 January 2024.

2. Attended and presented a paper (poster) International conference on advanced materials in sustainability entitled "X-Band Electromagnetic Interference Shielding Application of PVA-MWCNT-$BaTiO_3$ Metacomposites with Tuned Negative Permittivity" University of Calicut, 21-23, December,2023.

3. Attended and presented a paper (poster), National Photonics Symposium 2023 entitled 'The influence of electrical percolation on conductivity switching and permittivity shifting in $BaTiO_3$ – PVA – CB metacomposites at radio frequencies' CUSAT, 27 Feb-1 March, 2023

4. Attended and presented a paper (poster) "The effect of electrical percolation on conductivity switching and permittivity shifting in PVA – MWCNT metacomposites at radio frequencies" in SERB sponsored 10^{th} National conference on Condensed matter Physics and Applications (CMPA), Manipal institute of Technology, December 02-03,2022 Manipal.

AWARD AND RECOGNITIONS

Best paper award - Attended and presented a paper (poster) “The effect of electrical percolation on conductivity switching and permittivity shifting in PVA – MWCNT metacomposites at radio frequencies” in SERB sponsored 10th National conference on Condensed matter Physics and Applications (CMPA), Manipal institute of Technology, December 02-03,2022 Manipal.

PREFACE

The rapid advancement of technology has given rise to an ever-increasing demand for materials with unique properties that can meet the challenges of modern applications. Among these materials, metamaterials and metacomposites have emerged as revolutionary innovations with the potential to transform various fields, including telecommunications, aerospace, and defense. These materials, characterized by their ability to exhibit properties not found in naturally occurring substances, are at the forefront of scientific research and industrial application.

Metamaterials are artificially structured materials engineered to control electromagnetic waves in ways that conventional materials cannot. By manipulating their internal structures at the micro- or nanoscale, these materials can exhibit negative refractive indices, cloaking abilities, and enhanced electromagnetic interference (EMI) shielding properties. Due to the complex preparation process of metamaterial, in this study we chose metacomposite for getting these unusual properties.

Metacomposites, on the other hand, combine the properties of metamaterials with those of conventional composite materials. This fusion allows for the creation of multifunctional materials that offer superior mechanical strength, thermal stability, and electromagnetic performance. Such composites are particularly valuable in applications where multiple properties are required, such as in aerospace engineering, where lightweight, strong, and EMI-resistant materials are crucial.

One of the most promising applications of metamaterials and metacomposites lies in the field of EMI shielding. As electronic devices become more prevalent and powerful, the need to protect sensitive equipment from electromagnetic interference has become paramount.

Metamaterials and metacomposites offer a tailored solution to this problem, providing effective shielding across a broad range of frequencies, including the challenging X-band frequency range.

Chapter 1. Introduction

In the first chapter gives a detailed introduction about metamaterial and metacomposites and the history about the metamaterial. The theory behind metamaterial and metacomposites are given in depth. Elaborate description of Drude model, Lorentz model, Drude – Lorentz model and percolation theory. A thorough analysis of negative permittivity models, metacomposites, and the materials used for their creation are provided. In-depth explanations of the causes of electromagnetic interference shielding, frequency band differences, and factors influencing EMI shielding are provided.

Chapter 2. Synthesis Methods and Characterization Techniques

The second chapter explained about synthesis method and characterization techniques used in this study. The elaborate discussion about solvothermal synthesis method and Die – casting method for the synthesis of nanoparticle and polymer films respectively. Additionally discussed is the comprehensive theory underlying the various methods utilized to characterize the produced materials. In this study, the synthesized samples were subjected to study their structural, morphological, thermal and dielectric properties through various techniques. The structural analysis was carried out using XRD and Raman analysis. Chemical bonding is analyzed by FTIR. Morphological analysis was carried out using SEM and TEM. Broad band dielectric spectrometer was used to study the dielectric characteristics of the fabricated samples. Scattering parameters were measured by using Vector network analyzer. Detailed description about the theory behind the broad band dielectric spectrometer and vector network analyzer were also given in this chapter.

Chapter 3. Cost efficient fabrication of flexible polymer metacomposites: Impact of carbon in achieving tunable negative permittivity at low radio frequency range and X – band EMI shielding.

In this study, metacomposites were fabricated using die-casting with polyvinyl alcohol (PVA) as a flexible, low-cost, environmentally friendly polymer matrix and carbon black (CB) particles as the filler. Notably, the PVA-CB metacomposites, with varying CB concentrations from 0.5 to 2.5 wt%, demonstrated a transition in conductivity and a shift in permittivity occurred due to electrical percolation. The PVA-CB metacomposites shows Drude model, exhibiting weakly negative permittivity at low frequencies. The metacomposite with 2.5 wt% CB showed the highest negative permittivity of -443 at a frequency of 15 kHz and surprisingly exhibited epsilon-near-zero permittivity, when the CB content was just above the percolation threshold (1.25 wt%). The electromagnetic interference shielding performance of the sample are also carried out. The maximum shielding efficiency of 23 dB obtained with 2.5 wt% CB content.

Chapter 4. Tunable Negative Permittivity and X-band Microwave Absorption in Polyvinyl Alcohol–MWCNT Metacomposites.

In the fourth chapter, a polyvinyl alcohol (PVA) - multi-walled carbon nanotube (MWCNT) metacomposite was fabricated, demonstrating tunable permittivity by varying the MWCNT concentration. As the MWCNT content in the composite increases, negative permittivity behavior is observed according to both the Drude-Lorentz and Drude models. At a 1 wt% MWCNT loading, percolation is achieved, leading to increased conductivity and a transition from positive to negative permittivity, with values of -9 at 10 kHz and -200 at 34 kHz. PVA with 3 wt% MWCNT exhibits negative permittivity across the entire tested frequency range, following the Drude model. Additionally, the composites demonstrate excellent X-band

microwave absorption properties, achieving up to -50 dB reflection loss and a shielding efficiency of 22 dB. The shielding by reflection is below 1 dB, indicating an absorption-dominant shielding mechanism.

Chapter 5. Flexible PVA-graphite metacomposites with variable negative permittivity for electromagnetic interference shielding applications.

In this chapter, polyvinyl alcohol (PVA) – graphite flakes (G) metacomposites were fabricated using conventional, cost-effective die-casting methods, with varying concentrations of graphite flakes. Notably, a negative permittivity of -0.71 was achieved in the composites with 1 wt% graphite flakes. Across the entire tested frequency range, higher concentrations of graphite particles exhibited negative permittivity and percolation, explained by the Drude model. The composite with 1 wt% graphite flakes also displayed epsilon-near-zero behavior around 52 Hz. Furthermore, at 3 wt% graphite flakes, the AC conductivity spectra indicated a shift from hopping conduction to metal-like conduction. Interestingly, negative permittivity in PVA-G composites was observed prior to percolation. This novel framework of PVA-G metacomposites simplifies applications in microwave absorption, electromagnetic interference (EMI) shielding, and other fields by enabling controllable negative permittivity. Double-layer composites (negative-positive sandwich layer) exhibited high positive permittivity with low dielectric loss. Additionally, the composites' EMI shielding properties were thoroughly discussed, with a shielding efficiency of -37 dB achieved at 2.5 wt% graphite flakes in the X-band region.

Chapter 6. Metacomposites of $BaTiO_3$ and TiN in polyvinyl alcohol matrix with different carbon nanostructures

In the 6th chapter, a ceramic metacomposite is fabricated $BaTiO_3$/TiN (BTN) by uing mesoporous $BaTiO_3$ as the matrix, combined with varying concentrations of TiN as the filler.

$BaTiO_3$ was synthesized by novel solvothermal synthesis method. When the TiN content rose, dielectric characteristics examined in the frequency range of 100 Hz to 100 kHz revealed a switch in the permittivity, going from positive to negative. For flexibility, this ceramic metacomposite added to the polymer matrix and dielectric measurements are carried out. Interestingly, its negative permittivity disappears and shows positive permittivity in the whole test frequency region. For improving the conductivity, carbon nanostructures (CB, MWCNT, Graphite) added to this polymer matrix and dielectric measurements are carried out. With the presence of carbon fillers, conductivity greatly increased and negative permittivity is obtained. The EMI shielding efficiency of all the synthesized samples are carried out and shows good shielding efficiency.

Chapter – 7 Conclusion and future outlook

In the concluding section, the present research study is summarized and detailed description about the necessity of metacomposite fabrication and their future use are given. Flexible polymer composites with tuned negative permittivity are suitable for variety of applications. The improved EMI shielding efficiency with lower thickness are suitable for commercial applications.

ആമുഖം

സാങ്കേതികവിദ്യയുടെ ദ്രുതഗതിയിലുള്ള മുന്നേറ്റം, ആധുനിക ആപ്ലിക്കേഷനുകളുടെ വെല്ലുവിളികളെ നേരിടാൻ കഴിയുന്ന തനതായ ഗുണങ്ങളുള്ള മെറ്റീരിയലുകളുടെ വർദ്ധിച്ചുവരുന്ന ഡിമാൻഡിന് കാരണമായി. ഈ മെറ്റീരിയലുകൾക്കിടയിൽ, ടെലികമ്മ്യൂണിക്കേഷൻ, എയ്റോസ്പേസ്, പ്രതിരോധം എന്നിവയുൾപ്പെടെ വിവിധ മേഖലകളെ പരിവർത്തനം ചെയ്യാൻ കഴിവുള്ള വിപ്ലവകരമായ നവീകരണങ്ങളായിമെറ്റാമെറ്റീരിയലുകളും മെറ്റാകോംപോസിറ്റുകളും ഉയർന്നുവന്നിട്ടുണ്ട്. പ്രകൃതിദത്തമായ പദാർത്ഥങ്ങളിൽ കാണപ്പെടാത്ത ഗുണങ്ങൾ പ്രകടിപ്പിക്കാനുള്ള കഴിവിൻ്റെ സവിശേഷതയായ ഈ പദാർത്ഥങ്ങൾ ശാസ്ത്രീയ ഗവേഷണത്തിലും വ്യാവസായിക പ്രയോഗത്തിലും മുൻപന്തിയിലാണ്.

സാമ്പ്രദായിക വസ്തുക്കൾക്ക് സാധിക്കാത്ത വിധത്തിൽ വൈദ്യുതകാന്തിക തരംഗങ്ങളെ നിയന്ത്രിക്കാൻ രൂപകൽപ്പന ചെയ്ത കൃത്രിമമായി ഘടനാപരമായ വസ്തുക്കളാണ് മെറ്റാമെറ്റീരിയലുകൾ. മൈക്രോ- അല്ലെങ്കിൽ നാനോ സ്കെയിലിൽ അവയുടെ ആന്തരിക ഘടനകൾ കൈകാര്യം ചെയ്യുന്നതിലൂടെ, ഈ മെറ്റീരിയലുകൾക്ക് നെഗറ്റീവ് റിഫ്രാക്റ്റീവ് സൂചികകൾ, ക്ലോക്കിംഗ് കഴിവുകൾ, മെച്ചപ്പെടുത്തിയ വൈദ്യുതകാന്തിക ഇടപെടൽ (ഇഎംഐ) ഷീൽഡിംഗ് പ്രോപ്പർട്ടികൾ എന്നിവ പ്രദർശിപ്പിക്കാൻ കഴിയും. മെറ്റാമെറ്റീരിയലിൻ്റെ സങ്കീർണ്ണമായ തയ്യാറെടുപ്പ് പ്രക്രിയ കാരണം, ഈ പഠനത്തിൽ ഈ അസാധാരണ ഗുണങ്ങൾ ലഭിക്കുന്നതിന് ഞങ്ങൾ മെറ്റാകോംപോസിറ്റ് തിരഞ്ഞെടുത്തു.

CONTENTS

TUNING OF NEGATIVE PERMITTIVITY AND X-BAND MICROWAVE ABSORPTION IN PVA - NANOSTRUCTURED CARBON METACOMPOSITES

Swetha P

Department of Nanoscience and Technology

Abstract

The rapid advancement of technology has given rise to an ever-increasing demand for materials with unique properties that can meet the challenges of modern applications. Among these materials, metamaterials and metacomposites have emerged as revolutionary innovations with the potential to transform various fields, including telecommunications, aerospace, and defence. Metacomposites, on the other hand, combine the properties of metamaterials with those of conventional composite materials. This fusion allows for the creation of multifunctional materials that offer superior mechanical strength, thermal stability, and electromagnetic performance. Such composites are particularly valuable in applications such as in aerospace engineering, where lightweight, strong, and EMI-resistant materials are crucial.

In the present study, polymer metacomposites are fabricated with polyvinyl alcohol as the matrix and three different carbon nanostructures such as carbon black, MWCNT and graphite is used as the conducting fillers. All fabricated sample shows negative permittivity and good shielding efficiency in the X- band region. After that a ceramic metacomposites are also fabricated with $BaTiO_3$ is the dielectric matrix and TiN is the conducting filler and the negative permittivity is obtained. Then to impart flexibility this ceramic metacomposite is added in the polymer matrix and in order to get negative permittivity different carbon nanostructures added and this four-component system have high shielding efficiency and suitable for electromagnetic interference shielding applications.

Swetha P. Tuning of negative permittivity and x band microwave absorption in pva nanostructured carbon metacomposites. Thesis.2024. Nanoscience and Technology, University of Calicut.

പോളി വിനൈൽ ആൽക്കഹോളിലെ നെഗറ്റീവ് പെർമിറ്റിവിറ്റിയുടെ ട്യൂണിംഗും എക്സ്-ബാൻഡ് മൈക്രോവേവ് ആഗിരണം - നാനോസ്ട്രക്ചർ ചെയ്ത കാർബൺ മെറ്റാകോംപോസിറ്റുകളും

ശ്വേത പി

നാനോ സയൻസ് ആൻഡ് ടെക്നോളജി വകുപ്പ്

ആമുഖം

സാങ്കേതികവിദ്യയുടെ ദ്രുതഗതിയിലുള്ള മുന്നേറ്റം, ആധുനിക ആപ്ലിക്കേഷനുകളുടെ വെല്ലുവിളികളെ നേരിടാൻ കഴിയുന്ന തനതായ ഗുണങ്ങളുള്ള മെറ്റീരിയലുകളുടെ വർദ്ധിച്ചുവരുന്ന ഡിമാൻഡിന് കാരണമായി. ഈ മെറ്റീരിയലുകൾക്കിടയിൽ, ടെലികമ്മ്യൂണിക്കേഷൻ, എയ്റോസ്പേസ്, പ്രതിരോധം എന്നിവയുൾപ്പെടെ വിവിധ മേഖലകളെ പരിവർത്തനം ചെയ്യാൻ കഴിവുള്ള വിപ്ലവകരമായ നവീകരണങ്ങളായി മെറ്റാ മെറ്റീരിയലുകളും മെറ്റാകോംപോസിറ്റുകളും ഉയർന്നുവന്നിട്ടുണ്ട്. മെറ്റാകംപോസിറ്റുകളാകട്ടെ, മെറ്റാമെറ്റീരിയലുകളുടെ ഗുണങ്ങളെ പരമ്പരാഗത സംയോജിത വസ്തുക്കളുമായി സംയോജിപ്പിക്കുന്നു. മികച്ച മെക്കാനിക്കൽ ശക്തി, താപ സ്ഥിരത, വൈദ്യുതകാന്തിക പ്രകടനം എന്നിവ വാഗ്ദാനം ചെയ്യുന്ന മൾട്ടിഫങ്ഷണൽ മെറ്റീരിയലുകൾ സൃഷ്ടിക്കാൻ ഈ സംയോജനം അനുവദിക്കുന്നു. എയ്റോസ്പേസ് എഞ്ചിനീയറിംഗ് പോലുള്ള ആപ്ലിക്കേഷനുകളിൽ അത്തരം സംയുക്തങ്ങൾ പ്രത്യേകിച്ചും വിലപ്പെട്ടതാണ്, അവിടെ ഭാരം കുറഞ്ഞതും ശക്തവും EMI-റെസിസ്റ്റൻ്റ് മെറ്റീരിയലുകളും നിർണായകമാണ്.

നിലവിലെ പഠനത്തിൽ, പോളിമർ മെറ്റാകോമ്പോസിറ്റുകൾ പോളി വിനൈൽ ആൽക്കഹോൾ ഉപയോഗിച്ച് മെട്രിക്സായി നിർമ്മിക്കുകയും കാർബൺ ബ്ലാക്ക്, എം.ഡബ്ല്യു.സി.എൻ.ടി, ഗ്രാഫൈറ്റ് തുടങ്ങിയ മൂന്ന് വ്യത്യസ്ത കാർബൺ നാനോസ്ട്രക്ചറുകൾ ചാലക ഫില്ലറായി ഉപയോഗിക്കുകയും ചെയ്യുന്നു. എല്ലാ കെട്ടിച്ചമച്ച സാമ്പിളും എക്സ്-ബാൻഡ് മേഖലയിൽ നെഗറ്റീവ് പെർമിറ്റിവിറ്റിയും നല്ല ഷീൽഡിംഗ് കാര്യക്ഷമതയും കാണിക്കുന്നു. അതിനുശേഷം, ബേരിയം ടൈറ്റനേറ്റ് ഉപയോഗിച്ച് ഒരു സെറാമിക് മെറ്റാകോംപോസിറ്റുകളും നിർമ്മിക്കപ്പെടുന്നു, ഇത് ഡൈഇലക്ട്രിക് മെട്രിക്സും ടൈറ്റാനിയം നൈട്രൈഡ് ചാലക ഫില്ലറും ആണ്, കൂടാതെ നെഗറ്റീവ് പെർമിറ്റിവിറ്റി ലഭിക്കും. ഫ്ലെക്സിബിലിറ്റി നൽകാൻ ഈ സെറാമിക് മെറ്റാകോംപോസിറ്റ് പോളിമർ മാട്രിക്സിൽ ചേർക്കുന്നു, കൂടാതെ നെഗറ്റീവ് പെർമിറ്റിവിറ്റി ലഭിക്കുന്നതിന് വ്യത്യസ്ത കാർബൺ നാനോസ്ട്രക്ചറുകൾ ചേർക്കുന്നു, കൂടാതെ ഈ നാല്-ഘടക സംവിധാനത്തിന്ഉയർന്നഷീൽഡിംഗ്കാര്യക്ഷമതയും വൈദ്യുതകാന്തിക ഇടപെടൽ ഷീൽഡിംഗ് ആപ്ലിക്കേഷനുകൾക്ക് അനുയോജ്യവുമാണ്.

INTRODUCTION

1.1 General background

Metamaterials are artificially created materials with properties such as negative permittivity, permeability and refractive index capable of exhibiting unique and far-reaching electromagnetic (EM) properties in the frequencies ranging from microwave to visible [1–4]. The Greek word "meta" means "beyond," signifying that it refers to everything that occurs outside the parameters of material behaviour as it exists naturally. In other words, it reflects metamaterials can react to external electromagnetic radiation in totally different ways compared to conventional materials. A class of structures known as Metamaterials is frequently constructed using novel or artificial structures created by unit cells whose dimensions are significantly lower than the wavelength. Theoretical justification of the appealing properties of metamaterials was introduced by V G Vesalago in 1968, which attracted interest globally due to its possibilities in creation of invisibility cloaks, sub-wavelength imaging, wireless power transfer, super lenses, novel capacitors, and Electro Magnetic (EM) interference shielding etc [5]. Furthermore, these metamaterials are also capable of exhibiting special properties such as inverse Doppler Effect, inverse Cerenkov radiation, negative index of refraction and so on. Initially, John Pendry in 1996 practically demonstrated the fabrication of left-handed metamaterials by the periodical arrangement of thin wires which exhibited negative values of permittivity at microwave frequencies [6]. Later, the split ring resonator structure was introduced in 1999, which exhibited negative magnetic permeability in gigahertz range [7]. In 2001, Schultz and co-workers experimentally verified the negative index of refraction at microwave frequencies [8]. Studies on metamaterials were motivated by these results and has influenced researchers globally to work on it for understanding the fundamental mechanism and to realise their capabilities towards the manipulation of electromagnetic waves, perfect

absorption and so on [9–12]. Metamaterials with narrow wire arrangement shows negative permittivity, split ring resonator structure showing negative permeability and their combination that is capable of exhibiting double negative properties [13–15]is depicted in Fig.1.1

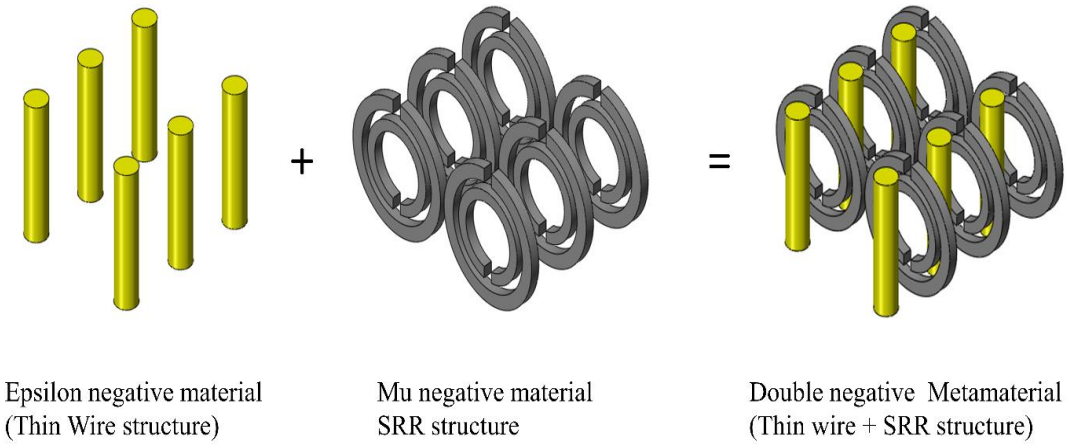

Figure 1.1 Structure determined metamaterials

Fundamentally, the interaction of waves and materials are characterised by two parameters *viz*., electric permittivity (ε) and magnetic permeability (μ). Therefore, the response of EM field on the solid-state materials can be represented through the parameter space as shown in Fig.1.2. The first quadrant of Fig.1.2 correspond to the materials exhibiting both positive values of ε and μ and are termed as double positive material (DPS), which include almost all dielectric materials. II and III quadrants of Fig.1.2 are classified respectively as negative epsilon (ENG) and permeability (Mu) negative (MNG) materials and are termed as single negative materials. At specific frequencies, metals and semiconductors can display negative permittivity, while some ferrites with negative permeability tend to lose their magnetic response above microwave frequencies. In the fourth quadrant both permittivity (ε) and permeability (μ) are simultaneously negative and classified as double negative materials (DNG) or **Metamaterials**. Negative values of ε, μ and refractive index were realized through periodic structures in the form of thin wires, spilt ring resonator and integrated thin wires/split ring resonator structures [16–22].

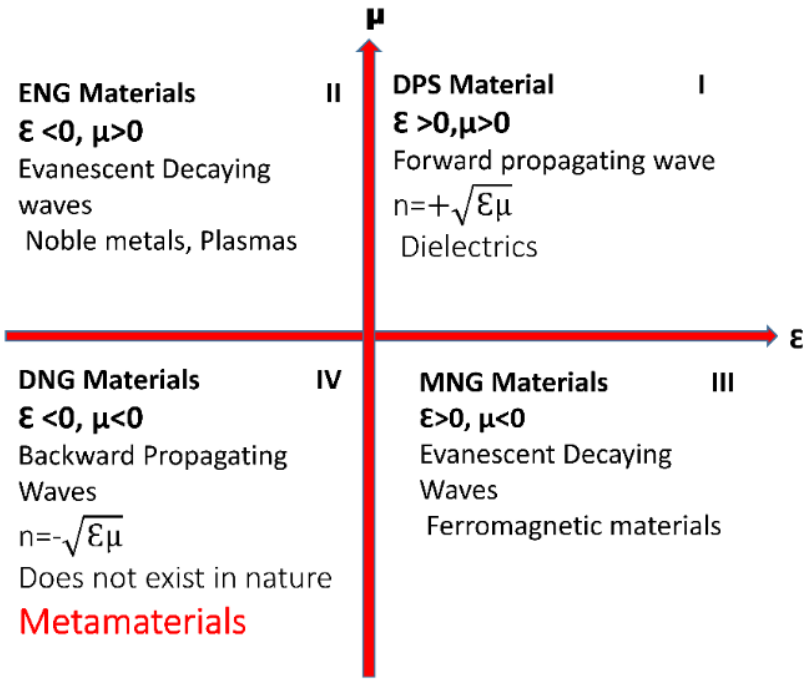

Figure 1.2 Classification of electromagnetic metamaterials based on ε and μ

1.2 Fundamental Physics of metamaterials

Typically, DPS materials follow the Flemings right hand thumb rule as the wave vector and Poynting vector are in the same direction (Poynting vector $\vec{S}$ and wave vector $\vec{k}$ are in the same direction) enabling their forward propagation as an EM wave as shown in Fig.1.3b. ENG and MNG materials behave like evanescent waves and cannot propagate as an EM wave since their energy is concentrated spatially in the vicinity of source. Surprisingly, the direction of transmission of the EM waves in DNG materials are in the backward direction. Because, in the case of metamaterials or DNG material, the Poynting vector determined by the electric vector $\vec{E}$ (or magnetic vector $\vec{H}$) is against to the wave vector $\vec{k}$ (Poynting vector $\vec{S}$ and wave vector $\vec{k}$ are in the opposite direction) as shown in Fig.1.3a. It is worthwhile noting that metamaterials do not violate any fundamental laws of physics, despite exhibiting peculiar properties and the theory behind this is based on invariance of Maxwell's equations. The equations are

$$\nabla \times \vec{E} = -\mu_0 \frac{\partial \vec{E}}{\partial t} \qquad \nabla \times \vec{H} = \varepsilon_0 \frac{\partial \vec{E}}{\partial t} + \vec{J} \qquad (1.1)$$

$$\vec{D} = \varepsilon\varepsilon_0 \vec{E} \qquad \vec{B} = \mu\mu_0 \vec{H} \qquad (1.2)$$

$$\nabla^2 \vec{E} = \frac{\mu\varepsilon}{c^2}\frac{\partial^2 E}{\partial t^2} \qquad K^2 = \frac{\mu\varepsilon}{c^2}\omega^2 \qquad n = \sqrt{\varepsilon\mu} \qquad (1.3)$$

In the above equations, $\vec{E}$ represents the electric field and $\vec{H}$ represents the magnetic field of the electromagnetic waves while ε_0 is the permittivity and μ_0 is the permeability in vacuum. $\vec{E}$, $\vec{B}$ and $\vec{J}$ are electric flux, magnetic flux and current density respectively. Frequency dependent changes in the properties of materials have been described through several models. Among the many models, Drude and Lorentz models are predominantly used for describing the negative properties of materials.

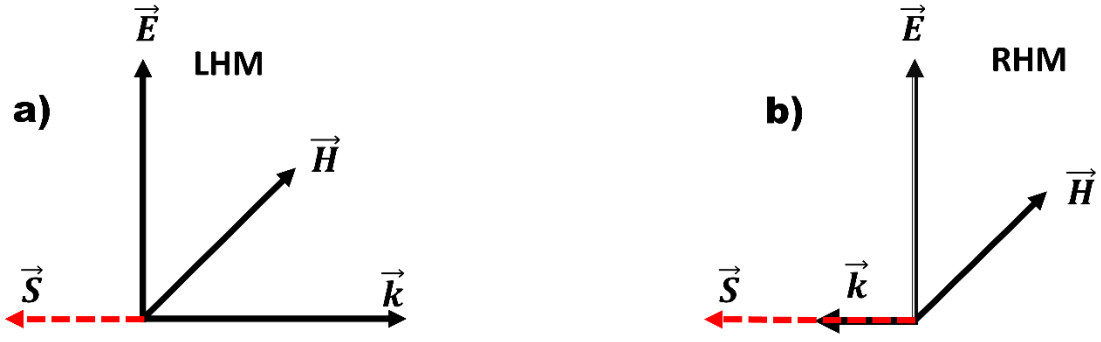

Figure 1.3 (a) Double negative materials (DNG), (b) Double positive materials (DPS)

Due to the complicated preparation process of structure determined metamaterials (The creation of Split ring resonator and thin wire structure is more complex) and their insufficient band response, researchers focus on an alternative method for the fabrication of metamaterials. Manipulation of material composition and structures enabled the fabrication of periodic metamaterials, wherein the negative permittivity obtained from material composites itself was completely different from those derived from structural arrays [23–25]. Chui and Hu [26],theoretically predicted the double negative properties of composites and Guo *et. al.,* fabricated nanocomposites of polyaniline/tungsten oxide which exhibited negative permittivity in the lower frequency region and termed them as "metacomposites" [27]. Flexible metacomposites fabricated with insulating ceramics or polymers as matrix and conductive

metals, carbon, and certain ceramics as fillers began trending [28–31]. These studies triggered renewed interest in researchers to design and development of various metacomposites owing to the ease of fabrication, low cost and flexibility [24,29,32,33].

1.3 Metacomposites

Metacomposites or intrinsic metamaterials, such as nanocomposites as metamaterial is an alternate for obtain negative electromagnetic parameters. Mostly percolating composites are used to create metacomposites (Fig.1.4). Percolating composites containing both conducting filler and dielectric matrix. Percolation is accomplished by adjusting the conducting filler's concentration. It should be noted that metacomposites can display both positive and negative permittivity values by adjusting their percolation threshold is one of its unique advantages. Below the percolation, it is positive dielectric materials and above the percolation it is lossy Left-handed material. Because of its intriguing applications in a variety of fields, metacomposites with negative electromagnetic properties are receiving a lot of interest. Among them single negative (SNG) metamaterial, or epsilon negative metacomposites receive more research interest due to their fascinating applications such as electromagnetic wave blocking, high-power microwave filters, perfect lens absorption and wireless power transfer [34–37].

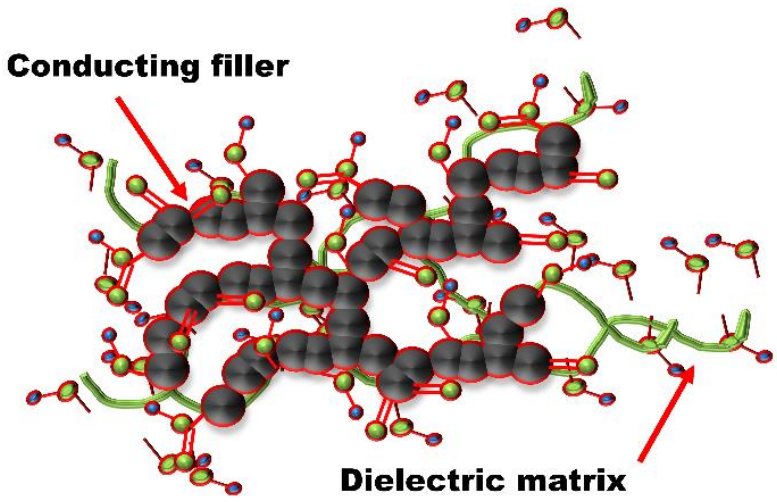

Figure 1.4 Metacomposite consists of dielectric matrix and conducting filler

1.4 Dielectric Properties and Negative permittivity

In dielectric media, Permittivity (Ɛ) is considered as a most important parameter and it has both real (ϵ_r') and imaginary (ϵ_r'') part. The equation is

$$\varepsilon_r = \varepsilon_r' - i\varepsilon_r'' \qquad (1.4)$$

The ability of a material to hold electric charges is represented by the dielectric constant, which is the real component of permittivity and the imaginary component known as dielectric loss. When an electric field is applied to a material that is electrically non-conductive (dielectric), it causes the electric charge to slightly deviate from its usual equilibrium location, creating dielectric polarization. The mathematical description of the electrostatic dielectric constant is supplied by the electric displacement vector ($\vec{D}$), which is determined by the electric field ($\vec{E}$) and polarization (P).

$$\vec{D} = \varepsilon_o(1 + \chi_e)\vec{E} \qquad (1.5)$$

χ_e is the electric susceptibility, $\epsilon_o$is the permittivity of free space. Due to the limited distance that charges can travel, permittivity displays positive values. The movement of electron play key role to generate permittivity. A conductor-dielectric composite experiences simple harmonic motion when an alternating current is applied, and the electrons' polarization direction matches that of the external electric field. This results in negative permittivity behaviour, also referred to as plasma oscillation, and allows the electrons to travel more. When conducting filler is added to a dielectric matrix (percolating composite), at particular concentration and at critical frequency a dramatic change of conductivity occurs. Electrons in conductors produce cumulative harmonic oscillations under the combined action of restoring force and inertia, resulting in a change in permittivity from positive to negative. This transition

occurred under the influence of both forces, and the Drude model provides a good explanation for it. In certain situations, the dipoles' dielectric resonance adds to the negative permittivity. One way to conceptualize the dipole charge's resonance is as mechanical linear oscillators, with their restoring force counteracting the force generated by the applied electric field. Typically, a resonance happens at a specific frequency, and the permittivity can be described as Lorentz model. At particular cases, both plasma oscillations and dielectric resonance contribute to negative permittivity and the Drude-Lorentz model provides a good description of this phenomenon [38–40].

The equation of motion of a free electron in an electric field yields the long wavelength dielectric response of an electron gas, which is given by

$$m\frac{d^2x}{dy^2} = -eE \tag{1.6}$$

If x and E have time dependence $e^{-i\omega t}$, then

$$-\omega^2 mx = -eE\ ;\ x = eE/m\omega^2 \tag{1.7}$$

The one electron dipole moment is $-ex = -\frac{e^2E}{m\omega^2}$ and the polarization is

$$P = -nex = -\frac{ne^2}{mw^2}\,E \tag{1.8}$$

Where n is the electron number

The function Ɛ at particular frequency ω is $\mathrm{Ɛ}(\omega) = 1 + \frac{P(\omega)}{\mathrm{Ɛ}_o E(\omega)}$ (1.9)

Free electron gas dielectric function is $\varepsilon(\omega) = 1 - \frac{ne^2}{\varepsilon_o m\omega^2}$ (1.10)

The plasma frequency is $\omega_p^2 = \frac{ne^2}{\mathrm{Ɛ}_o m}$ (1.11)

The dielectric function as $\varepsilon(\omega) = 1 - \frac{\omega_p^2}{\omega^2}$ (1.12)

Positive and negative charges are equally concentrated in plasma, a medium in which at least one charge is mobile. These positive and negative charges split from one another in the presence of an external electric field, and this electron can result in collective harmonic oscillation. Permittivity displays negative values when the test frequency (ω) is lower than the plasma oscillation frequency (ω_p). Frequency dependence of permittivity is called dispersion and the corresponding medium is called dispersive.

In dielectric the equation of motion is given by

$$m\frac{d^2x}{dt^2} + m\gamma\frac{dx}{dt} + m\omega^2 x = qE\cos(\omega t) \qquad (1.13)$$

The acceleration of the charges is explained by the first term of the above equation, the damping mechanisms of the system with the damping coefficient are explained by the second term, and the restoring forces with the characteristic frequency $f_0 = \omega_0/2\pi$ are explained by the third term.

The system oscillate at operating frequency $x(t) = x_o e^{-i\omega t}$ (1.14)

The solution of the above equation is given by $x_o = \frac{q/m}{\omega_o^2 - \omega^2 - i\gamma\omega} E_o$ (1.15)

The dipole moment is given by

$$P(t) = qx(t) = \frac{q^2 m}{\omega_o^2 - \omega^2 - i\omega\gamma} E_o e^{-i\omega t} \qquad (1.16)$$

The polarization P, given N molecules per unit volume, is determined by

$$P = N\frac{q^2}{m}\sum_j \frac{f}{\omega j^2 - \omega^2 - i\gamma j\omega} E \qquad P = \varepsilon_o \chi_e E \qquad (1.17)$$

χ_e is the complex susceptibility.

In this model complex dielectric constant is

$$\varepsilon_r = 1 + \frac{Nq^2}{m\varepsilon_o}\sum_j \frac{f_j}{\omega j^2 - \omega^2 - i\gamma j\omega} \qquad (1.18)$$

The electron's mass is denoted by m, its charge by q, and the oscillator's natural frequency is represented by τ_o [41–43].

1.5 Lorentz model

In Lorentz model, electron motion is described by damped harmonic oscillator. The dielectric resonance happens when the frequency of the external electric field is in resonance with the frequency of the dipoles in the material. The permittivity changes from positive to negative just above this resonance frequency. The dielectric resonance is related to both the concentration of electric dipoles and interfacial polarization, in the higher frequency range. Negative permittivity is obtained using the following formula.

$$\varepsilon^* = \varepsilon' - i\varepsilon'' = 1 + \frac{\omega_p^2}{\omega_o{}^2+\omega^2+i\omega\Gamma_L} \tag{1.19}$$

$$\varepsilon' = 1 + \frac{\omega_p^2\,(\omega_o{}^2-\omega^2)}{(\omega_o{}^2-\omega^2)^2+\omega^2\Gamma_L^2} \tag{1.20}$$

The angular frequency is $\omega = 2\pi f$, characteristic frequency is $\omega_o = 2\pi f_0$, ω_p is the plasma frequency Γ_L is the damping constant. Fig.1.5 shows Lorentz type negative permittivity model [44].

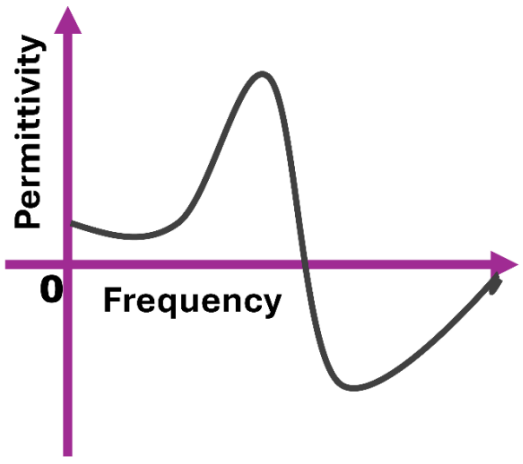

Figure 1.5 Lorentz type permittivity plot model

1.6 Drude model

The explanation for plasma type negative permittivity is given by Drude model. A plasma medium is very similar to a gaseous medium expect that electrons are free and there is no restoring force and the equation (1.18) becomes

$$\varepsilon^* = \varepsilon' - \varepsilon'' = 1 - \frac{\omega_p^2}{\omega^2 - i\omega\Gamma_D}\ ,\ \varepsilon_r{}' = 1 - \frac{\omega_p^2}{\omega^2 + \omega_\tau^2}\ ,\ \omega_p^2 = \frac{n_{eff}e^2}{m_{eff}\varepsilon_o} \qquad (1.21)$$

Γ_D is the damping constant, $\omega_p = 2\pi f_p$ is the Plasmon's angular frequency, m_{eff} and n_{eff} are the effective weight and concentration of electron. In conducting filler, the low frequency plasmonic state of delocalized electrons is the source of the plasma type negative permittivity. In a broad frequency range, the Drude model provides a real section of negative permittivity. that is $\omega < \sqrt{\omega_p^2 - \Gamma_D^2}$. When $\omega > \omega_p$ the permittivity is real and the wave propagate freely. For frequencies below the plasma frequency, permittivity is purely imaginary and the EM wave incident on a plasma will be reflected from the surface. Fig.1.6 shows Drude type negative permittivity model [45,46].

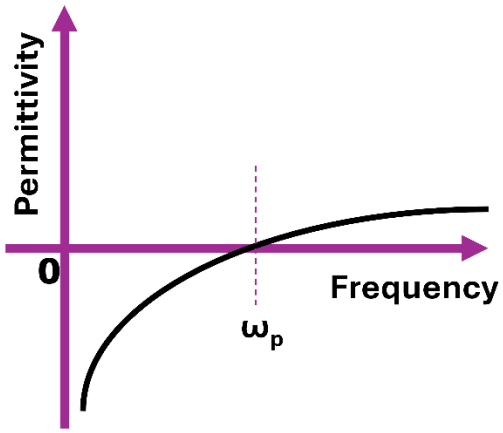

Figure 1.6 Drude type permittivity plot model

1.7 Lorentz - Drude model

The epsilon negative property is the result of the combined action of electric dipole resonance and the low frequency plasmonic state of delocalized electrons, and it is mostly obtained around the percolation zone. This type of negative permittivity is explained by the Lorentz-Drude model.

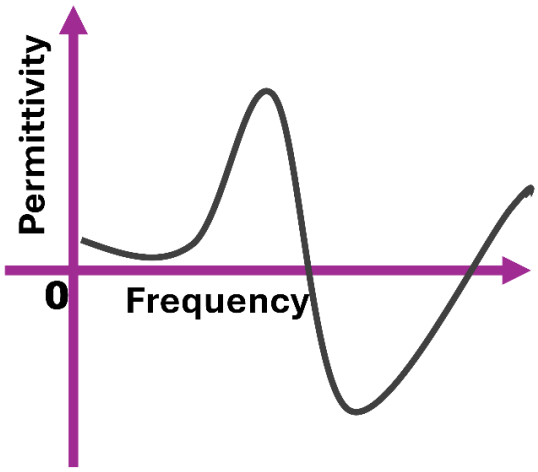

Figure 1.7 Drude - Lorentz type permittivity plot model

The equation is

$$\varepsilon(\omega) = 1 - \frac{\omega_p^2}{\omega^2 + \Gamma_D^2} + \frac{K\omega_L^2(\omega_L^2 - \omega^2)}{(\omega_L^2 - \omega^2)^2 + \omega^2\Gamma_L^2} \qquad (1.22)$$

Γ_L is the damping constant of Lorentz resonance, ω_L is the Lorentz resonance angular frequency, $\omega = 2\pi f$ is the angular frequency, $\omega_p = 2\pi f_p$ is the plasma frequency K is the dc electric susceptibility. Fig.1.7 shows Drude – Lorentz negative permittivity model [37,38].

1.8 Percolation Theory

Percolation behaviours have been widely used because they may be tailored, especially in the case of multifunctional materials. Percolation theory explains why physical properties vary

dramatically close to the percolation threshold *fc*. This theory explains the physical properties in terms of basic law, where

$$\text{Properties } \alpha\ |f_c - f|^{-q} \qquad (1.23)$$

f is the mass fraction f_c is the percolation threshold and q is critical exponent. Particle size, shape, and orientation are geometrical properties of fillers that affect the value of the percolation threshold.

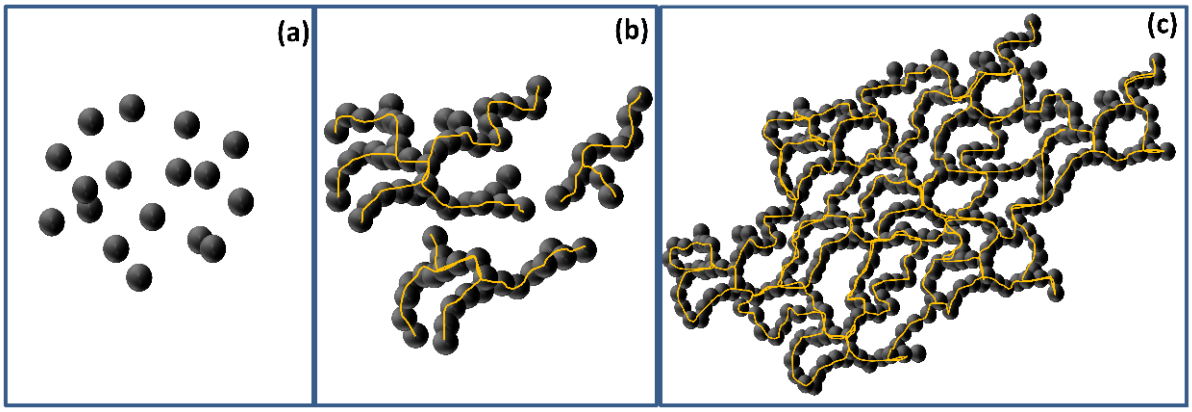

Figure 1.8 Percolation model

Percolation transition strongly depend upon the microstructure of the composites. A filler's distribution inside a matrix is a crucial factor in figuring out the percolation threshold. Below the percolation, conducting filler is randomly distributed as shown in Fig.1.8a. Further increase of content a path for percolation is created as shown in Fig.1.8b. Percolation is achieved in Fig.1.8c by showing continues connecting path [47,48].

1.9 Epsilon Negative Metacomposites

In terms of epsilon negative property, metacomposites offer a flexible substitute for metamaterials due to their price, ease of preparation, and versatility. Polymer-based metacomposites have garnered significant attention recently because of their low manufacturing costs and good processability [49–53]. Both conducting and insulating

polymers are used for the preparation of metacomposites. The conductive polymers have many advantages, but flexibility and processability are very less [54]. But synthesis of non-conducting polymer is very easy, cheap and environmentally stable. In order to improve these insulating polymer's mechanical qualities and conductivity, suitable conducting fillers like metal, alloy and carbon fillers are added and that improves absorption and reflection properties [52,53,55–58]. For the polymers involved in metamaterial system, they were usually considered as insulating host / matrix and suitable conducting inclusion leads to resonance. Negative permittivity that results from a continuous conductive network forming in the polymer matrix. In the visible and ultraviolet spectrum, metals and conductive polymers frequently exhibit negative permittivity, which is a common behaviour.

Negative permittivity has a strong correlation with electron density. Metals and conductive polymers have high electron density and possess huge negative permittivity. To obtain moderate electron density and weakly negative permittivity, insulating polymer matrix with conducting filler composites are mainly used. Random nanocomposites or metacomposites effectively reduce the plasma frequency from visible or UV region and suitable for lower frequency electromagnetic applications [59–66].

1.10 Literature survey - Metacomposites

Recently researchers are mainly focussed on polymer based metacomposites. Non conducting polymers such as Polyvinyl alcohol (PVA), polyurethane (PU), Polydimethylsiloxane (PDMS) etc. are selected as matrix [32,67–70] and carbon materials or metal nanowires or ceramic materials are used as the conducting fillers. Carbon-based materials like, carbon nanotubes (CNTs), carbon fiber, graphene, carbon black, graphite, etc. are appropriate for the creation of metacomposites because of their moderate electron density [71–74]. When such conducting fillers are added to the insulating polymers, their bulk conductivity increase in several orders of magnitude and negative permittivity was obtained. Metal nanostructures are also suitable

for metacomposites fabrication. Metal nanostructures such as Nickel, aluminium, silver etc. and Ceramic composites such as TiN, Ti_3SiC_2 max phase etc. are also used for metacomposites fabrication [75].

1.10.1 Insulating polymers compounding with carbonaceous materials /metal nanostructures /ceramic materials

Composites of polyvinyl alcohol and carbon fibers with adjustable negative permittivity have been reported by Kai Sun et al. Carbon fibres and polyvinyl alcohol composites were prepared by facile impregnation method. Frequency depended permittivity studies of CF/PVA with different PVA content gives negative permittivity with test frequency range of 1 kHz to 1MHz [67]. Biao Zhao and Chul B. Park reported PVDF-Ni chain composites shows negative permittivity and suitable for electromagnetic interference shielding properties. Carbon coated iron nanoparticle – PDMS [32] and MWCNT- PDMS [76] composites are also made to meet metamaterial properties. Graphite-PDMS [70] metacomposites shows negative permittivity at radio-frequency region. Table.1.1 shows polymer based metacomposites with carbon/metal/ ceramic conducting fillers and their negative permittivity models and conductivity.

Table 1.1: A comparison of several polymer matrix metacomposites' negative permittivity and conductivity.

Polymer (vol% or wt %)	Conducting filler (vol% or wt. %)	Test frequency region	Permittivity	Conductivity (S/cm)	Ref
PVA	Graphene (0% - 26%)	10 kHz to 1 MHz	Drude model 1000 - -6 × 10^4	10^{-7} to 10^{-1}	[77]
PVA (0%-35.4%)	Carbon nanofiber	10 kHz to 1 MHz	Drude model -3×10^4 to 0	0.002 -0.035	[67]
PVA	PVA: PVP modified graphene (7.75:1, 3.75:1, 2:1, 1:1, and 1:1.5)	20 kHz to 1 MHz	Drude model 40 to -1200	10^{-6} to 10^{-1}	[68]
PVDF	Carbon nanofiber (1%-3%)	10^3 Hz to 10^7 Hz	0 to -2500	-	[33]

PVDF	PVP modified graphenes (3.75%-25%)	10MHz – 1 GHz	Drude model 100 to -500	0 to .025	[69]
PVDF	Nickel (0.3% to 12%)	10^2 Hz to 10^5 Hz	Drude model 30 to -40000	6.38×10^{-4} to 1.56×10^{-2}	[78]
PVDF	Ti_3SiC_2 max phase (10 % to 85%)	20 MHz to 1 GHz	Drude model 0 to 600 then -400	10^{-3} to 1	[29]
PVDF	Cu Nanowire	20 kHz to 1 MHz	Drude model -1.5×10^3	10^{-3}	[79]
PDMS	Graphene (1wt% to 4 wt. %)	10 kHz to 1 MHz	Drude model 0 to 100 -60000	10^{-7} to 10^1	[25]
PDMS	Carbon coated Fe nanoparticle (5wt % to 50 wt. %)	10^2 to 10^8 Hz	Drude model 4×10^3 to -4000	10^{-8} to 10^1	[32]
PDMS	Graphite (10 wt % to 30 wt. %)	10^2 to 10^8 Hz	Drude model 0 to 100 then -150	10^{-9} to 10^1	[70]
PDMS	Graphene aerogel (5, 7.5, 10, 12.5 mg/mL)	0 to 1 GHz	Drude model 0 to -5×10^3	10 to 20	[80]
Thermoplastic Polyurethane	MWCNT (20 wt% to 60 wt. %)	10 kHz to 1 MHz	Drude model 0 to -6×10^7	0 to $3.5*10^2$	[23]
Polyurethane sponge	Silver nanowire (3.1, 6.3, 7.3, 9.1, 12.3 and 13.2 wt% were	100 kHz to 1 MHz	Drude model 0 to -160	10^{-5} to 10^{-3}	[52]
Acrylic Polyurethane	Graphene (0.9, 1.2, 1.5, 3, 6 vol %)	40 MHz to 1 GHz	Drude model 0 to -6×10^3	0 to 0.06	[81]
Acrylic Polyurethane	Aluminium (3.58, 7.72, 12.54, 18.24, 25.07, 33.42, 43.84, 57.23, 75.07 vol %)	10 MHz to 1 GHz	Drude model 0 to -400	0 to 1.2	[82]
Epoxy	Graphene (4, 10, 15,20,25,30 wt %)	10 MHz to 1 GHz	0 to -1000	0.1 to 10^2	[83]
Epoxy	CNT (1, 5,10,20,30,40,50,60, 70 wt%)	10^7 to 10^9 Hz	2.4×10^2 to -1.2×10^4	-	[84]
Epoxy	Graphene foam (5, 7.5, 10, 12.5 wt. %)	10^7 to 10^9 Hz	0 to -3000	10 to 20	[85]

PET	TiN (0.49, 0.53, 0.61, 0.69, 0.81, 0.85, 0.89 and 0.93) volume fraction	10 MHz to 1GHz	Drude model 0 to -1500	0.01 to 1	[24]
Polyphenylene sulphide	TiN (30,40,50,60,70,80,85 wt%)	10 MHz to 1GHz	Drude model 0 to -3×10^{3}	10^{-3} to 10^{1}	[86]

1.10.2 Ceramic composites

Because of their excellent mechanical and thermal qualities, metacomposites based on ceramics are also attracting increased attention from researchers. Alumina, barium titanate, silicon nitride etc. are used as dielectric matrix and metal particles, conducting polymers, carbon materials, ceramics etc. are used as conducting fillers. Metals have giant negative permittivity at ultraviolet region due to large concentration of free electrons. To reduce this huge negative permittivity suitable dielectric ceramics added to the metal leads to decrease the concentration of electrons. Xiao Sun et.al. reported negative permittivity in molybdenum-alumina composites [87] and used Drude-Lorentz model to analyze negative permittivity. The Drude model can be used to explain the negative permittivity that Ni/alumina and Ag/alumina metacomposites exhibit. Chuanxin Hou et.al reported TiN-alumina metacomposites with negative permittivity at kHz frequencies. Graphene network in alumina ceramic possess plasma like negative permittivity [88].

Barium titanate is also used for metacomposite fabrication as a matrix due to its extraordinary properties such as high permittivity and excellent ferroelectric behaviour [89–91]. Qilin Gu and Zhongyang Wang reported negative permittivity in Cu/$BaTiO_3$ composites that have moderate electrical conductivity and strong thermal conductivity [92]. Negative permittivity caused by dielectric resonance and described by the Lorentz model is obtained when the Cu content is below the percolation threshold. Negative permittivity is caused by plasma oscillations over the percolation threshold, as explained by the Drude model. In both

Ag/$BaTiO_3$ [93] and Fe/$BaTiO_3$ [94] composites, negative permittivity obtained above the percolation threshold and explained by Drude model. Conductive polymers also used for getting negative permittivity. Polyaniline-$BaTiO_3$ composites also shows negative permittivity at lower frequency region [95]. Low frequency plasmonic state is obtained in graphite – $BaTiO_3$ metacomposite. MWCNT/ $BaTiO_3$ metacomposite shows electrical percolation and negative permittivity [96,97]. Z. Wang et al. reported $BaTiO_3$ – Nickel composites with Drude-Lorentz model and Drude model negative permittivity at megahertz region [98]. Table 1.2 shows a comparison of different ceramic matrix-based metacomposites with negative permittivity.

Table.1.2: A comparison of different ceramic matrix metacomposites' negative permittivity and conductivity.

Dielectric Matrix	Conducting Filler	Test frequency region	Permittivity	Conductivity (S/cm)	Ref
Alumina	Molybdenum (10,30,50,60,70 wt%)	10 MHz to 1 GHz	Drude-Lorentz model 50 to -150k	0.001 to 10	[87]
$BaTiO_3$	Nickel (6.98, 10.64, 14.44, 22.44, 26.66, 31.03, 35.58 Vol%)	1 MHz to 1 GHz	Drude-Lorentz model Drude-model	-------	[98]
$BaTiO_3$	Silver (20, 30, 40, 60 wt. %)	10 MHz to 1 GHz	Drude-model 0 to -6×10^6	---------	[93]
$BaTiO_3$	Copper (6.9, 10.6.14.4, 18.3, 22.3, 26.5 wt. %)	10 MHz to 1 GHz	Lorentz model (0 to -2×10^{-3}) Drude model 0 to -10×10^6	--------	[92]
$BaTiO_3$	MWCNT (1, 4, 7,10,12,14 wt. %)	10 MHz to 1 GHz	Drude model 0 to -30000	10^{-3} to 2	[97]
$BaTiO_3$	Graphite (1, 2, 3, 4 wt. %)	0 Hz to 1 MHz	Drude model 0 to -3×10^{-5}	10^{-3} to 1	[96]
Silicon nitride	Graphenes (2, 5, 8, 10wt %)	10 MHz to 1 GHz	Drude model 0 to -6000	10^{-3} to 1	[71]
Silicon nitride	Silver (34, 38, 44, 50 wt. %)	10 MHz to 1 GHz	Drude model 0 to -2500	10^{-3} to 10	[99]

Silicon nitride	Carbon fiber (1, 4, 8, 10,12wt %)	10 MHz to 1 GHz	Drude model 0 to -4000	0.01 to 1	[100]
Alumina	TiN (10%, 20%, 30%, and 40%)	10 kHz to 1 MHz	Drude model 0 to -15×10^{4}	10^{-4} to 10^{-1}	[101]
$CaCu_3Ti_4O_{12}$	Graphitized MWCNT (1,3,5,7,9,11,13,15 wt%)	30 MHz to 1 GHz	Drude-Lorentz model 0 to -2000	10^{-2} to 1	[102]

1.10.3 Ternary metacomposites

For getting weakly negative permittivity binary metal and insulator composites strategy is employed in MWCNT/TiN/CCTO ($CaCu_3Ti_4O_{12}$) ternary composites [103]. Titanium nitride is a good candidate for metacomposites with better physiochemical stability and lower electrical conductivity. In this case, MWCNT acted as a bridge to allow free electron transfer between TiN particles, reducing the total electron density and paving the way for weakly negative permittivity. Both Lorentz type and Drude model negative permittivity obtained in ternary metacomposites. Additionally, ternary composites made of graphene, CNT, and CCTO have epsilon near zero and epsilon negative properties [104]. Weakly negative permittivity can be obtained by using the conductive nature of graphene and the connectivity of carbon nanotubes. Drude – Lorentz type negative permittivity is obtained in this composite. IBLC (Internal barrier layer capacitor) structure of CCTO composite enhance leakage current and this benefitted for decreasing positive permittivity and got epsilon near zero behaviour. Similar behaviour is obtained in graphene-carbon black-CCTO composites [105]. The heterogeneous dual unit may be benefitted for getting dielectric resonance near percolation. Lorentz and Drude type negative permittivity is gained in Fe_3O_4-graphene- phenolic resin composites [106].

1.11 Electromagnetic interference shielding

Technological advancements have significantly changed our way of life. Communication devices such as laptops, smartphones, global positioning systems (GPS), Bluetooth, Wi-Fi

routers, and others are prevalent in the modern man's surroundings. All electronic devices emit or radiate waves especially those operating within the radio or microwave frequency range. These harmful electromagnetic waves can cause a variety of problems, such as information security breaches, malfunctioning electronic equipment, and broken vital systems. The disruptive phenomenon caused by electromagnetic waves is referred to as electromagnetic interference (EMI). In addition to data loss and technological device malfunction, electromagnetic radiation intake can lead to a number of health problems, such as fatigue, insomnia, anxiety, irritability, infertility, and even cancer [107] [108]. The development of appropriate shielding materials is required to prevent or mitigate the problem of signal interferences from communication or electrical devices [109–111].

A certain material is used in the shielding of EMI to reflect, absorb, or both in order to effectively create a barrier against electromagnetic (EM) waves that interfere with one another. The demand of EMI shielding materials increases annually particularly in industries such as aerospace, electrical, communication, and military sectors. EMI shielding materials are utilised as anti-radiation devices and stealth surface coatings in cars, battleships, and aeroplanes to protect people's health and electronic devices from electromagnetic fields. Even while reducing or eliminating, environmental pollution is gaining more and more attention, the majority of people are still unaware of EMI contamination because it cannot be physically touched, tasted, seen, or smelled. With the increasing usage of electronic gadgets and communication instruments in a wide range of commercial, military, and scientific applications, modern civilization is increasingly worried about protecting itself against radio frequency and microwave radiation. Therefore, a lot of industrial sectors are working hard to produce EMI shielding materials [112,113].

Modern electrical equipment uses a wide range of frequency bands for different applications. EMI issues can arise anywhere in the electromagnetic spectrum. Since most issues arise in the

radio and microwave frequency range (100 kHz to 40 GHz), this range is regarded as the typical shielding range. There are several applications for the S-band (2 - 4 GHz), such as television, radio, and wireless networking. Next, the C-band is widely used for long-distance radio equipment, communications, and Wi-Fi (4 - 8.2 GHz). Moreover, radar, wireless computer networks, air traffic management, satellite communication, defence tracking, and vehicle speed detection for law enforcement all make use of the X-band (8.2–12.4 GHz). Because most signal disruption occurs within the X-band frequency range, the current work is primarily focused on producing EMI shielding materials appropriate in this range, highlighting the need for effective shielding solutions customized to the X-band region [114–116].

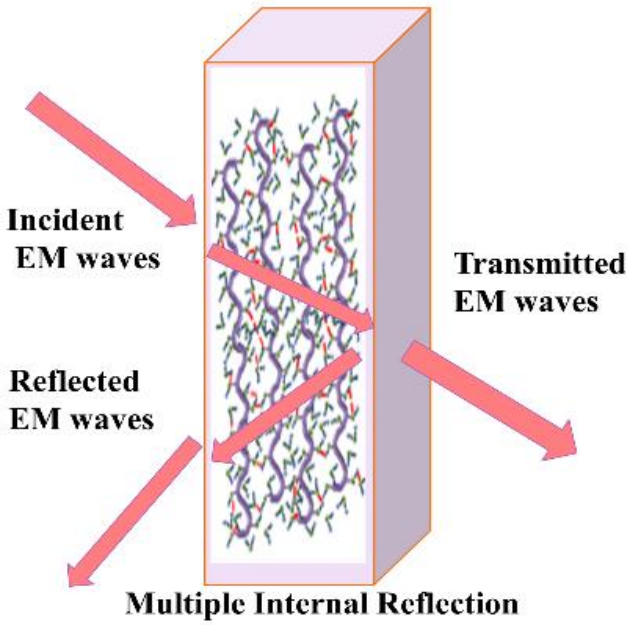

Figure 1.9 Schematic of the EMI shielding mechanisms

One of the most efficient ways to stop the wave is by EMI shielding, which doesn't need a circuit design. Additionally, shielding lessens waveform distortions and cross talk without sacrificing system dependability. Any shielding material's performance can be evaluated using the standard metric known as EMI shielding effectiveness (SE_T). Three mechanisms—reflection (R), absorption (A), and multiple internal reflections (M) of the EM waves—were used to achieve the EMI shielding and the Fig.1.9 shows shielding mechanisms. Reflection and

absorption decrease the energy of electromagnetic waves when they hit on shielding material. The residual electromagnetic wave energy exits the EMI shielding material after passing through the material via repeated internal reflections (M). The shielding efficiency by reflection (SE_R), multiple reflections (SE_M), and absorption (SE_A) of electromagnetic waves adds up to the shielding effectiveness of the material, as per the principles of electromagnetic shielding (EMI) [117]. Total shielding efficiency is given by

$$SE_T = SE_R + SE_A + SE_M \quad (1.24)$$

SE_M is negligible when $SE_A \geq 10\ dB$.

An EMI shielding material's overall performance is influenced by its capacity to absorb and/or reflect electromagnetic radiation. The ability of a material to produce dielectric, magnetic, or conductive losses during an electromagnetic wave's passage through it determines how much of the wave is absorbed by the material. Dielectric loss happens when the material's internal dipoles' periodic rotation exceeds by the electromagnetic field's frequency. This is caused by polarization effects. Conversely, materials with a high concentration of free electronic carriers experienced conduction losses because they might cause a conduction current to be induced in the presence of an electromagnetic wave, which would attenuate the energy of the EM wave and produce heat. The magnetic loss process in magnetic materials was found in contrast to electrical losses (conductive and dielectric losses) due to a variety of phenomena, including hysteresis loss, eddy current, domain-wall resonance, natural resonance, etc. The impedance mismatch between the shielding material's surface and free space is the cause of the reflection losses. The wave is deflected away from the material's surface and away from its bulk as a result of this mismatch in impedance. When the shielding material is thin, numerous reflection losses contribute significantly to total shielding efficiency. When thick conductive shielding materials are used, the SE_M component becomes insignificant at higher frequencies. From the above EMI shielding principles, it can be reliably deduced that permittivity, permeability,

electrical conductivity, thickness, size, distribution, and filler morphology are among the many material qualities that affect the efficiency of EMI shielding materials [118,119].Fig.1.10 shows factors affecting EMI shielding materials.

1.11.1. Factors affecting EMI shielding

1.11.1.1 Permittivity

The material's permittivity has a big impact on how well it shields. Interfacial polarization, orientational, electrical, and ionic processes play a role in controlling the dielectric loss. The material's bound charges are responsible for the orientational and ionic polarization. Interfacial polarization results from the accumulation of space charges caused by the variations in electrical conductivity and dielectric constant between two separate materials. At epsilon close to zero, real permittivity gives perfect absorption. The delocalized electrons are responsible for the reflection-dominant shielding mechanism and the high SE_T values seen over the testing frequency range, which are linked to the negative real permittivity. Electronic and Ionic polarization mechanisms are also active at the low frequencies. While dipolar polarization is restricted up to sub-IR, Ionic is restricted to Sub-Optical frequency range. Electronic polarisation exists even after the Optical range. In addition, dipole polarisation resulted from residual groups and flaws in the material, which are largely determined by the sintering process, the materials used, the production methods, and other factors [120]. Dielectric losses occur from the dissipation of internal energy in a material when an electric field is applied. Polarization loss and conduction loss work together to produce the dielectric losses. Conduction losses are associated with the material's conduction mechanism. Electromagnetic waves are dissipated by the material's charge carrier mobility. Static charges interacting with other particles in the medium also resulted in the loss of energy for the electromagnetic wave. It is reasonable to say that any of the polarisation techniques can cause dielectric loss at lower frequencies (MHz frequency range), but only a limited number of polarisation mechanisms can

cause dielectric loss at higher frequencies (GHz frequency range), which leads to a decrease in dielectric loss at higher frequencies [121].

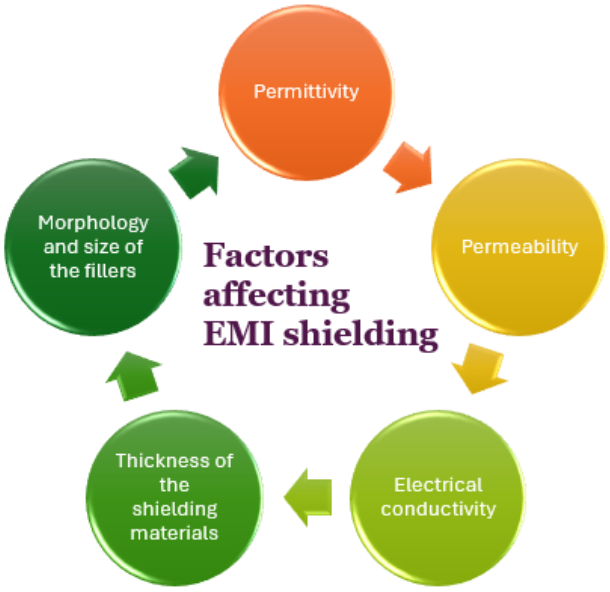

Figure 1.10 Factors affecting EMI shielding materials

1.11.1.2 Permeability

EMI shielding has a significant impact on magnetic permeability ($\mu' - j\mu''$). Magnetic loss is correlated with the material's imaginary permeability (μ''), but magnetic energy storage is connected to the real permeability (μ'). Magnetic loss is made up of residual loss, magnetic hysteresis loss, and eddy current loss. The current produced in a magnetic material by a fluctuating magnetic field is known as eddy current. In response to the entering electromagnetic field, they release heat. The electrical conductivity, permeability, and thickness of the material all affect Eddy current loss. In addition, morphology, particle size, surface roughness, domain orientation, and other variables affect eddy current loss. The loss is higher for conducting and thicker samples. Magnetic hysteresis loss is caused by irreversible domain movement and magnetic moment rotation, and it is mostly determined by the shielding material's magnetic characteristics. Residual loss is the term used to describe magnetic losses resulting from many reasons such as temperature changes, ferromagnetic and

domain wall resonance, etc. In general, polymers are not magnetic. The magnetic characteristics of the polymer composites have been enhanced by the addition of magnetic elements like hexaferrite and ferrites. Magnetic filler can produce magnetic dipoles and absorb electromagnetic radiation when it is applied to a polymer composite. By increasing the material's magnetic loss enhances the EM wave absorption [121].

1.11.1.3 Electrical conductivity

One of the key components in the preparation of EMI shielding materials is thought to be the electrical conductivity of the materials. Metals are good electrical conductors. Metal-based EMI shielding materials can increase electromagnetic wave reflections because of their high conductivity. On the other hand, the metal-based EMI shielding materials' significant secondary reflections also increase their reflective power.

Conversely, polymers have an insulating property. Composites can have conductive particles added to them, such as metal- and carbon-based nanofillers, to increase their electrical conductivity. The polymer composite will attenuate electromagnetic radiation by producing mobile charge carriers by the incorporation of nanofillers. Filler loading causes an increase in charge carrier mobility in the composite, which increases electrical conductivity. Electrical conductivity (σ) affects both EM wave reflection and dielectric loss (ε"). Achieving the ideal balance between dielectric loss and reflection can be difficult. Consequently, matching impedance is made simpler by a sufficient electrical conductivity, which also balances dielectric loss and EM wave reflection. [122,123].

1.11.1.4 Morphology, Size, Distribution, Thickness

The particle's size and dispersion have a significant impact on the shielding effectiveness. An essential component of increased shielding effectiveness is the addition of nanofillers. Nanoparticles have higher inherent characteristics and a greater surface area than micro and

macro particles. Shielding efficiency is also influenced by the morphology of the nano fillers. In the polymer composites, 1D and 2D anisotropic conductive nanofillers offer appropriate electrical conductivity at reduced filler loadings. Multiple interfaces are formed in polymer composites including fillers with large aspect ratios and surface area; this leads to the accumulation of bound charges at the contact, which causes interfacial polarization. It follows that multi-interfaces in polymer composites are likely to be highly advantageous for the electric loss-induced attenuation of electromagnetic waves. The multiple reflections of electromagnetic waves are improved in porous composites due to the porosity formed in the polymer composites, which increases the EMI shielding performance. Another crucial design factor in the preparation of EMI shielding materials is thickness, as the thickness of the shielding material grows, the EMI shielding performance also increases [117,118].

1.11.2 EMI shielding effectiveness

The logarithmic ratio of the entering (Pi) to leaving (Po) power of radiation is known as the total electromagnetic interference shielding effectiveness (EMI SE).

$$SE(dB) = -10 \log (P_o/P_i) \qquad (1.25)$$

Decibels (dB) are used to express the EMI SE. In practical applications, 20–30 dB EMI SE, or 99–99.9% shielding, is thought to be a sufficient amount of shielding for typical applications. Vector network analysers (VNA) are used in EMI shielding tests [124–126].

1.11.3 Metacomposites for EMI shielding application

Negative permittivity metacomposites are used mainly in electromagnetic interference shielding. Positive electromagnetic characteristics are present in conventional shielding materials. Before discovering the negative permittivity property, researchers focused on increasing the permittivity to enhance the electromagnetic shielding effect of materials. This

approach was based on the principle that when an electromagnetic wave passes through a dielectric material, a higher permittivity requires more energy for dipole polarization within the material, leading to a stronger attenuation of the electromagnetic wave. Electromagnetic waves will be reflected by the hidden field in the negative permittivity materials, which offers a design suggestion for novel electromagnetic shielding materials.

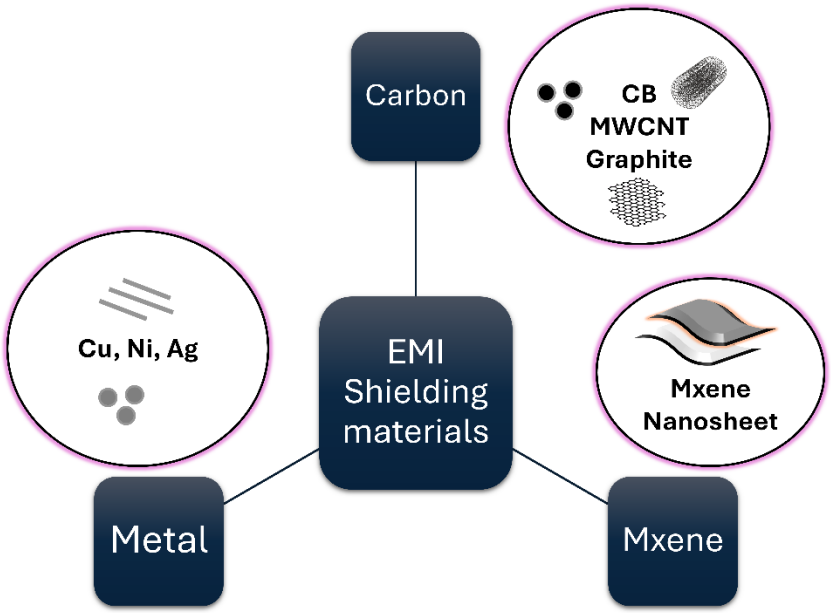

Figure 1.11 Mainly used EMI shielding materials

Park et al., for example, created Ni-chain/poly (vinylidene fluoride) metacomposites that exhibited negative permittivity at frequencies lower than 100 kHz and an average shielding effectiveness (SE) of 35.4 dB throughout a range of 18–26.5 GHz [78]. Negative permittivity and electromagnetic interference shielding efficiency in the 2–18 GHz range were reported by Cheng et al [127]. In a sandwich-like structure including Bucky paper, Yttrium iron garnet and graphene aerogel. Luo et al. observed negative permittivity and EMI shielding performance in the 2–18 GHz range [128]. At a filler level of 25 weight percent, the TiO_2/MXene metacomposites exhibit an excellent total EMI shielding performance of 73.98 dB in the X band area [129]. In the X-band region, the hollow carbon nanofiber/polyaniline

metacomposites exhibit outstanding EMI shielding ability [130]. The mainly used Metacomposite EMI shielding materials are given in Fig.1.11.

1.12 Aim and scope of the work

The main aim of this research work is to fabricate metacomposite using polymer as the matrix and different carbonaceous conducting materials as fillers for improving the properties of composite film. For this, Polyvinyl alcohol is chosen as the matrix. Polyvinyl alcohol is a water soluble, biocompatible, semi crystalline green polymer. Then, Different carbon nanostructures such as carbon black, MWCNT and graphite are chosen as the conducting fillers. Simple and low-cost, die – casting procedure is followed for the fabrication of flexible polymer composite films. The concentration of the conducting filler is varied for improving the properties of composite films. For improving mechanical and thermal properties of the films, nitrides and ternary oxides are also used as the fillers. Applicability and performance of the sample is to be investigated. For this broadband dielectric spectrometer and vector network analyser are used. Highly conductive flexible polymer composite films are suitable for variety of electronic applications and also used as EMI shielding materials.

1.13 Objectives and Methodology

The main objective of the proposed work is to synthesis flexible polymer metacomposite films by properly intercalating carbon-based nanomaterials. For this, different carbon nanostructures such as carbon black, MWCNT and graphite flakes are chosen as the conducting fillers. The structure of these carbon materials is given in Fig.1.12. For getting flexible polymer film, water soluble polyvinyl alcohol is used as the matrix in the whole study. Tuning of negative permittivity of the composite by changing the concentration of conducting filler is the main focus of this work. Fabrication of polymer composite film with homogeneously dispersed filler

being the challenging task for metacomposites preparation. Here, simple and low-cost, die – casting procedure is followed for the fabrication of flexible metacomposite films.

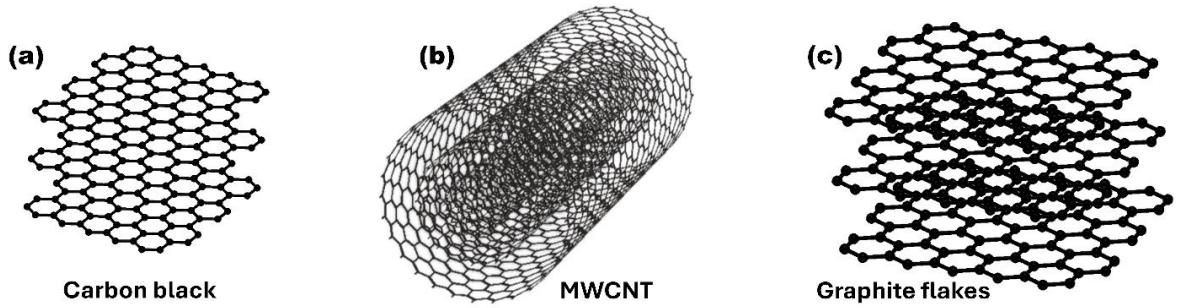

Figure 1.12 Different carbon nanostructures, Carbon black (a), MWCNT (b), Graphite flakes (c)

One of the low-cost conducting materials from carbon family, carbon black, is identified as the conducting filler. Carbon black has a spherical nanoparticle-like structure. The structural, morphological, dielectric and EMI shielding properties are to be analyzed to optimize the permittivity change and its EMI shielding efficiency. Another carbon nanostructure, MWCNT, is fixed as the filler in the PVA matrix. MWCNT is a 2D carbon material with good electrical conductivity. Here also, structural, morphological, thermal, dielectric and EMI shielding performance are to be analyzed in detail. Then, sheet like carbon nanostructure, graphite, is selected as the conducting filler in the PVA matrix. In addition to this a ceramic metacomposite is also designed to study the dielectric and EMI shielding behaviour. For this, $BaTiO_3$ is chosen as the matrix and TiN as the conducting filler. $BaTiO_3$ is a good dielectric material it also shows ferroelectric property. TiN is a good conducting filler with semi metallic nature and high thermal and mechanical stability. $BaTiO_3$ will be synthesized via solvothermal method. In order to impart flexibility to the composite, we will be adding this ceramic composite into PVA matrix. A detailed analysis on the dielectric and EMI shielding characteristics is planned for these three component composite materials. Further to improve the conductivity, carbon nanostructures are chosen as additional fillers to make a four-component system. Carbon black,

MWCNT and graphite are identified as filler components. Dielectric and EMI shielding performance of the samples will also be measured.

Solvothermal synthesis method will be used for the synthesis of ceramic $BaTiO_3$ nanoparticle. Die – casting procedure will be followed for the fabrication of flexible polymer films. Structural analysis of the synthesized samples will be carried out by using X-ray diffraction (XRD), Fourier transform infrared spectroscopy (FTIR) and Raman spectroscopy. Size and morphological analysis of the synthesized sample will be carried out using Sanning Electron Microscope (SEM) and Transmission electron microscope (TEM). Thermogravimetric analysis can be used to check thermal stability of the sample. Broadband dielectric spectrometer (BDS) is going to use for the dielectric measurement. Vector network analyser will be used for the scattering parameter measurements.

****

References

[1] W. J. Stewart, J. Opt. U. K. **19**, 1 (2017).
[2] D. A. Lee, L. J. Vedral, D. A. Smith, R. L. Musselman, and A. O. Pinchuk, AIP Adv. **5**, (2015).
[3] P. M. Valanju, R. M. Walser, and A. P. Valanju, Phys. Rev. Lett. **88**, 187401 (2002).
[4] S. Foteinopoulou, E. N. Economou, and C. M. Soukoulis, Phys. Rev. Lett. **90**, 107402 (2003).
[5] V. G Vesalago, Physics **10**, 509 (1968).
[6] J. B. Pendry, Phys. Rev. Lett. **76**, 4773 (1996).
[7] J. B. Pendry, A. J. Holden, D. J. Robbins, and W. J. Stewart, IEEE Trans. Microw. Theory Tech. **47**, 2075 (1999).
[8] R. A. Shelby, D. R. Smith, and S. Schultz, Science **292**, 77 (2001).
[9] G. Lipworth, J. Ensworth, K. Seetharam, Da Huang, J. S. Lee, P. Schmalenberg, T. Nomura, M. S. Reynolds, D. R. Smith, and Y. Urzhumov, Sci. Rep. **4**, 3642 (2015).
[10] E. Plum, J. Zhou, J. Dong, V. A. Fedotov, T. Koschny, C. M. Soukoulis, and N. I. Zheludev, Phys. Rev. B **79**, 035407 (2009).
[11] H. Chen, B. Wu, B. Zhang, and J. A. Kong, Phys. Rev. Lett. **99**, 063903 (2007).
[12] Y. Cheng, H. Yang, Z. Cheng, and N. Wu, Appl. Phys. Mater. Sci. Process. **102**, 99 (2011).
[13] P. Markoš and C. M. Soukoulis, Opt. Lett. **28**, 846 (2003).
[14] D. R. Smith, W. J. Padilla, D. C. Vier, and S. Schultz, Phys. Rev. Lett. **84**, 4184 (2000).
[15] F. J. Rachford, D. L. Smith, P. F. Loschialpo, and D. W. Forester, Phys. Rev. E **66**, 036613 (2002).
[16] Z. Chen, B. Guo, Y. Yang, and C. Cheng, Phys. B Condens. Matter **438**, 1 (2014).
[17] A. Pandey and S. B. Rana, **17**, 359 (2016).
[18] Y. Liu and X. Zhang, Chem. Soceity Rev. **40**, 2494 (2011).
[19] S. Roychoudhury, V. Rawat, A. H. Jalal, S. N. Kale, and S. Bhansali, Biosens. Bioelectron. **86**, 595 (2016).
[20] A. A. A. Abdelrehim and H. Ghafouri-shiraz, Microw. Opt. Technol. Lett. **58**, 382 (2015).
[21] J. Bonache, F. Martı, F. Falcone, J. D. Baena, T. Lopetegi, J. Garcı, M. A. G. Laso, I. Gil, and A. Marcotegui, Microw. Opt. Technol. Lett. **46**, 508 (2005).
[22] I. Arnedo, J. Illescas, M. Flores, T. Lopetegi, M. A. G. Laso, F. Falcone, J. Bonache, and J. Garcı, IET Microw. Antennas Propag. **1**, 65 (2007).
[23] Z. Wang, K. Sun, Q. Jiang, K. Yin, L. Xie, S. Cao, Y. Zhang, X. Li, and R. Fan, Mater. Today Commun. **24**, 101230(1 (2020).
[24] C. Xu, Y. Qu, G. Fan, P. Xie, H. Ren, J. Chen, Y. Liu, Y. Wu, and R. Fan, J. Mater. Sci. Mater. Electron. **29**, 15994 (2018).
[25] K. Sun, J. Dong, Z. Wang, Z. Wang, G. Fan, Q. Hou, L. An, M. Dong, R. Fan, and Z. Guo, J. Phys. Chem. C **123**, 23635 (2019).
[26] S. T. Chui and L. Hu, Phys. Rev. B **65**, 144407 (2002).
[27] J. Zhu, S. Wei, L. Zhang, Y. Mao, J. Ryu, A. B. Karki, and P. Young, J. Mater. Chem. **22**, 342 (2011).
[28] Z. Wang, K. Sun, P. Xie, Q. Hou, Y. Liu, Q. Gu, and R. Fan, Acta Mater. **185**, 412 (2020).
[29] Y. Liu, Y. Qu, J. Xin, Z. Wang, G. Fan, P. Xie, and K. Sun, J. Inorg. Organomet. Polym. Mater. **29**, 248 (2019).
[30] H. Gu, X. Xu, M. Dong, P. Xie, Q. Shao, R. Fan, C. Liu, S. Wu, R. Wei, and Z. Guo, Carbon **147**, 550 (2019).
[31] K. Sun, J. Xin, Y. Li, Z. Wang, Q. Hou, X. Li, X. Wu, R. Fan, and K. Leong Choy, J. Mater. Sci. Technol. **35**, 2463 (2019).

[32] H. D. Shetty and V. Prasad, Mater. Chem. Phys. **196**, 153 (2017).
[33] L. Sun, N. Wu, and R. Peng, J. Appl. Polym. Sci. **137**, 49582(1 (2020).
[34] X. Yao, X. Kou, J. Qiu, and M. Moloney, RSC Adv. **6**, 35378 (2016).
[35] X. Yao, X. Kou, J. Qiu, and M. Moloney, J. Phys. Chem. C **120**, 4937 (2016).
[36] P. Xie, Z. Wang, K. Sun, C. Cheng, Y. Liu, and R. Fan, Appl. Phys. Lett. **111**, 112903 (2017).
[37] H. Wu, X. Huang, and L. Qian, Eng. Sci. **2**, 17 (2020).
[38] P. Di Sia, Nanoscale Syst. Math. Model. Theory Appl. **3**, 1 (2014).
[39] David J Griffiths, *Introduction to Electrodynamics, 3rd Edtion* (1999).
[40] S. Anantha Ramakrishna, Rep. Prog. Phys. **68**, 449 (2005).
[41] C. Kittel, John wiley & Sons, Inc.
[42] P. W. Milonni, *Fast Light , Slow Light and Left-Handed Light P W Milonni* (2004).
[43] J. D. Jacksons, *Classical Electrodynamics, 8th Edition* (1962).
[44] Horiba, Tech. Notes (2017).
[45] E. M. Chudnovsky, Phys. Rev. Lett. **99**, 206601 (2007).
[46] R. W. Z. and N. Engheta, *Double-Negative (DNG) Metamaterials 1* (2006).
[47] C. W. Nan, Y. Shen, and J. Ma, Annu. Rev. Mater. Res. **40**, 131 (2010).
[48] K. Sun, Z. D. Zhang, L. Qian, F. Dang, X. H. Zhang, and R. H. Fan, Appl. Phys. Lett. **108**, 061903 (2016).
[49] J. Dai, H. Luo, M. Moloney, and J. Qiu, ACS Appl. Mater. Interfaces **12**, 22019 (2020).
[50] C. Zhang, Z. Shi, F. Mao, C. Yang, X. Zhu, J. Yang, H. Zuo, and R. Fan, ACS Appl. Mater. Interfaces **10**, 26713 (2018).
[51] S. P., A. R., B. M., M. S. T.H., K. Sridharan, and S. Swaminathan, Mater. Today Commun. **34**, 105287 (2023).
[52] Z. Wang, K. Sun, H. Wu, P. Xie, Z. Wang, X. Li, and R. Fan, J. Mater. Sci. **55**, 15481 (2020).
[53] B. Fan, Y. Liu, D. He, and J. Bai, Appl. Phys. Lett. **112**, 052902 (2018).
[54] K. Namsheer and C. S. Rout, RSC Adv. **11**, 5659 (2021).
[55] K. Sun, P. Xie, Z. Wang, T. Su, Q. Shao, J. Ryu, X. Zhang, J. Guo, A. Shankar, J. Li, R. Fan, D. Cao, and Z. Guo, Polymer **125**, 50 (2017).
[56] Z. Shi, R. Fan, Z. Zhang, K. Yan, X. Zhang, K. Sun, X. Liu, and C. Wang, J. Mater. Chem. C **1**, 1633 (2013).
[57] H. Kavas, M. Günay, A. Baykal, M. S. Toprak, H. Sozeri, and B. Aktaş, J. Inorg. Organomet. Polym. Mater. **23**, 306 (2013).
[58] D. Jiang, V. Murugadoss, Y. Wang, J. Lin, T. Ding, Z. Wang, Q. Shao, C. Wang, H. Liu, N. Lu, R. Wei, A. Subramania, and Z. Guo, Polym. Rev. **59**, 280 (2019).
[59] H. Massango, T. Tsutaoka, T. Kasagi, S. Yamamoto, and K. Hatakeyama, J. Appl. Phys. **121**, 103902 (2017).
[60] T. Tsutaoka, T. Kasagi, S. Yamamoto, and K. Hatakeyama, Appl. Phys. Lett. **102**, 181904 (2014).
[61] D. Schurig, J. J. Mock, B. J. Justice, S. A. Cummer, J. B. Pendry, A. F. Starr, and D. R. Smith, Science **314**, 977 (2006).
[62] W. Tang, L. Wang, X. Chen, C. Liu, A. Yu, and W. Lu, Nanoscle **8**, 15196 (2016).
[63] Q. Chen, Nanoscale **5**, 9615 (2013).
[64] K. Sun, R. Fan, X. Zhang, Z. Zhang, Z. Shi, N. Wang, P. Xie, Z. Wang, G. Fan, H. Liu, C. Liu, T. Li, C. Yan, and Z. Guo, J. Mater. Chem. CMaterials Chem. C **6**, 2925 (2018).
[65] T. Ergin, Science **328**, 337 (2010).
[66] C. Liu and N. Behdad, J. Appl. Phys. **113**, 064909 (2013).
[67] K. Sun, J. Qin, Z. Wang, Y. An, X. Li, B. Dong, X. Wu, Z. Guo, and R. Fan, Surf. Interfaces **21**, 100735 (2020).
[68] Z. Wang, K. Sun, J. Tian, Q. He, P. Yang, W. Duan, P. Xie, Q. Hou, and R. Fan, J. Mater. Sci. Mater. Electron. **32**, 23081 (2021).
[69] Z. Sun, Z. Yan, R. Yin, X. Huang, K. Yue, A. Li, and L. Qian, Compos. Commun. **17**, 18 (2020).

[70] H. D. Shetty, K. P. Maity, and V. Prasad, Surf. Interfaces **21**, 100670 (2020).
[71] G. Palareti, C. Legnani, B. Cosmi, E. Antonucci, N. Erba, D. Poli, S. Testa, A. Tosetto, V. De Micheli, A. Ghirarduzzi, M. R. Veropalumbo, U. M. Chiara, D. Prisco, O. Paoletti, A. Falanga, S. Luigi, M. Donadini, E. Rancan, R. Quintavalla, P. M. Ferrini, R. C. Santoro, F. Orlandini, R. Benedetti, M. Cattaneo, F. Lussana, E. Bertinato, R. Cappelli, A. M. Pizzini, L. Angeloni, A. D'angelo, L. Crippa, R. Bortolotti, and M. R. Vandelli, J. Am. Ceram. Soceity **38**, 42 (2016).
[72] Z. Guo, A. Li, Z. Sun, Z. Yan, H. Liu, and L. Qian, Appl. Surf. Sci. **613**, 156074 (2023).
[73] B. Fan, Y. Liu, D. He, and J. Bai, Appl. Phys. Lett. **112**, 052902 (2018).
[74] J. Zhu, H. Gu, Z. Luo, N. Haldolaarachige, D. P. Young, S. Wei, and Z. Guo, Langmuir **28**, 10246 (2012).
[75] S. P, D. M. Vidyadharan, K. Sridharan, M. S. T. H, B. M, and S. Swaminathan, Mater. Chem. Phys. **317**, 129156 (2024).
[76] Z. Wang, X. Li, L. Wang, Y. Li, J. Qin, P. Xie, Y. Qu, K. Sun, and R. Fan, Adv. Compos. Hybrid Mater. **3**, 1 (2020).
[77] K. Sun, Z. Wang, J. Xin, Z. Wang, P. Xie, G. Fan, V. Murugadoss, R. Fan, J. Fan, and Z. Guo, Macromol. Mater. Eng. **305**, 1900709 (2020).
[78] B. Zhao and C. B. Park, J. Mater. Chem. C **5**, 6954 (2017).
[79] K. Sun, A. Ma, P. Yang, J. Qi, Y. Lei, F. Zhang, W. Duan, and R. Fan, Polymers **15**, 4486 (2023).
[80] G. Z. Ni, Jingnan,Zhan Ruoyu , Qiu Jun, Fan Binbin, Dong Binbin, J. Mater. Chem. C **8**, 11748 (2020).
[81] H. Wu, Y. Qi, Z. Wang, W. Zhao, X. Li, and L. Qian, Compos. Sci. Technol. **151**, 79 (2017).
[82] Z. Wang, K. Sun, P. Xie, Y. Liu, Q. Gu, and R. Fan, Compos. Sci. Technol. **188**, 107969 (2020).
[83] K. Sun, J. Xin, Z. Wang, S. Feng, Z. Wang, R. Fan, H. Liu, and Z. Guo, J. Mater. Sci. Mater. Electron. **30**, 14745 (2019).
[84] H. Luo and J. Qiu, Ceram. Int. **45**, 843 (2019).
[85] J. Ni, R. Zhan, and J. Qiu, Org. Electron. **82**, 105706 (2020).
[86] Y. Liu, G. Fan, Y. Qu, P. Xie, Z. Wang, Z. Zhang, R. Fan, and X. Yin, J. Mater. Sci. Mater. Electron. **29**, 12144 (2018).
[87] X. Sun, J. Shen, C. Cheng, T. Wang, Y. Liu, and R. Fan, Ceram. Int. **45**, 16618 (2019).
[88] C. Hou, G. Fan, X. Xie, X. Zhang, X. Sun, Y. Zhang, B. Wang, W. Du, and R. Fan, J. Alloys Compd. **855**, 157499 (2021).
[89] W. Watson, Phys. Rev. **71**, 890 (1947).
[90] H. Fu and L. Bellaiche, Phys. Rev. Lett. **91**, 257601 (2003).
[91] K. Tewatia, K. Tewatia, A. Sharma, M. Sharma, and A. Kumar, Mater. Today Proc. **44**, 4548 (2021).
[92] Z. Wang, K. Sun, P. Xie, Y. Liu, Q. Gu, R. Fan, and J. Wang, J. Materiomics **6**, 145 (2020).
[93] Z. Wang, P. Xie, G. Fan, Z. Zhang, Y. Liu, Q. Gu, and R. Fan, Ceram. Int. **46**, 9342 (2020).
[94] Y. Liu, C. Xu, H. Ren, Z. Wei, and Z. Zhang, World Sci. **13**, 2050017 (2020).
[95] X. Zhang, S. Wei, N. Haldolaarachchige, H. A. Colorado, Z. Luo, D. P. Young, and Z. Guo, J. Phys. Chem. C **116**, 15731 (2012).
[96] X. T. Song, G. Shi, G. Fan, Y. Liu, and R. Fan, Ceram. Int. **48**, 832 (2022).
[97] H. Ren, Z. Wang, G. Fan, Y. Qu, C. Xu, J. Chen, Y. Jiang, and Y. Liu, J. Mater. Sci. Mater. Electron. **30**, 10138 (2019).
[98] Z. Wang, K. Sun, P. Xie, Q. Hou, Y. Liu, Q. Gu, and R. Fan, Acta Mater. **185**, 412 (2020).
[99] C. Cheng, Y. Jiang, X. Sun, J. Shen, T. Wang, G. Fan, and R. Fan, Compos. Part Appl. Sci. Manuf. **130**, 105753 (2020).

[100] C. Cheng, Y. Liu, S. Shi, R. Ma, T. Wang, Q. Zheng, Y. Zhao, X. Yu, J. Shen, and R. Fan, Ceram. Int. **47**, 35201 (2021).
[101] G. Fan, Y. Zhao, J. Xin, Z. Zhang, P. Xie, C. Cheng, Y. Qu, Y. Liu, K. Sun, and R. Fan, J. Am. Ceram. Soc. **103**, 403 (2019).
[102] К. В. Иванов, А. В. Носков, О. В. Алексеева, and А. В. Агафонов, Compos. Commun. J. **66**, 464 (2021).
[103] K. Sun, P. Yang, Q. He, J. Tian, W. Duan, X. Wu, Y. Qu, and H. Du, Ceram. Int. **47**, 32297 (2021).
[104] R. Ma, C. Cheng, Y. Qu, and R. Fan, Ceram. Int. **47**, 9971 (2021).
[105] Y. Qu, J. Lin, J. Wu, Z. Wang, K. Sun, M. Chen, B. Dong, Z. Guo, and R. Fan, J. Phys. Chem. C **124**, 23361 (2020).
[106] H. Wu, Y. Zhang, R. Yin, W. Zhao, X. Li, and L. Qian, Adv. Compos. Hybrid Mater. **1**, 168 (2017).
[107] J. T. Orasugh and S. S. Ray, ACS Omega **8**, 8134 (2023).
[108] A. Zamanian and C. Hardiman, Hum. Health (n.d.).
[109] J. T. Orasugh, O. J. Botlhoko, L. T. Temane, and S. S. Ray, Funct. Compos. Mater. **5**, 5 (2024).
[110] M. M. Hasan, M. Moniruzzaman, P. Kirawanich, T. Alam, I. Bin Yahya, A. M. Alrashdi, M. Mobarak, M. S. Soliman, and M. T. Islam, Opt. Laser Technol. **172**, 110515 (2024).
[111] X. Hou, X.-R. Feng, K. Jiang, Y.-C. Zheng, J.-T. Liu, and M. Wang, J. Mater. Sci. Technol. **186**, 256 (2024).
[112] L. Omana, A. Chandran, R. E. John, R. Wilson, K. C. George, N. V. Unnikrishnan, S. S. Varghese, G. George, S. M. Simon, and I. Paul, ACS Omega **7**, 25921 (2022).
[113] P. Kumar, U. Narayan Maiti, A. Sikdar, T. Kumar Das, A. Kumar, and V. Sudarsan, Polym. Rev. **59**, 687 (2019).
[114] Ruchi, V. Gupta, R. Dalal, and S. L. Goyal, Polym. Bull. **81**, 5155 (2024).
[115] R. R. Mohan, A. Thejas Prasannakumar, J. John, S. J. Varma, and S. Jayalekshmi, New J. Chem. **47**, 2565 (2022).
[116] T. Govindasamy, N. K. Mathew, V. K. Asapu, V. Asokan, V. Subramanian, and B. Subramanian, Phys. Chem. Chem. Phys. **25**, 30501 (2023).
[117] J. T. Orasugh and S. S. Ray, ACS Omega **8**, 8134 (2023).
[118] A. A. Isari, A. Ghaffarkhah, S. A. Hashemi, S. Wuttke, and M. Arjmand, Adv. Mater. **2310683**, (2024).
[119] J. T. Orasugh and S. S. Ray, ACS Omega **8**, 8134 (2023).
[120] Z. Leng, Z. Yang, X. Tang, M. H. Helal, Y. Qu, P. Xie, Z. M. El-Bahy, S. Meng, M. M. Ibrahim, C. Yu, H. Algadi, C. Liu, and Y. Liu, Adv. Compos. Hybrid Mater. **6**, (2023).
[121] C. J. Li, X. Wang, X. Liu, J. Zhang, S. Bi, and Z. L. Hou, Carbon **214**, (2023).
[122] J. Hong, J. Kwon, D. Im, J. Ko, C. Y. Nam, H. G. Yang, S. H. Shin, S. M. Hong, S. S. Hwang, H. G. Yoon, and A. S. Lee, Chem. Eng. J. **455**, (2023).
[123] J. Kruželák, A. Kvasničáková, M. Džuganová, R. Dosoudil, I. Hudec, and H. Krump, Polymers **16**, (2024).
[124] M. Panahi-Sarmad, M. Noroozi, M. Abrisham, S. Eghbalinia, F. Teimoury, A. R. Bahramian, P. Dehghan, M. Sadri, and V. Goodarzi, ACS Appl. Electron. Mater. **2**, 2318 (2020).
[125] Z. Jia, M. Zhang, B. Liu, F. Wang, G. Wei, and Z. Su, ACS Appl. Nano Mater. **3**, 6140 (2020).
[126] F. M. Oliveira and R. Gusmão, ACS Appl. Electron. Mater. **2**, 3048 (2020).
[127] C. Cheng, R. Fan, Y. Ren, T. Ding, L. Qian, J. Guo, X. Li, L. An, Y. Lei, Y. Yin, and Z. Guo, Nanoscale **9**, 5779 (2017).
[128] H. Luo, Y. Lu, and J. Qiu, Carbon **183**, 34 (2021).
[129] X. Xu, Y. Wang, Y. Yue, C. Wang, Z. Xu, and D. Liu, Ceram. Int. **48**, 32427 (2022).

[130] X. Xu, F. Yao, O. A. A. Ali, W. Xie, S. F. Mahmoud, P. Xie, S. M. El-Bahy, M. Huang, C. Liu, R. Fan, Z. Guo, A. Du, D. Estevez, F. Qin, H. Peng, D. P. Young, and H. Gu, Adv. Compos. Hybrid Mater. **5**, 2002 (2022).

SYNTHESIS METHODS AND CHARACTERIZATION TECHNIQUES

2.1 Synthesis methods

2.1.1 Solvothermal synthesis method

Research on nanotechnology is still ongoing, and numerous techniques have been developed to produce nanoparticles (NPs) of a wide variety of materials, such as metals, semiconductors, ceramics, metal oxides, polymers, etc. Depending on the source and synthesis techniques employed, different physicochemical, structural, and morphological features of nanoparticles (NPs) are presented [1–5]. Numerous applications in the domains of electronics, optoelectronics, biomedicine, optics and the environment depend on those features [6]. The most popular techniques for creating uniformly sized crystalline nanoparticles at comparatively low temperatures and pressures are hydrothermal and solvothermal synthesis [7–9].

By using this technique, the vapour pressure is saturated and the temperature is raised above the boiling point of the solvent. The internal pressure of the system depends on two factors such as temperature of the reaction and the volume of the solvent used. In the hydrothermal synthesis method, water is used as the solvent. In the solvothermal process different solvents are used for the synthesis other than water. The final products are separated, cleaned thoroughly, dried, and stored for further analysis and application [10–14]. In the current study, ceramic material is synthesized via a solvothermal process. Fig. 2.1 shows schematic of the stainless-steel autoclave. An autoclave made of stainless steel with a Teflon liner and the sample is taken in the Teflon liner. In both, hydrothermal and solvothermal process are carried out in the autoclave. Solvothermal synthesis allows for excellent control of both particle size and shape.

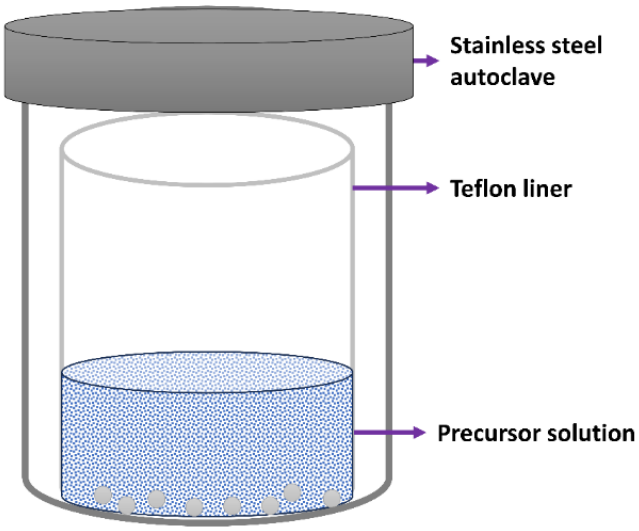

Figure 2.1 Schematic diagram of stainless-steel autoclave

2.1.2 Die- casting method

Flexible polymer composites are suitable for variety of applications such as electromagnetic interference shielding, energy and piezoelectric applications, wearable sensors etc [15–18]. Different methods are used for the fabrication of flexible polymer composites films such as calendaring, Die-casting, Rotational casting, Injection moulding etc. Among them, Die-casting procedure is the simple and cost-effective method for the fabrication of flexible polymer films [19]. It consists of a prepolymer liquid and converted them into solid object with desired shape. Different solvents are used for the fabrication of polymer films. Some polymers are water soluble and some others are dissolved in organic solvents such as dimethyl sulfoxide (DMSO), dimethyl formamide (DMF), N-methyl pyrrolidone (NMP) etc. Polymer powders are dissolved in solvents by stirring or sonication and poured into the petridish and drying at ambient temperature flexible films are obtained. For improving its conductivity and other properties suitable fillers are added and same procedure is repeated and flexible polymer composite films are obtained [20–22]. The schematic of the die – casting procedure is shown in Fig.2.2

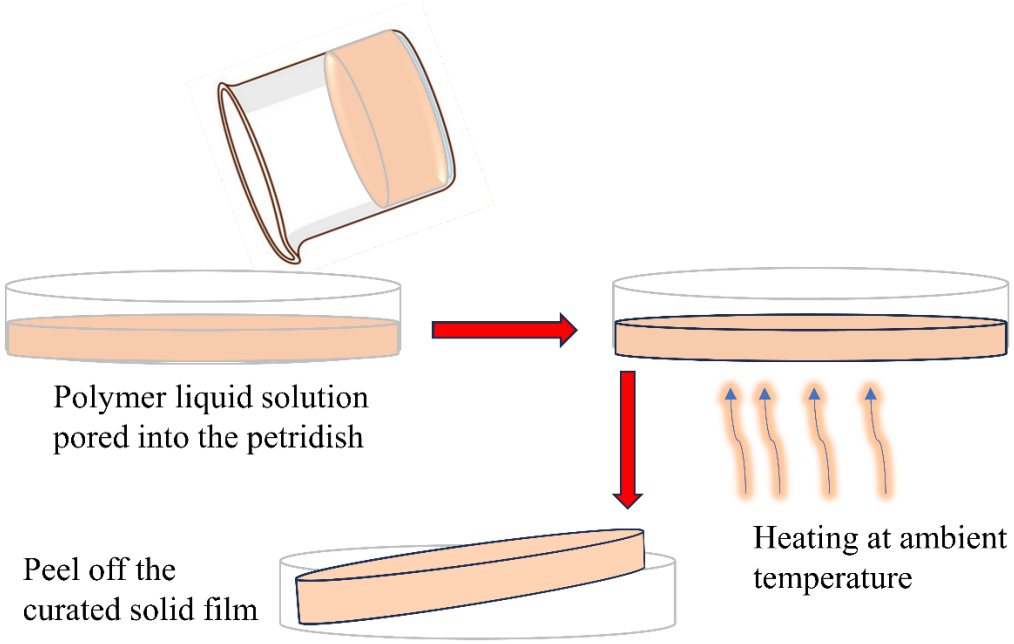

Figure 2.2 Demonstration of die-casting process

Materials properties are realised by using several techniques include X – Ray diffraction (XRD), Fourier transform infrared spectroscopy (FTIR), Scanning electron microscopy (SEM), Transmission electron microscopy (TEM), Raman analysis, Broadband dielectric spectrometer (BDS), Vector network analyzer (VNA) etc. XRD and FTIR are used to analyze crystallinity and structure of the sample. The morphology and size of the samples are understood when using the imaging techniques, SEM and TEM. Dielectric measurements are carried out using BDS. Scattering parameters are measured using VNA. Detailed explanations of these methods are given below.

2.2 Structural, chemical and Phase Characterizations

2.2.1 X-ray Diffraction (XRD) Analysis

An approach used in materials research to determine a material's crystallographic structure is called X-ray diffraction analysis, or XRD. The scattering angles and intensities of peaks are measured when it is subjected to incoming X-rays. According to its name, X-ray diffraction is

a diffraction-based study in which atoms in a crystal scatter X-rays and the diffraction peak that results from the constructive interference of these scattered beams [23]. An X-ray's wavelength in the electromagnetic spectrum is analogous to the interplanar distance of a crystal, which typically ranges from 0.15 to 0.4 nm. Therefore, X-ray's interaction with atoms in a crystal can result in a pattern of interference, either constructive or destructive. The synthetic material's average crystallite size, lattice spacing, preferred orientation growth, and crystallinity are all inferred from the XRD pattern. X-ray diffractometer, which is essentially composed of X-ray tube, a sample holder, and a detector, is used to perform XRD. Monochromatic Copper Kα radiation, with a wavelength of 1.5418Å, is the most widely utilized x-ray source. It is collimated and directed to come into touch with the sample [24]. Every atom acts as a scattering center when these X-rays strike the lattice plane, as seen in Fig. 2.3. Since the reflected beam satisfies Bragg's condition, its intensity is measured when constructive interference occurs.

$$n\lambda = 2d \sin \theta \qquad (2.1)$$

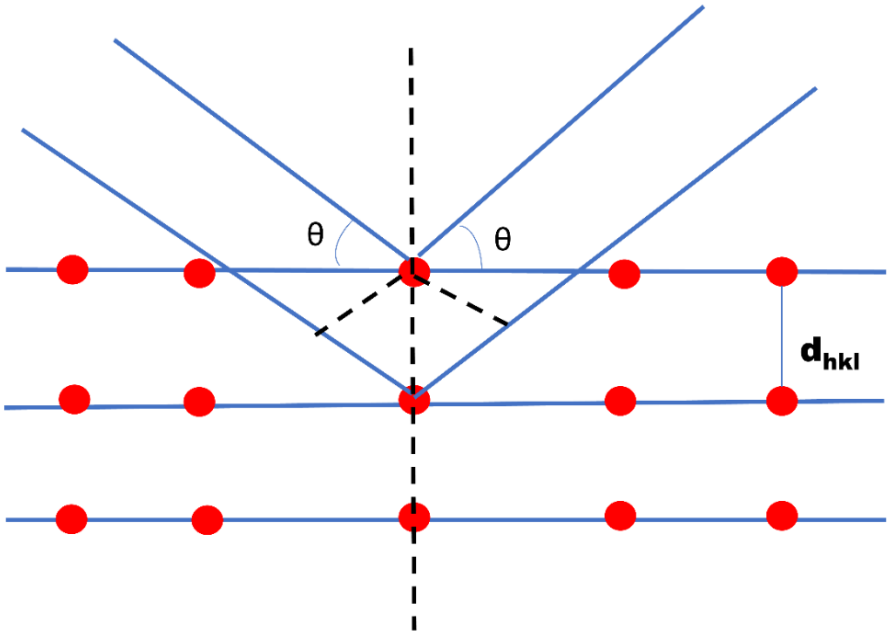

Figure 2.3 Schematic illustration of X-ray diffraction on crystal planes

This produces X-ray correlation between the lattice spacing (d) of the sample and the diffraction angle (θ). Following that, these reflected rays are detected, investigated, and documented. Since the powdered sample under examination involves diffraction from all orientations, scanning the sample over a range of 2θ may yield the greatest number of diffraction peaks. The conversion of the diffraction peak to the comparable 'd' value helps to identify the chemical because each molecule has a unique inter-planar spacing. Peak intensity and broadness provide information about the crystallinity of the material. It helps to determine the crystal structure of materials generated, such as metals, minerals, polymers, ceramics, plastics, fluids, and thin films, by comparing with the standard patterns found in JCPDS files. The Scherrer equation can be used to calculate the sample's crystallite size. [25].

$$t = \frac{0.9\,\lambda}{\beta \cos\theta} \qquad (2.2)$$

Where θ is the Bragg's angle, β is the FWHM of the most intense peak in radiance, λ is the wavelength, and t is the crystallite size in Å.

2.2.2 Fourier Transform Infrared Spectroscopy (FTIR)

Fourier transform infrared spectroscopy is the most advanced method in the infrared spectroscopy. Fourier transform is a mathematical tool that convert frequency domain to time domain. Infrared spectroscopy involves exposing a sample to an IR radiation source. Radiation was partially absorbed and partially being transmitted. The resulting spectrum determines the substances molecular fingerprint by displaying the molecules' absorption and transmission. Similar to fingerprints, each distinct chemical structure has a unique infrared spectrum. Because every material is different from the other in terms of composition and atom structure, no two compounds have exactly the same infrared spectrum. This method helps identify materials because no two have the same bonding and the peak features offer quantitative information [26].

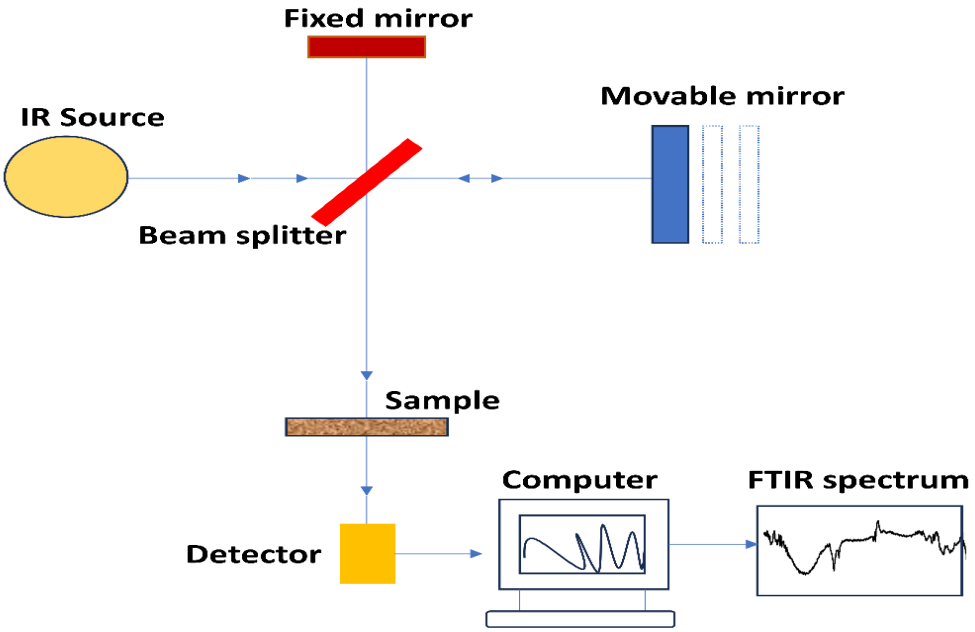

Figure 2.4 Schematic diagram of FTIR spectrometer

The first form of infrared spectroscopy technique was dispersive, which divided the incident IR light frequency using a prism or grating. An intensity plot is created by the detector by recording the interaction of this light with the molecules in the sample and measuring the amount of energy that is passed through the sample at each frequency. The two main shortcomings of this approach are that it takes longer to record the spectrum and has insufficient scanning speed. These drawbacks could be fixed by using the Fourier transformation function, which enables the simultaneous measurement of all frequencies. This is achieved with the use of an interferometer as shown in Fig.2.4. Infrared light from the light source flows down the optical path, through a Michelson interferometer during FTIR investigations. The moving mirror, fixed mirror, and beam splitter comprise the Michelson interferometer. The beam splitter, which looks like a prism, divides the light beam into two parts after it has been reflected off its moving and stationary mirrors. Because of the reciprocating movements of the moving mirror, which modify the optical path difference with the fixed mirror, the phase difference changes with time. Recombining the light beams in the Michelson interferometer results in interference light. An optical path difference along the horizontal axis of the interference light

is recorded together with its intensity in a time-domain interferogram. To find bond correlations, the energy is transformed into frequency-domain spectra.

Material identification is achieved by comparing the spectrum with a standard spectrum that is kept in the database. Functional groups are responsible for the absorption bands spanning 4000–1500 cm^{-1}, whereas chemical bonding within the molecule is the only factor contributing to the peaks falling between 1500–400 cm^{-1}. Analyzing the area under the curve in the typical region of the spectrum can yield quantitative information [26,27].

2.2.3 Raman spectroscopy

One of the most widely used laboratory methods for analyzing molecular structure is Raman spectroscopy. It is predicated on light scattering. A very tiny percentage of scattered light involves an energy shift and is classified as Raman scattering, whereas the majority of scattered light is considered conventional Rayleigh scattering and doesn't include any energy change. The interaction of photons with molecule vibration and resulting energy exchange are responsible for this energy shift. Low-energy scattered radiation is referred to as Stokes lines, and high-energy scattered radiation is referred to as anti-Stokes lines. This change in frequency of the scattered photon is termed Raman scattering, and this gives information about the sample structure. Based on all Raman bands and their corresponding intensities, the Raman spectrum facilitates in material identification because it is thought of as a signature that is specific to each chemical. In addition, information regarding the amount of pressure in the material created and its crystallinity can be revealed by changes in peak broadening, peak intensity variation, and band frequency shift [28,29].

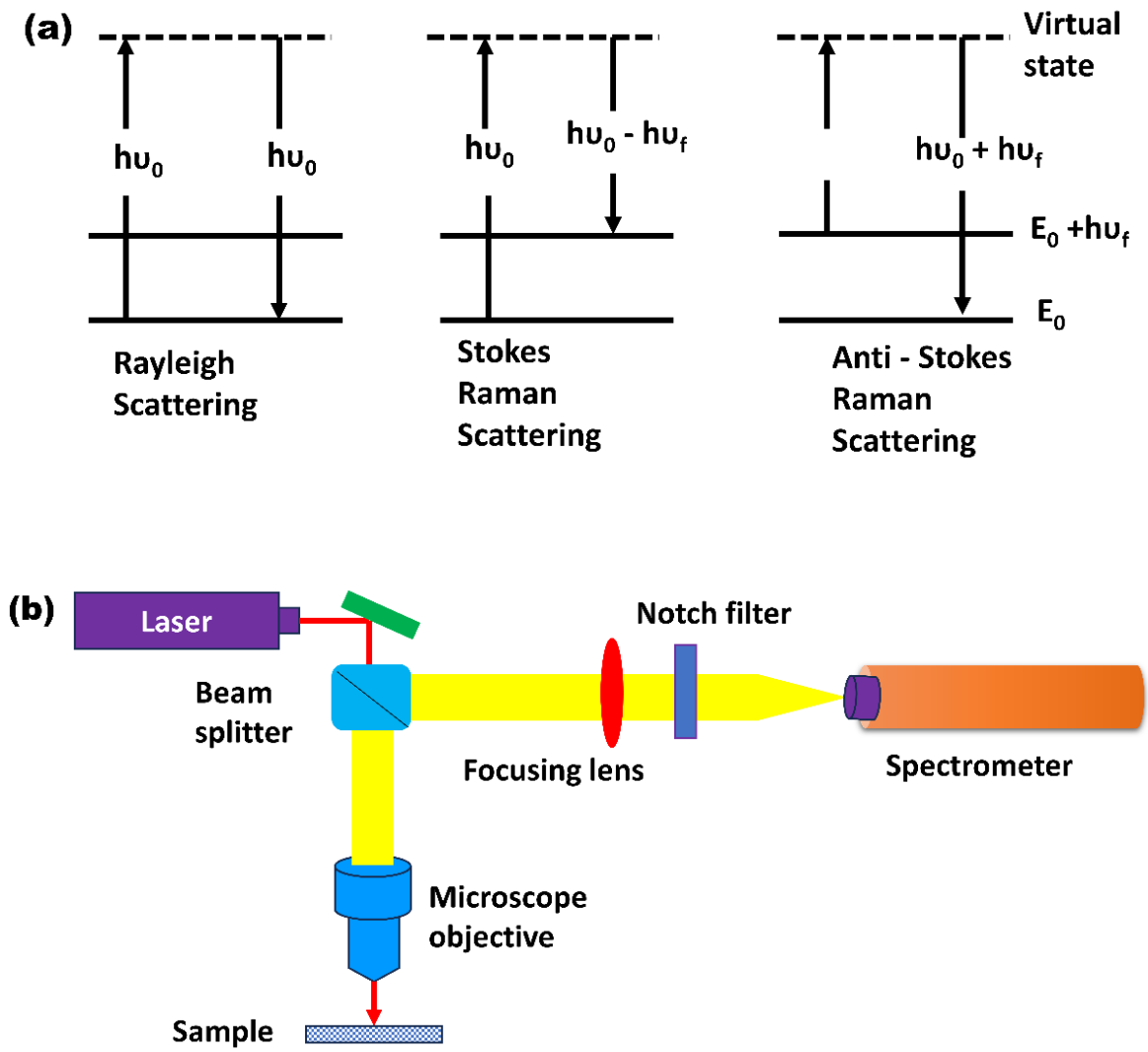

Figure 2.5 (a) Energy levels diagram of Rayleigh and Raman scattering, and (b) Schematic diagram of Raman spectrometer

A schematic representation of the Raman spectrometer is depicted in Fig.2.5. A typical Raman spectrometer comprises an excitation source (laser), collimator optics, detector, and beam splitter. The incident laser beam coming out from the excitation source passes through the interference filter, and the focusing lens directs it to the sample. After interaction with the sample, the incident laser beam scattered in all directions. The scattered laser beam coming from the sample passes through the monochromator and is dispersed. The Raman scattering was collected at a right angle using a notch filter by blocking the Rayleigh scattering. The weak

Raman scattering signals were detected using charged coupled device (CCD) and converted to a Raman spectrum [30].

2.3 Size and morphology analysis

2.3.1 Field Emission Scanning Electron Microscope (FE – SEM)

One of the most sophisticated imaging methods is scanning electron microscopy. A scanning electron microscope can be used to take high-resolution three-dimensional pictures of a sample's surface and assess the sample's composition at the micro- and nanoscale size range. As a result of inelastic scattering, the scanning electron microscope creates a variety of dispersed beam shapes by interacting with the sample surface with a high intensity focused electron beam. FE-SEM and conventional SEM are the two main types of SEM, which vary based on the electron source. Because of its high-resolution pictures, field emission SEM analysis is the most recommended method [31].

A typical SEM instrument consists of an electron gun, electron lenses, high vacuum electron column, sample stage, detectors, and display as shown in Fig.2.6. Electrons are produced by an electron gun and travel through the electron column at high energies ranging from 0.5 keV to 40 keV. The condenser lenses focus the high energy electron beam to a spot with a diameter of 0.4 to 5 nm in a raster fashion. The electron beams can raster scan the sample surface over a rectangular region due to the final lens's ability to divert them into the x- and y-axes. A number of display monitors are created by the interaction of an electron beam with atoms in a sample. Energy Dispersive Spectroscopy (EDS) is a technique that can be used to detect the characteristic X-Rays generated by a sample in order to evaluate its elemental composition, amount of doping, and purity [32–34]. A representative SEM images is shown in Fig.2.7.

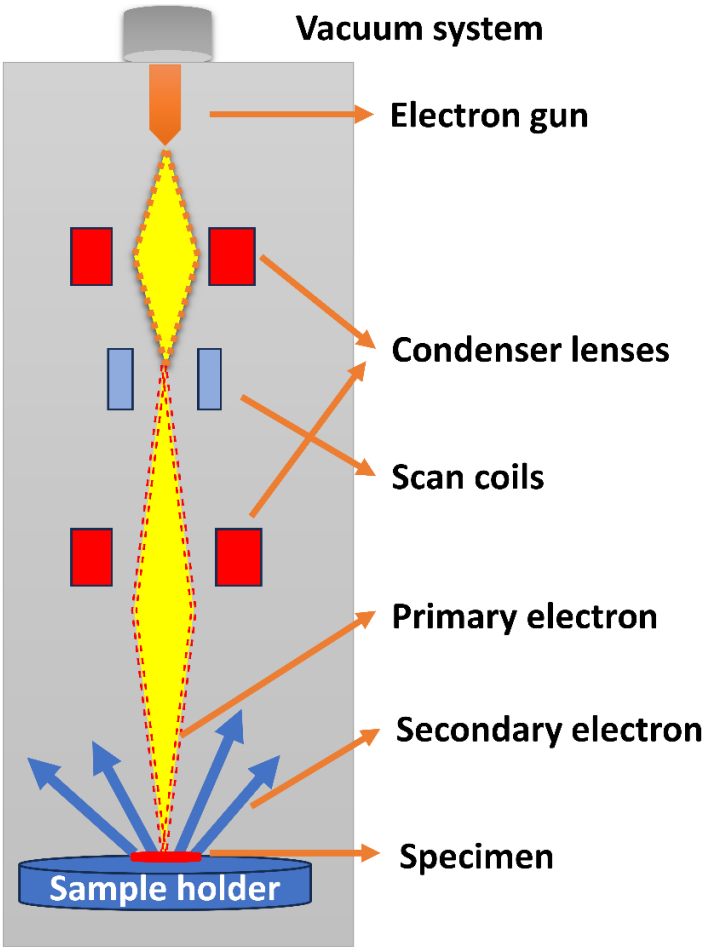

Figure 2.6 Schematic diagram of field emission scanning electron microscope

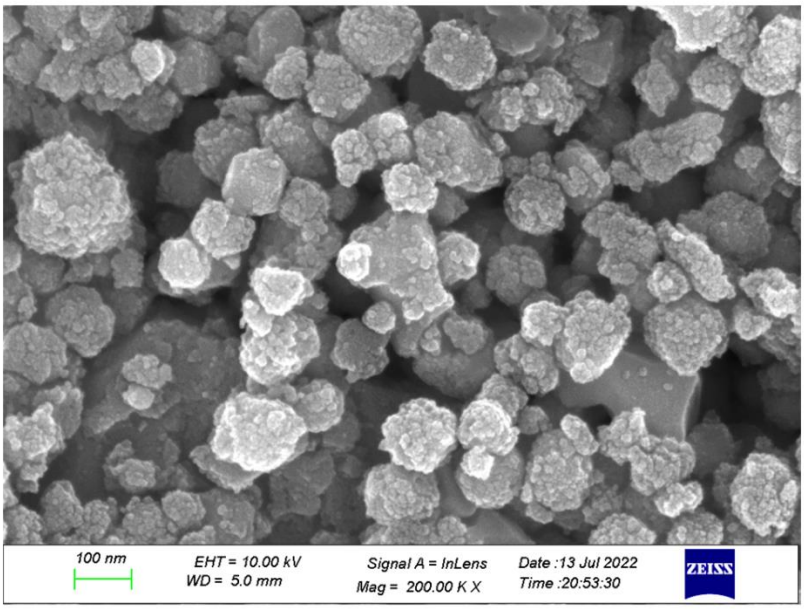

Figure 2.7 A representative FESEM image

2.3.2 Transmission electron microscope (TEM)

The sophisticated method of transmission electron microscopy (TEM) can be used to examine a materials size, shape, and morphology. To be analyzed using a TEM, the sample needs to be thin enough for electrons to flow through it. The resolution of TEM is very high, reaching several sub-nano meter scales. TEM involves high energy electron beam, emitted from an electron gun, to transmit through a specimen that is in part transparent to electrons and carries the information about the inner structure of the specimen [35,36]. Figure 2.8 represents a schematic diagram of TEM.

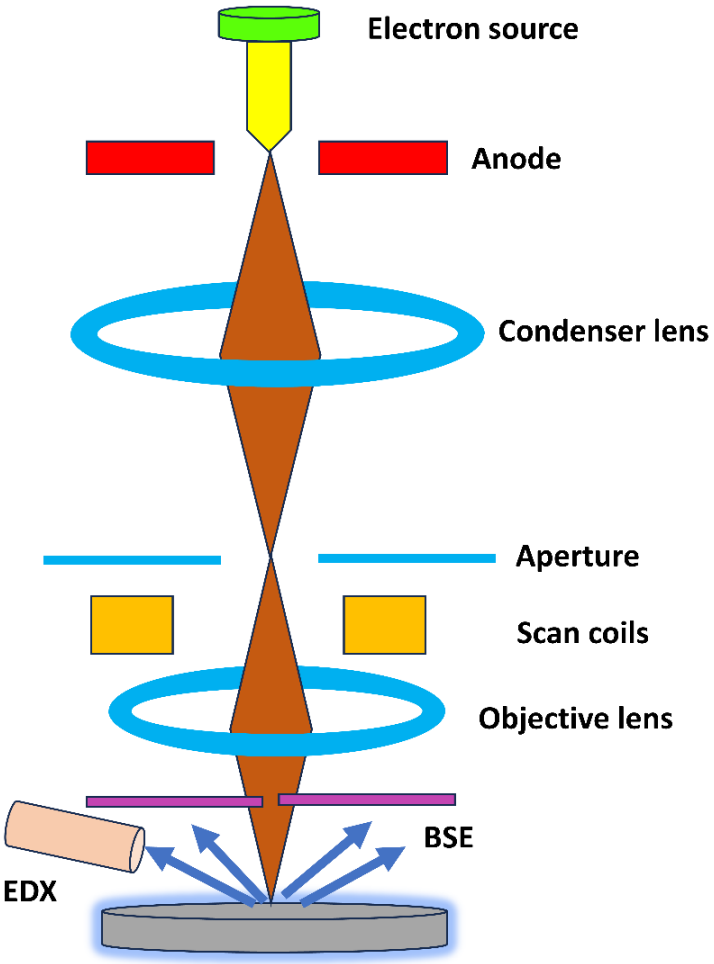

Figure 2.8 Schematic diagram of transmission electron microscope

A typical TEM consists of several components: a vacuum system, an electron source for the emitting of the electron beam, electromagnetic lenses, and electrostatic devices. In TEM, an electron gun initially produces an electron beam through a field emission source with an acceleration voltage of 100 to 300 keV. The incident beam focus on the specimen surface through two condense lenses. Among these, the first lens controls the spot size of the electron beam, while the second lens controls the illuminated area. After the electron beam enters the specimen, the part of it are transmitted. This transmitted portion is focussed by the objective lens into an image. By altering the focal length of the electron lens, both the micrograph and diffraction pattern can be observed [37,38]. The selected area aperture, located at the image plane below the sample, creates contrast through elastically scattered electrons. Magnetic lenses then direct these scattered beams to form a pattern of spots, each representing a specific plane in the crystal. This pattern provides insights into the sample's crystallinity, orientation, atomic arrangements, and phases present. When the transmitted beam is selected, the observation mode is called the bright-field mode, and the obtained images are bright-field images. On the other hand, when the observation mode uses diffracted beam, it is called darkfield mode, and the images are called dark-field images [36].

2.4 Thermogravimetric analysis

Thermogravimetric analysis (TGA) is a valuable method for determining the heat stability of a material, especially for polymers. This technique makes it possible to monitor how a specimen’s weight varies as its temperature rises. The amount of matter in the sample material is quantified using this analytical approach as a function of temperature or time. When the sample material is heated or cooled, its weight is measured. The samples are typically put in a clean platinum crucible and heated under a controlled program. A thermobalance is then used to measure the changes in mass of the sample as a function of temperature. In a controlled

temperature program, the sample is heated or cooled at a predetermined and defined rate. The typical range for the heating or cooling rate is 1 ºC/min to 100 ºC/min. TGA can be performed in various environment such as inert atmosphere and reactive atmosphere. For inert one nitrogen is used and for reactive one oxygen or sulphur dioxide is used. Furthermore, the analysis can be performed in vacuum, and even at high vacuum of up to 10^{-6} torr are achievable with specific equipment [39,40]. A representative TGA graph is shown in Fig.2.9.

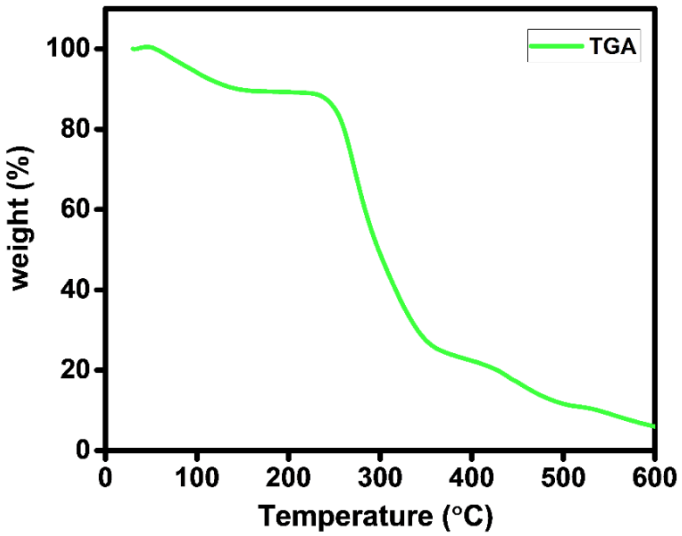

Figure 2.9 A representative of TGA graph

2.5 Dielectric and scattering parameter analysis

2.5.1 Broadband dielectric spectrometer (BDS)

An experimental method that gives a precise account of the interaction between electromagnetic waves and materials is called broadband dielectric spectroscopy, or BDS. Examining the materials' electrical and dielectric properties when they are exposed to a fluctuating electric field over time is the primary goal of the sample's dielectric measurement across a broad frequency range. It is one of the most widely used experimental techniques for dielectric measurements and simplifies molecular dynamics because of its direct coupling of the electric field to the reorientation motion of the dipolar molecules and the translational motions of the charged species of the molecules. BDS can be used to determine the complex

impedance of the material, from which a variety of physical properties can be inferred, including complex dielectric permittivity and complex conductivity.

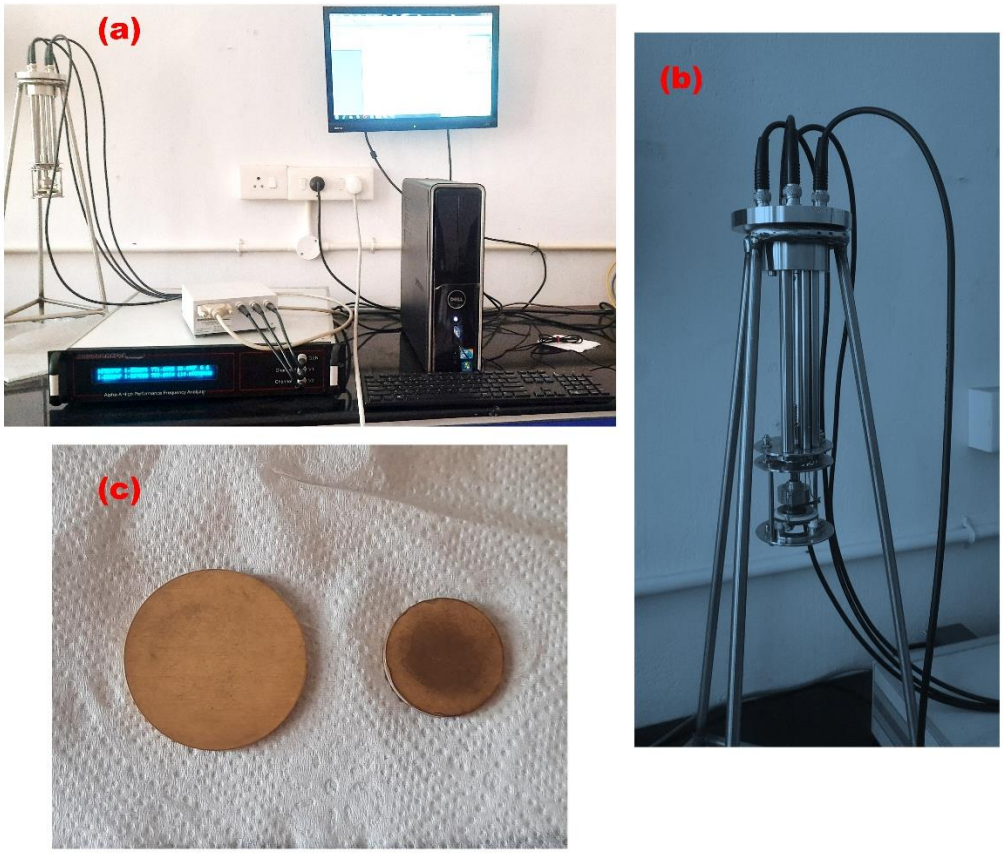

Figure 2.10 (a) The whole Broadband Dielectric measurement set up (b) Sample holder (c) upper and lower electrode the sample is placed between these electrodes

Multiple forms of dielectric polarization are induced when an electric material sandwiched between two parallel plate capacitors subjected to a time-varying field. The dielectric response of the materials is indicated by the complex dielectric permittivity, conductivity, etc., plotted against the applied electric field frequency. This plot is known as a complex dielectric spectrum. By sandwiching the sample material between the dielectric cell's upper and lower electrodes, a capacitor is created. Applying a time varying electric field with a magnitude $E = E_0 + e^{i(\omega t)}$ with specific measuring frequencies to the sample capacitor yields a displacement current with a magnitude of $I = I_0\, e^{i(\omega t - \varphi)}$. Phase angle refers to the phase difference that exists between the applied electric field and the current. The complex impedance, complex

permittivity, complex electric modulus (M^*), complex conductivity (σ^*), and so on can then be retrieved from the ratio of applied voltage to complex current. The equation can be expressed as follows

$$\epsilon^*(\omega) = \frac{1}{i\,\omega Z^*(\omega) C_0} \quad (2.3)$$

$$M^*(\omega) = \frac{1}{\epsilon^*(\omega)} = i\omega Z^*(\omega) C_0 \quad (2.4)$$

$$\sigma^*(\omega) = \frac{d}{Z^*(\omega) A} \quad (2.5)$$

Where ω is the frequency of the applied electric field, $Z^*(\omega)$ is the complex impedance of the material under study, C_0 is the empty cell capacitance, d is the spacing of the electrodes of the parallel plate capacitor, and A is the area of the electrode [41]. Fig.2.10a shows the whole dielectric measurement set up. Fig.2.10b shows the sample holder and Fig.2.10c shows upper and lower electrode, the sample is placed between these electrodes. Here, we used Novacontrol Alpha – A Broadband dielectric spectrometer with WinDETA software. From above mentioned equations, the permittivity and conductivity values are extracted using this software. The measurement frequency range is 10^{-2} Hz to 10^7 Hz. Initially the sample is kept between two gold plated electrode with 20 mm or 40 mm diameter. Then, it is placed in the four-probe connection set up as shown in 2.10b. After that frequency range is selected between these 10^{-2} Hz to 10^7 Hz or full-length frequency range, then an AC electric field of appropriate voltage is applied and measurements are carried out. After performing the Dielectric measurements, frequency dependent real and imaginary part of complex dielectric permittivity and modulus are plotted. From these plot, various dielectric measurements are extracted.

2.5.2 Vector Network Analyser (VNA)

Electromagnetic interference arises anywhere in the electromagnetic spectrum. In the present thesis we concentrate on X – band (8-12 GHz) region. The X – band is utilised for radar and satellite communications. EMI shielding experiments are performed using vector network

analyser (VNA). Different techniques such as open space, shielded room, shielded box and coaxial transmission line methods are used for the scattering parameter measurements. Among them transmission line method is the most advanced method and this method is used for the measurements. In VNA, there are two ports as shown in Fig.2.11, port 1 and port 2. The test specimen is placed between the two port which is connected to the VNA. The waves are analysed using scattering parameters S_{11}, S_{12}, S_{21} and S_{22}. Here, S_{12} and S_{21} are the transmission scattering parameter and S_{11} and S_{22} are the reflection scattering parameters [42]. The schematic of the scattering parameters is shown in Fig.2.12. The basic calculations for shielding effectiveness are as follows: The reflection and transmission coefficients of material are related to the scattering through the relation

$$T = |S_{12}|^2 = |S_{21}|^2 \quad R = |S_{11}|^2 = |S_{22}|^2 \tag{2.6}$$

The effective absorbance is based on the formula, $A_{eff} = \frac{1-R-T}{1-R}$ (2.7)

The shielding effectiveness (SE) can be calculated as follows,

$$SE_R(dB) = 10\log\frac{1}{1-R} = 10\log\frac{1}{1-{S_{11}}^2} \tag{2.8}$$

$$SE_A\,(dB) = 10\log\left(\frac{1-R}{T}\right) = 10\log\frac{1-{S_{11}}^2}{{S_{21}}^2} \tag{2.9}$$

$$SE_T = SE_R + SE_A = 10\log\frac{1}{{S_{12}}^2} \tag{2.10}$$

$$\text{EMI SE (\%)} = 100 - \left(\frac{1}{10^{\frac{SE}{10}}}\right) \times 100 \tag{2.11}$$

The shielding properties of the prepared samples are carried out using two – port vector network analyzer in the X – band frequency range. The sample is placed in the waveguide adapter and placed between the waveguide and measurements are carried out. The dimensions of X – Band holders are 22.86 (Width) and 10.16 (Height). Four scattering parameters are obtained from this. Then, shielding efficiency is calculated from above equations.

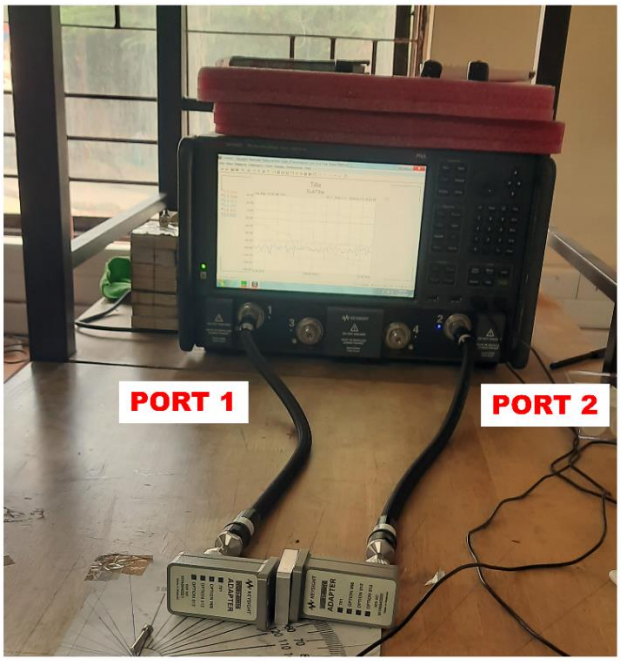

Figure 2.11 VNA (Model: N5224B, Brand: Keysight, measurement frequency range: 10 MHz-43.5 GHz)

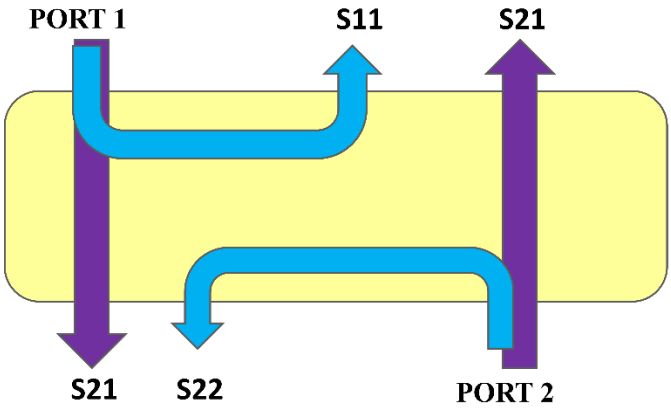

Figure 2.12 Schematic of the scattering parameters

Relationship between EMI shielding effectiveness (SE) in dB and shielding efficiency in percentage (%) is shown in the Table 1. Among the different methods for measuring SE, waveguide method is used for the measurement.

A waveguide is a linear structure that guides electromagnetic waves. The frequency range that a waveguide can support is determined by its dimension. Hence, there are different waveguides having different dimensions for the EMI SE measurement at different frequency bands of the

microwave region. The data obtained from this method can be resolved into absorption, reflection and transmission components [43].

Shielding effectiveness (dB)	Shielding efficiency (%)
0	0
10	90
20	99
30	99.9
40	99.99
50	99.999
60	99.9999
70	99.99999
80	99.999999
90	99.9999999

Table 2.1 Relation between Shielding efficiency in dB and percentage

****

References

[1] M. Sajid and J. Płotka-Wasylka, Microchemical Journal **154**, 104623 (2020).

[2] I. Khan, K. Saeed, and I. Khan, Arabian Journal of Chemistry **12**, 908 (2019).

[3] K. A. Altammar, Front Microbiol **14**, 1 (2023).

[4] M. Aliofkhazraei, *Handbook of Nanoparticles* (2015).

[5] N. Baig, I. Kammakakam, W. Falath, and I. Kammakakam, Mater Adv **2**, 1821 (2021).

[6] L. A. Kolahalam, I. V. Kasi Viswanath, B. S. Diwakar, B. Govindh, V. Reddy, and Y. L. N. Murthy, Mater Today Proc **18**, 2182 (2019).

[7] S. Pawar and H. Deshmukh, International Journal of Innovative Knowledge Concepts **6**, 126 (2018).

[8] L. Ndlwana, N. Raleie, K. M. Dimpe, H. F. Ogutu, E. O. Oseghe, M. M. Motsa, T. A. M. Msagati, and B. B. Mamba, Materials **14**, (2021).

[9] Y. Huo, S. Xiu, L. Y. Meng, and B. Quan, Chemical Engineering Journal **451**, (2023).

[10] W. Wang, H. Chai, X. Wang, X. Hu, and X. Li, Appl Surf Sci **341**, 43 (2015).

[11] M. Sethi, U. S. Shenoy, S. Muthu, and D. K. Bhat, Front Mater Sci **14**, 120 (2020).

[12] A. UmaSudharshini, M. Bououdina, M. Venkateshwarlu, C. Manoharan, and P. Dhamodharan, Surfaces and Interfaces **19**, 1 (2020).

[13] S. Mohan, M. Vellakkat, A. Aravind, and U. Reka, Nano Express **1**, (2020).

[14] S. P, D. M. Vidyadharan, K. Sridharan, M. S. T. H, B. M, and S. Swaminathan, Mater Chem Phys **317**, 129156 (2024).

[15] K. Zhou, K. Dai, C. Liu, and C. Shen, SmartMat **1**, 1 (2020).

[16] S. S. Pradhan, L. Unnikrishnan, S. Mohanty, and S. K. Nayak, J Electron Mater **49**, 1749 (2020).

[17] I. O. Oladele, T. F. Omotosho, and A. A. Adediran, Int J Polym Sci **2020**, (2020).

[18] Y. Xu, W. Lu, G. Xu, and T. W. Chou, Compos Sci Technol **204**, (2021).

[19] S. P., A. R., B. M., M. S. T.H., K. Sridharan, and S. Swaminathan, Mater Today Commun **34**, 105287 (2023).

[20] L. E. Richter, A. Carlos, and D. M. Beber, *Synthesis Technique for Polymer Nanocomposites* (n.d.).

[21] G. Mittal, K. Y. Rhee, V. Mišković-Stanković, and D. Hui, Compos B Eng **138**, 122 (2018).

[22] K. Markandan and C. Q. Lai, Compos B Eng **256**, (2023).

[23] G. B. Greenough, *X-Ray Diffraction by Polycrystalline Materials*, Vol. 4 (1956).

[24] A. A. Bunaciu, E. gabriela Udriştioiu, and H. Y. Aboul-Enein, Crit Rev Anal Chem **45**, 289 (2015).

[25] D. Chateigner, J Appl Crystallogr **39**, 925 (2006).

[26] A. A. Ismail, F. R. van de Voort, and J. Sedman, in *Techniques and Instrumentation in Analytical Chemistry*, Vol. 18 (1997), pp. 93–139.

[27] S. Thomas, R. Thomas, A. K. Zachariah, and R. K. Mishra, *Spectroscopic Methods for Nanomaterials Characterization*, Vol. 4 (2017).

[28] Z. Xu, Z. He, Y. Song, X. Fu, M. Rommel, X. Luo, A. Hartmaier, J. Zhang, and F. Fang, Micromachines (Basel) **9**, (2018).

[29] Z. Xu, Z. He, Y. Song, X. Fu, M. Rommel, X. Luo, A. Hartmaier, J. Zhang, and F. Fang, Micromachines (Basel) **9**, (2018).

[30] C. N. Banwell, 1983.

[31] SciMed, SciMed (2023).

[32] W. Zhou, R. Apkarian, Z. L. Wang, and D. Joy, Scanning Microscopy for Nanotechnology: Techniques and Applications 1 (2007).

[33] B. Hafner, 1 (2007).

[34] J. Cazaux, J Microsc **217**, 16 (2005).

[35] Y. Lin, M. Zhou, X. Tai, H. Li, X. Han, and J. Yu, Matter **4**, 2309 (2021).

[36] Z. L. Wang, Advanced Materials **15**, 1497 (2003).

[37] L. E. Franken, K. Grünewald, E. J. Boekema, and M. C. A. Stuart, Small **16**, (2020).

[38] L. E. Franken, K. Grünewald, E. J. Boekema, and M. C. A. Stuart, Small **16**, (2020).

[39] L. E. Richter, A. Carlos, and D. M. Beber, *Principles and Applications of Thermal Analysis* (n.d.).

[40] O. O. Olatunji, S. A. Akinlabi, M. P. Mashinini, S. O. Fatoba, and O. O. Ajayi, IOP Conf Ser Mater Sci Eng **423**, 0 (2018).

[41] A. S. F. Kremer, *Broadband Dielectric Spectroscopy* (2003).

[42] National Instruments, National Instruments RF Academy 1 (2012).

[43] S. B. Kondawar and P. R. Modak, in *Materials for Potential EMI Shielding Applications* (Elsevier, 2020), pp. 9–25.

Cost efficient fabrication of flexible polymer metacomposites: Impact of carbon in achieving tunable negative permittivity at low radio frequency range and X – band EMI shielding

Metamaterials have fascinated researchers for more than a decade primarily due to their capability to exhibit negative permittivity that has gained momentous attention towards applications such as electromagnetic absorption, negative field effect transistors, wireless power transfer, energy storage etc [1–7]. Research on metamaterials is quite complex since it is predominantly structure dependent and regrettably the response is only in a narrow bandwidth. These limitations in metamaterials prompted the shift in the research attention towards metacomposites since a wider bandwidth and unusual properties was achieved through a relatively simple and cost-effective fabrication process [8–14].

Recently, the epsilon-negative materials are receiving momentous attention in comparison to the conventional positive dielectric constant materials owing to the advances in metacomposites and their ludicrously potential applications *viz.* electromagnetic wave blocking, absorption, high-power microwave filters, perfect lens and wireless power transfer [11,13,15–18]. One of the distinct advantages of metacomposites is their ability to exhibit both positive and negative values of permittivity by tuning their percolation threshold. Composites become lossy left-handed materials above the percolation threshold and are applied as electromagnetic wave shielding materials as they hinder the propagation of electromagnetic waves through them [6,19–21]. Typically, the magnitude of the negative permittivity in metacomposites is influenced by the electron density of the conducting fillers in the composites. In addition to having a large electron density, metals have a large negative permittivity located in the ultraviolet frequency region. Therefore, the negative permittivity in metals dramatically decreases with decreasing frequency. Furthermore, metals have high dielectric losses and impedance mismatches that make them impossible to be employed in

practical applications [22–24]. Alternatively, carbon materials and conductive polymers also exhibit negative permittivity like metals, while their dielectric losses and impedance mismatches are minimal. Towards this end, the solution to shifting of the frequency from ultraviolet to radio frequency or lower frequency region was to mix the conducting particles with a suitable dielectric matrix or to replace the metals with carbon-based fillers [25–27].

Metacomposites containing carbon-based materials like graphene, graphite and CNT are characterized by moderate electron density and weakly negative permittivity. These properties make them well-suited for impedance matching applications such as high permittivity capacitors and perfect absorbers. Polymer matrix metacomposites are the subject of considerable research recently, due to their flexibility, low manufacturing costs, easy processability, and negative permittivity at lower frequencies (10kHz- 1MHz). Materials containing carbon fiber-PVA, graphene-Polydimethylsiloxane (PDMS), and MWCNT-polyurethane behave similarly. Typical applications of flexible metacomposites include wearable cloaking, sensors, flexible electronic devices and EMI shielding [26,28,29].

Electromagnetic waves (EMW) have become a commonplace part of our everyday lives due to technological improvements in home appliances, displays, and communication gadgets during the past few decades. The introduction of autonomous vehicles, drones, and the Internet of Things (IoT) is driving an additional acceleration in the complexity of the electromagnetic environment, together with the rapid development of fifth-generation (5G) wireless communication technology. This leads to a great deal of interference and electromagnetic radiation coming in this direction. Appropriate EMI shielding materials are needed to tackle this issue. Highly conductive and flexible polymer composites are suitable for EMI shielding applications. X-band EMI shielding is the main focus of this study since X-band frequency is utilized in the majority of civil and military applications.

In this study, we used polyvinyl alcohol (PVA) as the matrix, since it is a low-cost, water-soluble, highly-resistant, biocompatible, and thermostable semi-crystalline green polymer. PVA exhibits unique optical properties and has a large charge storage capacity. It can easily be customized by adding appropriate fillers to alter its optical, electrical, and mechanical properties [30,31]. As a conducting filler, carbon black (CB) is selected by considering its good electrical conductivity, high surface area, and stability [32–34]. In this context, a simple, low-cost die-casting technique was employed for the fabrication of metacomposites, and the effects of varying CB concentrations in the PVA matrix are examined. A variety of compositional, microstructural, conductivity, and dielectric analyses are conducted on the prepared samples for observing negative permittivity in PVA-CB composites. To the best of our knowledge, there are no reports in the literature pertaining to PVA-CB metacomposites and their tunable negative permittivity. Composites produced in this way are easy to prepare, minimal in cost, and versatile enough to be used in electronic applications. Using a Vector Network analyzer, the EMI shielding effectiveness of all prepared samples is also examined.

3.1 Experimental

3.1.1 Materials

Carbon black (carbon 50 percent compressed, 99.9+ % S.A, 75 m^2/g, bulk density 80-120 g/L) and Polyvinyl alcohol (PVA) powder (molecular weight 89,000–98,000, 99+ % hydrolysed) was purchased from Alfa-Aesar and Sigma Aldrich, USA, respectively and were used as received.

3.1.2 Fabrication of Polyvinyl Alcohol – Carbon Black (PVA-CB) composites

A simple and low-cost die-casting process was used to prepare the PVA-CB composites as depicted in Scheme.3. 1. The PVA powder was dispersed in deionized water at 80 °C using a magnetic stirrer at 1000 rpm until the powder was completely dissolved, yielding a 5 wt% PVA solution. Next, CB powder of various concentrations (0.5, 0.75, 1.25, 1.75, 2 and 2.5 wt%) was

added to the PVA solution. The PVA-CB slurry was magnetically stirred at 1000 rpm for 2 h and the uniform black slurry was allowed to stand for a few minutes to eliminate the bubbles prior to being slowly poured into a Petri-dish. The flexible PVA-CB films were successfully made after drying at room temperature for 4 h to remove the moisture. The thickness of the films (PC1 – PC6) are 0.07 mm, 0.1 mm, 0.16 mm, 0.2 mm, 0.27 mm and 0.31 mm respectively.

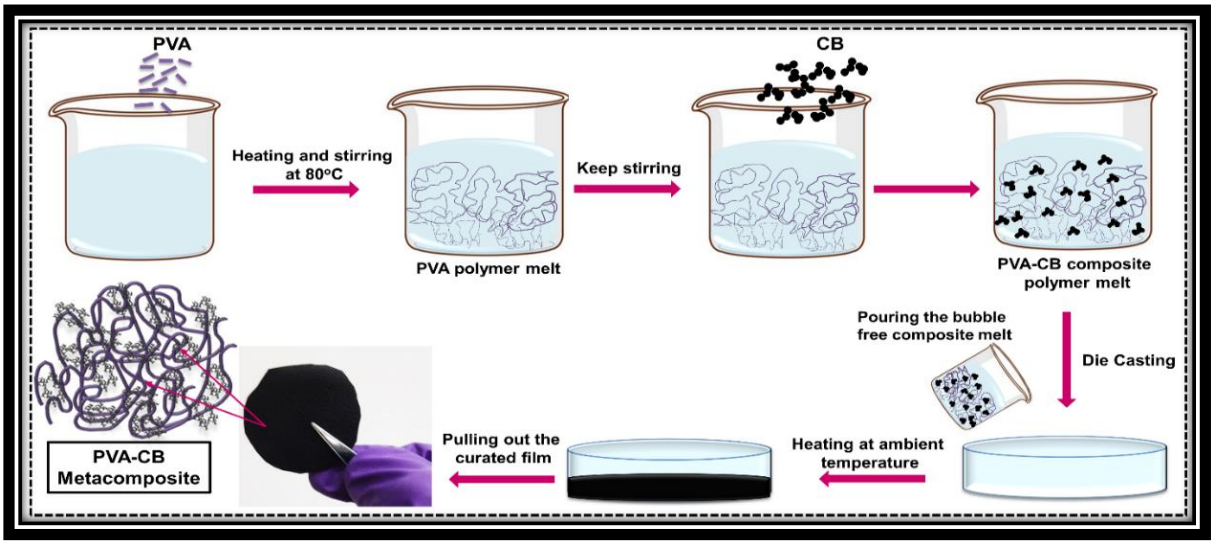

Scheme 3.1 Schematic of the various steps involved during the synthesis of PVA-CB flexible metacomposite films

PVA composite films were named PC0 (pure PVA), PC1 (PVA + 0.5 wt% CB), PC2 (PVA + 0.75 wt% CB), PC3 (PVA + 1.25 wt% CB), PC4 (PVA + 1.75 wt% CB), PC5 (PVA + 2 wt% CB), and PC6 (PVA + 2.5 wt% CB). Photographs of the as-fabricated metacomposite films are presented in Fig.3.1. Another set of metacomposite films were also fabricated by increasing the PVA solution concentration to 10 wt% and the obtained films were named as PVAC0 (pure PVA), PVAC1 (PVA + 0.5 wt% CB), PVAC2 (PVA + 0.75 wt% CB), PVAC3 (PVA + 1.25 wt% CB), PVAC4 (PVA + 1.75 wt% CB), PVAC5 (PVA + 2 wt% CB), and PVAC6 (PVA + 2.5 wt% CB).

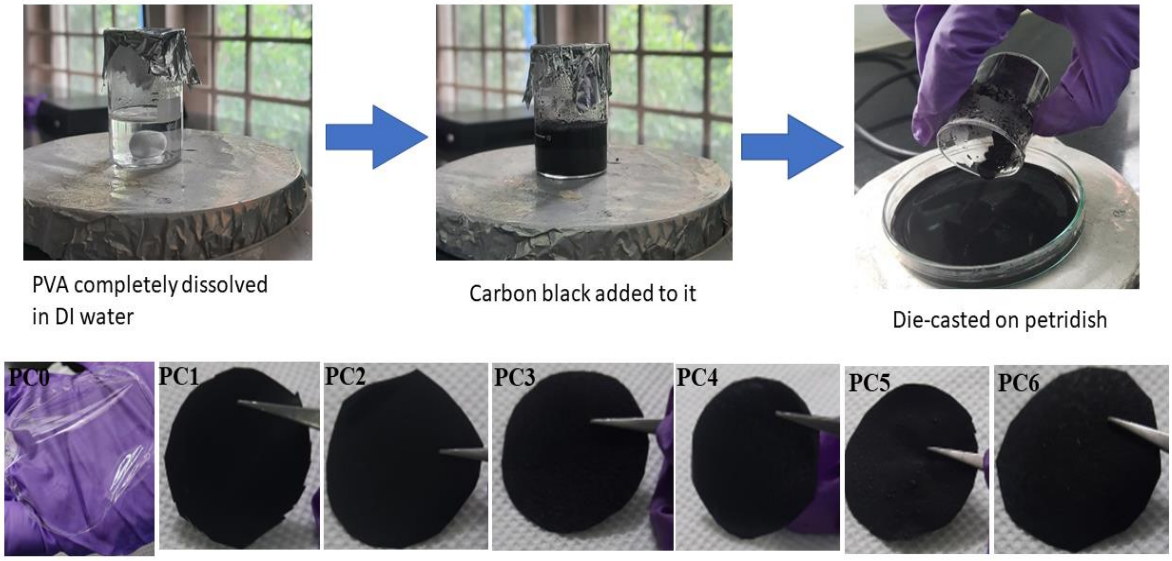

Figure 3.1 Photographs of pristine PVA (PC0) and PVA-CB composite films (PC1, PC2,PC3, PC4, PC5, PC6) fabricated through die-casting method

3.2 Formation mechanism of PVA-CB metacomposite thin films

When heated with water, PVA molecules, which contain hydroxyl-based functional groups, produce a hydrogel. Gelation is caused by intramolecular hydrogen bonds between polymer chains, as well as intermolecular hydrogen bonds between polymer chains and water. Physical cross-linking such as microcrystalline zones and hydrogen bonds in molecular chains causes three-dimensional structures or gelation. In contrast to hydrogen bonds, microcrystalline zones have strong contacts and neatly ordered chemical chains, making them more robust to crosslinking [31,35]. Due to its hydrophilic nature, PVA readily dissolves in water over a wide temperature range. With abundance of water molecules, H atoms can connect with polar groups like -OH in PVA molecular chains, increasing PVA crosslinking and forming a crosslinked structure that expands in a three-dimensional manner as depicted in Scheme.3 2.

Conducting carbon black is composed of a layer-like structure with hexagonal carbon rings that is similar to graphite. Surface of the CB contains a variety of functional groups such as quinonic, lactonic, carboxylic, and phenolic groups. In a hydrogel or polymer melt,

chemisorbed oxygen groups produce intermolecular hydrogen bonds with water and PVA molecular chains.

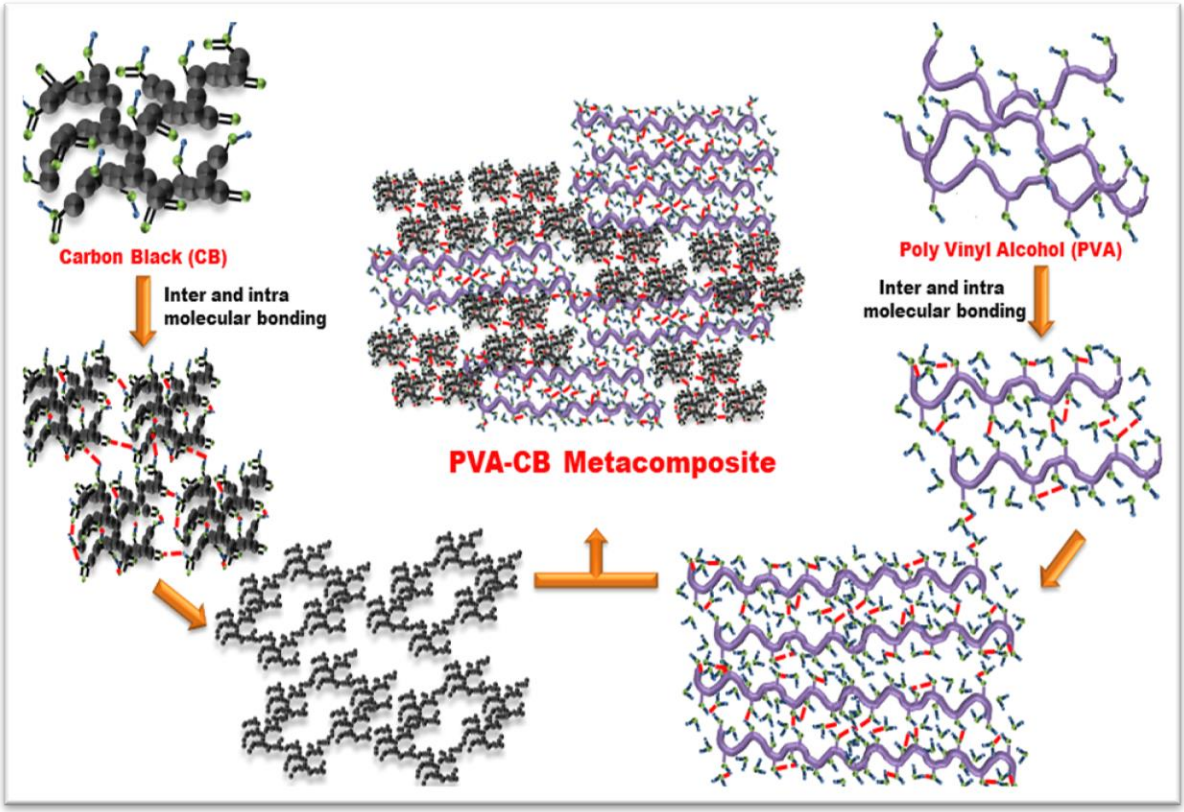

Scheme 3.2 Schematic depicting the mechanism of growth of PVA-CB metacomposite films fabricated through the die-casting method. Inter and intramolecular bonds formed between CB particles and PVA molecules with the addition of water are represented by red colour dashes

Similarly, CB particles are also coupled in solution by intramolecular hydrogen bonds, resulting in dispersion of conducting fillers in the polymer melt and the formation of flexible PVA-CB metacomposites [36,37], as illustrated in the schematic shown in Scheme 3.2. Having a consistent distribution of CB is one of the most critical factors in determining the final properties of the metacomposite film, especially its conductivity. Several orientations are possible when CB is added to the PVA polymer melt. As observed in Scheme 3.2, the CB particles that are randomly arranged are strewn across the polymer melt, which initially result in an unconnected arrangement. Later, the CB particles cluster together *via* Van der Walls forces and a conductive network is established. However, they retain their smaller particle

characteristics and form partially connected conducting lines. Finally, the inter and intra molecular H and OH^- bonds disperse the CB particles into a larger network-like structure resulting in a fully connected conducting channel.

3.3 Characterization

The phase composition and structural properties of the samples were analysed using an X-ray diffractometer (X'pert3 Powder, *PANalytical*) with Cu Kα radiation (λ = 1.5418 Å) at a scan rate of 2°/min in the 2θ range 10 – 50°. Thermogravimetric analysis (TGA, STA 8000) was performed in a nitrogen environment at temperatures between 30 °C and 600 °C. Infrared spectra of the samples are recorded using (Spectrum two, Perkin Elmer) FTIR spectrometer in the range of 1000 to 4000 cm^{-1}. The morphology of the samples was studied using a Field Emission Scanning Electron Microscope (FESEM, Gemini SEM300). Dielectric measurements are performed with a broadband dielectric spectrometer (BDS, Novacontrol GmbH, Germany). A vector network analyzer (VNA, N5224B-Keysight) was used to evaluate the complex scattering parameter values in the 8.2–12.4 GHz frequency band as part of a waveguide technique to estimate the metacomposites' EMI shielding capacities.

3.4 Microstructure and composition

3.4.1 X- Ray Diffraction

XRD patterns of PVA, CB, and PVA-CB composite films were measured in the 2θ range of 10° to 50° as shown in Fig. 3.2. The broad peak at 2θ = 19.5° in the XRD pattern of PC0 sample (pristine PVA) can be indexed to the (101) crystal plane of PVA, which reveals its semi-crystalline nature. Also, it can be observed that the intensity and nature of this (101) peak in the XRD patterns of PC1 to PC6 samples were unaffected by the incorporation of CB in the PVA matrix. This indicates that the filler does not affect the crystallinity or size of the PVA

crystals. On the other hand, the peak observed at 2θ = 25.7° in the XRD pattern of pristine CB sample correspond to the (002) plane of carbon black. The increase in the intensity of this (002) plane with increase in concentration of CB in the PVA-CB composites is evident from the XRD patterns of PC1 to PC6.

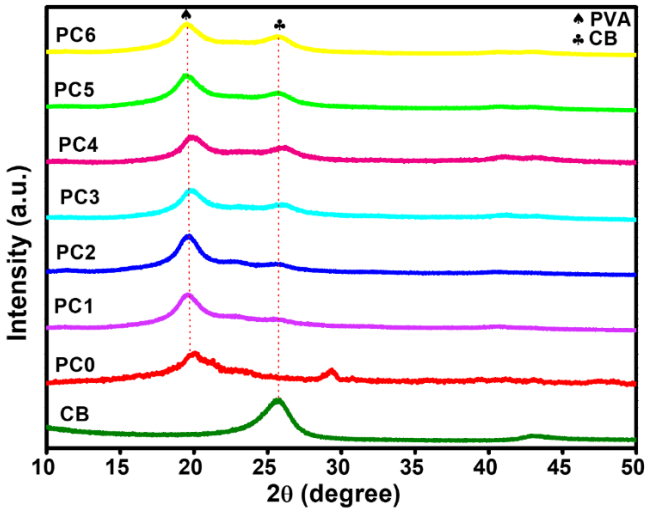

Figure 3.2 X-ray diffraction patterns of pristine carbon black (CB), pristine PVA (PC0) and PVA-CB (PC1 – PC6) metacomposites

3.4.2 Fourier transform infrared spectroscopy

FTIR spectrum of pure PVA in Fig. 3.3a shows a broad peak around 3562 cm^{-1} – 3123 cm^{-1} corresponding to the O-H stretching from water absorption or hydroxyl group present in the PVA structure. The peaks at 2930 cm^{-1} and 2855 cm^{-1} are recognized as the asymmetric and symmetric stretching vibrations of C-H bonds, respectively. The C=O stretching vibration of the carbonyl group of PVA is shown by the absorption band that appears at 1740 cm^{-1} and 1630 cm^{-1} [38]. The O–H bending and C–O stretching of the acetyl group is confirmed from the distinctive peak found at 1097cm^{-1} [39]. FTIR spectrum of pristine carbon black in Fig.3.3a, shows the characteristic peaks at 3432 cm^{-1} and 3138 cm^{-1} corresponding to the hydroxyl group and water absorption. On the other hand, the band at 1637 cm^{-1} originates from the conjugated C=C bonds and 1382 cm^{-1} corresponds to the C–C stretching vibrations [40,41]. Fig. 3.3b

shows FTIR spectra of PVA-CB metacomposites with different concentrations of carbon black. The spectra show a clear shift in the peaks, due to the PVA matrix, towards lower wavelength region indicating the formation of hydrogen bond and the substantial interaction of carbon black nanoparticles with the PVA indicating the successful formation of PVA-CB metacomposites.

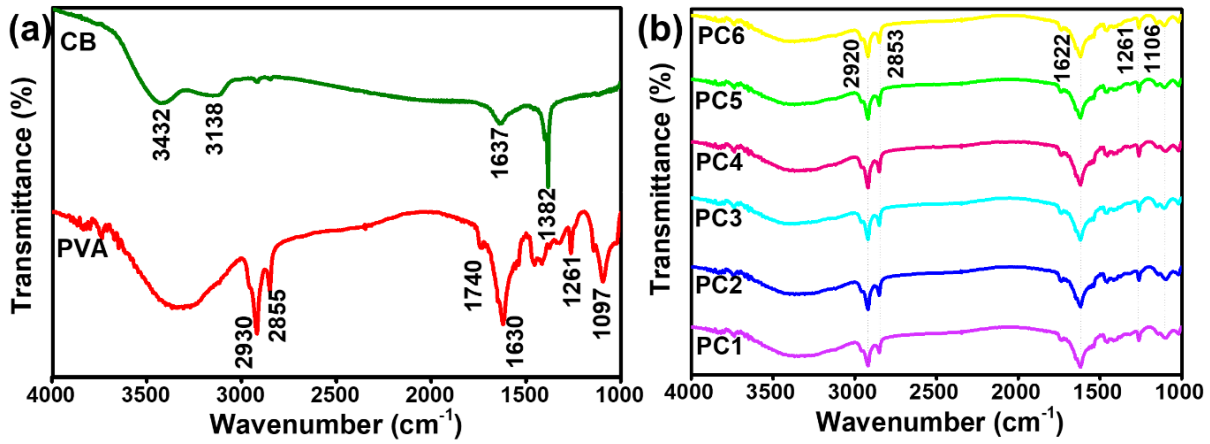

Figure 3.3 FTIR spectra of (a) pristine CB and PVA, and (b) PVA-CB metacomposites

3.4.3. Scanning electron microscopy

FESEM micrographs of PVA, CB, PC3 and PC6 are shown in Fig. 3.4a, 3.4b, 3.4c and 3.4d, respectively. Morphology of the pristine PVA film shown in Fig. 3.4a, exhibits a uniform surface texture without any deformations and as observed from Fig. 3.4b, particles of carbon black are observed to have a sphere-like morphology with chain-like clusters. On the other hand, the presence of CB particles distributed randomly over the surface of PVA film is clearly observed from Fig. 3.4c and 3.4d. Also, the increased concentration of CB in PC6 film in comparison to PC3 is evident from the micrographs. Distribution of CB particles and their concentration in the PVA matrix are expected to significantly influence the composite's dielectric and conductivity properties.

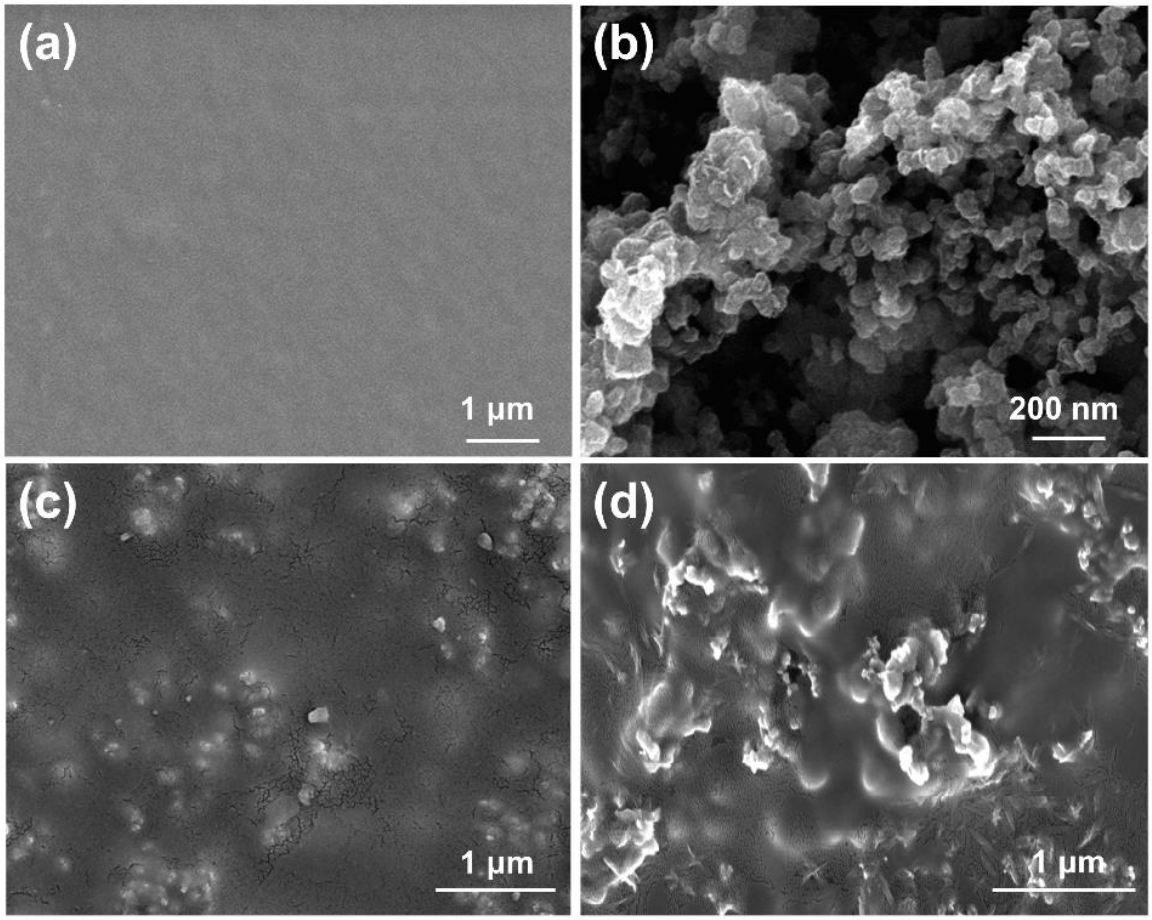

Figure 3.4 FESEM micrographs of (a) pristine PVA, pristine CB, (c) PC3 and (d) PC6 samples

3.4.4 Raman spectroscopy

Fig.3.5 depicts the Raman spectrum of the pristine carbon black particles that were employed in the fabrication of PVA-CB metacomposite films. The peak located at 1335 cm^{-1} and 1571 cm^{-1}, respectively can be attributed to the disordered (D) band and graphitic band (G) band of carbon black. The D band and G band corresponds to sp^3 and sp^2 carbon stretching modes. The band at 1571 cm^{-1} (G band) can be assigned to the in-plane vibration of the C–C bond and the band at 1335 cm^{-1} (D band) is typically activated by the presence of disorder in carbon systems. Higher intensity of G band compared to that of the D band is indicative of the good conductivity of carbon black [42][43] .

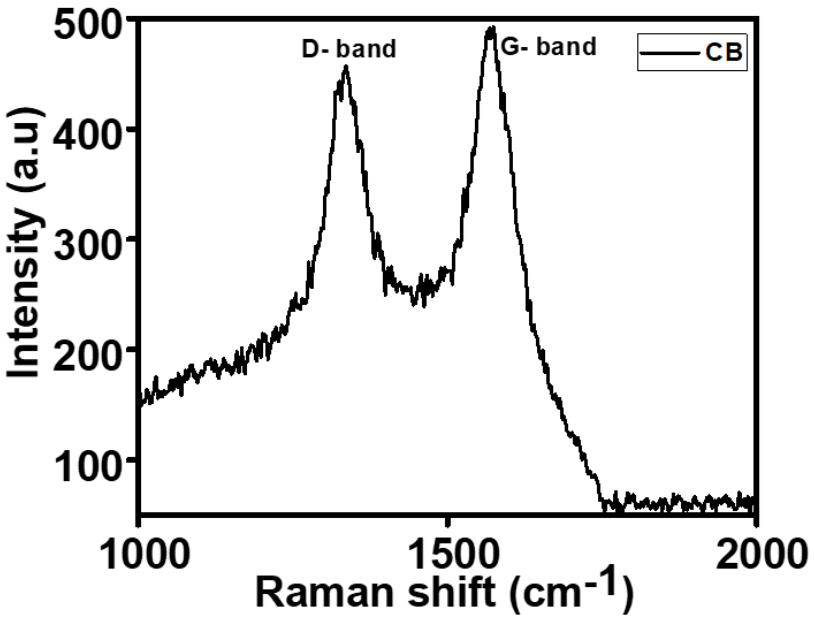

Figure 3.5 Raman spectrum of pristine carbon black particles

3.5 Thermal analysis

Thermogravimetric data of PVA and PVA-CB composites are depicted in the plot shown in

Thermogravimetric data of PVA and PVA-CB composites are depicted in the plot shown in

Fig.3.6. The TGA thermograph shows weight loss percentage as a function of temperature for PVA-CB composites with varying carbon black loadings. Pure PVA film was observed to lose 90% of its weight at 500 °C, while PC1, PC2, PC3, PC4, PC5 and PC6 were found to lose weight by 82%, 78%, 67%, 61%, 54%, and 55% respectively at 500 °C. As is known, almost all polymers decompose between 250 °C and 450 °C. As the concentration of CB increases, the weight loss percentage decreases significantly, indicating the strong interaction between the polymer chain and the CB nanoparticles. Therefore, the addition of CB nanoparticles in PVA resulted in a significant reduction in weight loss in comparison to pure PVA and reveals the enhanced thermal stability of the PVA-CB metacomposites.

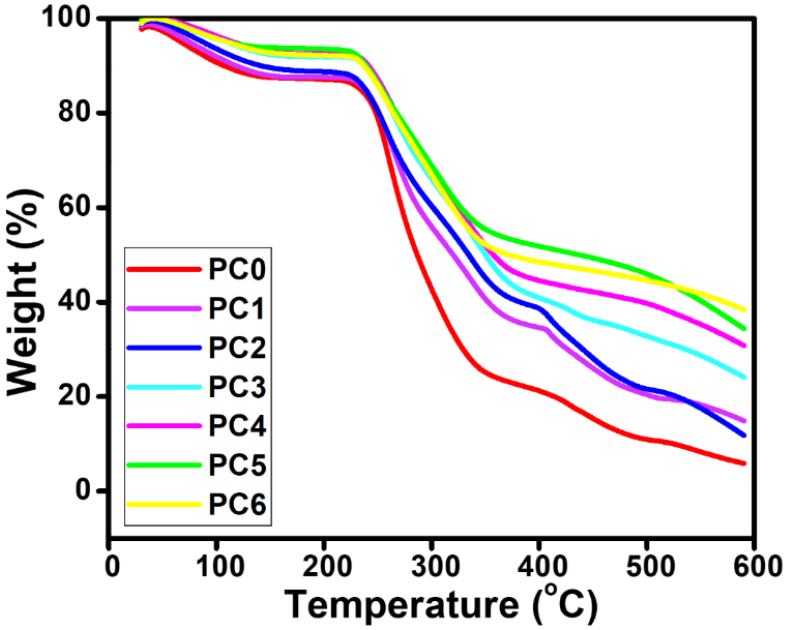

Figure 3.6 TGA curves of PVA and PVA-CB metacomposites

3.6 Conductivity behaviour

Frequency dispersion of AC conductivity in pristine CB, PVA, and PVA-CB composites are depicted in the plots shown in Fig. 3.7. Different conductive mechanisms, such as hopping and metal-like conduction, according to percolation theory are shown in Fig. 3.7a and 3.7b. As expected, the AC conductivity was found to increase with increase in the CB concentration in PVA-CB composite films in comparison to pristine PVA. When the carbon black concentration was lower in PVA-CB composites (PC1 and PC2), the electron transport was attributed to hopping and the conductivity increased as a function of frequency [44–46], which is in accordance with Johnscher's power law

$$\sigma_{ac} = \sigma_{dc} + A\,\omega^{n} \qquad (3.1)$$

where σ_{ac} and σ_{dc} are the conductivity due to alternating and direct current respectively. 'A' and 'n' are pre-exponential and exponential factors and ω is the angular frequency. As shown in Fig. 3.7a, the frequency dispersion of AC conductivity in PC1and PC2 was fitted with power law and the R^2 value obtained was 0.98.

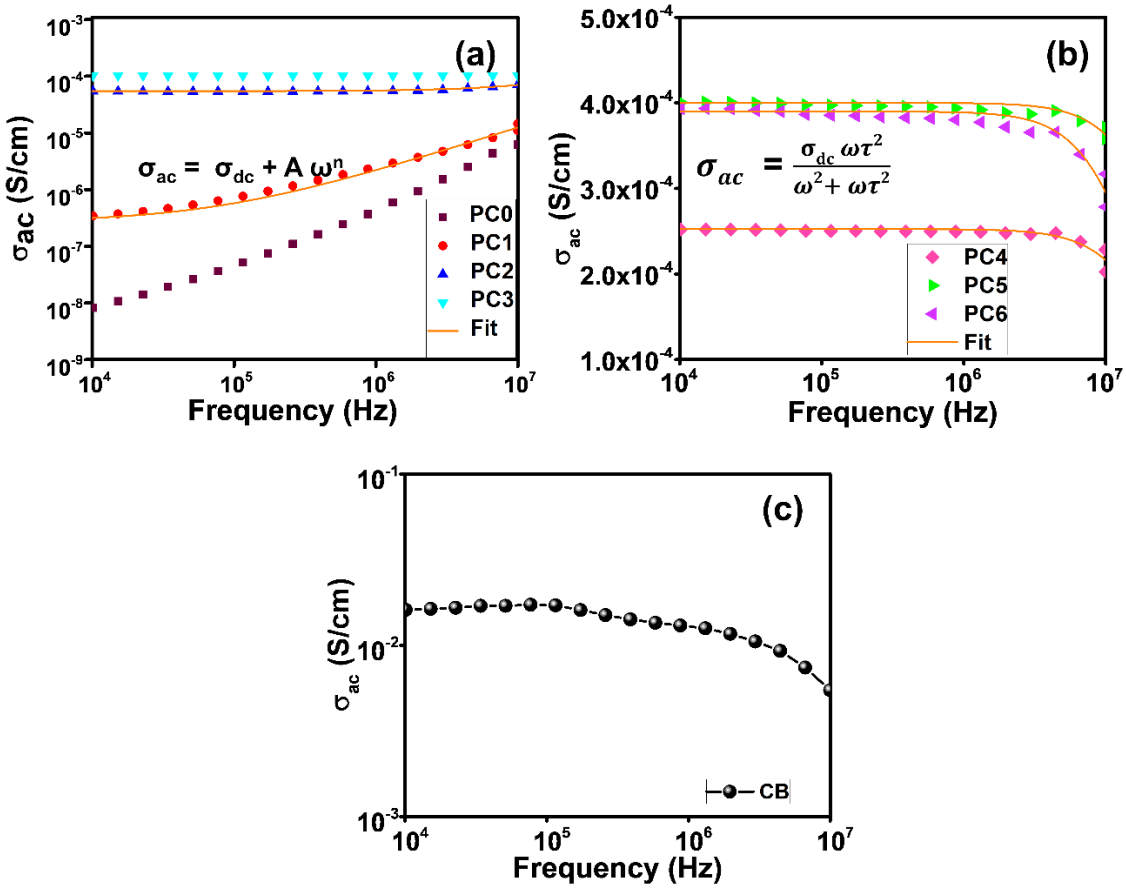

Figure 3.7 Frequency dispersion of AC conductivity in (a, b) PVA and PVA-CB composites and (c) pristine carbon black

On the other hand, the sample PC3 shows a flat electric response, indicates that the AC conductivity is independent of frequency in the test frequency range (10^4 to 10^7 Hz). Further increases in CB content (PC4, PC5, PC6), led to a subsequent decrease in conductivity due to skin effect [17,21,46,47], as shown in Fig. 3.7b. Skin effect increases the resistance, which affects the conductivity inversely, thereby reducing the skin depth. Therefore, the conductivity changes from hopping to metal-like when the carbon black content reaches the percolation threshold, and this can be explained using the Drude model [45,48]

$$\sigma_{ac} = \frac{\sigma_{dc}\,\omega_\tau^2}{\omega^2+\omega_\tau^2} \qquad (3.2)$$

$$\sigma_{dc} = \frac{\omega_p^2\,\tau}{4\pi} \qquad (3.3)$$

where σ_{dc} is direct current conductivity, $\omega_\tau = \frac{1}{\tau}$ is the relaxation rate and ω_p is the plasma frequency. Fig.3.7b, shows the fitted Drude model of conductivity observed in PVA-CB composites with high carbon black content.

A three-dimensional conductive network is expected to be formed when the carbon black content reaches the percolation threshold, resulting in metal-like conduction. When an alternating current is applied to this composite, the current in the higher frequency will crowd towards the surface of the conducting material and restrict the current to a smaller cross-sectional area, which will result in increased resistance and decreased skin depth. On the other hand, pristine carbon black shows conductivity around 0.01 S/cm at lower frequency region and shows a decreasing conductivity at higher frequency region as shown in Fig. 3.7c.

3.7. Negative permittivity behaviour

The complex permittivity spectra of PVA-CB composite films in the lower frequency region (10^4 to 10^7 Hz) are shown in Fig. 3.8a and 3.8b. PVA-CB composite films with low concentrations of carbon black (PC1 and PC2) were found to have a higher dielectric constant than pristine PVA films. The increase in dielectric constant may be attributed to the difference in conductivity between the adjacent materials, followed by the charge accumulation at the interface. The accumulated charges establish themselves as large numbers of micro-capacitors and increase the dielectric constant by means of interfacial polarization. Maxwell-Wagner-sillar effect also heavily influences the dielectric constant by how the filler is distributed in the matrix [21]. Pristine PVA (PC0) film had a relative permittivity of 8, while for PC1 and PC2 the value reached up to 50 in the lower test frequency range. Permittivity diminishes as frequency increases as a result of electric leakage from conducting carbon black assembly (Fig. 3.8a).

When the carbon black content is further increased from 1.25 wt% to 2.5 wt% (PC3 to PC6), ε' switches from positive to negative (Fig. 3.8b), at kHz frequency range, due to electrical percolation and the electrons become macroscopically delocalized within the interconnected conductive carbon black network. This process results in dilution of electron concentration, an increase in effective mass, and a plasma type negative permittivity that can be well described by the Drude model [8,25,49,50], which shows frequency-dependent permittivity for delocalized electrons. The equation governing Drude model is given as,

$$\varepsilon_r{}' = 1 - \frac{\omega_p^2}{\omega^2 + \omega_\tau^2} \tag{3.4}$$

$$\omega_p = \sqrt{\frac{n_{eff}e^2}{m_{eff}\epsilon_0}} \tag{3.5}$$

where 'ω' is the angular frequency of the applied electromagnetic field, ω_p is the plasma angular frequency, ω_τ is the collision frequency (the inverse of relaxation time $\omega_\tau = \frac{1}{\tau}$), $m_{eff\ and}\ n_{eff}$ are the effective mass and concentration of electrons, 'e' is the charge of electrons and ε_0 is the permittivity of free space.

As observed from Fig. 3.8c, the permittivity of carbon black shows both positive and negative values in the high and low frequency regions. Carbon black has a higher negative permittivity value around -20000, above 100 kHz, while PVA-CB composites show a higher value around -443 at 15 kHz. Therefore, it can be understood that carbon black and PVA work synergistically in the dilution of the overall electron density and result in a weakly negative permittivity at the lower frequency range. Compared to metal-ceramic metacomposites, the magnitude of the epsilon negative property in this work is very small and can be applied to applications including perfect absorption, negative capacitance field effect transistors, and high-power microwave filters [8,51–53].

Fig. 3.8d shows the frequency dependence of the imaginary part of permittivity. The imaginary dielectric constant measures dielectric losses and describes the capability of a material to

permanently absorb energy from an alternating electric field. Dielectric losses are primarily caused by dipole movement, interfacial polarization, and conduction. PVA is an insulating polymer and its ε" value is below 5. Adding carbon black to the PVA matrix shows frequency dispersion behaviour, and the ε" value decreases with increasing frequency. Conduction loss contributes largely to the total loss in the lower frequency region due to high values of ε" in that region. Conductivity loss results from a large leakage current caused by the continuous conductivity path created by the increase in carbon black content. The dominant dielectric loss in the higher frequency region changes from conduction loss to dipolar loss [20,29,54,55].

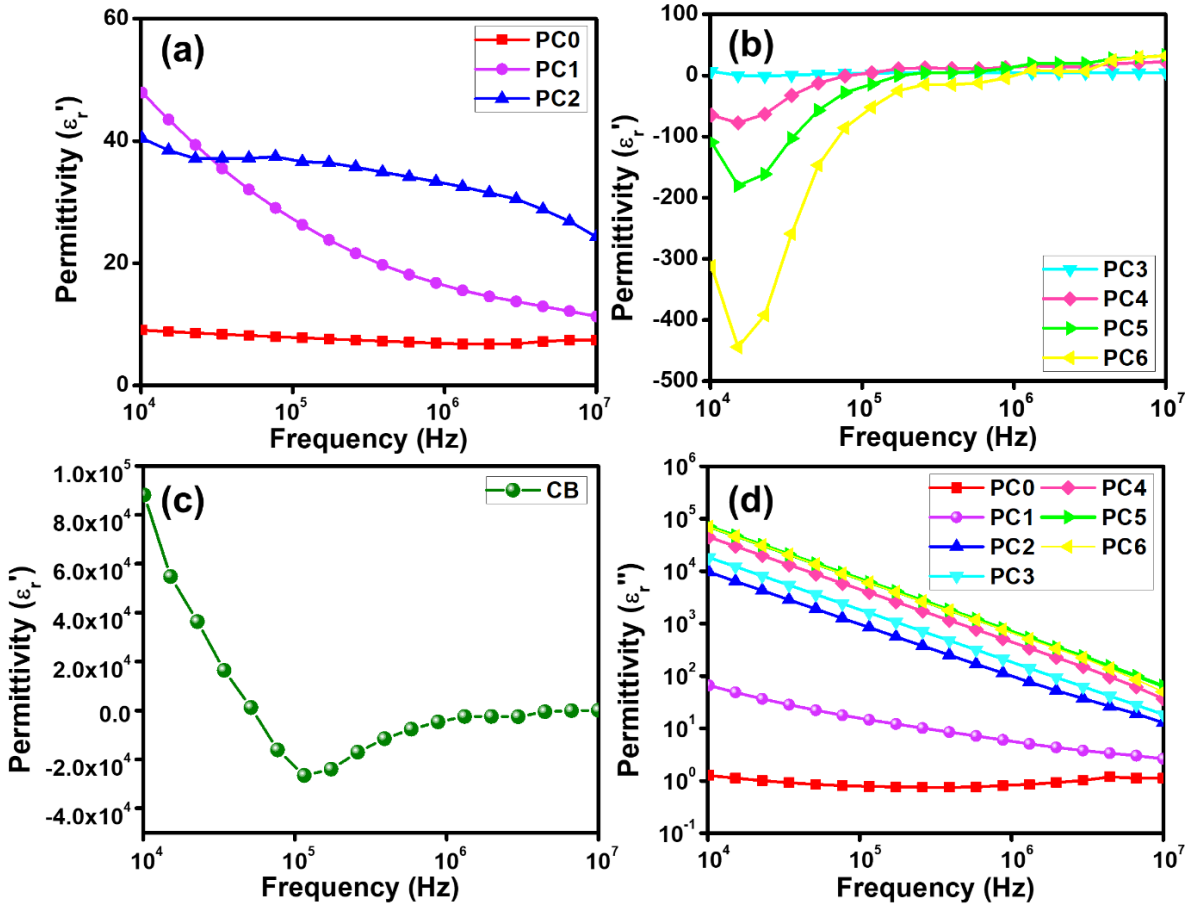

Figure 3.8 Frequency dependent permittivity of (a, b) PVA-CB composites with different carbon black content and (c) pristine carbon black; (d) frequency dependent imaginary permittivity of PVA-CB composites

Fig. 3.9a-d depict the frequency dependent reactance and phase angle of PVA-CB composites. Inductive and capacitive reactance are commonly summed up to form reactance. Composites

that exhibit capacitive characteristics and positive permittivity typically show negative value of reactance, indicating that the voltage phase lags behind the current phase. In contrast, the reactance with positive value has inductive characteristics and such composites exhibit negative permittivity [54–56]. Herein, the PVA-CB composites with lower carbon black contents (PC1, PC2) show negative reactance and phase angle values, which indicates their capacitive behaviour [57,58]. By the time the carbon black content exceeds the percolation threshold (PC3, PC4, PC5, PC6), the reactance and phase angle show a positive value in the negative permittivity region and a negative value in the positive permittivity region. The capacitive to inductive transition occurred at a higher frequency region corresponding to the negative to positive permittivity transition.

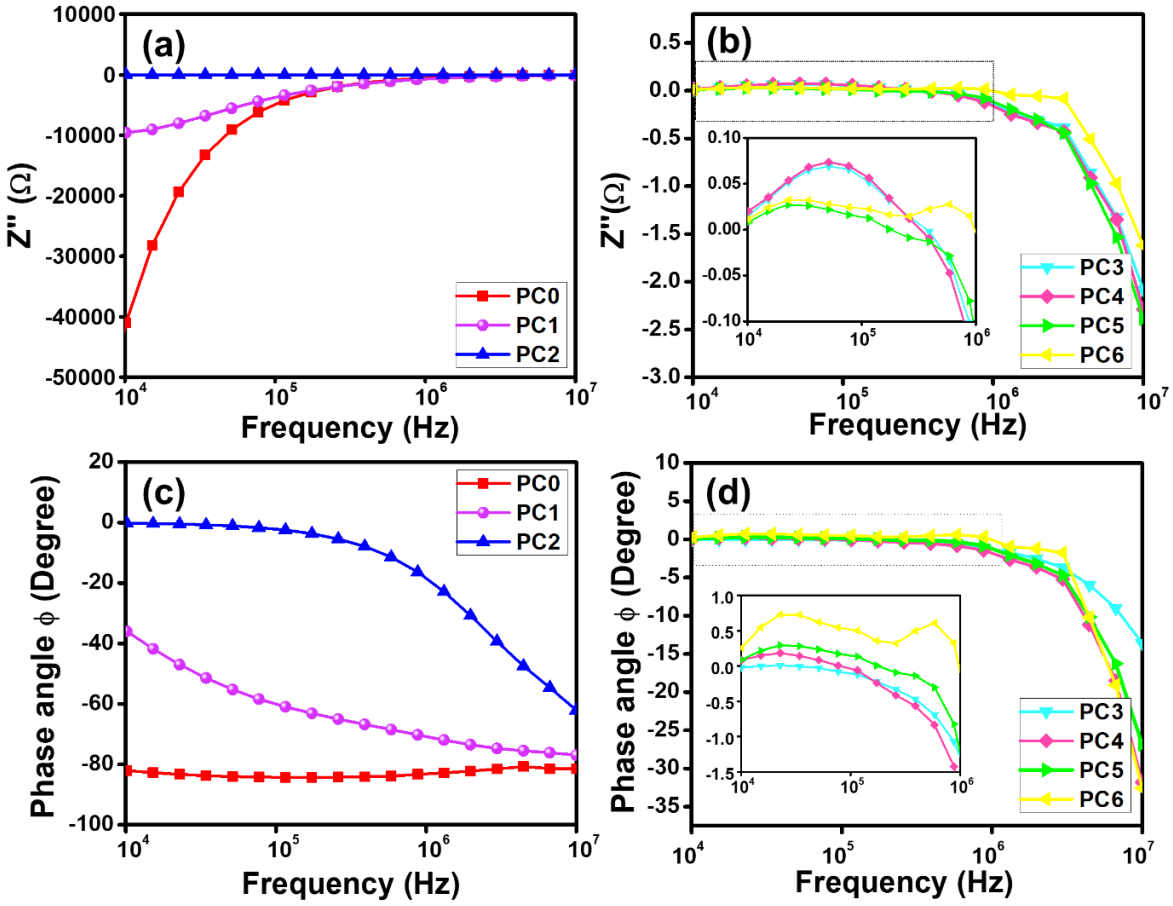

Figure 3.9 The frequency dependent (a, b) reactance spectra and (c, d) phase angle spectra of PVA-CB composites

The plot in Fig. 3.10 illustrates the variation of AC conductivity and permittivity at 10 kHz as a function of carbon black concentration in the PVA-CB composites. Pristine PVA (PC0) behaves as an insulator, but the addition of small amount of carbon black resulted in an increase in the conductivity and permittivity of the composite as a result of hopping conduction due to unconnected paths of carbon black in PC1 (0.5 wt%) and PC2 (0.75 wt%) films. When the carbon black content (1.25, 1.75, 2, 2.5 wt%) was increased further, the conductivity of the resulting films (PC3 – PC6) increases owing to the formation of a continuous conductive path resulting in metal-like conductivity. On the other hand, the plasma oscillation of delocalised electrons in carbon black resulted in negative permittivity. The PVA-CB composite exhibited weakly negative permittivity at lower frequencies due to the synergistic effect. The Drude type weakly negative permittivity contributes to the development of new metamaterials and their wide applications.

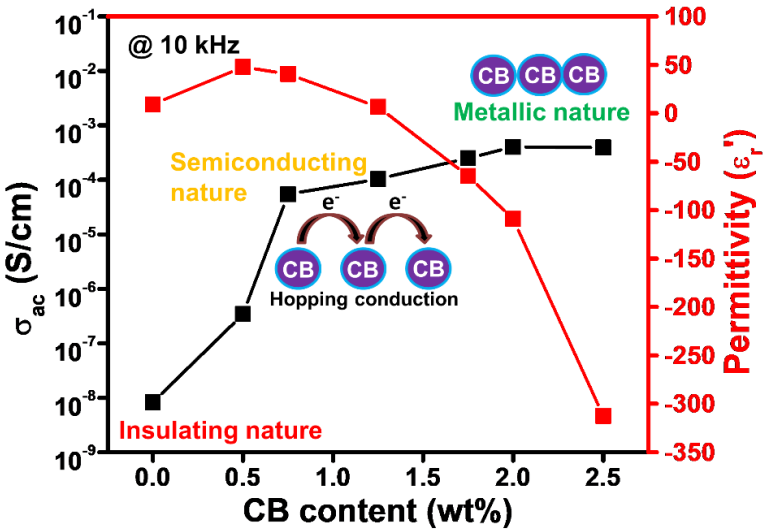

Figure 3.10 Plot depicting the variation in the conductivity and permittivity of PVA-CB composites with respect to the change in carbon black content at a radio frequency of 10 kHz. Interestingly, the insulating, semiconducting and metallic behaviour can be realized by adjusting the carbon black content in the PVA-CB metacomposite films

A review of the negative permittivity reported in the literature for various metacomposites is shown in Table 3.1 as a comparison. Typically, the electron density of metacomposites

composed of metals or conducting polymers is very high, so they have huge negative permittivity. For example, the iron-alumina composite reported by Sun et al. exhibited huge negative permittivity in gigahertz range. Similarly, Wang et al. also reported negative permittivity in higher frequency regions for silver-alumina composite. Also, polyaniline-Fe_3O_4 nanocomposites reported by Kavas et al. exhibited huge negative permittivity, but at a relatively lower frequency region.

Table.3.1 A comparison of the negative permittivity and conductivity of different metacomposites

Metacomposite	Test Frequency Range	Permittivity	Conductivity (S/cm)	Filler content	Reference
Iron - Alumina	10 MHz–1 GHz	~ -10^6 ~ -10^3	---------	30 mol%	[24]
Silver – Alumina	1 kHz-100 MHz	~ 0 to -100×10^4	10	10.52 vol%	[56]
Ag - $BaTiO_3$	10 MHz–1 GHz	~ 0 to -6×10^6	~ 1000	60 wt%	[57]
Polyaniline-Fe_3O_4	0.1 kHz to 10 MHz	~ 0 to -1.5×10^5	10^{-6} to 10^{-4}	20 vol%	[58]
Graphene - PDMS	10 kHz- 1 MHz	~ -4×10^4 to ~ -6×10^4	~ 10	4 wt%	[28]
CNT - Alumina	10 MHz–1 GHz	~ -10^2 ~ 10^1	~ 0.1	10.0 wt%	[25]
Pyrolitic carbon - Silicon nitride	20 MHz–1 GHz	~ -50 ~ -10	----------	12.5 wt%	[59]
PVA-CB	10 kHz – 10 MHz	~ 0 to ~ -1.23 & -443 at 15 kHz	(1.03×10^{-4}) (at 22.8 kHz)	1.25 wt% 2.5 wt%	This work

Conversely, carbonaceous materials have a moderate electron density and the composites made of carbonaceous material exhibit weak negative permittivity in the kHz to MHz frequency range and have great potential to be employed in stretchable and wearable electronics and microwave absorbers. In the present study, PVA-CB composite exhibited a negative permittivity value of -1.23 for sample PC3 (1.25 wt%), which is just above the percolation

threshold and is suitable for flexible electronic application as well as perfect absorption. At a higher concentration of 2.5 wt% carbon black (PC6), the composite showed a negative permittivity value of -443 at 15 kHz, a moderate negative permittivity reduces the impedance of the material and making it closer to the impedance of free space, which makes it suitable for impedance matching applications.

Film formed with the addition of more than 2.5 wt% of CB to the PVA solution was found to be mechanically unstable and appeared to be heavily agglomerated. Photographs of the as-fabricated composite film is presented in Fig. 3.11.

Figure 3.11 Photograph depicting the PVA-CB metacomposite film (PC7) fabricated with 3 wt% CB. As observed the film is non-uniform owing to the aggregation of CB on the surface

Figure 3.12 shows real and imaginary part of permittivity of PVA-CB composites with high concentration of PVA (10 wt%). Positive permittivity is achieved for the composites below the percolation threshold while negative permittivity is obtained over the percolation threshold. Interstingly positive permittivity is obtained in PVAC0, PVAC1,PVAC2, PVAC3 and PVAC4 samples. Here, percolation threshold is achieved in PVAC5 (2 wt%) sample and shows Drude – Lorentz model negative permittivity. PVAC6 sample also shows negative permittivity. In the intermediate frequency range, it exhibits negative permittivity, and the two zero-crossing points are visible. Both Electric dipole resonance (lower frequency region) and plasma oscillations

(higher frequency region) of delocalized electrons are the main causes of negative permittivity. The Drude model and the Lorentz model are typically employed to explain the electric dipole resonance and plasma oscillation of delocalized electrons, respectively. here, two negative permittivity models (Drude and Lorentz models) are combined [54,60]. the model can be expressed as follows.

$$\varepsilon(\omega) = 1 - \frac{\omega_p^2}{\omega^2 + \Gamma_D^2} + \frac{K\omega_L^2(\omega_L^2 - \omega^2)}{(\omega_L^2 - \omega^2)^2 + \omega^2\Gamma_L^2} \tag{3.6}$$

Γ_L is the damping constant of Lorentz resonance, ω_L is the Lorentz resonance angular frequency, $\omega = 2\pi f$ is the angular frequency, $\omega_p = 2\pi f_p$ is the plasma frequency K is the dc electric susceptibility.

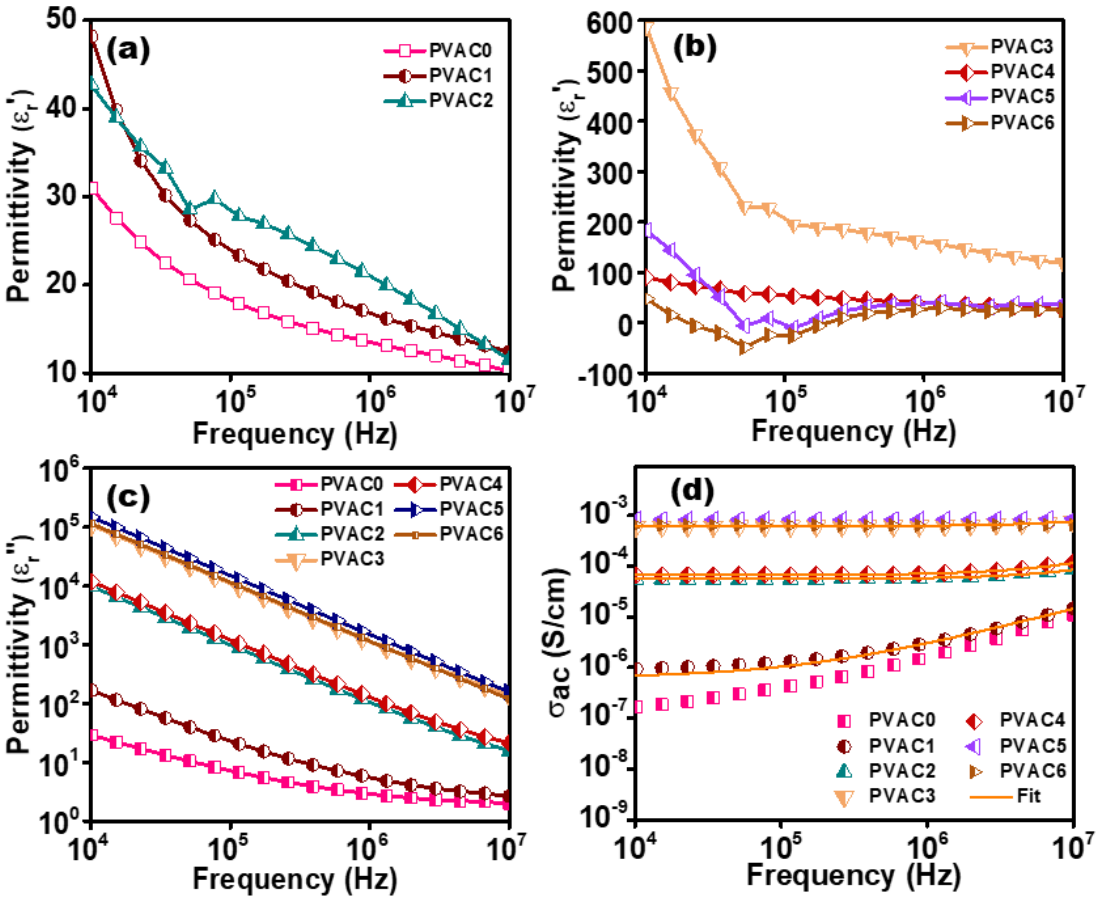

Figure 3.12 Frequency dependent real and imaginary part of permittivity (a, b, c) and conductivity (d) of PVA – CB composites with 10 wt% PVA

Fig. 3.12d shows conductivity of PVA-CB composites. Conductivity increase with increase in frequency in PVAC1, PVAC2, PVAC3 and PVAC4 samples and the electron transport was attributed to hopping in accordance with Johnscher's power law. Remaining samples shows frequency independent behaviour.

Interestingly, as observed from the data presented in Fig. 3.13a-c, the trend observed for frequency dependent reactance and phase angle of PVA-CB composites fabricated with 10 wt% PVA was comparable to those observed with 5 wt% PVA. PVAC0 – PVAC4 samples shows negative phase angle and reactance and PVAC5 and PVAC6 samples shows positive phase angle and reactance in the negative permittivity region.

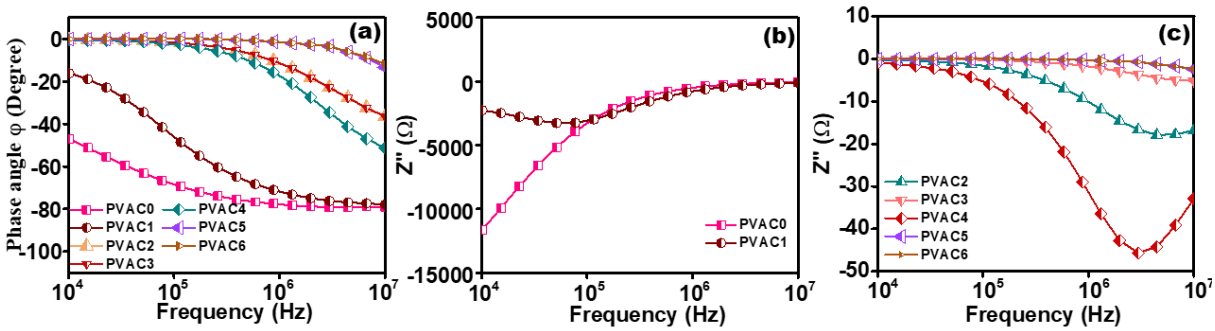

Figure 3.13 Frequency dependent reactance and phase angle of PVA-CB composites with 10 wt% PVA

3.8. Electromagnetic interference shielding application

Electromagnetic interference shielding performance of PVA - CB composites was characterized by vector network analyser using a transmission line method in the X-band region. The reflection, transmission and absorption coefficient of the composites are evaluated using S-parameters.

$$T = |S_{21}|^2 = |S_{12}|^2 \quad (3.7)$$

$$R = |S_{11}|^2 = |S_{22}|^2 \quad (3.8)$$

$$A = 1 - R - T \quad (3.9)$$

where S_{11} is forward reflection coefficient, S_{22} is backward reflection coefficient, S_{12} forward transmission coefficient, S_{21} backward transmission coefficient. The total shielding effectiveness can be calculated using the equation

$$SE_{Total} = SE_R + SE_A + SE_M \quad (3.10)$$

SE_A – Shielding by absorption, SE_R – Shielding by reflection, SE_M – Shielding by multiple internal reflection. Where SE_M can be ignored when SE_T is greater than 10dB.

$$SE_{Total} = 10 \log \frac{1}{|S_{21}|^2} = 10 \log \frac{1}{|S_{12}|^2} \quad (3.11)$$

$$SE_R = 10 \log \left(\frac{1}{1-|S_{11}|^2} \right) \quad (3.12)$$

$$SE_A = 10 \log \left(\frac{1-|S_{11}|^2}{|S_{12}|^2} \right) \quad (3.13)$$

$$\text{EMI SE (\%)} = 100 - \left(\frac{1}{10^{\frac{SE}{10}}} \right) \times 100 \quad (3.14)$$

Fig. 3.14(a-c) shows EMI shielding efficiency of PVA – CB composites with varying concentration of carbon black. Increasing the concentration of carbon black, its shielding efficiency greatly increased. At 0.5 wt% carbon black added to the polyvinyl alcohol matrix, its average total shielding efficiency is 8 dB. Further increase of carbon black, its total shielding efficiency is above 14 dB in the whole test frequency region. the highest shielding efficiency obtained is 23 dB with 2.5 wt% of carbon black. Shielding efficiency by reflection is below 1 dB in all samples, indicating absorption dominant shielding mechanism. The average total shielding efficiency of PC1, PC2, PC3, PC4, PC5 and PC6 samples are 8 dB, 14 dB, 17 dB, 19 dB, 20 dB and 23 dB respectively. The shielding efficiency in percentage is 99.5 in PC6 sample. Increasing the concentration of conducting filler, composite film conductivity is greatly increased and also increased its thickness. These two factors contribute shielding efficiency. The conductive network is formed by the carbon black content and provide a sufficient path to transport moving charge carriers freely. Several interfaces are produced by the PVA – CB composites and interfacial polarization also contribute shielding efficiency [61] [62] .

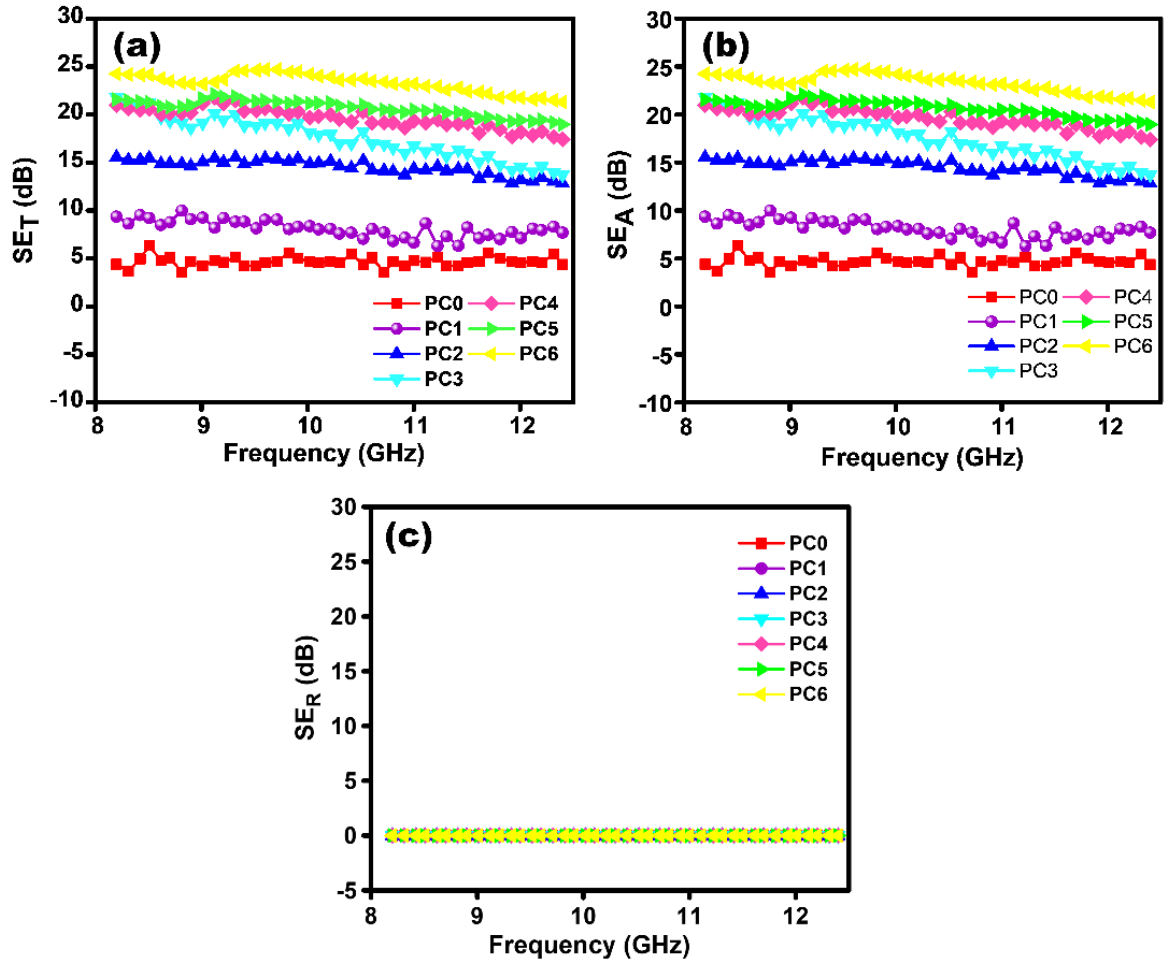

Figure 3.14 The shielding efficiency of PVA – CB composites with varying concentration of carbon black (a)Total shielding (b) Absorption and (c) Reflection shielding

3.9 Conclusion

PVA-CB percolative metacomposites were fabricated by a simple low-cost dye casting method. When the carbon black content was low, the isolated carbon black was randomly distributed in the PVA matrix and the composites exhibited hopping conduction, positive permittivity and capacitive character. Further increase of carbon black content reached the percolation threshold and the composites exhibited metal like conduction, negative permittivity and inductive character. Synergetic effect of PVA and carbon black resulted in low frequency plasmonic state of weakly negative permittivity. Pure carbon black exhibited a higher negative permittivity of

-20,000 at 100 kHz, while the PVA-CB composite exhibited a weakly negative permittivity of -443 at 15 kHz at a higher concentration of carbon black. Epsilon near zero negative permittivity of -1.23 was obtained when the CB content was just above the percolation threshold (1.25 wt%). Compared with ceramic metacomposites, PVA-CB metacomposites are well suited for applications in flexible electronics, perfect absorption and impedance matching by tuning the negative permittivity through adjustment of carbon black content. The electromagnetic interference shielding efficiency of the samples were also studied. The maximum shielding efficiency observed is 23 dB for sample PC6 (2.5 wt%). Shielding efficiency by reflection is below 1 dB in all samples, indicating absorption dominant shielding mechanism.

****

References

[1] K. Sun, Z. Wang, J. Xin, Z. Wang, P. Xie, G. Fan, V. Murugadoss, R. Fan, J. Fan, and Z. Guo, Macromol. Mater. Eng. **305**, 1900709 (2020).
[2] R. A. Shelby, D. R. Smith, and S. Schultz, Science **292**, 77 (2001).
[3] J. B. Pendry, A. J. Holden, D. J. Robbins, and W. J. Stewart, IEEE Trans. Microw. Theory Tech. **47**, 2075 (1999).
[4] P. Xie, Z. Wang, K. Sun, C. Cheng, Y. Liu, and R. Fan, Appl. Phys. Lett. **111**, 112903 (2017).
[5] Y. Shi, K. Pan, M. Gerard Moloney, and J. Qiu, Compos. Part Appl. Sci. Manuf. **144**, 106351 (2021).
[6] R. W. Ziolkowski and E. Heyman, Phys. Rev. E **64**, 056625 (2001).
[7] B. Li, G. Sui, and W.-H. Zhong, Adv. Mater. **21**, 4176 (2009).
[8] K. Sun, J. Xin, Y. Li, Z. Wang, Q. Hou, X. Li, X. Wu, R. Fan, and K. Leong Choy, J. Mater. Sci. Technol. **35**, 2463 (2019).
[9] J. Zhu, S. Wei, L. Zhang, Y. Mao, J. Ryu, P. Mavinakuli, A. B. Karki, D. P. Young, and Z. Guo, J. Phys. Chem. C **114**, 16335 (2010).
[10] C. Hou, G. Fan, X. Xie, X. Zhang, X. Sun, Y. Zhang, B. Wang, W. Du, and R. Fan, J. Alloys Compd. **855**, 157499 (2021).
[11] J. B. Pendry, Phys. Rev. Lett. **85**, 3966 (2000).
[12] Y. Peng, Y. Shen, Z. Geng, P. Li, J. Zhu, and X. Zhu, Sci. Bull. **65**, 1022 (2020).
[13] G. Lipworth, J. Ensworth, K. Seetharam, Da Huang, J. S. Lee, P. Schmalenberg, T. Nomura, M. S. Reynolds, D. R. Smith, and Y. Urzhumov, Sci. Rep. **4**, 3642 (2015).
[14] Y. Huang, Y. Feng, and T. Jiang, Opt. Express **15**, 11133 (2007).
[15] Y. Lu, B. Chi, D. Liu, S. Gao, P. Gao, Y. Huang, J. Yang, Z. Yin, and G. Deng, ACS Omega **3**, 11144 (2018).
[16] N. Joseph, S. K. Singh, R. K. Sirugudu, V. R. K. Murthy, S. Ananthakumar, and M. T. Sebastian, Mater. Res. Bull. **48**, 1681 (2013).
[17] C. Cheng, R. Fan, G. Fan, H. Liu, J. Zhang, J. Shen, Q. Ma, R. Wei, and Z. Guo, J. Mater. Chem. C **7**, 3160 (2019).
[18] C. Liu and N. Behdad, J. Appl. Phys. **113**, 064909 (2013).
[19] Z. Sun, Z. Yan, R. Yin, X. Huang, K. Yue, A. Li, and L. Qian, Compos. Commun. **17**, 18 (2020).
[20] H. Wu, R. Yin, Y. Zhang, Z. Wang, P. Xie, and L. Qian, J. Phys. Chem. C **121**, 12037 (2017).
[21] C. Xu, Y. Qu, G. Fan, P. Xie, H. Ren, J. Chen, Y. Liu, Y. Wu, and R. Fan, J. Mater. Sci. Mater. Electron. **29**, 15994 (2018).
[22] Z. Shi, R. Fan, K. Yan, K. Sun, M. Zhang, C. Wang, X. Liu, and X. Zhang, Adv. Funct. Mater. **23**, 4123 (2013).
[23] Z. Shi, R. Fan, Z. Zhang, L. Qian, M. Gao, M. Zhang, L. Zheng, X. Zhang, and L. Yin, Adv. Mater. **24**, 2349 (2012).
[24] M. Gao, Z. Shi, R. Fan, L. Qian, Z. Zhang, and J. Guo, J. Am. Ceram. Soc. **95**, 67 (2012).
[25] C. Cheng, R. Fan, Y. Ren, T. Ding, L. Qian, J. Guo, X. Li, L. An, Y. Lei, Y. Yin, and Z. Guo, Nanoscale **9**, 5779 (2017).
[26] H. D. Shetty, K. P. Maity, and V. Prasad, Surf. Interfaces **21**, 100670 (2020).
[27] H. Luo and J. Qiu, Adv. Electron. Mater. **5**, 1900011 (2019).
[28] K. Sun, J. Dong, Z. Wang, Z. Wang, G. Fan, Q. Hou, L. An, M. Dong, R. Fan, and Z. Guo, J. Phys. Chem. C **123**, 23635 (2019).
[29] Z. Wang, K. Sun, Q. Jiang, K. Yin, L. Xie, S. Cao, Y. Zhang, X. Li, and R. Fan, Mater. Today Commun. **24**, 101230(1 (2020).
[30] R. Nagarkar and J. Patel, **3**, 34 (2019).
[31] D. Feldman, AIMS Mater. Sci. **8**, 119 (2021).
[32] N. M. Renukappa, Siddaramaiah, R. D. Sudhaker Samuel, J. Sundara Rajan, and J. H. Lee, J. Mater. Sci. Mater. Electron. **20**, 648 (2009).
[33] Y. Fan, G. D. Fowler, and M. Zhao, J. Clean. Prod. **247**, 119115 (2020).
[34] K. Sun, Z. Wang, J. Xin, Z. Wang, P. Xie, G. Fan, V. Murugadoss, R. Fan, J. Fan, and Z. Guo, Macromol. Mater. Eng. **305**, 1900709 (2020).

[35] M. I. Baker, S. P. Walsh, Z. Schwartz, and B. D. Boyan, J. Biomed. Mater. Res. B Appl. Biomater. **100B**, 1451 (2012).
[36] H.-J. Choi, M. S. Kim, D. Ahn, S. Y. Yeo, and S. Lee, Sci. Rep. **9**, 6338 (2019).
[37] Q. Zhang, B.-Y. Zhang, Z.-X. Guo, and J. Yu, Polymers **9**, 404 (2017).
[38] N. A. Shamsuri, S. N. A. Zaine, Y. M. Yusof, W. Z. N. Yahya, and M. F. Shukur, Ionics **26**, 6083 (2020).
[39] M. Sabzi, M. J. Afshari, M. Babaahmadi, and N. Shafagh, Colloids Surf. B Biointerfaces **188**, 110757 (2020).
[40] N. Hauptman, M. K. Gunde, M. Kunaver, and M. Bešter-Rogač, J. Coat. Technol. Res. **8**, 553 (2011).
[41] C. D. Zappielo, D. M. Nanicuacua, W. N. L. Dos Santos, D. L. F. Da Silva, L. H. Dall'antônia, F. M. De Oliveira, D. N. Clausen, and C. R. T. Tarley, J. Braz. Chem. Soc. **27**, 1715 (2016).
[42] M. Youssry, F. Z. Kamand, M. I. Magzoub, and M. S. Nasser, RSC Adv. **8**, 32119 (2018).
[43] J.-G. Li, C.-Y. Tsai, and S.-W. Kuo, Polymers **6**, 1794 (2014).
[44] B. Zhao and C. B. Park, J. Mater. Chem. C **5**, 6954 (2017).
[45] Y. Liu, G. Fan, Y. Qu, P. Xie, Z. Wang, Z. Zhang, R. Fan, and X. Yin, J. Mater. Sci. Mater. Electron. **29**, 12144 (2018).
[46] K. Sun, J. Xin, Z. Wang, S. Feng, Z. Wang, R. Fan, H. Liu, and Z. Guo, J. Mater. Sci. Mater. Electron. **30**, 14745 (2019).
[47] D. C. Mattis and J. Bardeen, Phys. Rev. **111**, 412 (1958).
[48] Y. Qu, Y. Wu, J. Wu, K. Sun, and R. Fan, J. Alloys Compd. **847**, 156526 (2020).
[49] C. Cheng, Y. Jiang, X. Sun, J. Shen, T. Wang, G. Fan, and R. Fan, Compos. Part Appl. Sci. Manuf. **130**, 105753 (2020).
[50] Y. Qu, Y. Du, G. Fan, J. Xin, Y. Liu, P. Xie, S. You, Z. Zhang, K. Sun, and R. Fan, J. Alloys Compd. **771**, 699 (2019).
[51] K. Sun, P. Xie, Z. Wang, T. Su, Q. Shao, J. Ryu, X. Zhang, J. Guo, A. Shankar, J. Li, R. Fan, D. Cao, and Z. Guo, Polymer **125**, 50 (2017).
[52] Z. Wang, K. Sun, H. Wu, P. Xie, Z. Wang, X. Li, and R. Fan, J. Mater. Sci. **55**, 15481 (2020).
[53] Z. Wang, H. Li, H. Hu, Y. Fan, R. Fan, B. Li, J. Zhang, H. Liu, J. Fan, H. Hou, F. Dang, Z. Kou, and Z. Guo, Adv. Electron. Mater. **6**, 1901005 (2020).
[54] R. Ma, C. Cheng, Y. Qu, and R. Fan, Ceram. Int. **47**, 9971 (2021).
[55] Y. Liu, G. Fan, Y. Qu, P. Xie, Z. Wang, Z. Zhang, R. Fan, and X. Yin, J. Mater. Sci. Mater. Electron. **29**, 12144 (2018).
[56] Z. C. Shi, R. H. Fan, Z. D. Zhang, H. Y. Gong, J. Ouyang, Y. J. Bai, X. H. Zhang, and L. W. Yin, Appl. Phys. Lett. **99**, 032903 (2011).
[57] Z. Wang, P. Xie, G. Fan, Z. Zhang, Y. Liu, Q. Gu, and R. Fan, Ceram. Int. **46**, 9342 (2020).
[58] O. Polymers, I. M. Universitesi, A. Baykal, and M. Toprak, J. Inorg. Organomet. Polym. Mater. **23**, 306 (2013).
[59] C. Cheng, R. Fan, Z. Wang, Q. Shao, X. Guo, P. Xie, Y. Yin, Y. Zhang, L. An, Y. Lei, J. E. Ryu, A. Shankar, and Z. Guo, Carbon **125**, 103 (2017).
[60] Y. Qu, J. Lin, J. Wu, Z. Wang, K. Sun, M. Chen, B. Dong, Z. Guo, and R. Fan, J. Phys. Chem. C **124**, 23361 (2020).
[61] J. Ju, T. Kuang, X. Ke, M. Zeng, Z. Chen, S. Zhang, and X. Peng, Compos. Sci. Technol. **193**, 108116 (2020).
[62] X. Fan, M. Li, X. Li, F. Ye, J. Xue, L. Zhang, and L. Cheng, Chin. Chem. Lett. **31**, 1026 (2020).

Modified Negative Permittivity and X-band Microwave Absorption in Polyvinyl Alcohol–MWCNT Metacomposites

Artificially structured metamaterials with negative electromagnetic parameters hold potential for fascinating applications in diverse fields, attracting significant research interest. However, their complex fabrication processes necessitate the exploration of alternative approaches [1–3]. Random nanocomposites, also called metacomposites, present a promising avenue, exhibiting the ability to achieve negative permittivity and permeability through controlled microstructure and composition adjustments [4–6]. Epsilon-negative materials, exhibiting negative permittivity behaviour, have gained increasing research focus due to their unique properties [7,8]. Their advantages, including the permittivity tunability, simple fabrication process and cost-effectiveness, make them attractive for various applications. These applications encompass antennas, wireless power transfer systems, wave filters, frequency selective surfaces, wave absorbers, and electromagnetic interference shielding [9–13].

Epsilon's negative property is heavily influenced by the concentration of free electrons in metacomposites. Since metals have high electron densities, their epsilon values are negative, and their dielectric loss is high [14,15]. Metacomposites made from metals have a high dielectric loss, making them unsuitable for impedance and permeability matching. Tunable and weakly negative permittivity is ideal for perfect absorption, and weakly negative permittivity is difficult to achieve in metal metacomposites. Additionally, the weak bonding between metal particles and polymer matrix affects the flexibility of metal incorporated polymer composites. Carbon-based materials are another conducting filler with a moderate electron density that could be used to fabricate metacomposites [4,16–19]. Y. Qu. et.al, reported negative permittivity in combination of graphene- carbon black composites in $CaCu_3Ti_4O_{12}$ matrix with weakly and tunable negative permittivity in the megahertz (MHz) region [20]. Z. Wang et.al,

reported weakly negative permittivity in PVP modified PVA-Graphene composites at kilohertz (kHz) region. J. Song, G. Shi, X. Song et.al, reported weakly negative permittivity at kHz-MHz region in PVDF-MWCNT composites [4]. Fillers such as, amorphous carbon, single/multi-walled carbon nanotubes, and graphene are used with polymer matrix to achieve weakly negative permittivity. This negative electromagnetic parameter makes metamaterials and metacomposites good microwave absorbers.

Throughout the past few years, electromagnetic radiation and interference have become major concerns related to electronic devices such as mobile phones, satellite communications, and other communication devices. Both the environment and human health are negatively affected by these radiations [21–23]. To solve this problem, high-efficiency microwave absorption materials are urgently needed. Microwave absorbers are being researched to find those that are lightweight, flexible, and efficient. In general, microwave absorption characteristics of polymer-based composites are determined by the distribution of fillers within the polymer matrix, the interfaces between the filler and the continuous matrix, and microstructure of the filler distribution in the composites. Lightweight, corrosion resistance, high flexibility, and easy processing are the main reasons to choose polymer matrix for microwave absorption applications [24–27]. Si- modified rGO/Fe_3O_4/PVDF-co-HFP shows microwave absorption in 2- 18 GHz region [26]. Xu *et.al* reported that, hollow carbon nanofiber decorated polyaniline based nanocomposites showed negative permittivity with very high electromagnetic interference shielding in the X-band region [28]. Carbon nanostructures such as, carbon black, and carbon fibers/nanotubes (CNTs), exhibit excellent absorption properties with lightweight, high surface area, modifiable permittivity and electrical conductivity properties [24,29–33].

In this study, MWCNT is used as the conducting filler, it possesses moderate electron concentration, high electron mobility and mechanical flexibility. Percolation occurs at low

MWCNT loading due to their high aspect ratio [34–36]. The property of polyvinyl alcohol (PVA) makes it ideal for use as a matrix since it is water soluble, biocompatible, partially crystalline, and highly resistant [37–40]. A simple, inexpensive die-casting method is used to create PVA-MWCNT composite films, and the effects of changing the MWCNT content in the PVA matrix are investigated. In order to comprehend the tailored negative permittivity of PVA-MWCNT composites, the samples produced undergo compositional, structural, conductivity, and dielectric investigations. Using this technique, composites can be made inexpensively, quickly, and are adaptable enough for electronic applications. A study of microwave absorption in the X-band region is also conducted on the sample.

4.1 Experimental

4.1.1 Materials

Sigma Aldrich provided polyvinyl alcohol (PVA) powder with molecular weight 89,000–98,000 and 99+% hydrolyzed. MWCNTs powder (Type 5 Multi- walled carbon nanotubes, outer diameter is about 30-50 nm and length are about 10-30 μm) was purchased from Sisco Research laboratories Pvt. Ltd. India. Sodium dodecyl sulphate (SDS) was purchased from Merck. All chemicals are used as received.

4.1.2 Fabrication of PVA- MWCNT metacomposites

According to the schematic shown in scheme 4.1, PVA-MWCNT composites have been created using a feasible and inexpensive die-casting procedure. Typically, 1 wt% SDS was added to the deionised water and stirred for 1 hour. Mixtures of MWCNT with weight percentages ranging from 0.5 to 3 were added to the aforementioned solution, then sonicated for 30 minutes. Next, 5 wt% PVA powder was dropped in this SDS-MWCNT solution and this final solution was mechanically agitated for 2 h at 90 °C. The resultant uniform black slurry was then gently poured into a petri dish. After 3h of drying at 50 ^{o}C, the PVA-MWCNT films were successfully removed from the petri dish and these were found to be quite flexible. The

fabricated PVA-MWCNT composite films were named as PM0, PM1, PM2, PM3, PM4, PM5 and PM6 with a filler concentration of 0.0, 0.5, 1.0, 1.5, 2.0, 2.5 and 3 wt% respectively. Composite films created by adding more than 3 weight percent MWCNT to PVA solutions were found to be highly combined and mechanically unreliable (see Fig.4.1), due to which PM6 was fabricated as the final sample. The thickness of the films (PM1 – PM6) are 0.13 mm, 0.17 mm, 0.21 mm, 0.37 mm, 0.48 mm, 0.70 mm respectively. Additionally, films with variable thickness were also fabricated for microwave absorption studies.

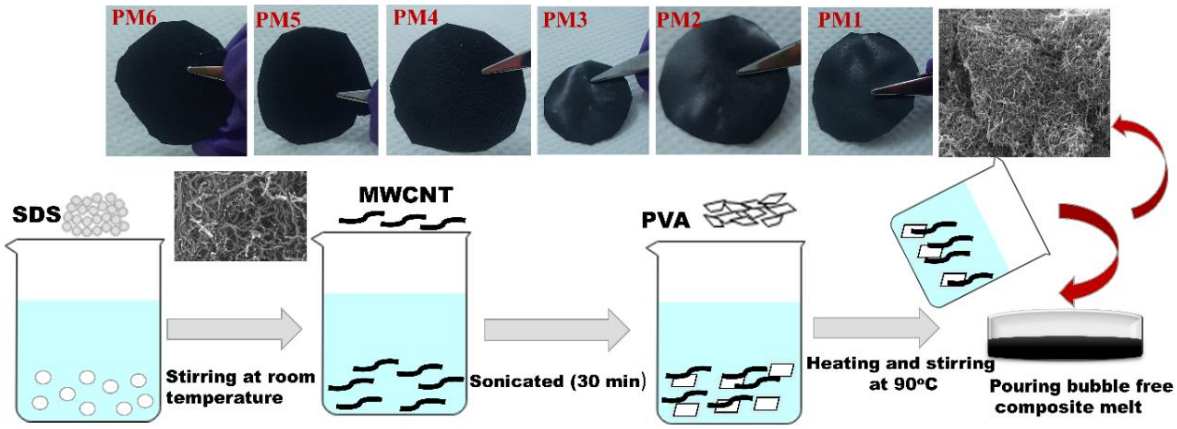

Scheme 4.1 A schematic illustrates different steps involved in the synthesis of a flexible metacomposite film made using PVA and MWCNT

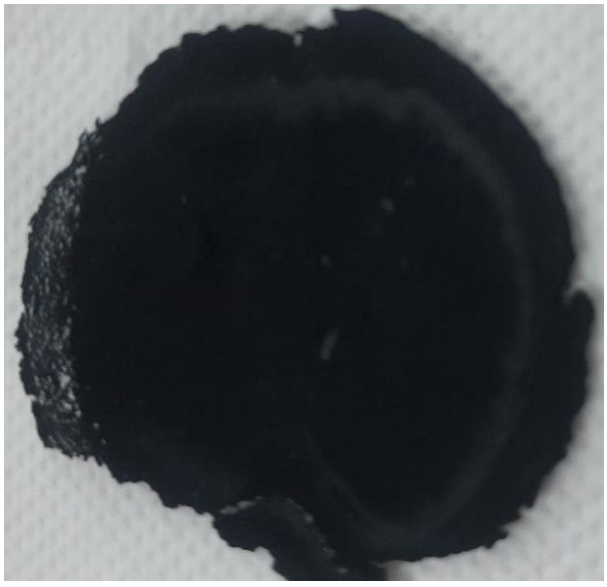

Figure 4.1 Photograph depicting the PVA – MWCNT metacomposite film (PM7) fabricated with 3.5 wt% MWCNT.As observed film is nonuniform

4.1.3 Characterisation techniques

X-ray diffraction analysis (X'pert^3 Powder, PANalytical, with Cu Kα radiation, λ = 1.5418 Å) was used at a scan rate of 2°/min in the range of 10° to 60° to study the composition and structural properties of the samples. Thermal analysis (TGA, STA 8000) was carried out at temperatures ranging from 30 °C to 600 °C in a nitrogen atmosphere. Using FTIR spectrometer (Spectrum two, PerkinElmer), the samples' infrared spectra were captured between 1000 and 4000 cm^{-1}. Field emission electron microscopy (FESEM, Gemini SEM300) was used to study the morphology of the materials. Dielectric behaviour of the metacomposites were studied using a broadband dielectric spectrometer (BDS, Novacontrol GmbH, Germany). A vector network analyzer (VNA, N5224B-Keysight) was used, in the frequency range of 8.2 to 12.4 GHz, to elucidate the EMI shielding behaviour and complex scattering parameters of the composite material.

4.2 Results and Discussion

4.2.1 Structural, morphological and thermal studies

FTIR spectra of pristine PVA, pristine MWCNT and PVA – MWCNT metacomposites are given in Fig.4.2a and 4.2b. The O-H stretching originate from the absorbed water or from the hydroxyl group present in the PVA/MWCNT is indicated by the presence of a wide band in the range 3436 –3148 cm^{-1}. The asymmetric and symmetric stretching vibrations of C-H bonds are identified by the bands at 2926 cm^{-1} and 2850 cm^{-1}, respectively. The carbonyl (C=O) stretching vibration is observed at 1642 cm^{-1}. The presence of O-H bending and C-O stretching of the acetyl group is evidenced by the presence of two bands respectively at 1379 cm^{-1} and 1085 cm^{-1} [41,42]. The band at 1636 /1642 cm^{-1} indicates the presence of C=C bonds, while the C–C stretching vibrations are identified by the presence of a band at 1384/1379 cm^{-1}

[43,44]. It is evident from the FTIR spectra that the composites differ significantly from pure PVA/MWCNT, suggesting a significant interaction between MWCNT and PVA.

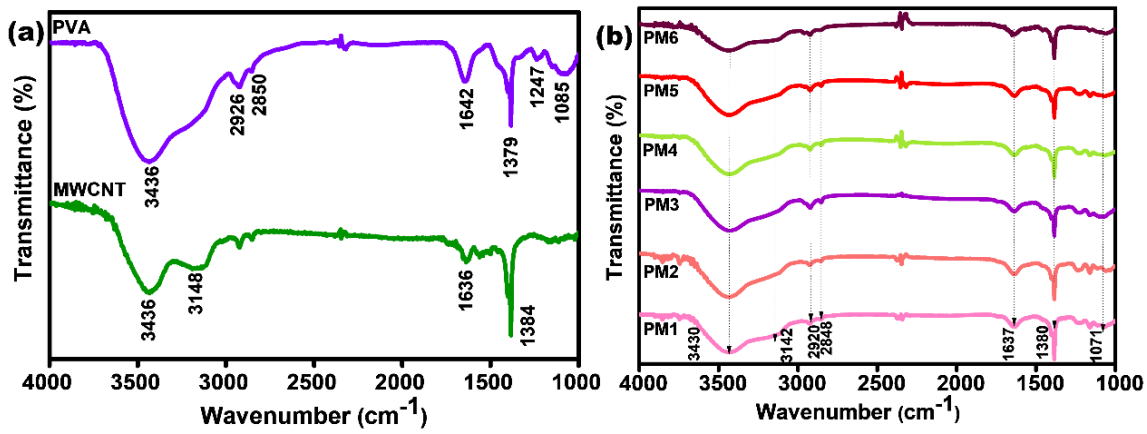

Figure 4.2 Fourier transform infrared spectra of (a) pure MWCNT and PVA, and (b) PVA-MWCNT metacomposites

Fig.4.3a shows the X-ray diffraction pattern of PVA, MWCNT, and PVA-MWCNT composite films in the 2θ range of 10° to 60°. The wide diffraction peak at 19.7° in the PM0 sample (pristine PVA) designates the (101) crystal plane of PVA, showing its semi-crystalline nature. The XRD patterns of PM1 to PM6 samples showed that the intensity and nature of the (101) peak is unaffected by the addition of MWCNT to the PVA matrix. XRD pattern of pristine MWCNT sample shows a peak at 26.01°, which corresponds to the (002) plane. This peak due to MWCNT is seen in all composite samples (PM1 to PM6).

FESEM micrographs of PVA, MWCNT and a representative composite sample (PM6 with highest concentration of MWCNT) are shown respectively in Fig.4.3b, 4.3c and 4.3d. Morphology of the pure PVA film given in Fig.4.3b, shows a homogeneous surface texture. Fig.4.3c shows pristine MWCNT with an entangled nature. MWCNTs are uniformly dispersed in the PVA matrix and a continuous conductive path is formed as shown in Fig.4.3d.

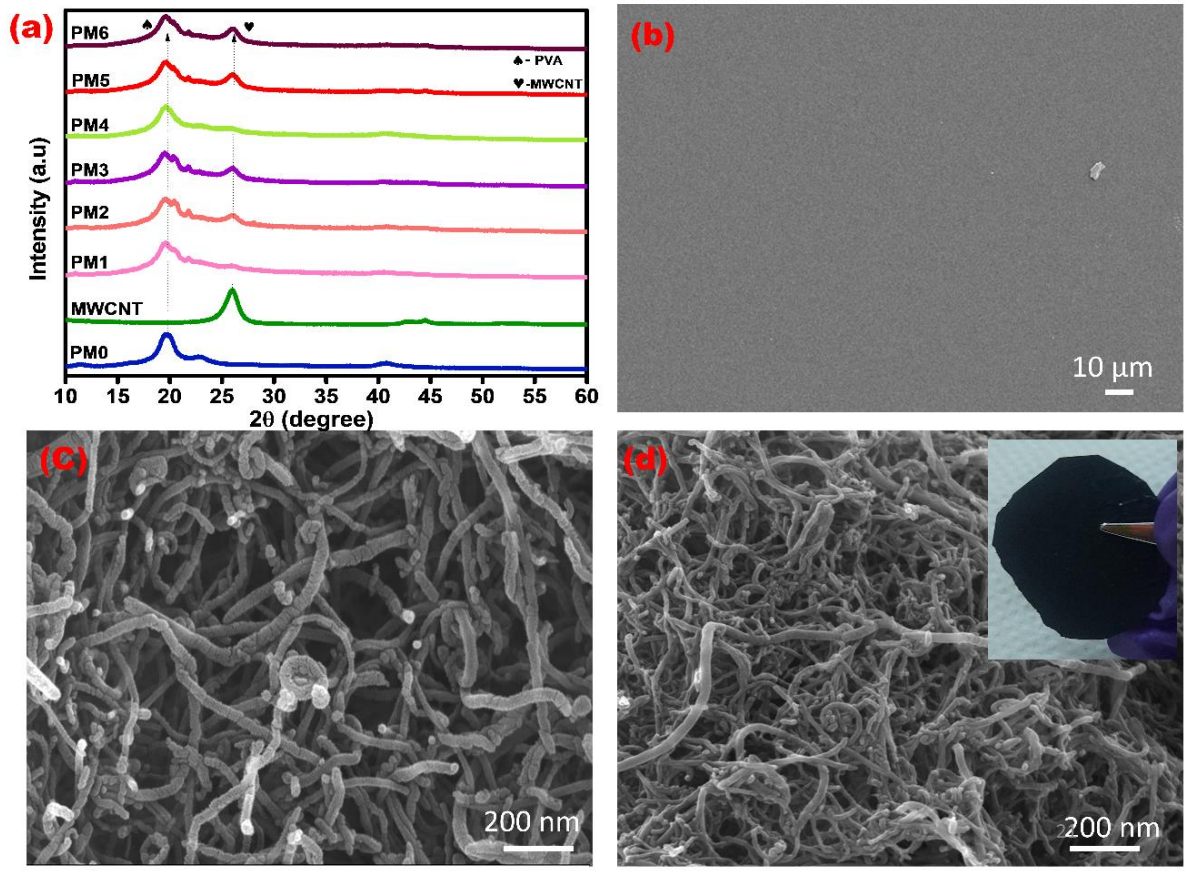

Figure 4.3 (a) XRD pattern of pure MWCNT, pristine PVA (PM0) and PVA-MWCNT (PM1 – PM6) metacomposites. FESEM micrographs of (b) pristine PVA, (c) pristine MWCNT, (d) PM6 composite (inset shows the photograph of PM6 composite film)

Thermogravimetric result of PVA and PVA-MWCNT composites are shown in Fig.4.4. The TGA thermograph for PVA-MWCNT composites with different MWCNT loadings displays the percentage of weight loss as a function of temperature. At 550 °C, pure PVA film was found to lose 92% of its weight, whilst PM1, PM2, PM3, PM4, PM5, and PM6 were found to lose 70%, 68%, 61%, 55%, 56%, and 46% of their weight, respectively. The temperature range between 250 °C and 450 °C at which most polymers decompose. The weight loss percentage dramatically drops as the MWCNT concentration rises, demonstrating the robust interaction between the MWCNT and the polymer chain. Consequently, adding MWCNT to PVA reduced weight loss compared to pure PVA, indicating increased thermal stability of PVA-MWCNT metacomposites.

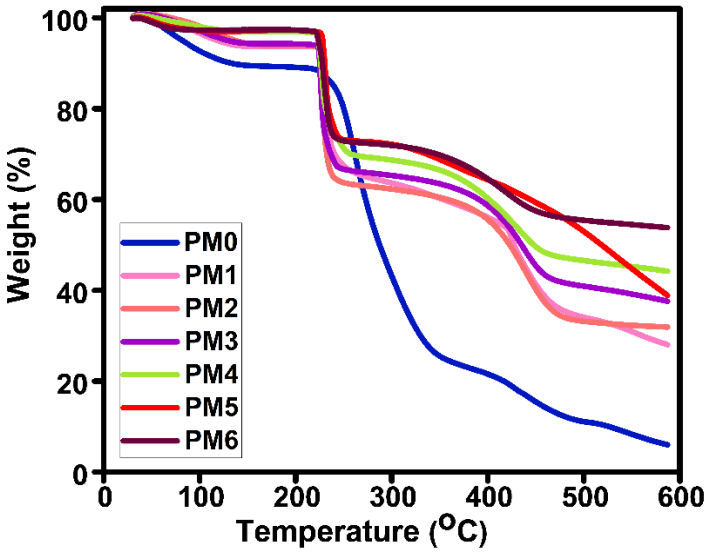

Figure 4.4. TGA curves of PVA and PVA-MWCNT metacomposites

4.2.2 Negative permittivity

Fig. 4.5a to 4.5c show the real permittivity spectra of PVA and PVA-MWCNT composite films in the lower frequency region (10^3 to 10^7 Hz). Permittivity behaviour of composites with different MWCNT loadings differs significantly. The permittivity of PVA-MWCNT film (PM1) with lower MWCNT concentration is positive and declines with frequency. Compared with pristine PVA film, the permittivity values are increased for PM1 (Fig. 4.5a). Charges building up at the interface between adjacent materials might explain the increased permittivity resulting from a change in conductivity between adjacent materials. Maxwell-Wagner-sillar effect is caused by charging accumulation and the resulting micro-capacitors, which increase the dielectric constant [45]. Permittivity falls with increase in frequency that observed in PM1 is due to the electric leakage of the conducting MWCNT assembly.

When the MWCNT content is further increased to 1 (PM2) and 1.5 wt% (PM3), it shows negative permittivity in the middle frequency region and two zero-crossing point is observed (Fig. 4.5b). The first zero crossing point is at lower frequency region and the other one is at higher frequency region. There are two main causes of negative permittivity, electric dipole

resonance (lower frequency region) and plasma oscillations (higher frequency region) of delocalised electrons. Here, both dielectric resonance and plasma oscillations contribute to negative permittivity. An electric dipole resonance is typically described by Lorentz model, while plasma oscillations of delocalized electrons are typically described by Drude model [46]. Here, a combination of Drude- Lorentz model [17,20] is used to describe the negative permittivity, and the model can be expressed as per equation (1).

$$\varepsilon_r' = 1 - \frac{\omega_p^2}{\omega^2 + \omega_\tau^2} + \frac{K\omega_L^2(\omega_L^2 - \omega^2)}{(\omega_L^2 - \omega^2)^2 + \omega^2\Gamma_L^2} \tag{4.1}$$

Γ_L is the damping constant of Lorentz resonance, ω_L is the Lorentz resonance angular frequency, $\omega = 2\pi f$ is the angular frequency, $\omega_p = 2\pi f_p$ is the plasma frequency, ω_τ is the collision frequency (the inverse of relaxation time $\omega_\tau = \frac{1}{\tau}$) and K is the dc electric susceptibility. Fig. 4.5c shows permittivity of PVA-MWCNT with 2, 2.5 and 3 wt% MWCNT. As a result of 3 wt% MWCNT concentration in PVA matrix (PM6), negative permittivity is observed in the entire test frequency region, and plasma oscillations of delocalised electrons contribute to this negative permittivity, as described by the Drude model. [4,15,47]. A Drude model can be expressed as follows:

$$\varepsilon_r' = 1 - \frac{\omega_p^2}{\omega^2 + \omega_\tau^2} \tag{4.2}$$

$$\omega_p^2 = \frac{n_{eff}\, e^2}{m_{eff}\, \varepsilon_o} \tag{4.3}$$

The metacomposite with a content of 2 (PM4) and 2.5 wt% (PM5) of MWCNT exhibits negative permittivity in the lower frequency region but it shows a huge positive permittivity before switching to negative permittivity. The experimental data shows that PM4 and PM5 exhibit higher permittivity than that predicted by Equation (2) in the high frequency region.

Here, permittivity is contributed by both isolated MWCNTs and MWCNT percolation networks. The Drude-Lorentz model provides a good description of this dielectric behaviour.

In Fig. 4.5d, we show how the imaginary part of permittivity behaves in relation to frequency. Dielectric loss is measured by an imaginary dielectric constant (ϵ"), which explains how well a material absorbs energy from alternating electric fields. Compared to the pure PVA, the ϵ" value is increased in PM1-PM6 samples, trends inversely with frequency ($\epsilon" \propto f^{-1}$). Lower frequency polarization is responsible for the large imaginary permittivity [19,48–50].

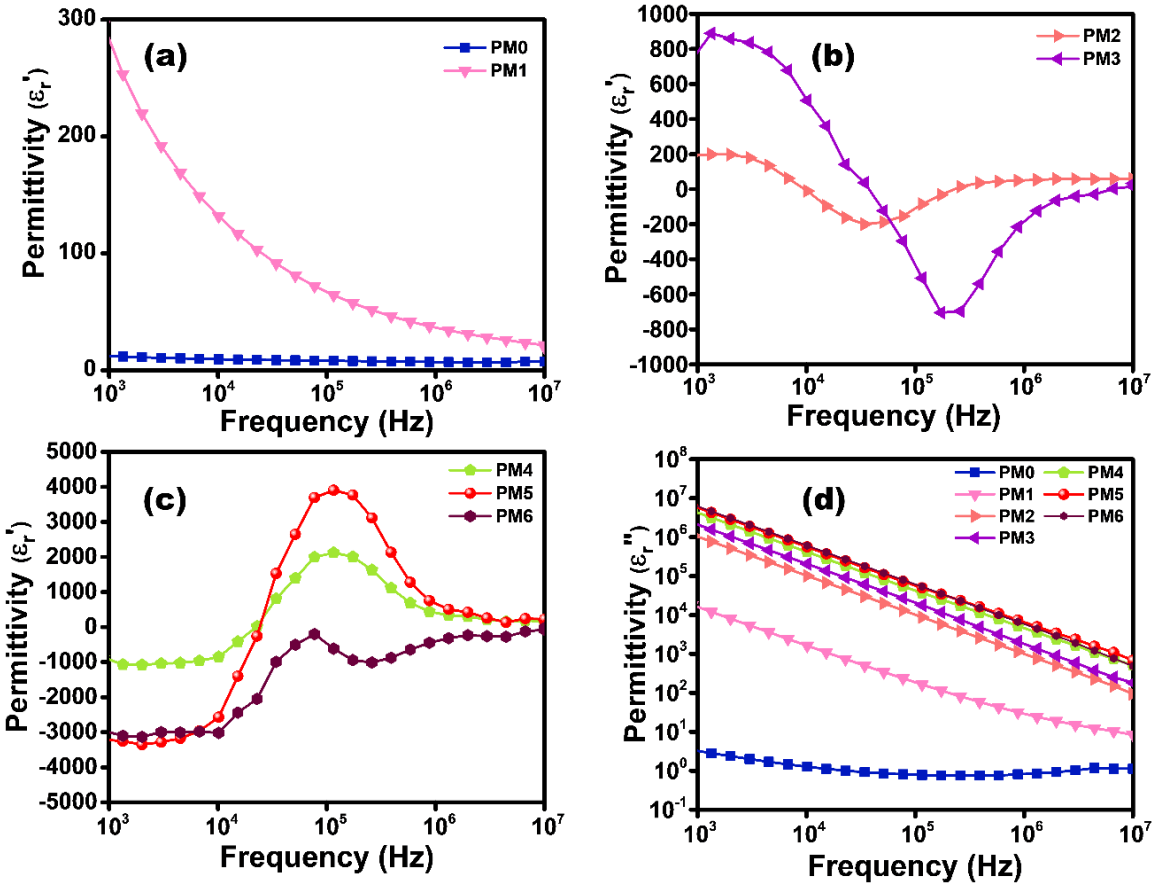

Figure 4.5 Permittivity that varies with frequency of (a, b, c) PVA and PVA-MWCNT composites (d) frequency dependent imaginary permittivity of PVA and PVA-MWCNT composites

4.2.3 Conductivity behaviour

Frequency dependent AC conductivity of PVA, and PVA- MWCNT composites are represent in Fig. 4.6a to 4. 6c. This figure illustrates various conducting mechanisms, such as hopping, metal-like conduction, and percolation theory conduction. The AC conductivity of PVA-MWCNT composite films increased with the increase in MWCNT concentration compared to pristine PVA. For lower content of MWCNT in PVA-MWCNT composites (PM1, PM2, PM3, PM4 and PM5), hoping was identified as the cause of the electron transit, and conductivity enhanced with frequency, which is in accordance with Johnscher's power law (Eqn.4.4).

$$\sigma_{ac} = \sigma_{dc} + A\,\omega^{n} \qquad (4.4)$$

where σ_{ac} is alternating current conductivity and σ_{dc} is direct current conductivity, 'A' and 'n' are pre-exponential and exponential factors, and ω represents the angular frequency [19,50,51]. Due to the skin effect, further increases in MWCNT content (PM6) resulted in a subsequent drop in conductivity, as shown in Fig. 4.6c. Skin effect elevates resistance, which has an inverse relationship with conductivity. As the MWCNT level approaches the percolation threshold, the conductivity changes from hopping to metal-like, as the Drude model explains (for PM6).

$$\sigma_{ac} = \frac{\sigma_{dc}\,\omega_{\tau}^{2}}{\omega^{2} + \omega_{\tau}^{2}} \qquad (4.5)$$

$$\sigma_{dc} = \frac{\omega_{p}^{2}\,\tau}{4\pi} \qquad (4.6)$$

where σ_{dc} is direct current conductivity, $\omega_{\tau} = \frac{1}{\tau}$ is the relaxation rate and ω_{p} is the plasma frequency [17,48,49]. In Fig. 4.6c, the fitted Drude model shows the conductivity of composites containing a high content of MWCNT in PVA. Applied alternating current will

cause the higher frequency current to concentrate near the surface of the conducting material, resulting in a reduction in skin depth and an increase in resistance. The equation governing skin depth is given by

$$\delta = \left(\frac{2}{\omega\mu\sigma_{dc}}\right)^{1/2} \qquad (4.7)$$

where, δ, ω, σ_{dc} and μ are respectively skin depth, angular frequency, dc conductivity and static permeability of the composites [19,52]. Scheme 4.2 shows how the percolation achieved in PVA – MWCNT metacomposites. Below the percolation it shows randomly dispersed MWCNT content. At percolation, continuously distributed MWCNT content shown in scheme 4.2. Above the percolation continues conductive path is formed and continued distribution of MWCNT is shown in scheme 4.2.

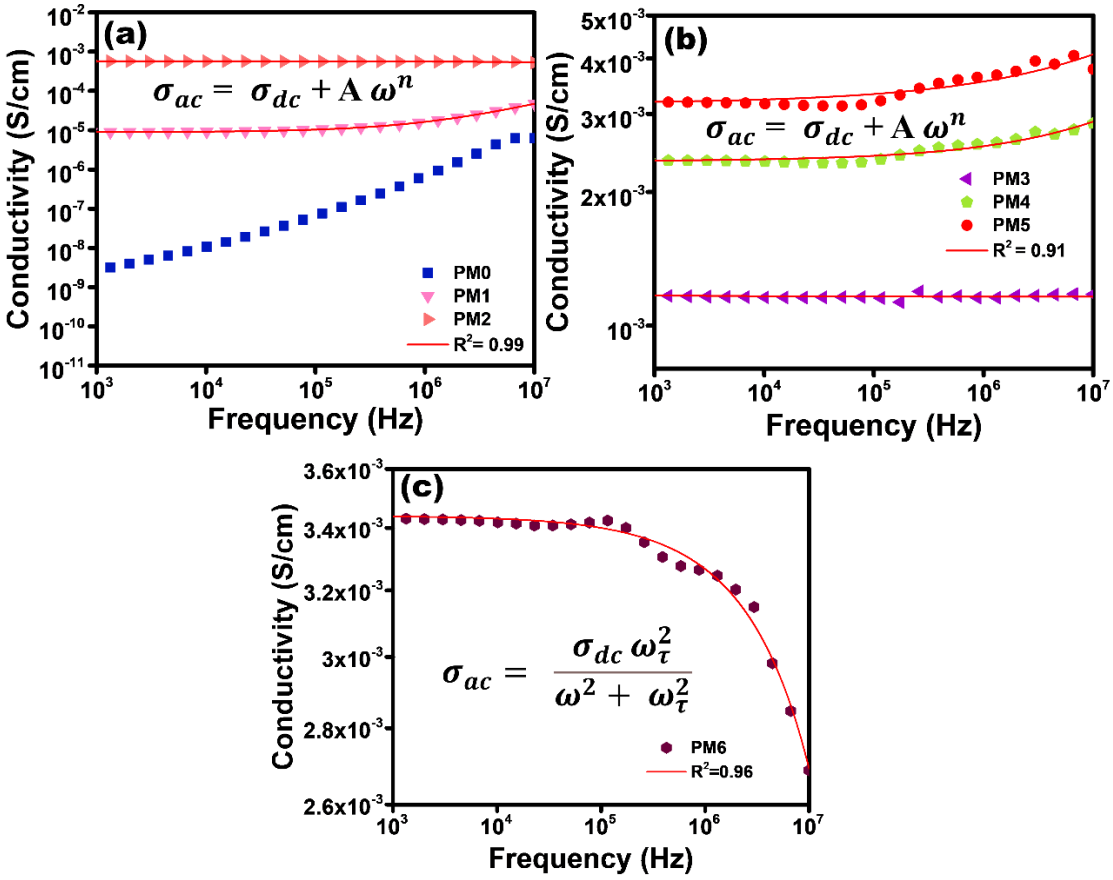

Figure 4.6a to 6c Frequency dependent AC conductivity of PVA, PVA - MWCNT composites.

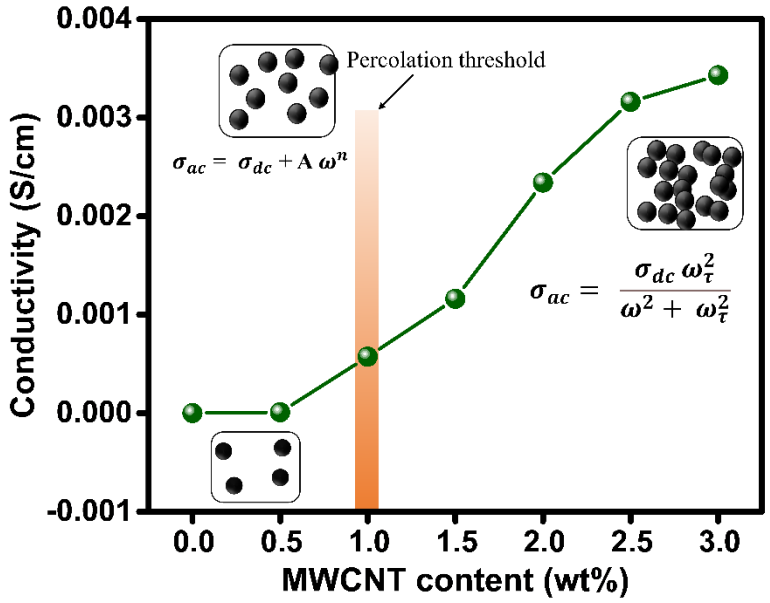

Scheme 4.2 Schematic illustration of the percolation achieved in PVA – MWCNT composites

Table 4.1 A comparison of various metacomposites negative permittivity and conductivity

Metacomposite	**Frequency Range**	**Permittivity**	**Conductivity**	**Filler content**	**Reference**
PDMS – MWCNT	10 MHz–1 GHz	-50	10^{-2} (S/cm)	5 wt%	[53]
Bi_2SiO_5 - MWCNT	1 MHz – 3 GHz	- 1300	10^{-1} (1/ Ω cm)	20 wt%	[5]
Alumina - CNT	10 MHz–1 GHz	$-10^2 \sim 10^1$	0.1 $(\Omega\ cm)^{-1}$	10 wt%	[19]
Polyimide - MWCNT	0 Hz - 1MHz	-60×10^3	0.07 (S/m)	4 wt%	[54]
PVDF – MWCNT	10 kHz- 1 MHz	-9.2	0. 025 (S/cm)	13 wt%	[6]
PVA - MWCNT	1 kHz – 1 MHz	- 9 - 3100	5.7×10^{-4} (S/cm) 0.003 (S/cm)	1 wt% 3 wt%	This work

Table 4.1 compares the negative permittivity for various MWCNT filler metacomposites reported in the literature. The negative permittivity of carbonaceous composites is generally weak in the lower frequency range (kHz to MHz), making them very useful for microwave absorbers and stretchable/wearable electronics. MWCNTs are unique in comparison to other

carbon materials owing to their extraordinary properties, such as moderate electron density and high electron mobility. Herein, we found that percolation is achieved when 1 wt% MWCNT content is added to the PVA solution, resulting in negative permittivity of -9 at 10 kHz. Therefore, in comparison to other MWCNT metacomposites, PVA-MWCNT metacomposites show Drude-Lorentz model and Drude model with weakly negative permittivity.

Fig. 4.7a – 4.7d depicts the frequency dependent phase angle and reactance of PVA-MWCNT composites. Reactance is frequently calculated by adding together inductive and capacitive reactance's. When a composite has capacitive characteristics and a positive permittivity, the reactance is usually negative to indicate that the voltage phase changes more slowly than the current phase. A composite with negative permittivity has positive reactance, whereas a composite with negative reactance has inductive characteristics. PVA-MWCNT composites with low MWCNT concentrations (PM1) display negative reactance and phase angle values, indicating capacitive behaviour. The negative permittivity region displays a positive reactance and phase angle, while the positive permittivity section displays a negative reactance (PM2, PM3, PM4, PM5, PM6) as MWCNT concentrations surpass the percolation threshold. Following equation connects the real permittivity with real and imaginary impedance.

$$\varepsilon' = -\frac{Z''}{2f\pi C_0(Z'^2+Z''^2)} \qquad (4.8)$$

Here, real and imaginary impedance is represented by Z' and Z'' and real permittivity is represented as ε'. Test frequency is represented by 'f' in the equation and the vacuum capacitance is given as C_0. According to this equation, the composite works as a switch by switching between capacitance and inductance based on the reactance value. [12,55]

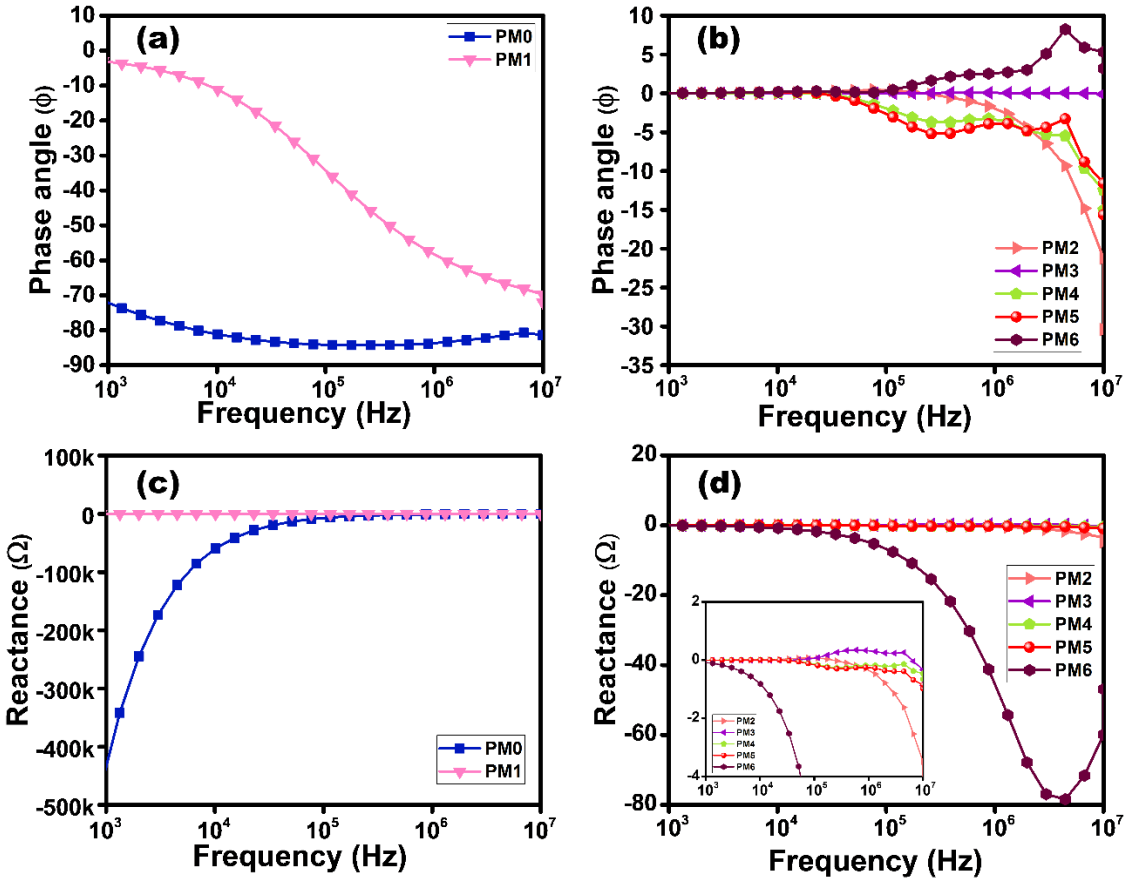

Figure 4.7 (a, b) Frequency versus phase angle spectra and (c, d) frequency versus reactance spectra, of PVA-MWCNT composites

.

4.2.4 Microwave absorption performance of PVA - MWCNT composites in the X-band region

With the rapid growth of flexible electronics, electromagnetic radiation and electromagnetic interference (EMI) have become more noticeable. Flexible electronics, as well as secure information transmission, will be threatened by these issues [56–59]. In order to mitigate electromagnetic radiation and electromagnetic interference (EMI), flexible EMI shielding materials are a significant technological solution. They can reduce electromagnetic radiation and prevent electromagnetic information leakage, and effectively protect flexible electronic devices. Flexible and conductive polymer films with good mechanical and thermal property are used for EMI shielding applications [28,60–65]. Electromagnetic interference shielding

performance of PVA - MWCNT composites was characterized by vector network analyser using a transmission line and open space method in the 8.2 -12.4 GHz frequency region

Fig. 4.8a to 4.8d shows the electromagnetic interference shielding efficiency of PVA – MWCNT composites film in the X – band region. Electromagnetic interference shielding efficiency of PVA – MWCNT is above 10 dB in the whole test frequency region for all samples (details shown in Table 4.2). Shielding efficiency above 10 dB indicate 90 % absorption. The composites' enhanced electrical conductivity is responsible for this increase in total shielding efficiency (SE_T). EMI shielding performance is generally affected by electrical conductivity. MWCNTs form conductive networks that act like bridges, providing sufficient paths for charge carriers to move freely [66,67]. Highest total shielding efficiency obtained is 22 dB in the PM6 sample with 0.7 mm thickness (Fig. 4.8c). Absorption dominant shielding mechanism is obtained for the PVA-MWCNT metacomposites (Fig. 4.8a). Here the reflection component is below 1 dB for all samples (Fig. 4.8b). The percentage shielding efficiency of PVA-MWCNT composites with different concentrations of MWCNT is shown in fig. 4.8d. Scheme 4.3 shows shielding mechanism of PVA – MWCNT composite.

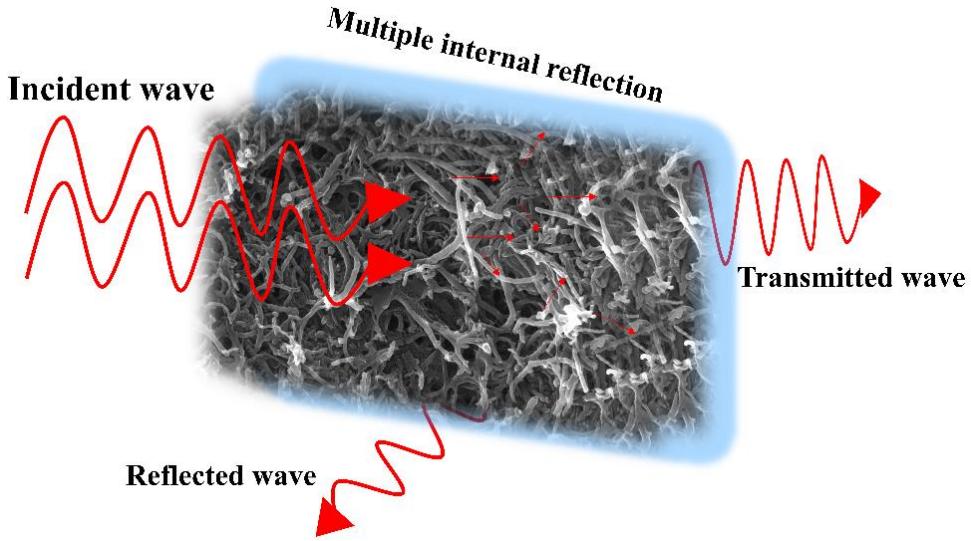

Scheme 4.3 Shielding mechanism of PVA – MWCNT composite

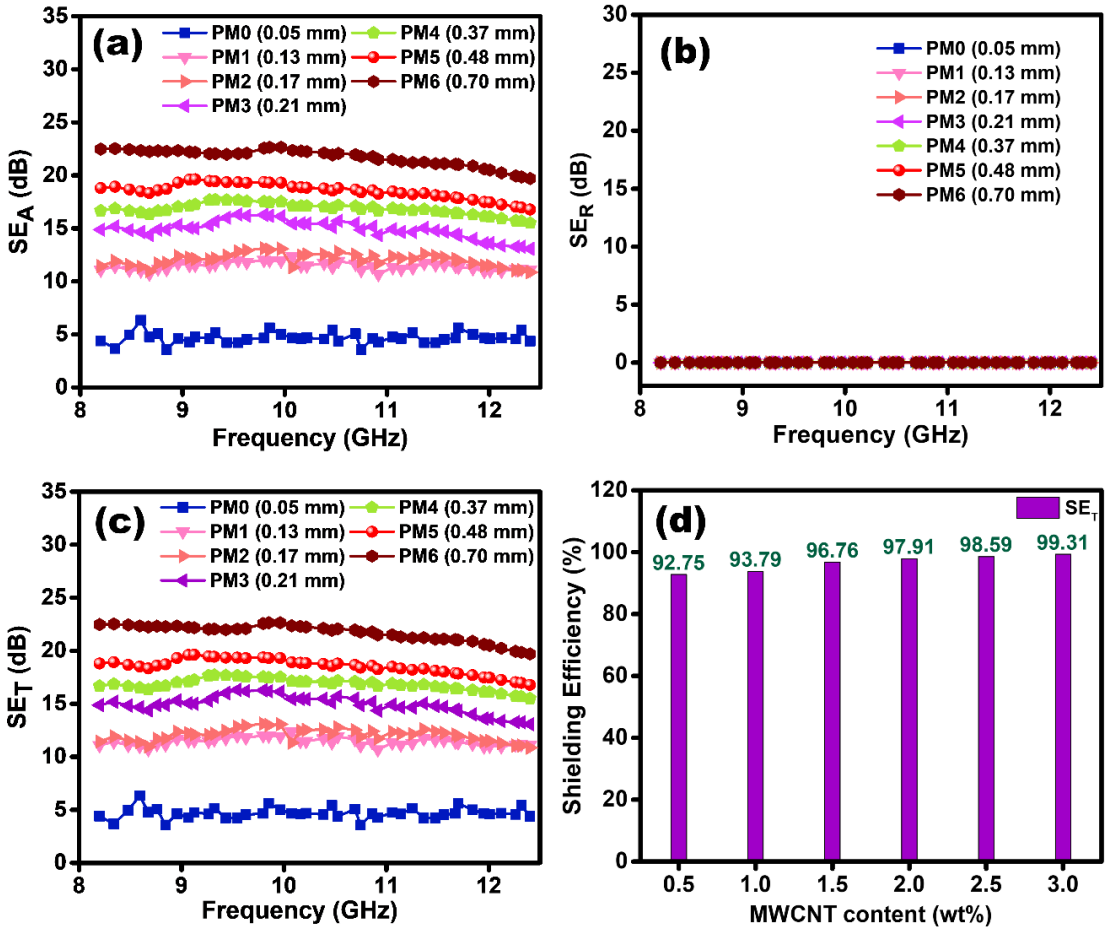

Figure 4.8 EMI shielding performance of PVA – MWCNT composites. (a) SE_A, (b) SE_R, (c) SE_T are the absorption, reflection and total shielding respectively and (d) total shielding efficiency in (%)

Sample	Average shielding efficiency (dB)
PM1	11.42
PM2	12.10
PM3	14.91
PM4	16.82
PM5	18.50
PM6	21.69

Table 4.2 Average shielding efficiency of the PVA – MWCNT composite with different concentration of MWCNT.

Thickness dependent reflection loss properties of PVA – MWCNT composite (PM6) is shown in Fig. 4.9. The equation given below connects the reflection loss (*RL*) and input impedance (Zin).

$$RL\ (dB) = 20\ \log\left|\frac{Z_{in} - Z_0}{Z_{in} + Z_0}\right| \quad (4.9)$$

$$Z_{in} = Z_0\left(\frac{\mu_r}{\epsilon_r}\right)^{\frac{1}{2}} \tanh\left[j\left(\frac{(2\pi f d)}{c}(\mu_r \epsilon_r)^{\frac{1}{2}}\right)\right] \quad (4.10)$$

Here, ε_r and μ_r are the relative permittivity and permeability of the material, c is the velocity of light in free-space, 'f' is the microwave frequency, d is the thickness of the absorber and Z_0 is the free-space impedance (377 Ω). The electromagnetic absorption characteristics is closely related to permittivity and permeability of the material. Symbolically, the real part of the complex permittivity and complex permeability represents the electric and magnetic energy storage capacities. Electromagnetic dissipation is associated with the imaginary parts of electric and magnetic energies. The lower the relative permittivity and permeability, the lower the reflection and the greater the absorption of EM waves. Furthermore, the EM wave absorption properties are also affected by dissipation capability and impedance matching. Conductivity loss and polarization loss are the main causes of dielectric loss. There are four types of polarization loss: ionic polarization, electronic polarization, dipole orientation polarization, and interfacial polarization. Electronic and Ionic polarization mechanisms are active at the low frequencies [24,26,30,31,68–70].

A vector network analyser in transmission line mode is used to determine the microwave absorption properties of PVA composites with 3 wt% of MWCNT (PM6) with three thicknesses (1 mm, 1.5 mm, and 1.9 mm). PM6 sample with 1 mm thickness shows two absorption peaks with an absorption of -50 dB at 10.01 GHz and -38 dB at 9.2 GHz. The sample with 1.5 mm thickness shows microwave absorption of -39 dB at 9.39 GHz and sample of 1.9 mm thickness shows the absorption of -37 dB at 8.89 GHz.

As a result of the large solid–air interface present in PVA – MWCNT nanocomposites, the composite exhibits excellent microwave absorption. Tuning the complex permittivity improves impedance matching, allowing more EM waves to enter the absorbers. The EM wave is reflected and scattered multiple times inside the composite interfaces, which prolongs its propagation path, causing it to become further attenuated, and its absorption ratio increases [71,72].

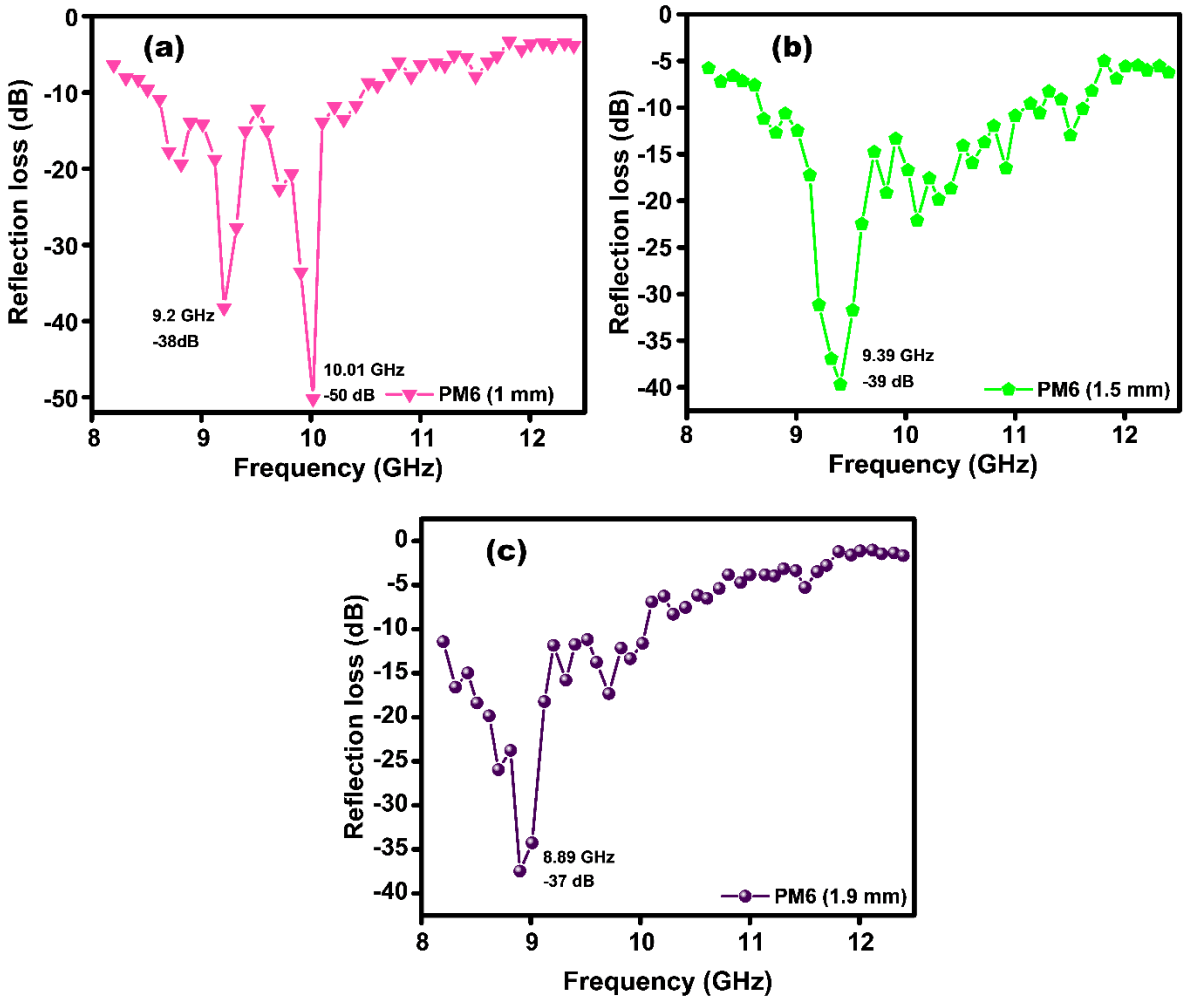

Figure 4.9 Reflection loss of PVA – MWCNT composite (PM6) with different thickness

4.3 Conclusion

Using a simple, cost-effective die casting technique, PVA-MWCNT percolative metacomposites were fabricated. Composites containing low loadings of MWCNTs in the PVA

matrix exhibited positive permittivity and capacitive properties because of hopping conduction. As the MWCNT content in PVA increased, a combination of dielectric resonance and plasma oscillation led to negative permittivity and a transition from capacitive to inductive behaviour. Further increase in MWCNT content in PVA led to negative permittivity and metal-like conduction due to the attainment of percolation threshold. Additionally, PVA-MWCNT films loaded with 3 wt% MWCNT fabricated by varying their thickness exhibited excellent microwave absorption properties (up to -50 dB at 10 GHz and -38 dB at 9.2 GHz) and shielding efficiency above 20 dB in the X-band region, suggesting their potential for applications in flexible electronics and wearable devices.

****

Reference

[1] J. Valentine, S. Zhang, T. Zentgraf, E. Ulin-Avila, D. A. Genov, G. Bartal, and X. Zhang, Nature **455**, 376 (2008).
[2] M. Chen, Z. Xiao, X. Lu, F. Lv, and Y. Zhou, Carbon **159**, 273 (2020).
[3] X. G. Zhang, W. X. Jiang, H. L. Jiang, Q. Wang, H. W. Tian, L. Bai, Z. J. Luo, S. Sun, Y. Luo, C.-W. Qiu, and T. J. Cui, Nat. Electron. **3**, 165 (2020).
[4] J. Song, G. Shi, X. Song, Z. Zhang, Y. Liu, and R. Fan, Mater. Lett. **318**, 132051 (2022).
[5] T. Haldar, U. Kumar, B. C. Yadav, and V. V. R. K. Kumar, Ceram. Int. **47**, 1389 (2021).
[6] K. Sun, W. Duan, Y. Lei, Z. Wang, J. Tian, P. Yang, Q. He, M. Chen, H. Wu, Z. Zhang, and R. Fan, Compos. Part Appl. Sci. Manuf. **156**, 106854 (2022).
[7] S. P., A. R., B. M., M. S. T.H., K. Sridharan, and S. Swaminathan, Mater. Today Commun. **34**, 105287 (2023).
[8] Z. Guo, A. Li, Z. Sun, Z. Yan, H. Liu, and L. Qian, Appl. Surf. Sci. **613**, 156074 (2023).
[9] L. Li, J. Wang, J. Wang, H. Du, H. Huang, J. Zhang, S. Qu, and Z. Xu, Appl. Phys. Lett. **106**, (2015).
[10] A. Guell Izard and L. Valdevit, Adv. Eng. Mater. **22**, (2020).
[11] K. Sun, R. Fan, X. Zhang, Z. Zhang, Z. Shi, N. Wang, P. Xie, Z. Wang, G. Fan, H. Liu, C. Liu, T. Li, C. Yan, and Z. Guo, J. Mater. Chem. C **6**, 2925 (2018).
[12] C. Cheng, R. Fan, G. Fan, H. Liu, J. Zhang, J. Shen, Q. Ma, R. Wei, and Z. Guo, J. Mater. Chem. C **7**, 3160 (2019).
[13] H. Massango, T. Tsutaoka, T. Kasagi, S. Yamamoto, and K. Hatakeyama, J. Magn. Magn. Mater. **442**, 403 (2017).
[14] Z. Shi, R. Fan, Z. Zhang, L. Qian, M. Gao, M. Zhang, L. Zheng, X. Zhang, and L. Yin, Adv. Mater. **24**, 2349 (2012).
[15] Z. Wang, P. Xie, G. Fan, Z. Zhang, Y. Liu, Q. Gu, and R. Fan, Ceram. Int. **46**, 9342 (2020).
[16] Y. Qu, Y. Du, G. Fan, J. Xin, Y. Liu, P. Xie, S. You, Z. Zhang, K. Sun, and R. Fan, J. Alloys Compd. **771**, 699 (2019).
[17] R. Ma, C. Cheng, Y. Qu, and R. Fan, Ceram. Int. **47**, 9971 (2021).
[18] K. Sun, P. Xie, Z. Wang, T. Su, Q. Shao, J. Ryu, X. Zhang, J. Guo, A. Shankar, J. Li, R. Fan, D. Cao, and Z. Guo, Polymer **125**, 50 (2017).
[19] C. Cheng, R. Fan, Y. Ren, T. Ding, L. Qian, J. Guo, X. Li, L. An, Y. Lei, Y. Yin, and Z. Guo, Nanoscale **9**, 5779 (2017).
[20] Y. Qu, J. Lin, J. Wu, Z. Wang, K. Sun, M. Chen, B. Dong, Z. Guo, and R. Fan, J. Phys. Chem. C **124**, 23361 (2020).
[21] F. Jia, Z. Lu, S. Li, J. Zhang, Y. Liu, H. Wang, X. Xu, A. Du, D. Guo, and N. Yan, Carbon **217**, (2024).
[22] M. A. Kazakova, G. V. Golubtsov, A. G. Selyutin, A. V. Ishchenko, A. N. Serkova, G. V. Gorokhov, P. Y. Misiyuk, and N. I. Valynets, Mater. Chem. Phys. **307**, (2023).
[23] X. Wang, F. Zou, Y. Zhao, G. Li, and X. Liao, Compos. Part Appl. Sci. Manuf. **176**, (2024).
[24] Y. Huo, K. Zhao, Z. Xu, F. Li, X. Zhao, Q. Meng, C. Tang, and Y. Tang, Ceram. Int. **47**, 25986 (2021).
[25] Y. Wang, Y. Du, P. Xu, R. Qiang, and X. Han, Polymers **9**, (2017).
[26] Y. Li, Y. Duan, and C. Wang, Materials **13**, (2020).
[27] H. Pang, Y. Duan, L. Huang, L. Song, J. Liu, T. Zhang, X. Yang, J. Liu, X. Ma, J. Di, and X. Liu, Compos. Part B Eng. **224**, (2021).
[28] X. Xu, F. Yao, O. A. A. Ali, W. Xie, S. F. Mahmoud, P. Xie, S. M. El-Bahy, M. Huang, C. Liu, R. Fan, Z. Guo, A. Du, D. Estevez, F. Qin, H. Peng, D. P. Young, and H. Gu, Adv. Compos. Hybrid Mater. **5**, 2002 (2022).
[29] J. C. Shu, X. Y. Huang, and M. S. Cao, Carbon **174**, 638 (2021).
[30] M. Zhang, S. Song, Y. Liu, Z. Hou, W. Tang, and S. Li, Materials **14**, (2021).
[31] Y. Zhou, X. Zhao, F. Liu, W. Chi, J. Yao, and G. Chen, ACS Omega **5**, 2899 (2020).

[32] J. Li, D. Zhou, P. J. Wang, C. Du, W. F. Liu, J. Z. Su, L. X. Pang, M. S. Cao, and L. B. Kong, Chem. Eng. J. **425**, (2021).
[33] M. S. Cao, W. L. Song, Z. L. Hou, B. Wen, and J. Yuan, Carbon **48**, 788 (2010).
[34] J. Chen, G. Qin, Y. Shi, K. Pan, J. Du, and J. Qiu, Org. Electron. **104**, 106470 (2022).
[35] L. Hu, D. S. Hecht, and G. Grüner, Chem. Rev. **110**, 5790 (2010).
[36] M. M. Shokrieh, A. Saeedi, and M. Chitsazzadeh, J. Nanostructure Chem. **3**, 20 (2013).
[37] A. Michelman-Ribeiro, F. Horkay, R. Nossal, and H. Boukari, Biomacromolecules **8**, 1595 (2007).
[38] Z. Yang, H. Peng, W. Wang, and T. Liu, J. Appl. Polym. Sci. **116**, 2658 (2010).
[39] B. Liu, J. Zhang, and H. Guo, Membranes **12**, 1 (2022).
[40] K. John U and S. Mathew, J. Non-Cryst. Solids **577**, 121321 (2022).
[41] Z. Yang, H. Peng, W. Wang, and T. Liu, J. Appl. Polym. Sci. **116**, 2658 (2010).
[42] K. Deshmukh, J. Ahmad, and M. B. Hägg, Ionics **20**, 957 (2014).
[43] D. Park, H. Ju, T. Oh, and J. Kim, RSC Adv. **8**, 8739 (2018).
[44] S. Lu, X. Wang, Z. Meng, Q. Deng, F. Peng, C. Yu, X. Hu, Y. Zhao, Y. Ke, and F. Qi, RSC Adv. **9**, 26691 (2019).
[45] X. Xia, Z. Zhong, and G. J. Weng, Mech. Mater. **109**, 42 (2017).
[46] S. P, D. M. Vidyadharan, K. Sridharan, M. S. T. H, B. M, and S. Swaminathan, Mater. Chem. Phys. **317**, 129156 (2024).
[47] Z. Wang, K. Sun, J. Tian, Q. He, P. Yang, W. Duan, P. Xie, Q. Hou, and R. Fan, J. Mater. Sci. Mater. Electron. **32**, 23081 (2021).
[48] X. Song, Z. Wei, G. Shi, G. Fan, Y. Liu, and R. Fan, ECS J. Solid State Sci. Technol. **10**, 113004 (2021).
[49] Z. Wang, K. Sun, Q. Jiang, K. Yin, L. Xie, S. Cao, Y. Zhang, X. Li, and R. Fan, Mater. Today Commun. **24**, 101230(1 (2020).
[50] C. Xu, Y. Qu, G. Fan, P. Xie, H. Ren, J. Chen, Y. Liu, Y. Wu, and R. Fan, J. Mater. Sci. Mater. Electron. **29**, 15994 (2018).
[51] Y. Liu, G. Fan, Y. Qu, P. Xie, Z. Wang, Z. Zhang, R. Fan, and X. Yin, J. Mater. Sci. Mater. Electron. **29**, 12144 (2018).
[52] T. Haldar, U. Kumar, B. C. Yadav, and V. V. R. K. Kumar, Ceram. Int. **47**, 1389 (2021).
[53] K. Sun, P. Xie, Z. Wang, T. Su, Q. Shao, J. Ryu, X. Zhang, J. Guo, A. Shankar, J. Li, R. Fan, D. Cao, and Z. Guo, Polymer **125**, 50 (2017).
[54] X. Song, Z. Wei, G. Shi, G. Fan, Y. Liu, and R. Fan, ECS J. Solid State Sci. Technol. **10**, 113004 (2021).
[55] C. Cheng, R. Fan, G. Fan, H. Liu, J. Zhang, J. Shen, Q. Ma, R. Wei, and Z. Guo, J. Mater. Chem. C **7**, 3160 (2019).
[56] B. K. Choi, H. J. Lee, W. K. Choi, M. K. Lee, J. H. Park, J. Y. Hwang, and M. K. Seo, Synth. Met. **273**, (2021).
[57] Y. Zhang, K. Ruan, and J. Gu, Small **17**, 1 (2021).
[58] E. G. R. dos Anjos, T. R. Brazil, G. F. de Melo Morgado, L. S. Montagna, N. F. Braga, E. Antonelli, J. Marini, M. C. Rezende, and F. R. Passador, J. Polym. Res. **30**, (2023).
[59] K. Tian, D. Hu, Q. Wei, Q. Fu, and H. Deng, J. Mater. Sci. Technol. **134**, 106 (2023).
[60] Z. Leng, Z. Yang, X. Tang, M. H. Helal, Y. Qu, P. Xie, Z. M. El-Bahy, S. Meng, M. M. Ibrahim, C. Yu, H. Algadi, C. Liu, and Y. Liu, Adv. Compos. Hybrid Mater. **6**, 195 (2023).
[61] J. Chen, Y. Shi, K. Pan, J. Du, and J. Qiu, Macromol. Rapid Commun. **43**, 1 (2022).
[62] B. Zhao and C. B. Park, J. Mater. Chem. C **5**, 6954 (2017).
[63] C. Cheng, Y. Liu, R. Ma, and R. Fan, Compos. Part Appl. Sci. Manuf. **155**, 106842 (2022).
[64] H. Luo, Y. Lu, and J. Qiu, Carbon **183**, 34 (2021).
[65] B. D. Che, B. Q. Nguyen, L. T. T. Nguyen, H. T. Nguyen, V. Q. Nguyen, T. Van Le, and N. H. Nguyen, Chem. Cent. J. **9**, 1 (2015).
[66] V. Lalan, A. Puthiyedath Narayanan, K. P. Surendran, and S. Ganesanpotti, ACS Omega **4**, 8196 (2019).
[67] J. B. Anooja, V. Lalan, and S. Ganesanpotti, Mater. Res. Bull. **142**, (2021).
[68] B. Zhao, J. Deng, C. Zhao, C. Wang, Y. G. Chen, M. Hamidinejad, R. Li, and C. B. Park, J. Mater. Chem. C **8**, 58 (2019).

[69] M. Akyol, C. Aka, O. İnözü, F. Ö. Alkurt, and M. Karaaslan, J. Mater. Sci. Mater. Electron. **34**, 1 (2023).
[70] A. Saleem, Y. Zhang, H. Gong, M. K. Majeed, X. Lin, J. Jing, M. Sheng, and C. Zhao, J. Mater. Sci. Mater. Electron. **31**, 2918 (2020).
[71] J. C. Shu, X. Y. Yang, X. R. Zhang, X. Y. Huang, M. S. Cao, L. Li, H. J. Yang, and W. Q. Cao, Carbon **162**, 157 (2020).
[72] W. L. Song, X. T. Guan, L. Z. Fan, Y. B. Zhao, W. Q. Cao, C. Y. Wang, and M. S. Cao, Carbon **100**, 109 (2016).

Flexible PVA-graphite metacomposites with variable negative permittivity for electromagnetic interference shielding applications

Metamaterials are engineered materials that exhibit exotic electromagnetic properties for frequencies spanning from microwave to visible that are not seen in natural materials and are made up of planned inclusions with negative permittivity, permeability, or index of refraction values [1–3]. These materials have the potential to allow the creation of several innovative gadgets because the physics underlying them is completely different. Much of the effort in material science, physics and optics communities are emphasized in constructing efficient metamaterials [4–6]. This may also find interesting application in the fields of microwave absorbers electromagnetic interference shielding, sensors, super lenses, microwave imaging, cloaking and miniaturization of antennas and filters. Some of these applications uses the intrinsic properties of the negative constituent 'atoms' of these materials while some others explore its bulk characteristics. Meta properties typically originates from thin wire, split ring resonator or from the combination of these two structures [7–9]. Due to its complex fabrication process and insufficient band response, significant attention is being devoted to develop alternative strategies for the fabrication of metamaterials.

Metacomposites or intrinsic metamaterials is an alternate for obtain negative electromagnetic parameters. Metacomposites also have several advantages over conventional metamaterials, such as the ability to easily vary their size, whereas the size of conventional metamaterials depends on the wavelength of the applied electromagnetic field [10,11]. The ε-negative characteristic, primarily determined by the concentration of free electrons in metacomposites, has garnered significant interest in the scientific community due to its potential applications [12]. Negative permittivity behaviour is the outcome of the harmonic motion, which aligns the polarization electric field's direction with the external electric field. To achieve

a negative permittivity, free electrons require a longer harmonic motion route, which provides a means of adjusting negative permittivity. Previous studies on carbon-based compounds indicate their capability to exhibit weakly negative permittivity due to moderate electron density. High permittivity capacitors and perfect absorption capacitors both benefit from this weakly negative permittivity feature that could be modified [13–16]. Negative permittivity was observed in rGO/CNT heterogeneous interface in the MHz region [17], while it was reported to be in the kHz region for percolated MWCNTs - PVDF metacomposites [18]. Graphite-PDMS metacomposite with 30 wt% of graphite exhibited negative permittivity with a value of -29 at a frequency of 3.35×10^7 Hz [19] . In another study, metacomposite formed by coupling polyolefin elastomer and graphene was reported to exhibit epsilon near zero behaviour at 126 MHz [20]. In addition to negative permittivity, polymer matrices with high positive permittivity are widely recognised for applications in energy storage and electronic devices. For example, high positive permittivity with low loss was observed when PVDF-Graphite layer exhibiting negative permittivity was coupled with another PVDF-Graphite layer exhibiting positive permittivity to form a sandwiched structure. Similarly, high positive permittivity with low loss was also reported in a study conducted on tri-layer sandwiched structure formed by incorporating $BaTiO_3$/PVDF – Graphite/PVDF - $BaTiO_3$/PVDF composites [21]. Evidently, metacomposites formed by the incorporation of various carbon fillers (MWCNT, graphene, graphite etc.) in different polymer matrix (PVDF, PDMS, POE, PVA etc.) have been investigated for their interesting weak negative permittivity and high positive permittivity. Surprisingly, there are no reports till date on the study of a metacomposite formed with graphite as filler in PVA matrix.

Electromagnetic pollution has become a significant issue for humanity due to the increased use of electronic and electrical devices. The effectiveness of EMI shielding is largely determined by a material's permeability and permittivity. Metamaterials and metacomposites, which are

artificially structured, are ideal for perfect absorption or EMI shielding because of their unique properties, such as negative refractive index, negative permittivity, and negative permeability. In a double-negative medium, where both permittivity and permeability are negative, the direction of wave propagation reverses when electromagnetic waves enter, resulting in minimal EM wave reflection and nearly complete absorption – properties not found in natural materials". Jiali chen et.al reported negative permittivity and electromagnetic interference (EMI) shielding in carbon nanofiber/ conductive polymer composites in the radar wave frequency region [22]. PVDF-Ni chain composites shows negative permittivity and electromagnetic interference shielding property [23]. Silver – silica random metamaterial also shows double negative property and high EMI shielding efficiency [24]. Bucky paper ,yttrium iron garnet and graphene aerogel sandwich structure metacomposites also shows negative permittivity and EMI shielding efficiency [25].

In this study, composites consisting of polyvinyl alcohol (PVA) and graphite flakes (G) were produced using the die-casting method. PVA, a synthetic polymer, is capable of forming effective films, is non-toxic, and environmental friendly [26]. Graphite flakes (G) are commonly utilized as additive fillers and refractory materials in composites due to their lightweight, high thermal conductivity, and cost-effectiveness [27]. Additionally, graphite flakes exhibit exceptionally high thermal and electrical conductivities parallel to the graphite layers. Interestingly, both negative permittivity and epsilon-near-zero behaviour were successfully tuned in the lower radio frequency range. The electrical properties of PVA-G metacomposites were analysed through impedance measurements. Furthermore, the electromagnetic interference shielding performance of the metacomposites was evaluated in the X-band region.

5.1. Experimental

5.1.1 Materials

Sigma Aldrich provided the polyvinyl alcohol powder with molecular weight 89,000–98,000 and it also 99+ % hydrolysed. We bought graphite flakes from Sigma Aldrich, USA. All chemicals were used as received.

5.1.2 Fabrication of Polyvinyl Alcohol – Graphite Flakes (PVA-G) composites

PVA – G metacomposites were fabricated as per the procedure depicted in Scheme 5.1. Graphite flakes at different concentrations (0.5, 1, 1.5, 2, and 2.5 weight percent) were probe-sonicated in deionized water for 20 minutes. Then, 5 weight percent PVA powder was added to the mixture and agitated at 80 °C and thousand rpm until the powder was fully dissolved. After allowing the uniform grey slurry to settle for some time to get rid of the bubbles, it was carefully transferred to a Petri plate. The mouldable PVA-Graphite flakes films were effectively created after the moisture was removed by drying at room temperature for 4 h.

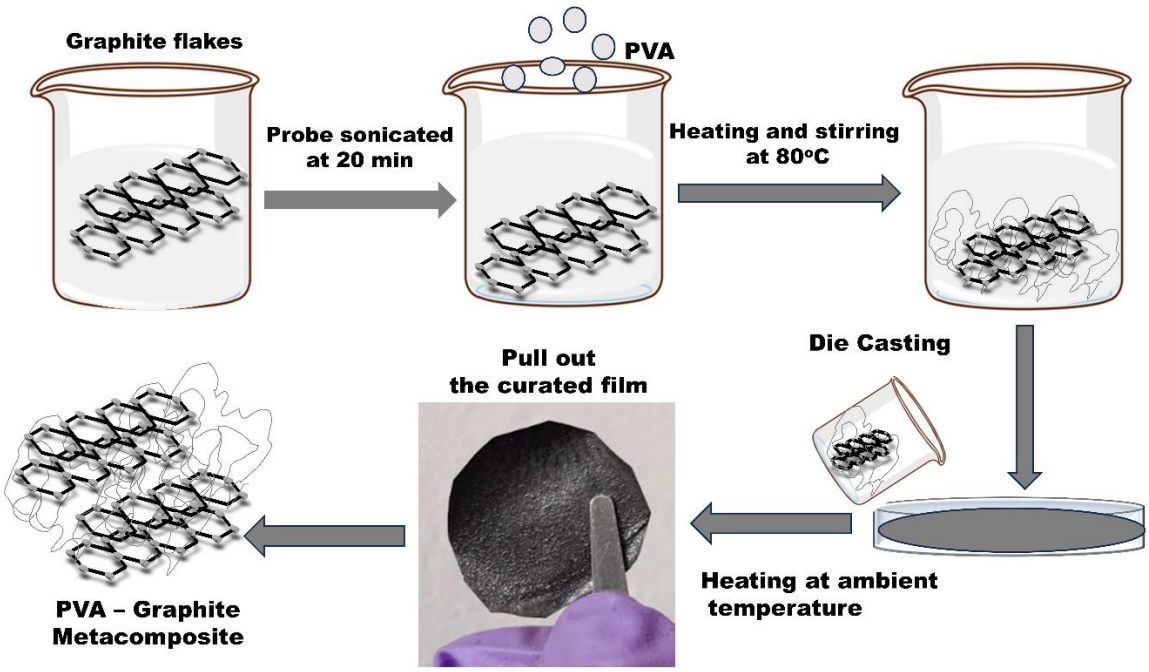

Scheme 5.1 Schematic illustration of the step-by-step process of fabricating flexible PVA-G metacomposites

PVA- G films were designated as PG0 (Pristine Polyvinyl alcohol with 5 wt%), PG1 (Polyvinyl alcohol with 0.5 wt% Graphite), PG2 (Polyvinyl alcohol with 1wt% graphite), PG3 (Polyvinyl alcohol with 1.5 wt% graphite), PG4 (Polyvinyl alcohol with 2 wt% graphite), PG5 (Polyvinyl alcohol with 2.5wt% graphite). Further increase of graphite flakes content to 3 wt% (PG6) and film are also fabricated. The flexible PVA-G composites films are obtained and the photograph of all synthesized samples are given in Scheme 5.2.

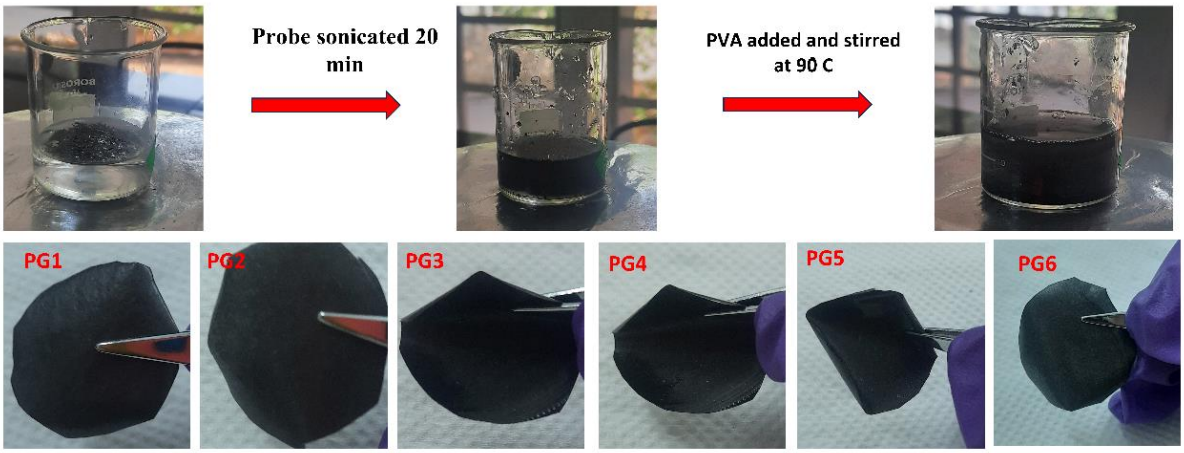

Scheme 5.2 Photographs of PVA – G fabrication procedure and composite films

5.1.3 Characterization

An X-ray diffractometer (X'pert3 Powder, PANalytical), was used for studying the phase composition and structural characteristics of the fabricated metacomposites in the 2θ range 10° to 60°. Thermogravimetric analysis (TGA, STA 8000) was performed in a nitrogen environment at temperatures between 30 °C and 600 °C. A Perkin Elmer Spectrum 2 FTIR spectrometer is used to record the infrared spectra of the metacomposites between 1000 to 4000 cm^{-1}. Morphology of the metacomposites were studied with a field-emission scanning electron microscope (FESEM, Gemini SEM300). A broadband dielectric spectrometer was used to measure the dielectric properties (BDS, Novacontrol GmbH, Germany). The values of complex scattering parameters were measured using a vector network analyzer (VNA, N5224B-

Keysight) in a frequency range of 8.2–12.4 GHz as part of a waveguide approach to estimate the EMI shielding capabilities of the metacomposites.

5.2. Result and Discussion

5.2.1 Characterisation of morphology, composition and thermal study

Fig.5.1 shows the XRD patterns of graphite flakes, PVA and PVA-G composite films measured over the 2θ range of 10° to 60°. The broad peak at 2θ = 19.7° in PG0 corresponds to the (101) crystal plane of PVA, indicating its semi-crystalline nature. For pristine graphite flakes, two distinct peaks were observed at 2θ = 26.5° and 54.6°, associated with the (002) and (004) planes, respectively. In the PVA-G composites (PG1 to PG5), the XRD pattern reveals a prominent peak for graphite and a significantly weaker peak for PVA. Additionally, it is evident that the intensity of the 19.7° peak in PVA - G samples decrease as the content of graphite flakes in the PVA matrix increases.

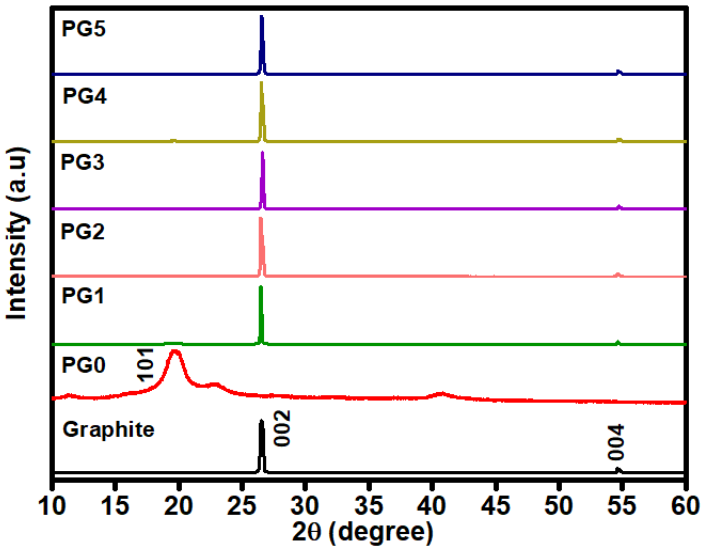

Figure 5.1 X-ray diffraction patterns of pristine Graphite flakes (G), pristine PVA (PG0) and PVA-G (PG1 – PG5) metacomposites

FESEM micrographs of PVA, graphite flakes and PVA – G composites are presented in Fig.5.2. Fig.5.2a displays the micrographs of pure PVA, while Fig.5.2b illustrates the layered structure

of pristine graphite flakes. At low graphite flake content, as shown in Fig.5.2c, many isolated graphite flakes are observed, and it is anticipated that the conduction would occur via hopping between adjacent graphite flake layers. When the content reaches 2.5 wt%, interconnections are observed between the graphite flakes forming a continuous path as shown in Fig.5.2d. As a result, percolation is achieved, leading to a significant increase in conductivity. The subsequent discussion explores the relationship between composition, microstructure, and permittivity or conductivity.

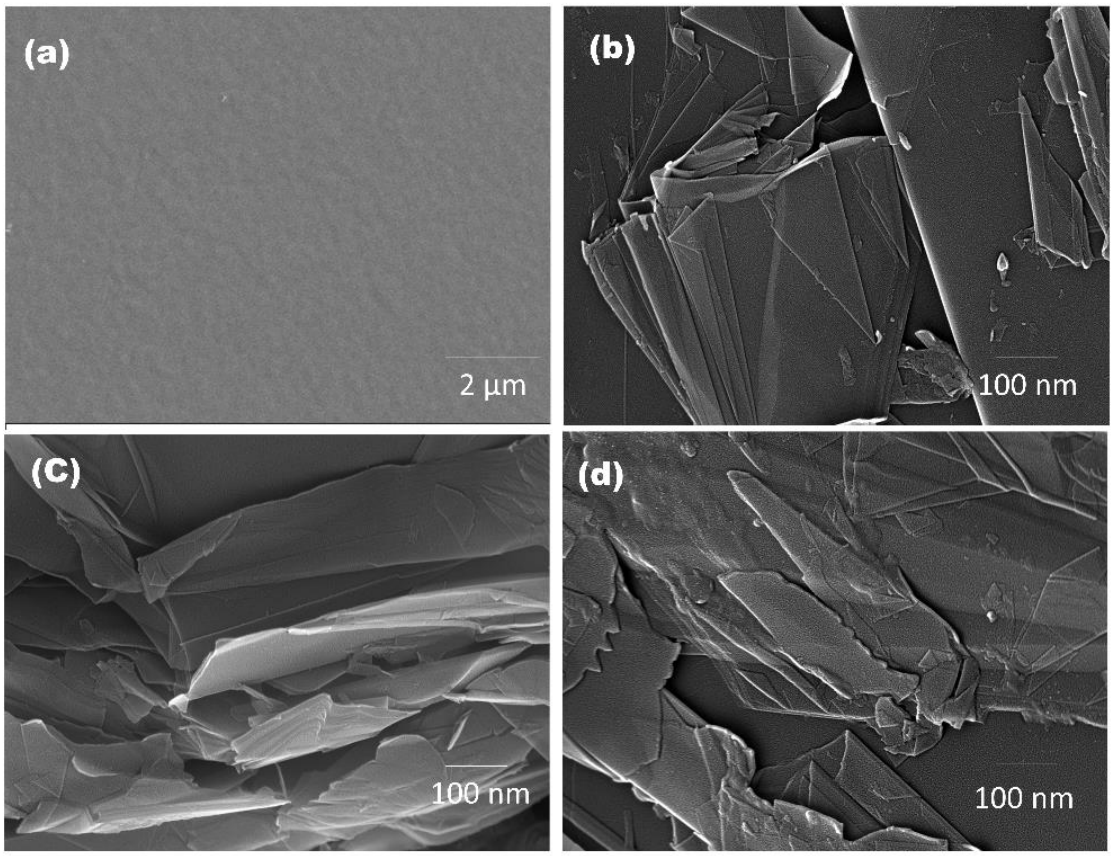

Figure 5.2 FESEM micrographs of (a) pristine PVA, (b) pristine Graphite flakes, (c) PG3 and (d) PG5 samples

Fig.5.3 presents the FTIR spectra of graphite, pure PVA, and PVA-graphite composites. In Fig.5.3a, a broad peak between 3500 and 3125 cm^{-1} is observed, indicative of the O-H stretching from either water absorption or the presence of hydroxyl groups in the PVA structure. Peaks at 2926 cm-1 and 2850 cm^{-1} correspond to the asymmetric and symmetric stretching

vibrations of C-H bonds, respectively. The peak at 1740 cm^{-1} signifies the C=O stretching vibration of the acetate group in the PVA molecule. An absorption band at 1642 cm^{-1} represents the carbonyl group in PVA, indicating C=O stretching vibration. The characteristic peak at 1085 cm^{-1} confirms C–O stretching of the acetyl group [28,29]. The graphite flakes spectrum in Fig.5.3b shows a distinct peak at 3436 cm^{-1}, attributed to the O-H stretching vibrational mode of intercalated water. Another peak at 1645 cm^{-1} is associated with C=C stretching bonds [30]. Peaks at 2922 $cm^{-1}$and 2852 cm^{-1} indicate O-H stretching vibrations, while those at 1382 cm^{-1} and 1756 cm^{-1} correspond to C-O stretching and C=O stretching vibrations, respectively. Fig.5.3c displays the FTIR spectra of PVA-graphite flake composites, where distinct peaks corresponding to both PVA and Graphite flakes are present. The FTIR spectra of PVA-graphite flake metacomposites show various band shifts due to restrictions imposed by the surrounding polymer network, indicating the intercalation within the composites.

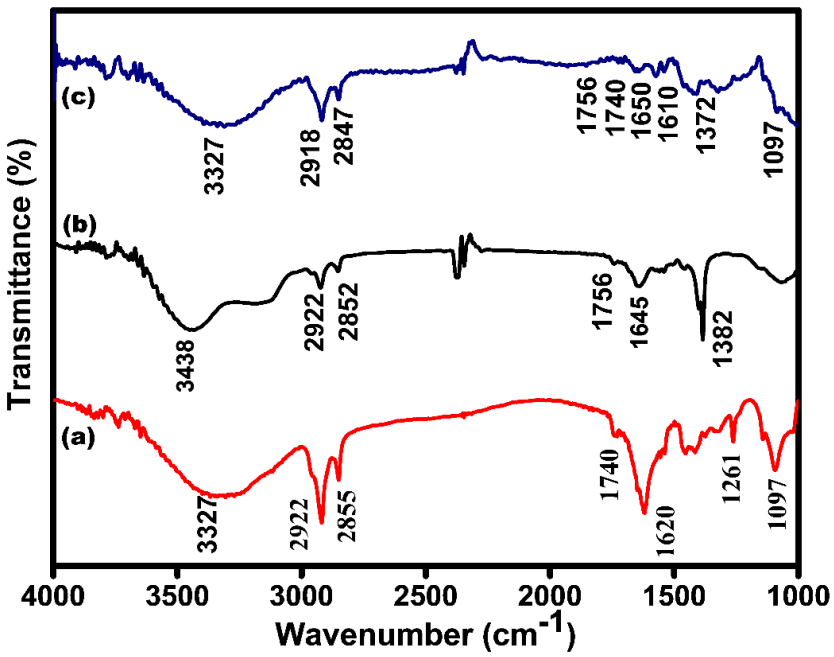

Figure 5.3 FTIR spectra of pristine (a) PVA and (b) Graphite flakes, and (c) PVA-G metacomposites

Fig.5.4 shows thermogravimetric data for samples PG0 to PG5. The TGA thermographs for PVA-G composites with varying graphite flakes loadings illustrate the percentage of weight loss as a function of temperature. At 500 °C, the pure PVA film lost 89% of its weight. In contrast, at 500°C, the PG1, PG2, PG3, PG4, and PG5 samples exhibited 88%, 83%, 75%, and 77%, respectively. The decrease in weight loss percentage with increasing graphite flake content suggests a strong interaction between the polymer chains and the graphite flakes. Furthermore, Consequently, the reduced weight loss of the PVA-G metacomposites in comparison to pure PVA indicates enhanced thermal stability.

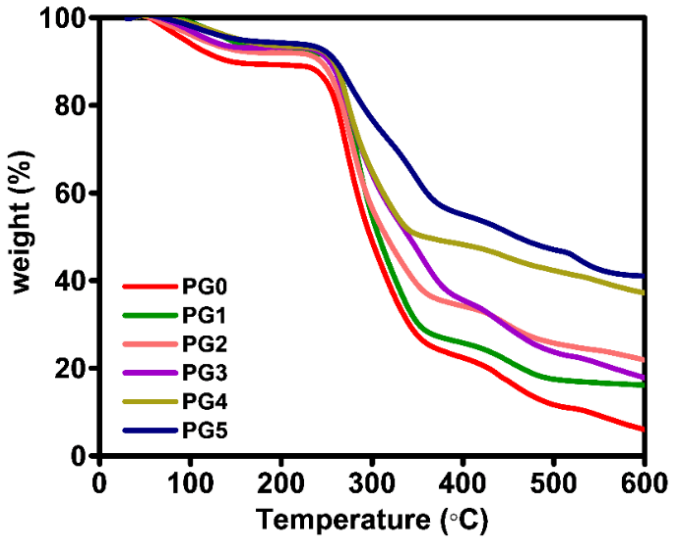

Figure 5.4 TGA curves of PVA and PVA-G metacomposites

5.2.2 Conductivity Behaviour

Fig.5.5 shows the frequency-dependent AC conductivity of pure PVA and PVA-G metacomposites with varying concentrations of graphite flakes. Compared to pure PVA, PVA-G composites with a lower graphite flake content exhibit higher electrical conductivity and show frequency-dependent behaviour. This can be attributed to two primary conductive mechanisms according to percolation theory: hopping conduction and metal-like conduction. Below the percolation threshold, the conductivity of the metacomposites consistently increases with frequency, a phenomenon described by Johnscher's power law,

$$\sigma_{ac} = \sigma_{dc} + A\,\omega^{n} \quad (5.1)$$

For alternating and direct current, conductivity is denoted by σ_{ac} and σ_{dc}, respectively, where ω represents angular frequency, and A and n are the pre-exponential and exponential components, respectively [10,15,18,31]. In higher frequency regions, enhanced electrical conductivity is observed, likely due to electrons undergoing hopping conduction, receiving additional energy from an external electric field. Free electrons can hop between adjacent graphite flakes when exposed to an external electric field. As the concentration of the graphite flakes increases, the particles form interconnected three-dimensional conductive networks within the composite. The samples PG1 to PG4 demonstrate hopping conduction and align with Johnscher's power law (Equation 5.1). Above the percolation threshold, the conductivity increases by an order of 10^{-2} and exhibits metallic conduction characteristics. Specifically, at low frequencies, AC conductivity is almost frequency-independent, while at high frequencies, AC conductivity decreases due to the skin effect. Skin depth is expressed as

$$\delta = \left(\frac{2}{\omega\mu\sigma_{dc}}\right)^{1/2} \quad (5.2)$$

Where δ is the skin depth, ω denotes the angular frequency, σ_{dc} is the DC conductivity, and μ is the static permeability of the composites [32,33]. The metal-like conduction behaviour observed in composites with a graphite flakes content of 3 wt% can be explained using the Drude model and expressed as,

$$\sigma_{ac} = \frac{\sigma_{dc}\,\omega_{\tau}^{2}}{\omega^{2} + \omega_{\tau}^{2}} \quad (5.3)$$

$$\sigma_{dc} = \frac{\omega_{p}^{2}\,\tau}{4\pi} \quad (5.4)$$

Here, σ_{dc} is direct current conductivity, $\omega_{\tau} = \frac{1}{\tau}$ is the relaxation rate, and ω_{p} is the plasma frequency [34]. The PG5 sample exhibits metal-like conduction and fits the Drude model. Additionally, in the higher frequency range, the conductivity of the composites steadily

decreases with increasing frequency. This occurs because the resistance increases due to enhanced skin effects and reduced skin depth, mainly at high frequencies. The percolation threshold is determined by the geometric properties of the fillers within the matrix, including the size, shape, and orientation of the particles.

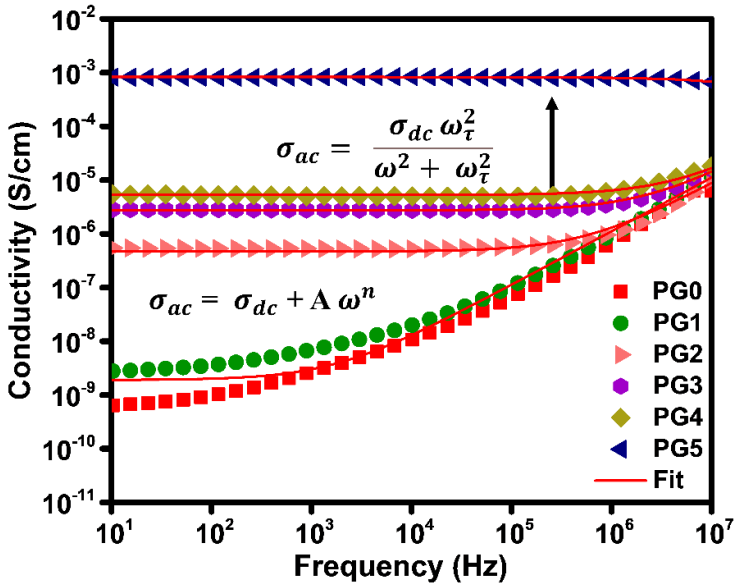

Figure 5.5 Plot depicting the frequency dependent AC conductivity in pristine PVA and PVA-G metacomposites

5.2.3 Epsilon negative property

Fig.5.6 displays the frequency-dependent real and imaginary permittivity of pure PVA and PVA-G composites with varying amounts of graphite particles. Fig. 5.6a,5.6b and 5,6c shows frequency dependent real permittivity of Pure PVA and PVA – G metacomposites. Pure PVA film shows positive permittivity with a value around 27 at 10 Hz, which decreases as the frequency increases. Interestingly, when a lower concentration of graphite flakes is added to the PVA matrix, the composites also display positive permittivity due to interfacial polarisation at the heterogeneous interfaces. Graphite flakes act as micro-capacitors in the interfacial polarisation process, facilitating the creation of percolation pathways, with permittivity reaching 93 at 10 Hz. The Maxwell-Wagner-sillar effect accounts for the enhanced permittivity of the composites compared to the PVA matrix [35–37].

Once the concentration of graphite flakes exceeds the percolation threshold, a 3D network is formed within the microstructure, containing numerous free electrons. Interestingly, the abnormal phenomenon occurs where permittivity shift from positive to negative. Negative permittivity arises when positive and negative charges are separated by an external electric field, forming a collective oscillation known as plasma oscillation. Most research on metacomposites has focused on samples above the percolation threshold where negative permittivity is achieved. In this study, however, negative permittivity is attained below the percolation threshold. Depending on the graphite flake loading, the frequency range over which negative permittivity occurs and the switching frequency at which permittivity transitions from positive to negative vary.

For 1 wt% graphite flakes (PG2) added to the PVA sample, negative permittivity appears at 34 Hz with a value of -0.71. Increasing the graphite flakes content to 1.5 wt% (PG3) and 2wt% (PG4) results in higher negative permittivity and shifted transition frequency. For PG3 and PG4 samples, positive-to-negative transition occurs at 78 Hz and 396 Hz, with negative permittivity values of -0.72 and -3.6, respectively. For 2.5 wt% added to the PVA matrix (PG5), negative permittivity is across the entire test frequency region. This shift to negative permittivity is due to plasma oscillation of delocalised electrons, described by Drude model. The Drude model equation is given as:

$$\varepsilon_r' = 1 - \frac{\omega_p^2}{\omega^2 + \omega_\tau^2} \tag{5.5}$$

$$\omega_p^2 = \frac{n_{eff} e^2}{m_{eff} \varepsilon_o} \tag{5.6}$$

where m_{eff} is effective electron mass, ω_τ is collision frequency. ω_p, ω, n and n_{eff} represent the plasma frequency, test angular frequency effective electron density and effective electrons concentration, respectively [38–41].

In Fig.5.6d, the frequency-dependent imaginary permittivity of samples PG0-PG5 is presented. The imaginary permittivity PVA-G composites shows an increase compared to pure PVA, with a tendency towards inverse fluctuation relative to frequency as $\epsilon \propto f^{-1}$, highlighting the importance of significance of conductive loss in relation to total dielectric loss [42]. Lower imaginary permittivity are attributed to polarisation loss. At very low graphite flakes content, these flakes might can be conceptualized as micro-capacitors embedded within the insulting PVA matrix. The increase in graphite flake content leads to the formation of conductive networks and the appearance of leakage current, resulting in higher conductive loss in the composite. It is noteworthy that composites with higher losses find wide application in microwave absorption and shielding applications.

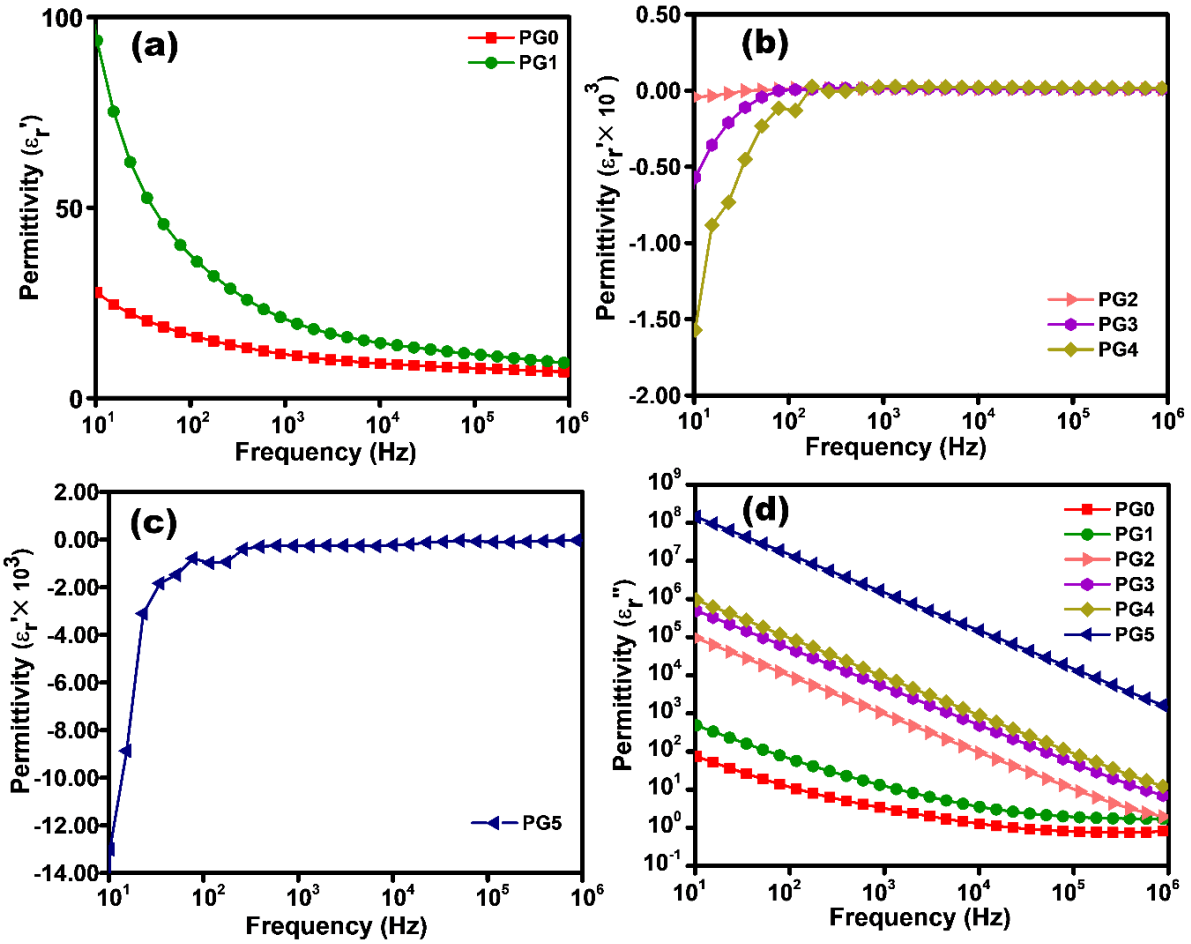

Figure 5.6 Frequency dependent permittivity of (a, b, c) PVA and PVA-G composites with different carbon black content (d) frequency dependent imaginary permittivity of PVA-G composites

The PG6 sample (PVA + 3 wt% graphite flakes) exhibits positive permittivity across the entire test frequency region. This concentration is not suitable for metacomposite fabrication because the graphite particle surpasses the percolation threshold and may be heavily agglomerated in some regions, resulting in positive permittivity value (see Fig.5.7).

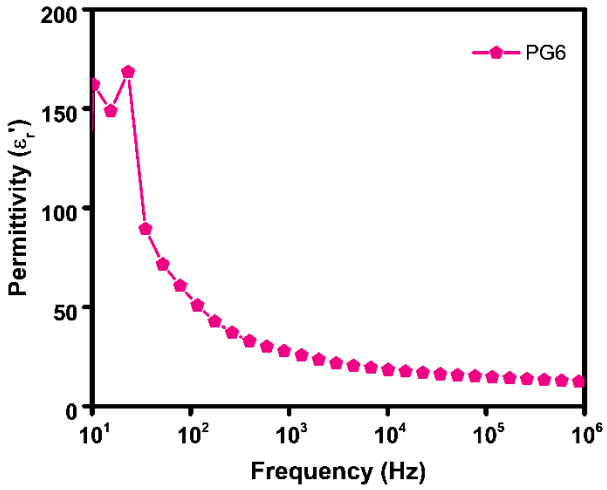

Figure 5.7 Frequency dependent real permittivity of PG6 sample

Fig.5.8a and 5.8b illustrate the impedance and phase angle response of PVA-G. The he frequency-dependent phase angle reflects the phase correlation between voltage and current in electric circuits, as depicted in Fig.5.8a. A negative phase angle indicates capacitive characteristics, where the voltage phase lags behind the current phase. Conversely, an inductive characteristic is observed when the current phase lags behind the voltage phase, resulting in a positive phase angle. The transition from positive to negative phase angle values signifies a change in permittivity [14].

In Fig.5.8b, the frequency dependent |Z| spectra of PVA-G composites are depicted. Composites with low graphite flakes content exhibit significant |Z| values that decrease with frequency, owing to their hopping conductivity. Conversely, |Z| values decrease with higher graphite flakes content, demonstrating frequency-dependent characteristics [15,43,44]. To

model the frequency-dependent |Z| spectra, an inductive circuit using inductors was employed [39,45]. Specifically, composites containing 2.5 wt% graphite flakes were utilized to establish substantial 3D conductive networks. These percolated networks, comprising dense clusters of graphite flakes, can be analogized to a hypothetical inductor comprised of an infinite number of micro-inductors. Consequently, as the graphite flake content in a composite increases, the loop diameter and winding count of the theoretical inductor increase, while the loop length decreases, thereby enhancing the composite's inductive characteristics, which are correlated with negative permittivity [46].

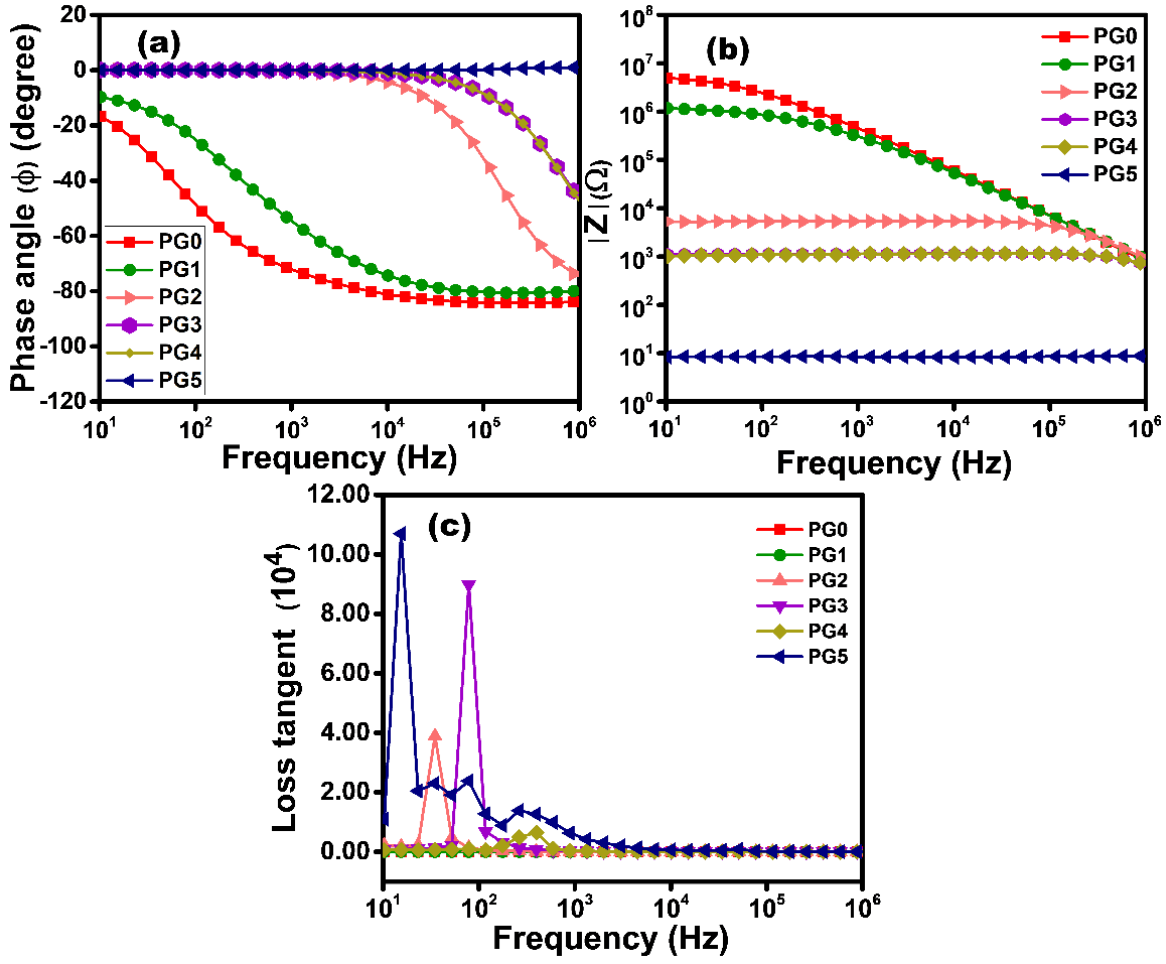

Figure 5.8 The frequency dependent (a) phase angle (b) impedance and (c) loss tangent spectra of PVA-G composites

Fig.5.8c illustrates the frequency-dependent tanδ of PVA-G metacomposites.The dielectric loss tangent ($tan\delta = \epsilon''/\epsilon'$) represents the ratio of energy lost to energy stored. As the graphite

content increases, the tanδ value rises due to the formation of a continuous conductive network. Notably, the graph exhibits a peak close to the frequency at which the permittivity value transitions from from positive to negative [47,48].

5.3 Dielectric performance of double-layer composites

In Fig.5.9a and 5.9b, the frequency-dependent permittivity and tangent loss of double-layer composites are depicted. These composites consist of a positive permittivity PG1 layer stacked with negative permittivity PG2 to PG5 layers, and dielectric measurements were conducted accordingly. Compared to pristine PVA, the double-layer composites exhibit significantly higher positive permittivity, which decreases with increasing frequency. For instance, at 10Hz, PG1-2, PG1-3, PG1-4, and PG1-5 samples exhibit permittivity values of 332.135, 917.255, 1046.58, and 1418.69, respectively. Conversely, the negative permittivity layers display values of -42.383, -569.426, -1571.88, and -13002 at 10Hz. Interestingly, despite the considerable increase in permittivity, the loss tangent of the double-layer composite remains low. The use of materials with both positive and negative permittivity layers can greatly enhance capacitance. The positive permittivity layer exhibits capacitive characteristics, while the negative permittivity layer demonstrates negative capacitance or inductive characteristics. This complementary behavior of capacitance and inductance is crucial for the development of energy storage components. Scheme 5.3a illustrates a positive permittivity and positive capacitance layer, while the negative permittivity layer indicates negative capacitance. Scheme 5.3b depicts a double-layer composite with both positive and negative permittivity layers, resulting in significant positive capacitance, indicating the capacitive nature of the film along with high positive permittivity. The double-layer composite facilitates charge accumulation at the interface between adjacent layers, contributing to additional enhancement of permittivity through polarization. The blocked transport of carriers and ohmic conduction between adjacent

layers result in high permittivity and low loss. These double-layer composites offer a substantial boost in permittivity without a significant increase in tangent loss, making them suitable for high-permittivity electronic device applications [49–51].

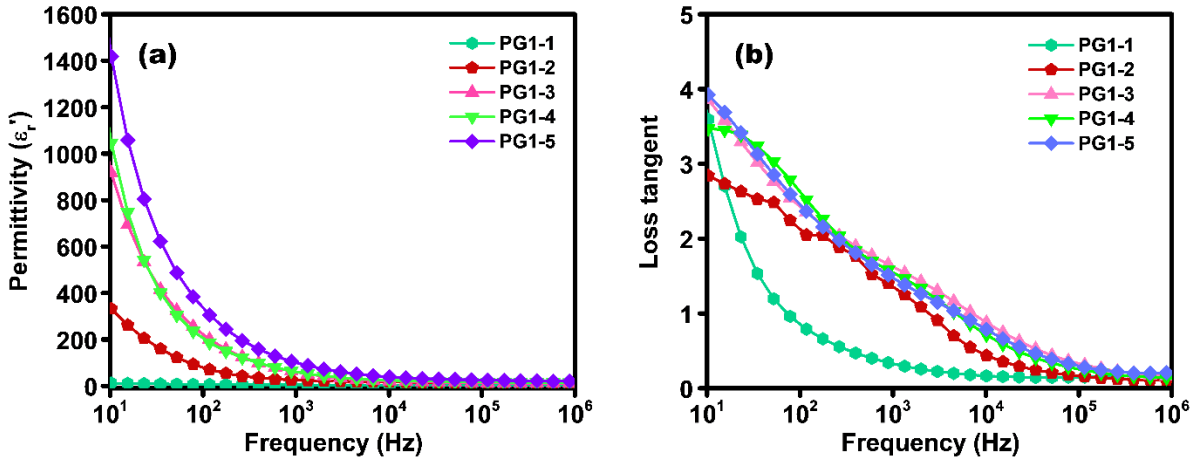

Figure 5.9 The frequency dependent (a) permittivity (b) loss tangent spectra of PVA-G double-layer composites

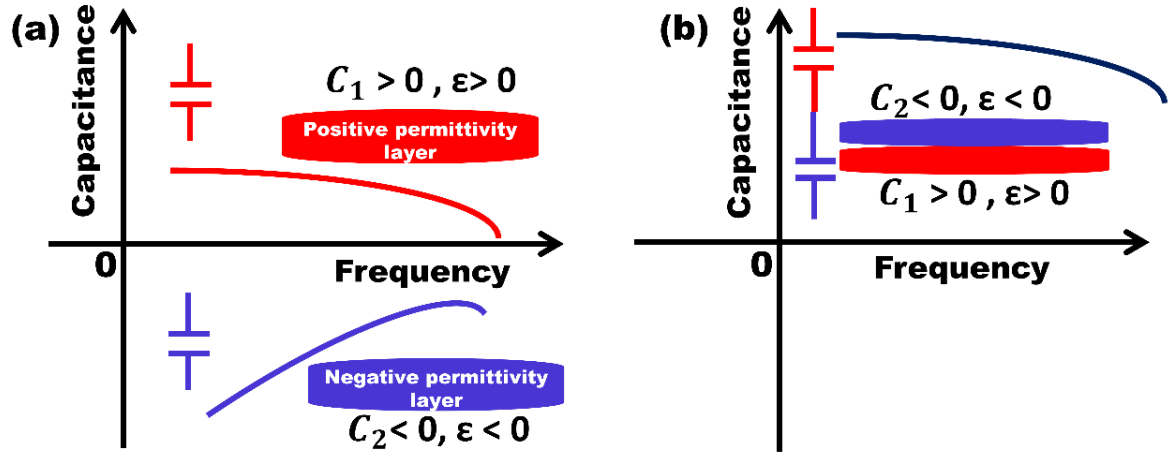

Scheme 5.3 Schematic of double layer composite with positive and permittivity layer

5.4. Electromagnetic interference (EMI) shielding performance of PVA-Graphite flakes composites in the X-band region

The electromagnetic interference shielding performance of PVA-G composites was assessed using a vector network analyzer through a transmission line and open space method within the

frequency range of 8.2 to 12.4 GHz. The reflection, transmission, and absorption coefficients of the composites were determined using S-parameters. Scheme 5.4 illustrates the shielding mechanism of PVA-G metacomposites.

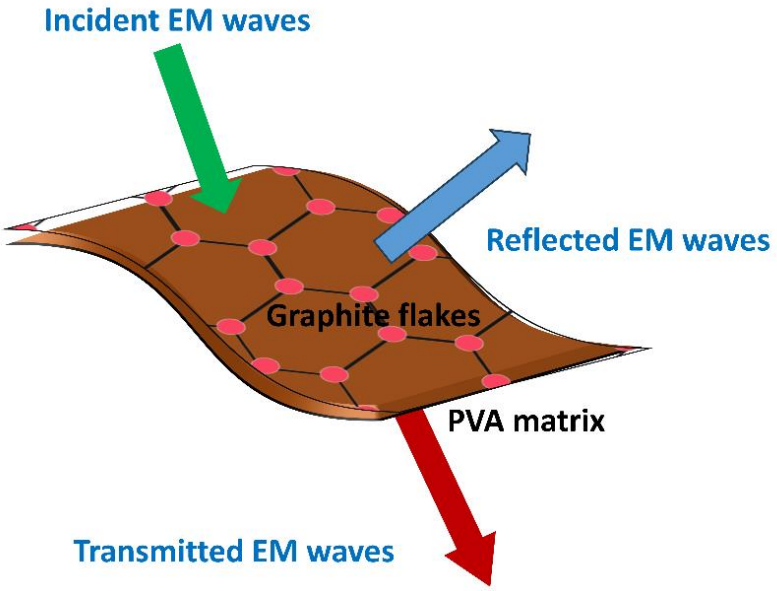

Scheme 5.4 Electromagnetic interference shielding mechanism in PVA – G composites flexible film

Fig.5.10 illustrates the shielding effectiveness of PVA-G composites in the X-band region. Both electric and magnetic loss, along with strong electrical conductivity, are crucial for effective microwave absorption [52]. The ability of polymer composites to provide shielding largely depends on the conductivity, dispersion, and concentration of the conducting filler material. The observed shielding efficiency of PVA-G composites with lower concentrations of graphite flakes (PG1 and PG2) is below 10 dB. However, with a further increase in graphite flake content, a continuous conductive path is formed, leading to improved shielding effectiveness in the X-band region. In general, a shielding effectiveness (SE) of 20 dB indicates 99% attenuation of electromagnetic (EM) radiation, while values above 10 dB correspond to 90% attenuation. Both PG3 and PG4 samples exhibit a total shielding efficiency above 10 dB, while the PG5 sample demonstrates a total shielding efficiency above 20 dB across the entire test frequency range [53]. Notably, the maximum shielding efficiency value of 31 dB is achieved

in the PG5 sample with a thickness of 0.5 mm. Increasing the thickness of the film to 1 mm with the same graphite concentration leads to an increased shielding efficiency, reaching a maximum of 37 dB.

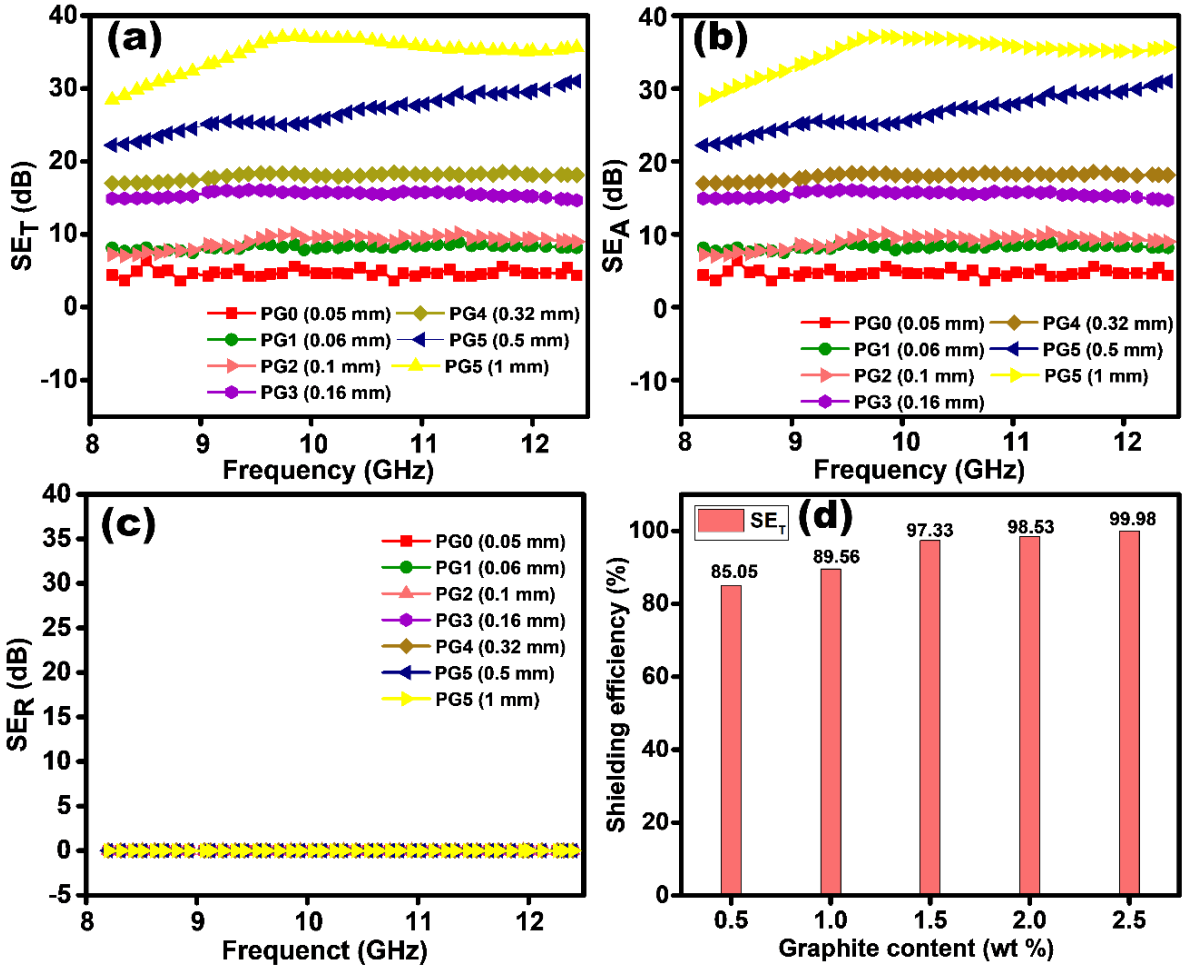

Figure 5.10 The EMI SE_T (a), SE_A(b), SE_R (c) and total shielding efficiency in percentage (d) as a function of frequency of PVA -G composites with different concentration of graphite content

The conductive network formed by the graphite content provides a sufficient path for transporting moving charge carriers freely. Moreover, the numerous interfaces between graphite flakes and PVA induce interfacial polarization, while the accumulation of free charges further enhances interfacial polarization and boosts EM wave absorption [54]. The shielding mechanism observed in this study is predominantly absorption-based, with reflection below 1 dB. Consequently, PG3 to PG5 samples exhibit promising potential for EMI shielding

applications. The average shielding efficiency of PVA-G composites is depicted in Fig.5.11, clearly indicating an absorption-dominant shielding mechanism.

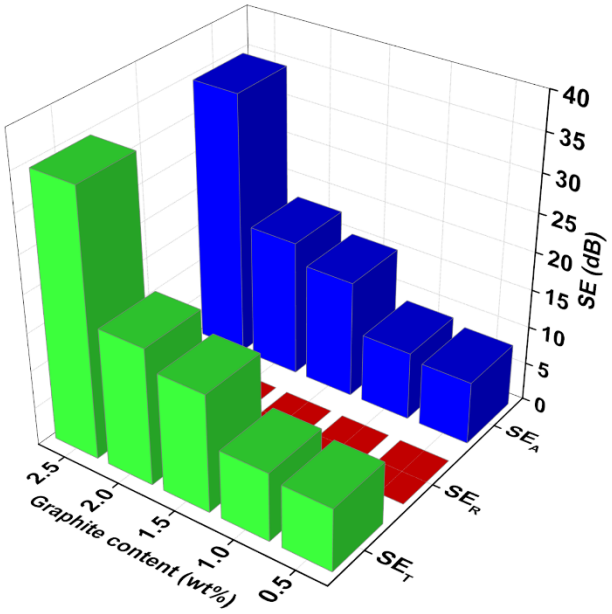

Figure 5.11 Average reflection, absorption and transmission shielding efficiency of PVA – G composites

5.5. Conclusion

In conclusion, polyvinyl alcohol (PVA) matrices with varying concentrations of graphite flakes were successfully fabricated using a simple and cost-effective die-casting method. When the graphite flake content reached 1 wt%, the real permittivity transitioned from positive to negative, a phenomenon well-explained by the Drude model. Notably, percolation was achieved with 3 wt% graphite flakes, resulting in negative permittivity across the entire test frequency range. This study observed negative permittivity even before reaching the percolation threshold, with an epsilon near zero value also recorded. The lowest negative permittivity value, -0.71, was observed at 1 wt% and 34 Hz. These PVA-G metacomposites thus present a novel approach to designing materials with weak and controllable negative permittivity, greatly enhancing their potential applications in electromagnetic interference (EMI) shielding, microwave absorption, and other fields. Additionally, high permittivity and

low dielectric loss double-layer composites were fabricated, proving suitable for high permittivity electronic device applications. The EMI shielding effectiveness (SET) of composites with 2.5 wt% graphite flakes and a thickness of 1 mm reached 37 dB, demonstrating an absorption-dominant shielding mechanism.

****

Reference

[1] R. Grimberg, Mater. Sci. Eng. B **178**, 1285 (2013).
[2] A. Danisi and C. Zannini, Sci. Rep. **13**, 3236 (2023).
[3] W. J. Padilla and R. D. Averitt, J. Opt. **19**, 084003 (2017).
[4] A. Valipour, M. H. Kargozarfard, M. Rakhshi, A. Yaghootian, and H. M. Sedighi, Proc. Inst. Mech. Eng. Part J. Mater. Des. Appl. **236**, 2171 (2022).
[5] R. Kumar, M. Kumar, J. S. Chohan, and S. Kumar, Mater. Today Proc. **56**, 3016 (2022).
[6] I. M. Pryce, K. Aydin, Y. A. Kelaita, R. M. Briggs, and H. A. Atwater, Nano Lett. **10**, 4222 (2010).
[7] M. Rashedul Islam, M. Tariqul Islam, A. Hoque, A. S. Alshammari, A. Alzamil, H. Alsaif, M. Samsuzzaman, and M. S. Soliman, Alex. Eng. J. **67**, 547 (2023).
[8] M. B. Hossain, M. R. I. Faruque, M. T. Islam, M. Singh, and M. Jusoh, J. Mater. Res. Technol. **18**, 1653 (2022).
[9] C. R. Simovski, P. A. Belov, A. V. Atrashchenko, and Y. S. Kivshar, Adv. Mater. **24**, 4229 (2012).
[10] C. Hou, G. Fan, X. Xie, X. Zhang, X. Sun, Y. Zhang, B. Wang, W. Du, and R. Fan, J. Alloys Compd. **855**, 157499 (2021).
[11] Y. Liu, G. Fan, Y. Qu, P. Xie, Z. Wang, Z. Zhang, R. Fan, and X. Yin, J. Mater. Sci. Mater. Electron. **29**, 12144 (2018).
[12] Y. Qu, J. Lin, J. Wu, Z. Wang, K. Sun, M. Chen, B. Dong, Z. Guo, and R. Fan, J. Phys. Chem. C **124**, 23361 (2020).
[13] K. Sun, W. Duan, Y. Lei, Z. Wang, J. Tian, P. Yang, Q. He, M. Chen, H. Wu, Z. Zhang, and R. Fan, Compos. Part Appl. Sci. Manuf. **156**, 106854 (2022).
[14] Y. Qu, Y. Du, G. Fan, J. Xin, Y. Liu, P. Xie, S. You, Z. Zhang, K. Sun, and R. Fan, J. Alloys Compd. **771**, 699 (2019).
[15] R. Ma, C. Cheng, Y. Qu, and R. Fan, Ceram. Int. **47**, 9971 (2021).
[16] X. Song, Z. Wei, G. Shi, G. Fan, Y. Liu, and R. Fan, ECS J. Solid State Sci. Technol. **10**, 113004 (2021).
[17] Z. Guo, A. Li, Z. Sun, Z. Yan, H. Liu, and L. Qian, Appl. Surf. Sci. **613**, 156074 (2023).
[18] J. Song, G. Shi, X. Song, Z. Zhang, Y. Liu, and R. Fan, Mater. Lett. **318**, 132051 (2022).
[19] H. D. Shetty, K. P. Maity, and V. Prasad, Surf. Interfaces **21**, 100670 (2020).
[20] J. Dai, H. Luo, M. Moloney, and J. Qiu, ACS Appl. Mater. Interfaces **12**, 22019 (2020).
[21] Z. Shi, J. Wang, F. Mao, C. Yang, C. Zhang, and R. Fan, J. Mater. Chem. A **5**, 14575 (2017).
[22] J. Chen, Y. Shi, K. Pan, J. Du, and J. Qiu, Macromol. Rapid Commun. **43**, 1 (2022).
[23] B. Zhao and C. B. Park, J. Mater. Chem. C **5**, 6954 (2017).
[24] P. Xie, Z. Zhang, Z. Wang, K. Sun, and R. Fan, Research **2019**, 1 (2019).
[25] H. Luo, Y. Lu, and J. Qiu, Carbon **183**, 34 (2021).
[26] T. Gaaz, A. Sulong, M. Akhtar, A. Kadhum, A. Mohamad, and A. Al-Amiery, Molecules **20**, 22833 (2015).
[27] S. Ningaraju and H. B. Ravikumar, J. Polym. Res. **24**, 11 (2017).
[28] N. A. Althubiti, A. Atta, E. Abdeltwab, N. Al-Harbi, and M. M. Abdel-Hamid, Inorg. Chem. Commun. **153**, 110779 (2023).
[29] A. S. Abouhaswa and H. M. Abomostafa, Polym. Bull. (2023).
[30] A. A. Naqvi, Z. Awan, A. A. Shaikh, and M. Younas, J. Test. Eval. **51**, 20220409 (2023).
[31] S. P, D. M. Vidyadharan, K. Sridharan, M. S. T. H, B. M, and S. Swaminathan, Mater. Chem. Phys. **317**, 129156 (2024).

[32] T. Haldar, U. Kumar, B. C. Yadav, and V. V. R. K. Kumar, Ceram. Int. **47**, 1389 (2021).
[33] C. Cheng, R. Fan, Y. Ren, T. Ding, L. Qian, J. Guo, X. Li, L. An, Y. Lei, Y. Yin, and Z. Guo, Nanoscale **9**, 5779 (2017).
[34] Z. Wang, K. Sun, P. Xie, Y. Liu, Q. Gu, and R. Fan, Compos. Sci. Technol. **188**, 107969 (2020).
[35] H. Luo and J. Qiu, Ceram. Int. **45**, 843 (2019).
[36] B. Zhao and C. B. Park, J. Mater. Chem. C **5**, 6954 (2017).
[37] Z. Wang, K. Sun, P. Xie, Q. Hou, Y. Liu, Q. Gu, and R. Fan, Acta Mater. **185**, 412 (2020).
[38] C. Xu, Y. Qu, G. Fan, P. Xie, H. Ren, J. Chen, Y. Liu, Y. Wu, and R. Fan, J. Mater. Sci. Mater. Electron. **29**, 15994 (2018).
[39] Z. Wang, P. Xie, G. Fan, Z. Zhang, Y. Liu, Q. Gu, and R. Fan, Ceram. Int. **46**, 9342 (2020).
[40] J. Ni, R. Zhan, and J. Qiu, Org. Electron. **82**, 105706 (2020).
[41] S. P., A. R., B. M., M. S. T.H., K. Sridharan, and S. Swaminathan, Mater. Today Commun. **34**, 105287 (2023).
[42] X. Sun, J. Shen, C. Cheng, T. Wang, Y. Liu, and R. Fan, Ceram. Int. **45**, 16618 (2019).
[43] K. Sun, J. Xin, Y. Li, Z. Wang, Q. Hou, X. Li, X. Wu, R. Fan, and K. Leong Choy, J. Mater. Sci. Technol. **35**, 2463 (2019).
[44] C. Cheng, R. Fan, G. Fan, H. Liu, J. Zhang, J. Shen, Q. Ma, R. Wei, and Z. Guo, J. Mater. Chem. C **7**, 3160 (2019).
[45] M. Han, Z. Shi, W. Zhang, K. Zhang, H. Wang, D. Dastan, and R. Fan, Compos. Part Appl. Sci. Manuf. **149**, 106559 (2021).
[46] G. Fan, Y. Zhao, J. Xin, Z. Zhang, P. Xie, C. Cheng, Y. Qu, Y. Liu, K. Sun, and R. Fan, J. Am. Ceram. Soc. **103**, 403 (2019).
[47] T. Haldar, U. Kumar, B. C. Yadav, and V. V. R. K. Kumar, J. Mater. Sci. Mater. Electron. **31**, 11791 (2020).
[48] T. Haldar and V. V. R. Kanth Kumar, J. Alloys Compd. **772**, 218 (2019).
[49] J. Wang, Z. Shi, F. Mao, S. Chen, and X. Wang, ACS Appl. Mater. Interfaces **9**, 1793 (2017).
[50] Z. Shi, J. Wang, F. Mao, C. Yang, C. Zhang, and R. Fan, J. Mater. Chem. A **5**, 14575 (2017).
[51] C. Zhang, Z. Shi, F. Mao, C. Yang, X. Zhu, J. Yang, H. Zuo, and R. Fan, ACS Appl. Mater. Interfaces **10**, 26713 (2018).
[52] N. Agnihotri, K. Chakrabarti, and A. De, RSC Adv. **5**, 43765 (2015).
[53] A. Kaushal and V. Singh, J. Appl. Polym. Sci. **139**, (2022).
[54] G. Li, J. Zhao, Z. Wang, X. Yu, T. Zhao, X. Liang, R. Sun, L. Cao, and P. Zhu, Mater. Lett. **325**, 132814 (2022).

Metacomposites of $BaTiO_3$ and TiN in polyvinyl alcohol matrix with different carbon nanostructures

In recent times, there has been a growing interest in negative dielectric constants due to their crucial role in nanocomposite metamaterials also termed as metacomposites [1–3]. Their unique electromagnetic properties enable remarkable features such as perfect electromagnetic wave absorption and lossless wireless power transfer. Metacomposites, which are predominantly formed using percolating composites, leverage this phenomenon. In insulator-conductor metacomposites, negative permittivity primarily arises from plasma oscillation, whereas in ferroelectric metacomposites, dielectric resonance plays a key role [4–6]. Xie and co-workers reported negative permittivity in $BaTiO_3$/Cu metacomposites, where both dielectric resonance and plasma oscillations played a key role in contributing to this phenomenon [7]. On the other hand, Fan et al. also reported negative permittivity in $BaTiO_3$/Ag metacomposites, with plasma oscillations identified as the primary cause [8]. From these studies, it is understood that $BaTiO_3$ serves as a suitable ferroelectric and dielectric matrix for the fabrication of metacomposites [9,10].

For the last thirty years, researchers have focused their attention on ternary oxides possessing the classical ABO_3 perovskite structure, owing to their exceptional properties and diverse applications across various fields. Several ternary oxides, including $SrTiO_3$, $BaTiO_3$, $BaSnO_3$, $PbTiO_3$, and $PbZrO_3$, have been thoroughly investigated for their intriguing characteristics and their potential to be effectively employed in specific application areas [11–15]. $BaTiO_3$, a ferroelectric and dielectric ceramic material, distinguishes itself from others due to its remarkable properties. Notably, it exhibits a high dielectric constant and low dielectric loss, making it well-suited for multilayer ceramic capacitors, electro-optical devices and piezoelectric sensors [12,16–18]. Moreover, $BaTiO_3$ displays various crystal phases, including

rhombohedral, orthorhombic, tetragonal, cubic, and hexagonal depending on the transition temperature and interestingly its crystal structure exhibits flexible behaviour with change in temperature. Typically, the unit cell of $BaTiO_3$ consists of Ti ions situated at its center, forming octahedral coordination with oxygen ions found in the face centres. Barium ions, on the other hand occupy the corners of the cubic structure. Due to the difference in size between the cations, Ti^{4+} tends to shift from its stable position, resulting in high polarization [19,20]. Conventionally, solid-state reactions involving $BaCO_3$ and TiO_2 powder as precursors at high temperatures are widely accepted for the synthesis of $BaTiO_3$ [21]. However, this method suffers from drawbacks such as less uniformity, non-stoichiometry, and the presence of impurities. To overcome these limitations, the present study introduces an effective solvothermal method for synthesizing mesoporous $BaTiO_3$ nanoparticles. To the best of our knowledge, this approach represents a novel way to produce $BaTiO_3$ nanoparticles, and the comprehensive material characterization carried out allows us to understand its exceptional properties.

Further, our study focuses on exploring the dielectric properties $BaTiO_3$ and how we can adjust its dielectric constant by incorporating suitable conducting fillers. For fabricating metacomposites, transition metals (Cu, Ag, Fe) and carbonaceous materials have been widely reported to be introduced as fillers [4,7,8,22,23]. Also, ceramic conducting fillers offer an attractive alternative in the fabrication of metacomposites due to their chemical and heat resistance [24–26]. Among the ceramic conducting fillers, Titanium nitride (TiN) stands out as it exhibits plasmonic resonance within the visible to near-infrared spectrum [27]. Favourable combination of physicochemical characteristics *viz.*, its excellent electronic conductivity, chemical and thermal stability, as well as mobility, make TiN a superior choice for developing metacomposites [28–31]. Consequently, we chose to combine ferroelectric $BaTiO_3$ and plasmonic TiN to fabricate metacomposites through blending and compression

moulding, wherein their electrical performance was predominantly influenced by the percolation behaviour. Investigation of the temperature-dependent dielectric properties of the fabricated metacomposites revealed the dielectric resonance type negative permittivity that steadily followed the Lorentz model. Interestingly, we observed that the negative dielectric constant diminishes with an increase in annealing temperature, as highlighted in our study.

Electromagnetic interference and pollution from electronic devices and communication systems is an important concern these days due to their rapid growth. Therefore, flexible and light weight shielding materials are vital for controlling electromagnetic interference or pollution. For this $BaTiO_3$ – TiN composites is added to the Polyvinyl alcohol matrix and dielectric constant and electromagnetic interference shielding performance are also studied. Based on the previous reports and in our previous chapters we understood carbon-based materials are good shielding materials. For improving shielding efficiency conducting fillers such as carbon black, MWCNT, graphite flakes are also separately added to this polymer composites and EMI shielding efficiency also measured. Here, a four-component system is studied. Two dielectric materials and two conducting fillers and their dielectric response are also measured.

6.1. Experimental

6.1.1. Materials

Titanium (IV)butoxide (97%), Ba $(OH)_2$ (95%), and KOH (≥85%) were purchased from Sigma. Glacial acetic acid (99.99%) was purchased from Merck. Titanium nitride was purchased from Alfa-Aesar.

6.1.2. Synthesis of $BaTiO_3$ Nanoparticles

$BaTiO_3$ nanoparticles were synthesized through a solvothermal process. Typically, 0.25 M Titanium butoxide was added to a reaction medium containing 5 ml each of glacial acetic acid and ethanol under stirring for 20 min. Next, 0.25 M of Ba $(OH)_2$ was added to the above

solution under continuous stirring until a clear suspension without any lumps was formed, following which its pH was adjusted to 12 by the dropwise addition of 5 M KOH. Finally, the reaction mixture was transferred to a Teflon-lined stainless-steel autoclave of 100 ml capacity. The autoclave was carefully sealed and the solvothermal reaction was carried out at 180 °C for 18 h. Autoclave to cool down naturally and the sediments were collected through high-speed centrifugation after repeated washing with dilute acetic acid with excess DI water. Scheme 6.1 represents the schematic and photographs of the solvothermal synthesis method.

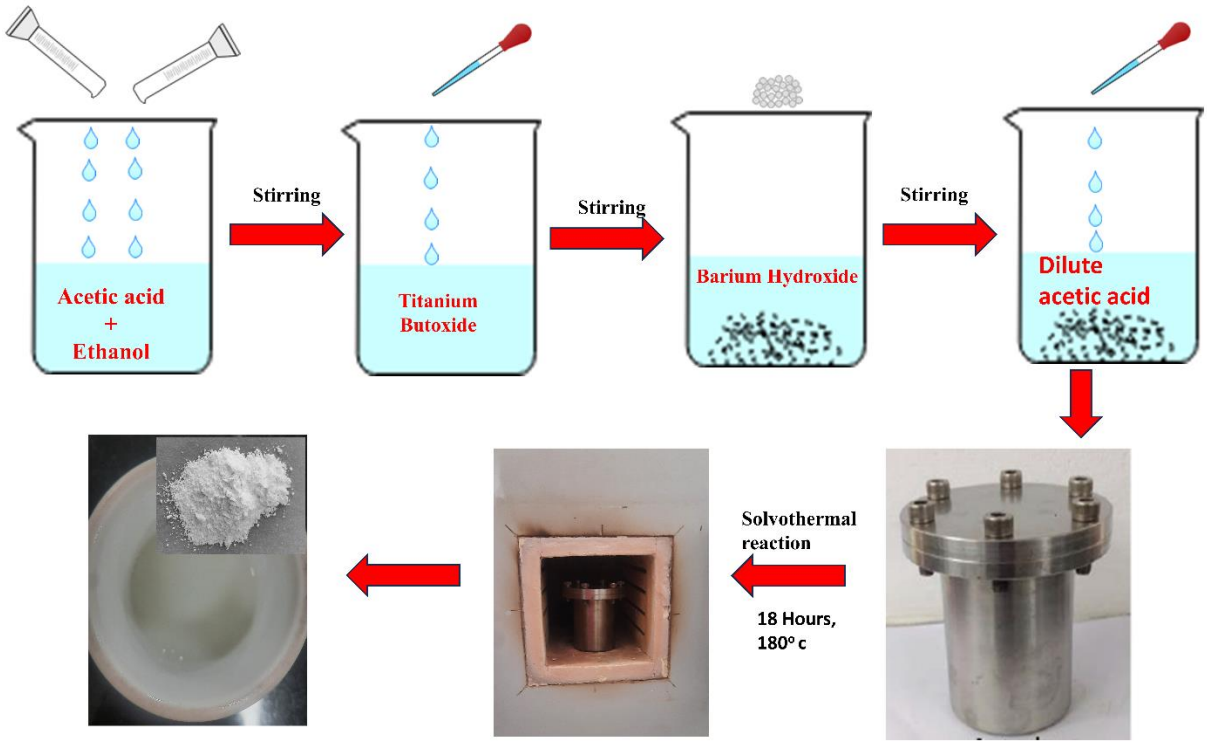

Scheme 6.1 Solvothermal synthesis method

6.1.3. Fabrication of $BaTiO_3$/TiN metacomposites

$BaTiO_3$/TiN ceramic metacomposites were fabricated through blending and compression molding technique followed by annealing at 200 °C to enhance their solidity and strength. Amount of $BaTiO_3$ was fixed to 0.1 g, while the TiN content was varied in steps of 0.05 g up to 0.3 g (0.05, 0.1, 0.15, 0.2, 0.25 and 0.3g) and the resulting composites were labelled as BTN1, BTN2, BTN3, BTN4, BTN5 and BTN6, respectively. These samples were annealed at

400°C for the study of temperature dependence. Scheme 6.2 provides the reaction mechanism corresponding to $BaTiO_3$ nanoparticles and $BaTiO_3$/TiN metacomposites.

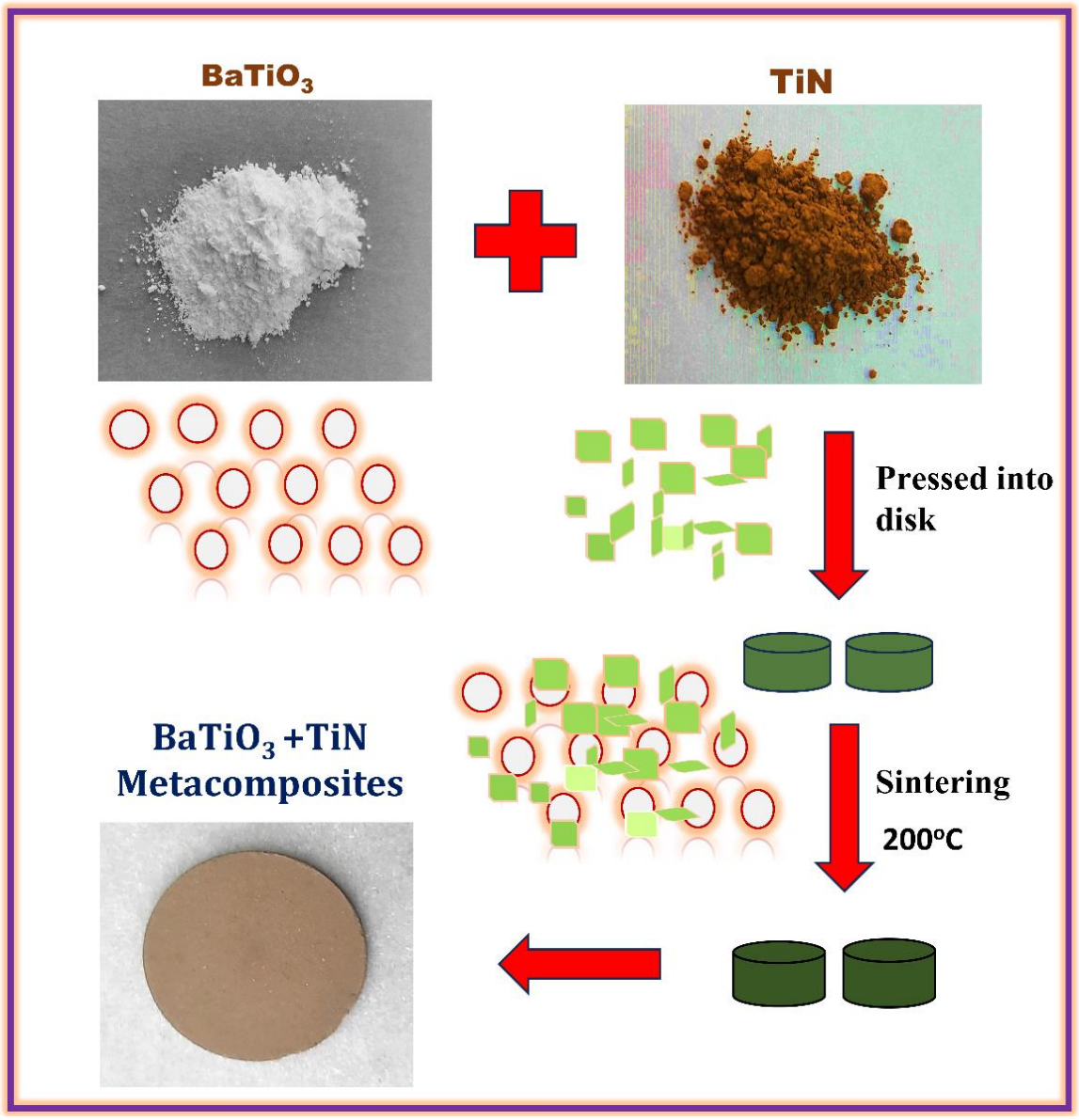

Scheme 6.2 Fabrication procedure of $BaTiO_3$/TiN metacomposites

6.1.4 Fabrication of PVA – $BaTiO_3$ – TiN composites

The PVA – $BaTiO_3$ – TiN composites film is fabricated by die – casting procedure. For these 5 wt% polyvinyl alcohols dissolved in deionized water (0.5g in 10 ml water) and TiN (0.3g in 10 ml water) and $BaTiO_3$ (0.1g in 10 ml water) is added to the above solution and sonicated for 20

min. Then carbon black/graphite flakes/MWCNT (0.25g in 10 ml water) is added to the above solution and flexible films are fabricated. The following table (Table 6.1) shows the details of metacomposites prepared with concentration of various filler taken. Scheme 6.3 shows the film fabrication procedure.

Table 6.1 Concentration of PVA and different fillers such as $BaTiO_3$, TiN and carbon nanostructures (CB, MWCNT and Graphite) for polymer composite fabrication.

Dielectric matrix		Conducting filler		Composite Code
PVA (5 wt%)	$BaTiO_3$ (1 wt%)	---	---	PBT
PVA (5 wt%)	---	TiN (3 wt%)	---	PTN
PVA (5 wt%)	$BaTiO_3$ (1 wt%)	TiN (3 wt%)	---	PBTN
PVA (5 wt%)	$BaTiO_3$ (1 wt%)	TiN (3 wt%)	CB (2.5 wt%)	PCBTN
PVA (5 wt%)	$BaTiO_3$ (1 wt%)	TiN (3 wt%)	MWCNT (2.5 wt%)	PMBTN
PVA (5 wt%)	$BaTiO_3$ (1 wt%)	TiN (3 wt%)	Graphite flakes (2.5 wt%)	PGBTN

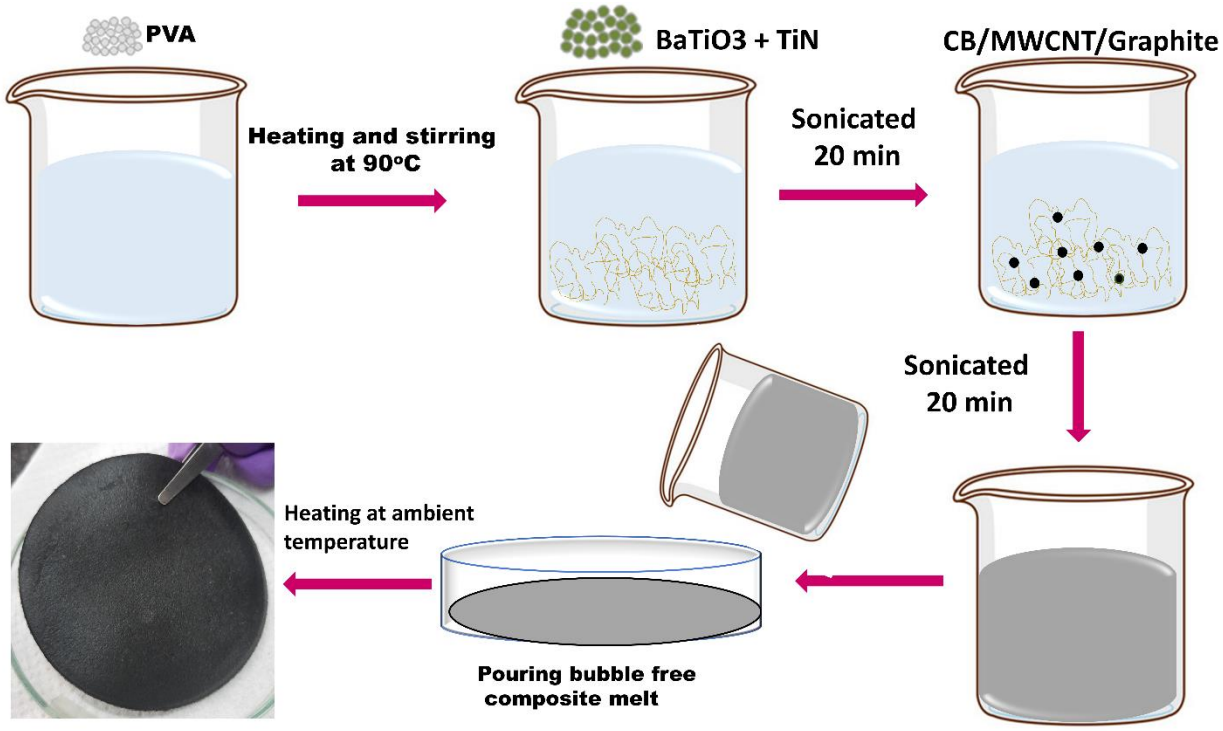

Scheme 6.3 Schematic of the composite film fabrication process

6.2. Results and discussion

6.2.1. Analysis of structure and morphology

XRD pattern of $BaTiO_3$, TiN and $BaTiO_3$ – TiN metacomposites are shown in Fig.6.1a and 6.1b. Fig.6.1a shows XRD pattern of $BaTiO_3$ and TiN. Characteristics peaks of the $BaTiO_3$ indicate that phase pure formation of cubic $BaTiO_3$ matching well with JCPDS file No. 75-0213. In the case of tetragonal $BaTiO_3$ [32], peak near 45° will be broad showing a peak split at 45.1° and 45.7° corresponding to the (002) and (200) planes respectively. However, the XRD patterns did not show such a peak split at 45°, revealing the phase pure formation of cubic $BaTiO_3$. XRD peak of commercially available TiN with JCPDS file number 87-0630 also shown in Fig.6.1a. Fig.6. 1b shows XRD pattern of barium titanate metacomposites (BTN) with different concentrations of TiN (annealed at 200 °C). With the increasing concentration of TiN, the intensity of the diffraction peaks is enhanced compared with pure $BaTiO_3$, while all samples still maintain the crystallinity.

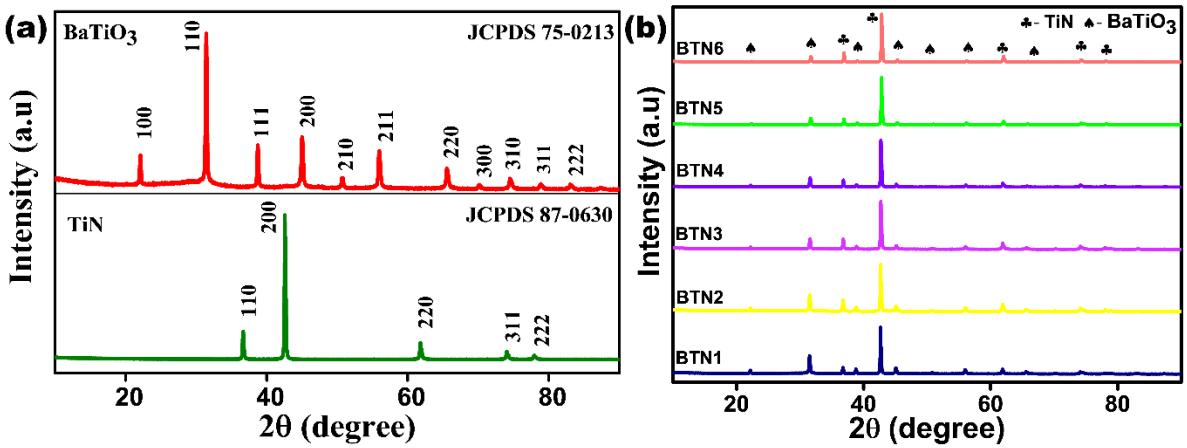

Figure 6.1 XRD patterns of (a) $BaTiO_3$ and TiN, (b) $BaTiO_3$-TiN metacomposites

Fig.6.1c shows XRD pattern of polymer composites with Carbon black, MWCNT, Graphite flakes. The broad peak at 19.5° is the XRD peak of polyvinyl alcohol and shows semi – crystalline nature. The peaks at 25.7° and 26.01° indicate XRD pattern of carbon black and

MWCNT and peaks at 26.5° and 54.6° indicate XRD of graphite. All the characteristics peak of $BaTiO_3$ and TiN also shown in figure.

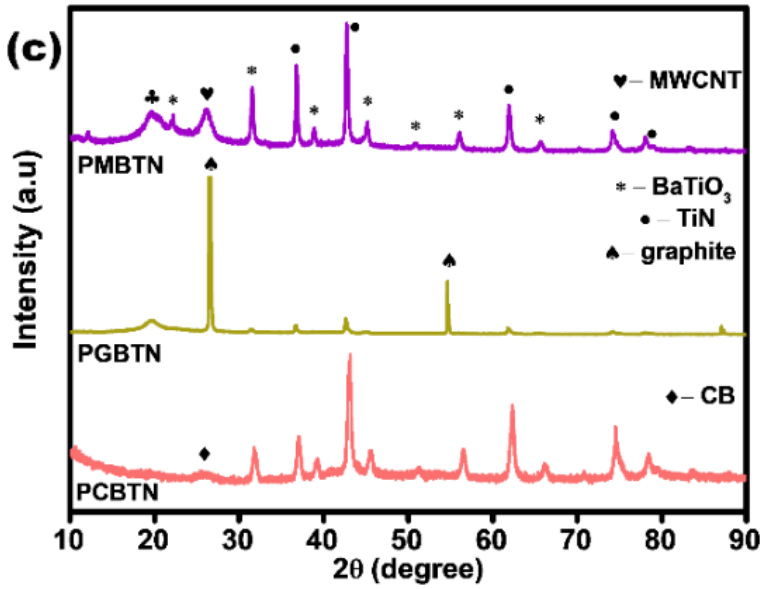

Figure 6.1(c) XRD pattern of Polymer composites (PVA – BTN – CB (PCBTN), PVA – BTN – graphite (PGBTN), PVA – BTN – MWCNT (PMBTN)

6.2.2. Analysis of morphology

FESEM, TEM, HRTEM and SEAD pattern of the as synthesized $BaTiO_3$ sample is shown in Fig.6.2. $BaTiO_3$ sample appeared to be composed of uniformly shaped spheres with a size ranging between 20-40 nm as observed from Fig.6.2a. The morphology of the $BaTiO_3$ samples was uniformly distributed in size and was granular/spherical. As seen from Fig.6.2b, the size range of the particles in the $BaTiO_3$ sample was 20-40 nm. Because the phase change entails distortion of the constituent TiO_6 structure, which is impeded by the structural flaws present in the nano domain, dealing with $BaTiO_3$ nanoparticles makes the entire phase transition rather problematic. This ultimately results in a dark and bright contrast in the TEM images that represents the lattice strain, suggesting the presence of a modest amount of tetragonality in the system. Their crystallinity was suboptimal as revealed through HRTEM images as shown in Fig.6.2c. Crystallinity of the materials was obtained from Selected area electron diffraction

(SAED) investigations. As observed from Fig.6.2d, the nano-sized particles that are destined to create concentric spotted rings are represented by the scattered diffraction spots, suggesting that the sample could exhibit the polycrystal behaviour.

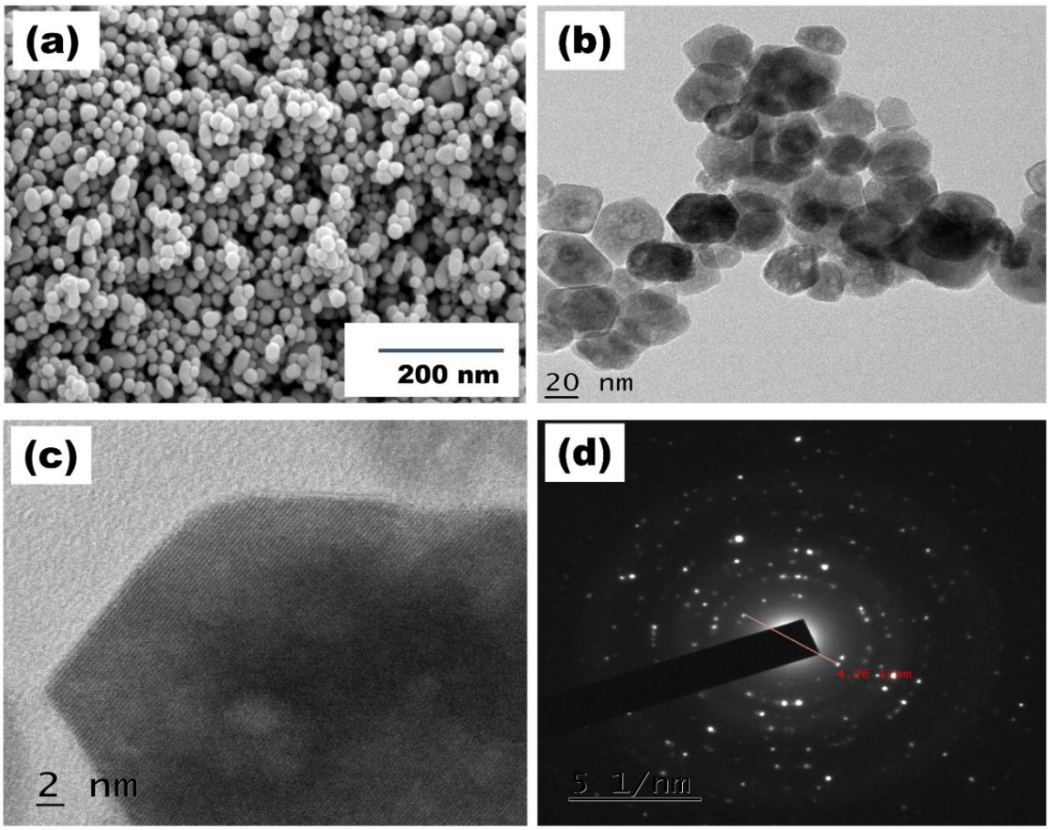

Figure 6.2 FESEM micrograph of $BaTiO_3$ (a), TEM micrograph of $BaTiO_3$ (b) HRTEM micrograph of $BaTiO_3$ (c) and SEAD pattern of $BaTiO_3$ (d)

FESEM micrograph of pristine TiN and the $BaTiO_3$-TiN metacomposites are presented in Fig.6.3a and Fig.6.3b-6.3f, respectively. As observed, the TiN layers in the composites are randomly distributed in the $BaTiO_3$ matrix forming composite with lower TiN concentration as seen in the FESEM micrographs (Fig.6.3b and 6.3c). Evidently the micrographs in Fig.6. 3c, 6.3d, 6.3e and 6.3f are indicative of the improved interconnection between the $BaTiO_3$ nanoparticles with TiN directed the formation of a conductive network due to the stepwise increase in concentration of TiN. Proper connection between the filler and the matrix is vital

for the formation of a percolative network and boosting the electrical property is reported in the literature [33].

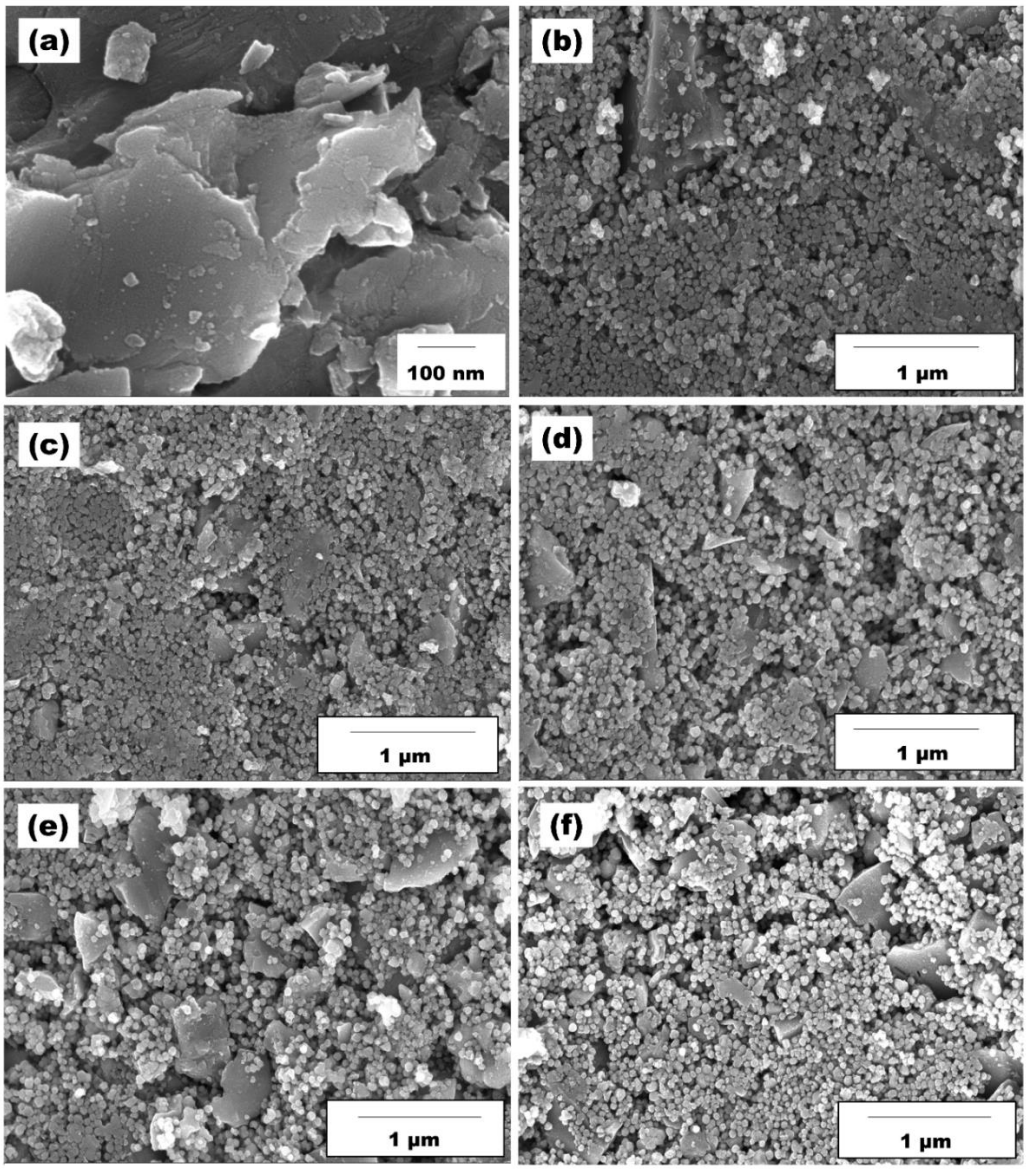

Figure 6.3 FESEM micrographs of pristine TiN (a) and $BaTiO_3$-TiN metacomposites BTN1 (b), BTN3 (c), BTN4 (d), BTN5 (e) and BTN6 (f)

6.2.3 Thermal analysis

Fig.6.4 shows thermal analysis of PVA – TiN, PVA – $BaTiO_3$, PVA – $BaTiO_3$ matrix with different carbon conducting fillers. The TGA thermograph shows weight loss percentage as a function of temperature. Pristine PVA film was observed to lose 92% of its weight at 550℃.

while PTN, PBTN, PGBTN, PCBTN and PMBTN were found to lose weight by 64%, 60%, 57%, 45%, and 35% respectively at 550℃. Therefore, after the addition of fillers its thermal stability greatly increased.

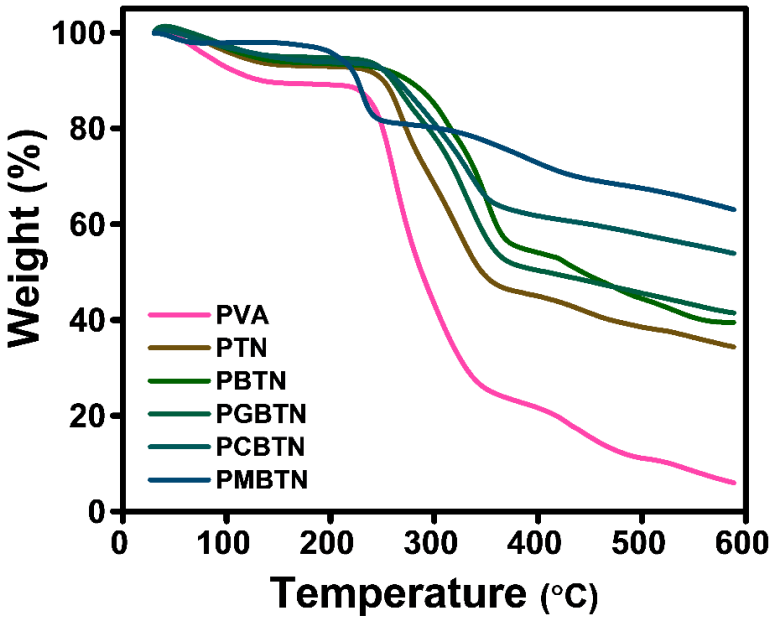

Figure 6.4 Thermogravimetric analysis of PVA – $BaTiO_3$ matrix with various conducting fillers

6.3. Dielectric properties

Frequency dependence on real part of complex permittivity (ε') of the as-synthesized pristine $BaTiO_3$ nanoparticles and pristine TiN samples with different temperature are presented in Fig.6.5a and 6.5b, respectively. As depicted in Fig.6.5a, the initial permittivity of BT at a frequency of 117 Hz exhibited a significant six-fold increase, rising from 302 to 1850, when subjected to heating at 200℃. The sintering temperature increases to 300℃, its permittivity decreases slightly compared to sintering temperature at 200℃ and permittivity value is 1620 at 117 Hz. Conversely, elevating the temperature of BT to 400℃ resulted in a more modest increase in permittivity, approximately 2.5 times, from 302 to 760, as illustrated in Fig. 6.5c. The effect of annealing temperature on the real permittivity of $BaTiO_3$ is found to be interesting by showing a decrease in permittivity with increase in annealing temperature above 200℃. This behaviour may be due to an inter-play between the crystallinity and crystallite size of the

barium titanate particles. On the other hand, as depicted in Fig.6.5b, pristine TiN, the initial negative permittivity of pristine TiN at 117 Hz, measuring -2478, transitioned to positive values of 1048 and 422 when heated to 200℃ and 400℃, respectively.

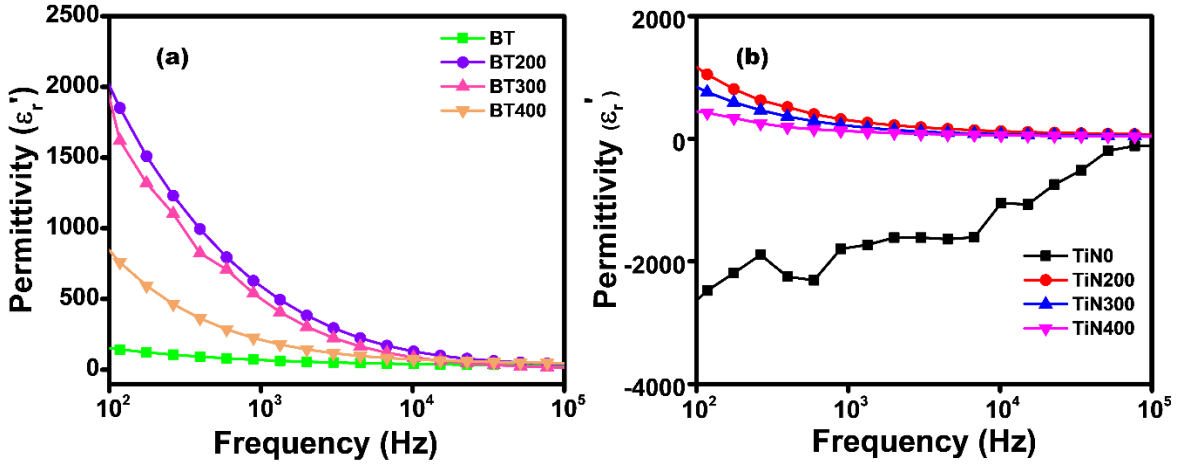

Figure 6.5 Frequency dependent real permittivity of $BaTiO_3$, TiN with different temperatures

Fig.6.6 shows frequency dependent real and imaginary permittivity of BTN metacomposites annealed at 200℃. When examining the fabricated BTN metacomposites, it was observed that they initially displayed positive permittivity values when the TiN content was lower and at lower frequencies. However, as the frequency increased and the TiN content rose, the permittivity transitioned to become negative as observed from Fig.6.6a, 6.6b and 6.6c. The introduction of more conductive TiN fillers led to an increase in the number of interfaces between TiN and BT, effectively behaving like micro-capacitors. Consequently, this gave rise to enhanced interfacial polarization, a phenomenon recognized as the Maxwell-Wagner-Sillars effect [34]. The substantial decrease in the permittivity of BTN1 and BTN2 metacomposites in comparison with sample BT (Fig.6.6a) in the lower frequency region could be attributed to the enhanced leakage current in partially connected TiN-$BaTiO_3$ interface. As noted from Fig.6.6a, 6.6b and 6.6c, negative permittivity was typically observed above 10 kHz in BTN3, BTN4, BTN5 and BTN6 metacomposites that could be attributed to the electric percolation phenomenon due to macroscopic delocalization of the electrons within the interconnected

network. Further, in comparison to BTN1, BTN2 and BTN3, the increase in permittivity was about 10 times for BTN4 (Fig.6.6b) and 100 times more for BTN5 and BTN6 (Fig.6.6c), respectively. Under the action of the external alternating electric field (for BTN3, BTN4, BNT5 and BTN6) induction of dielectric resonance happened in these composites and that could be attributed to the collective resonance of Ti^{4+} in Ti-O octahedral sites of BT. The dipole charge resonance can be considered as mechanical linear oscillators, and their restoring force would balance the force induced by the applied electric field. For such a resonance the permittivity can be described by the Lorentz model [4,35], based on the following equation

$$\epsilon' = 1 + \frac{\omega_p^2 (\omega_o{}^2 - \omega^2)}{(\omega_o{}^2 - \omega^2)^2 + \omega^2 \Gamma_L^2} \qquad (6.1)$$

where ω (ω = 2πf) is the angular frequency of the electric field, ω_0(ω_0 = 2πf_0) is the characteristic frequency (or resonance frequency), ω_p (ω_p = 2πf_p) is the angular plasma frequency describing the resonance strength, and Γ_L represents the damping constant related to the broadening of resonance.

Lorentz-type dielectric resonance occurs due to the induced electric dipole within isolated TiN layers embedded in the BT matrix. When the frequency of the external electric field approaches the resonance frequency range (approximately near f_0), it is suggested that negative permittivity can be achieved [25]. With respect to the increase in concentration of TiN in BT matrix the induced electric dipole concentration also increases and that enhances the angular plasma frequency or the resonance strength thereby showing 10 to 100 times increase in permittivity of BTN 1 to BTN6.

Frequency dependence on the imaginary part of permittivity (ε") for the fabricated BTN metacomposites are shown in Fig.6.6d. Typically, ε" is a measure of the dielectric loss of a material that primarily originates from polarization and conduction in composite materials. Herein, the dielectric loss depends on the conductive carriers (TiN) and the polarization dipoles present near the percolation threshold that could be expressed as,

$$\varepsilon'' = \varepsilon''_C + \varepsilon''_D + \varepsilon''_P \quad (6.2)$$

where ε''_C denotes the conduction loss, ε''_D is dipolar loss and ε''_P is the interfacial polarization related loss [4].

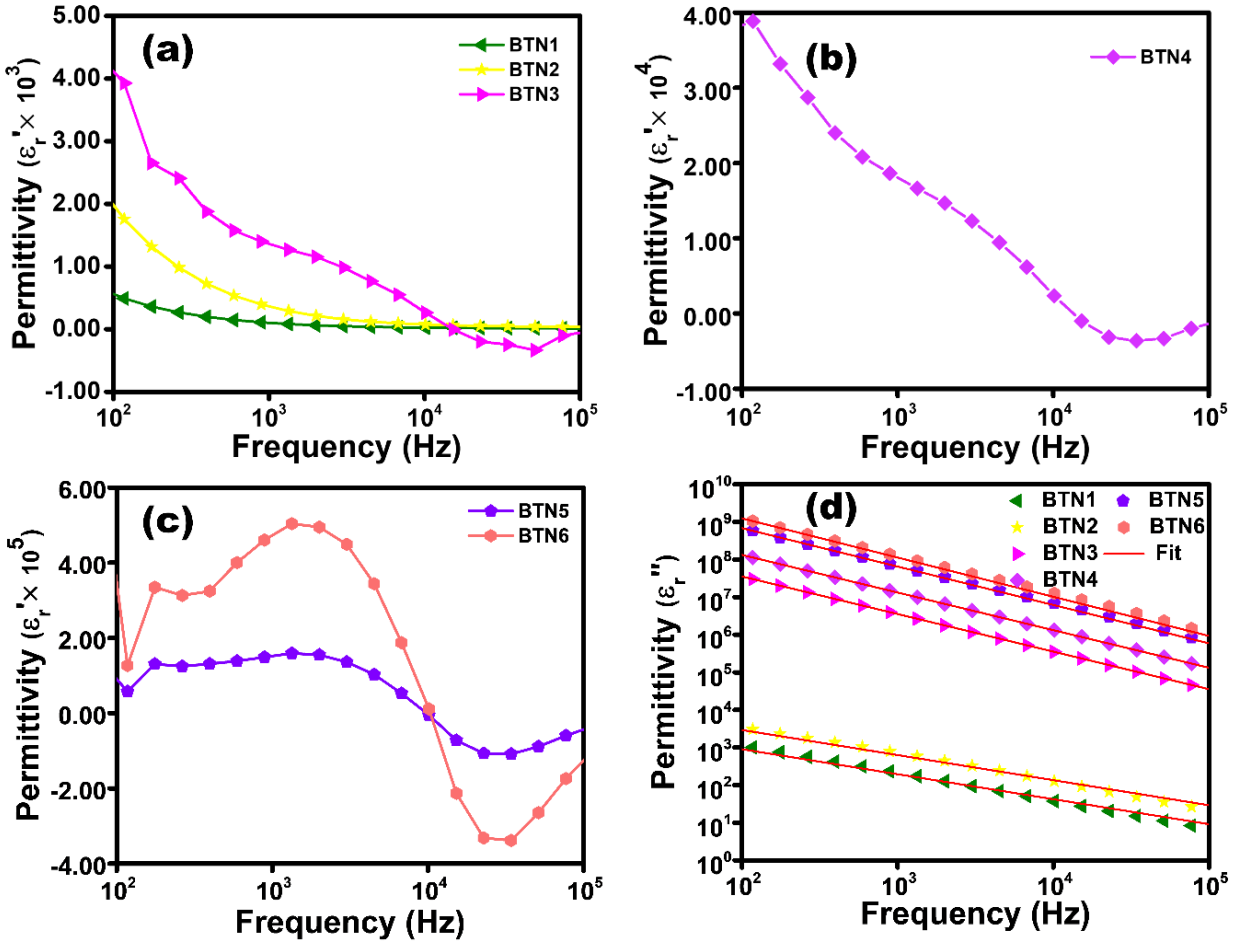

Figure 6.6 Frequency dependent real (a, b, c) and imaginary (d) permittivity of $BaTiO_3$/TiN metacomposites

As observed from Fig.6.6d, dielectric loss remains minimal below the percolation threshold and significantly escalates as the TiN content within the BTN metacomposites increases beyond this threshold. Furthermore, the ε''_C of composites surpassing the percolation threshold exhibits a linear decrease as the frequency rises, highlighting that conduction loss takes precedence in determining the overall dielectric loss. Conduction loss typically exhibits an inverse relationship with frequency, as described by $\varepsilon'' = \frac{\sigma_{dc}}{\omega \varepsilon_0}$ where, σ_{dc} is the electrical

conductivity. The results obtained from fitting this equation align closely with the measured data, indicating that conduction loss was the prevailing factor influencing dielectric loss. However, in case of BTN7 (with 0.35 g TiN, see Fig.6.7), the value of permittivity drastically decreased and the range was similar to that of BTN1 and BTN2, indicating the failure of the composite that could be attributed to very high content of TiN, exceeding the percolation threshold.

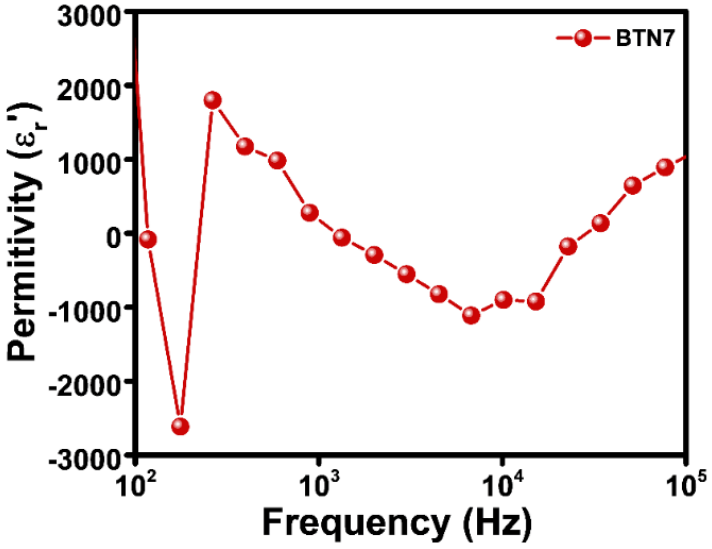

Figure 6.7 Frequency dependent permittivity of BTN7 sample

Fig.6.8 shows frequency dependent permittivity of polymer based metacomposites in the frequency range of 10^1 to 10^6. PTN, PBT and PBTN samples shows permittivity value of 94,126 and 761 respectively at 10 Hz. Interestingly, its negative permittivity disappears when BTN6 metacomposite added to the PVA matrix. Its shows huge positive permittivity according to Maxwell-Wagner-Sillars effect. When graphite flakes added to this PBTN matrix, it shows Drude model negative permittivity in between 10^1 to 10^2 Hz (Fig.6.8b). Addition of MWCNT to the PBTN matrix, shows Drude model negative permittivity (Fig.6.8c). Further, the addition of carbon black to PBTN results in huge Drude model negative permittivity (Fig.6.8d).

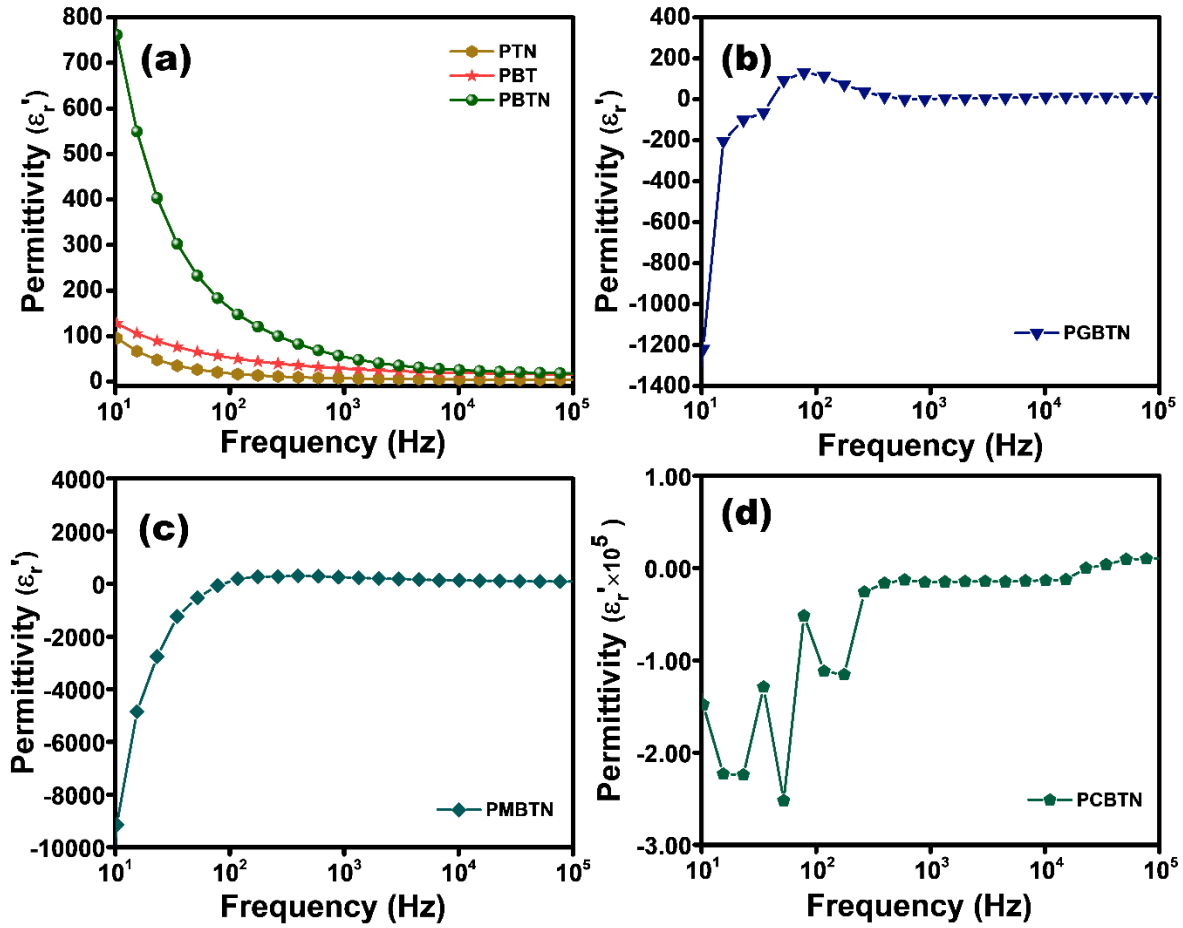

Figure 6.8 Frequency dependent real (a, b, c, d) permittivity of polymer metacomposites ((PVA – BTN – CB (PCBTN), PVA – BTN – graphite (PGBTN), PVA _ BTN – MWCNT (PMBTN)).

6.4 Conductivity behaviour and percolation threshold

The frequency dependence on AC electrical conductivities for pristine BT and TiN as a function of temperature is presented in Fig.6 9a and 6.9b. As noted from Fig.6.9a, when BT is heated to 200 °C and 400 °C, its conductivity at 117 Hz increases to 1.25×10^{-7} and then decreases to 7.30×10^{-8}, respectively, whereas its conductivity remained at 1.07×10^{-8} at room temperature. Conversely, TiN exhibits higher conductivity at room temperature and demonstrates a frequency-independent conductivity pattern as observed from Fig.6.9b. When heated to temperatures of 200 °C and 400 °C, TiN experienced a decrease in conductivity with values of approximately 5.30×10^{-5} and 4.63×10^{-5}, respectively. On the other hand, AC conductivity of BTN metacomposites rises with increase in frequency when the TiN content is lower, but it

exhibits a frequency-independent behaviour as the TiN content becomes higher. The distinct conductive characteristics observed in these metacomposites signify the presence of a percolation threshold. In metacomposites below this threshold (BTN1 and BTN2), they adhere to Jonscher's power law,

$$\sigma_{ac} = \sigma_{dc} + A\,\omega^{n} \qquad (6.3)$$

where σ_{ac} and σ_{dc} are the conductivity due to alternating and direct current, 'A' and 'n' are pre-exponential and exponential factors, and ω is the angular frequency [28,30,36].

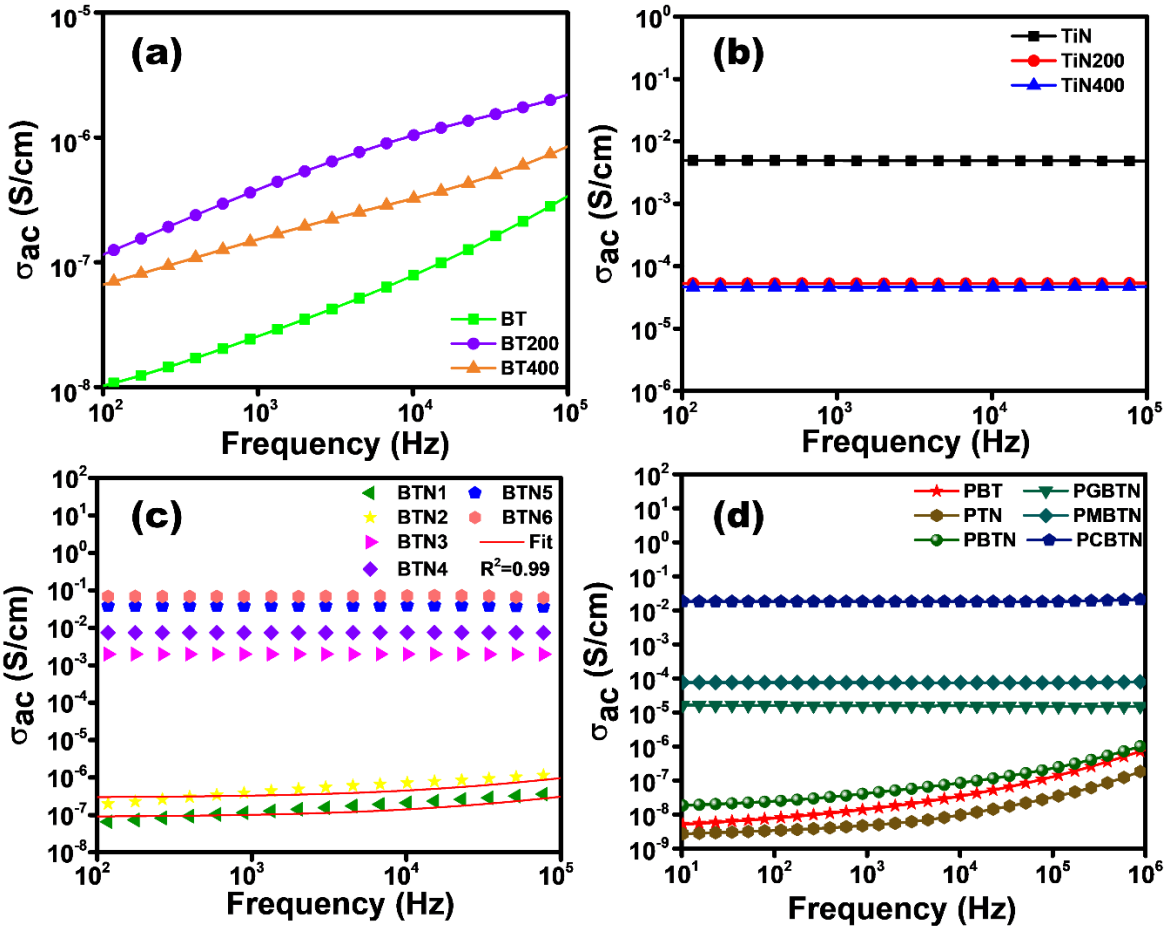

Figure 6.9 Frequency dependent conductivity of $BaTiO_3$ (a) TiN (b) at different temperatures. Frequency dependent conductivity of $BaTiO_3$- TiN composites with different TiN content (c). Frequency dependent conductivity of polymer metacomposites (d)

Under these circumstances, the metacomposites display a hopping conduction behaviour, signifying that when subjected to an external electric field, free electrons can "jump" between

adjacent conductive units. As the TiN content was further increased (BTN3, BTN4, BTN5 and BTN6), a sudden shift in electrical conductivity is observed due to percolation threshold, and the behaviour became independent of frequency (Fig.6.9c).

Fig.6.9d shows frequency dependent conductivity of polymer composites. PTN, PBT and PBTN samples shows conductivity increase with frequency according to Jonscher's power law. PGBTN, PMBTN and PCBTN samples shows frequency independent behaviour almost constant in the whole test frequency region. PCBTN sample shows highest conductivity. This is the reason for getting huge negative permittivity in PCBTN sample. PMBTN and PGBTN sample shows moderate change of conductivity.

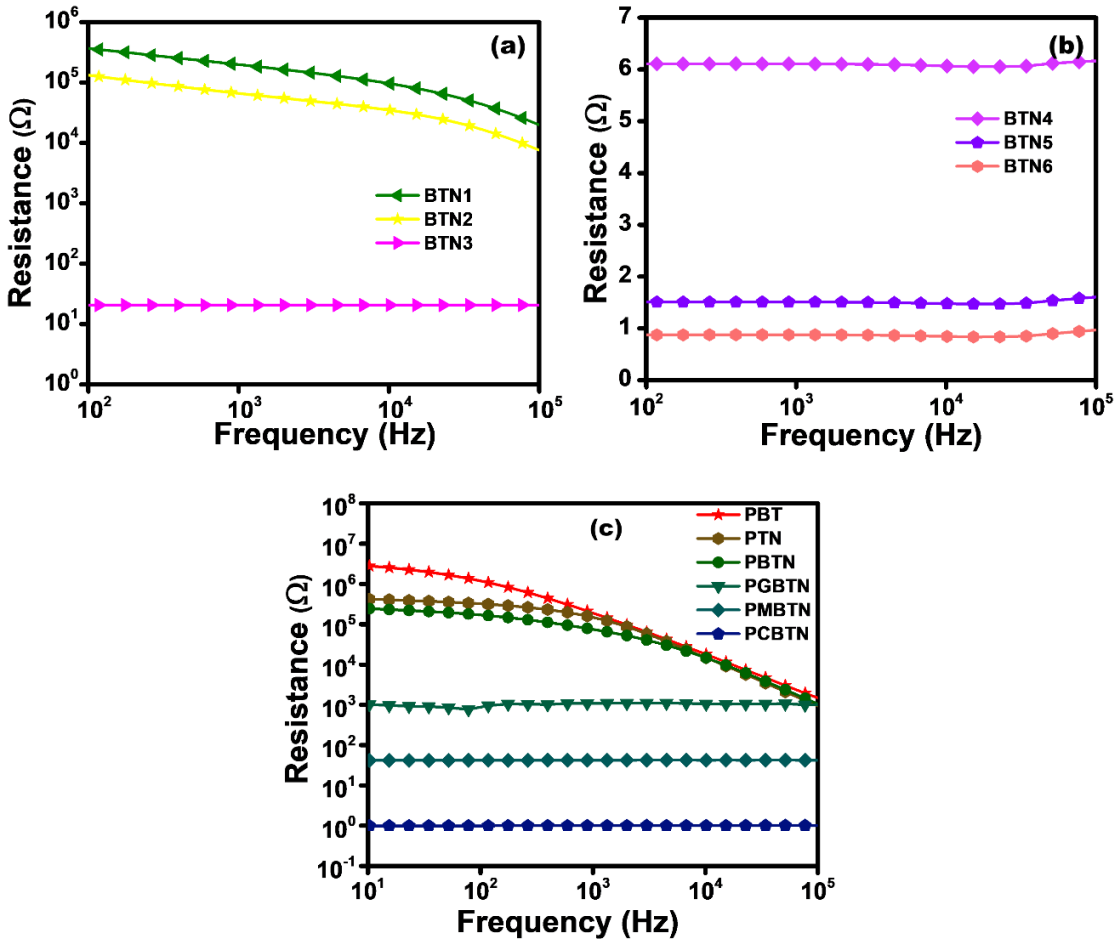

Figure 6.10 Frequency dependent resistance of (a) and (b) BTN metacomposites and (c) polymer composites (PVA – BTN – CB (PCBTN), PVA – BTN – graphite (PGBTN), PVA – BTN – MWCNT (PMBTN))

When subjected to external alternating electric field, it is feasible to conceptualize a metacomposite consisting of elements representing resistance (R), capacitance (C), and inductance (L). Much like the rise in electrical conductivity corresponding to the augmentation of TiN content, as observed from the data presented in Fig.6.10, an inverse relationship was observed between resistance and TiN content, leading to the manifestation of inductive features and negative permittivity. Notably, BTN6 demonstrates a resistance value of 0.8 Ω at 117 Hz (Fig.6.10b), displaying frequency-independent behaviour. Conversely, BTN1 exhibits a very large resistance of 3.5×10^5 Ω at 117 Hz (Fig.6.10a). Fig.6.10c shows frequency dependent resistance of polymer composites. PTN, PBT and PBTN sample shows huge resistance value and decrease with frequency due to interfacial polarization of the polymer composites. When carbon conducting fillers added it shows frequency independent behaviour or slight increase in the higher frequency region due to continues conductive path formed and resistance value greatly decreased.

Frequency dependence on reactance of BTN metacomposites is presented in Fig.6.11a and 6.11b. Inductive and capacitive reactance are often combined to create what is known as reactance and expressed as $Z'' = Z_L - Z_C$. In cases where composites display capacitive characteristics and positive permittivity, they tend to exhibit a negative reactance value, signifying a phase lag between voltage and current with lower concentration of TiN content. Further increase of TiN content Z" become positive and the composites shows inductive behaviour. There is a shift from negative to positive demonstrating that the composite be subjected to capacitive to inductive transition on increasing the frequency [37,38]. When the TiN content was low, a declining trend in the |Z| spectra was observed (Fig.6.11c), which can effectively be represented by a model involving resistors (R_s and R_p) and a capacitor (C_p) shown in the insert. Conversely, when the TiN content increases and percolation occurs in BTN composites, a rising trend in the |Z| spectra is observed, indicating the presence of inductive

characteristics. Therefore, to accurately depict the frequency-dependent |Z| spectra, an inductive circuit with inductors (L_1 and L_2) was employed, as shown in the insert. It is worth noting that the percolated networks, which consist of numerous TiN clusters, can be considered analogous to a theoretical inductor composed of an extensive number of micro-inductors [23,25,39,40].

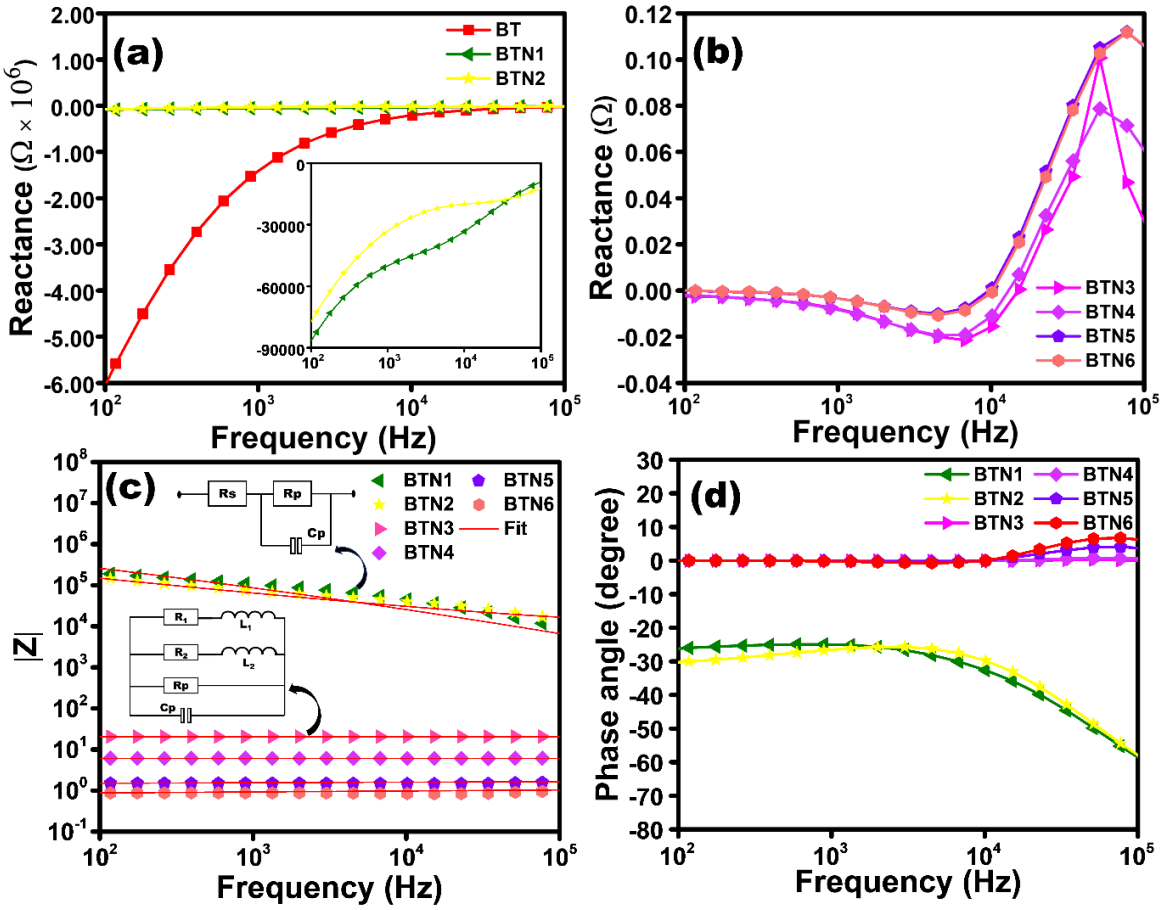

Figure 6.11 Frequency dependent reactance (a) and (b), modulus Z (c) and phase angle (d) of $BaTiO_3$ – TiN metacomposites and equivalent circuit models (e and f)

The phase angle of the metacomposites typically displays a dependence on the frequency. In cases where composites demonstrate capacitive characteristics and possess positive permittivity, they usually exhibit a negative phase angle, indicating that the voltage phase lags behind the current phase. Conversely, metacomposites with positive phase angles tend to possess inductive characteristics and typically display negative permittivity. As observed from

Fig.6.11d, below the percolation threshold (BTN1 and BTN2), the phase angle is negative while the dielectric constant is positive across the entire frequency spectrum. On the other hand, above the percolation threshold (BTN3, BTN4, BTN5 and BTN6), positive phase angle was observed in the negative permittivity region, and vice versa.

Frequency dependent permittivity of $BaTiO_3$/TiN composites annealed at 400 °C is shown in Fig.6.12. Annealing temperature is enhanced to 400 °C its negative permittivity disappears and shows positive permittivity in the whole test frequency region. Permittivity enhances with increase of TiN content due to Maxwell-Wagner-sillar effect. Our study proves that all BTN samples annealed at 200 °C show negative permittivity at higher frequency region due to the dielectric resonance. However, the BTN samples annealed at 400 °C shows only positive permittivity. This indicates the lack of dielectric resonance or a change in dielectric resonance that happens due to the annealing at 400 °C. The nature of grain boundaries within components and interfaces between components will be different for these two-sample system with respect to annealing temperature. Composites' permittivity declines with frequency, primarily because all types of polarization (ionic, interfacial, orientational, and electronic) exist in the low frequency zone and limit the movement of charge carriers. The relaxation processes caused by $BaTiO_3$'s inaction of dipolar mobility or Maxwell-Wagner relaxation is the reason for permittivity drop at high frequencies [41].

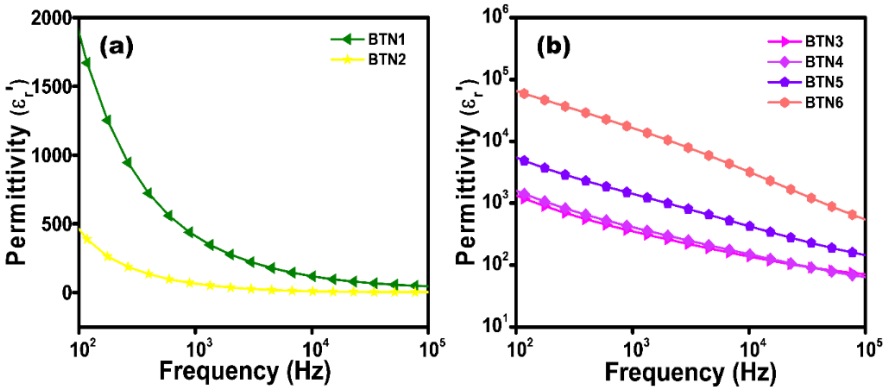

Figure 6.12 Frequency dependent permittivity of $BaTiO_3$ /TiN (a) and (b) composites annealed at 400 °C

6.5 Electromagnetic interference shielding properties

The EMI shielding properties of the polymer composites in the X-band region is shown in Fig.6.13 to Fig.6.16. The shielding efficiency of PBTN sample is shown in Fig.6.13 and the average total efficiency is 20 dB at 0.2 mm (PBTN1) thickness and the thickness is increased to 0.6 mm (PBTN2) the average efficiency is increased to 28 dB. $BaTiO_3$ – TiN metacomposites in PVA matrix is a good for EMI shielding. Its shows absorption dominant shielding mechanism. Increasing the thickness shielding efficiency is also increased. Titanium nitride is a good electrical conductor and shows ceramic properties [42] [43]. Dielectric and ferroelectric properties of $BaTiO_3$ also contribute to shielding. The interfacial polarization and conductivity also affect shielding efficiency. This result indicates that maximum efficiency of 90% at 0.2 mm thickness and 99.84% at 0.6 mm thickness is possible in PBTN samples. Therefore, PBTN sample is suitable for commercial applications.

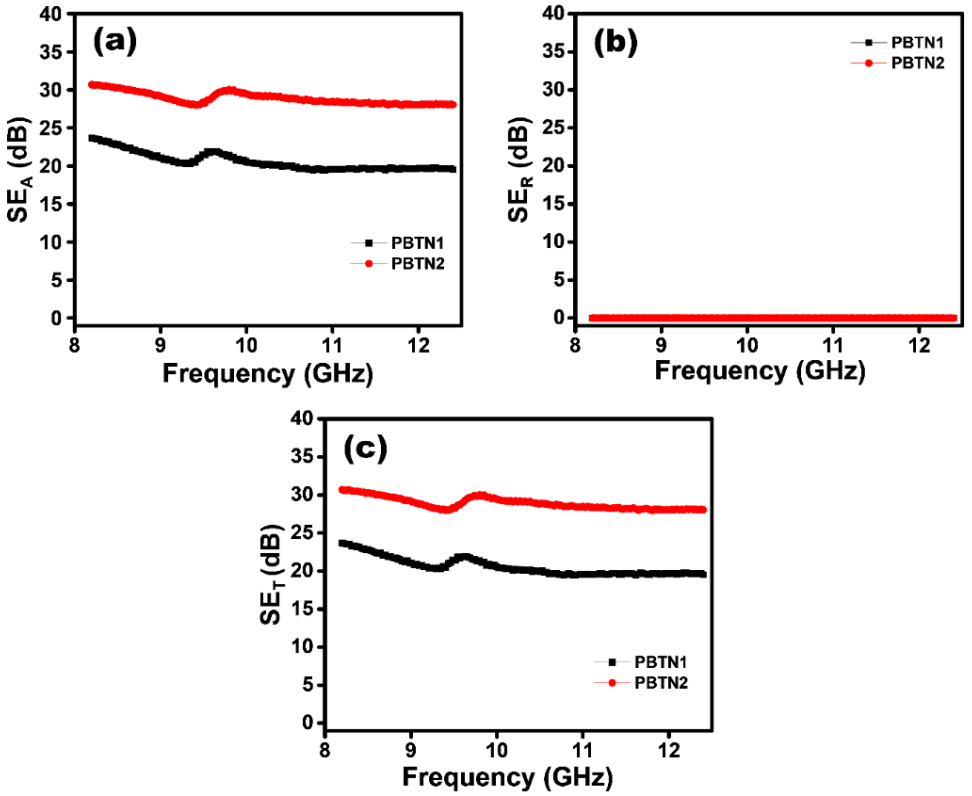

Figure 6.13 The EMI shielding efficiency of PBTN sample with two different thickness (0.2mm and 0.6 mm) (a) Absorption (b) Reflection (c) Total shielding.

For improving the efficiency of the PBTN sample, graphite flakes are added and samples are fabricated with different thickness and the shielding efficiency is given in Fig.6.14. The PGBTN sample shows average total shielding efficiency of 38 dB and 45 dB with thickness 0.8 and 1.4 respectively. Further increase of thickness to 1.8 mm, its average total shielding efficiency is 45 dB, but two absorption peaks are obtained with efficiency of 71 dB (8.6 GHz) and 77 dB (11.4 GHz). When graphite flakes added its shielding efficiency increased to 10 dB, and absorption dominant shielding is obtained. The reflection loss is below 1 dB. Carbon materials are good shielding materials with low percolation threshold [44] [45] [46]. Here, 2.5 wt% of graphite added to the PBTN matrix and its shielding efficiency is greatly increased. Thickness is also affecting shielding efficiency. Therefore, here thickness is varied to 1.4 mm its average SE_T is increased to 45 dB and at 9.6 GHz its shows SE_T of 75 dB. Further improved the thickness to 1.8 mm, the average shielding is same as that of 1.4 mm thickness, but it shows two absorption peaks one at 8.6 GHz with a total shielding efficiency of (SE_T) 71 dB and at the other peak at 11.4 GHz gives a shielding efficiency of (SE_T) of 77 dB. The details are given in table.6.2.

Table 6.2. Shielding efficiency of PGBTN samples

Sample code	Thickness (mm)	Shielding efficiency (dB)	Shielding efficiency (%)
PGBTN1	0.8	43 dB (at 8.2 GHz) SE_{avg} 38	99.99 99.98
PGBTN2	1.4	75 dB (at 9.6 GHz) SE_{avg} 45	99.9999 99.99
PGBTN3	1.8	71 dB (at 8.6 GHz) 77 dB (at 11.4 GHz) SE_{avg} 45dB	99.99999 99.99999 99.99

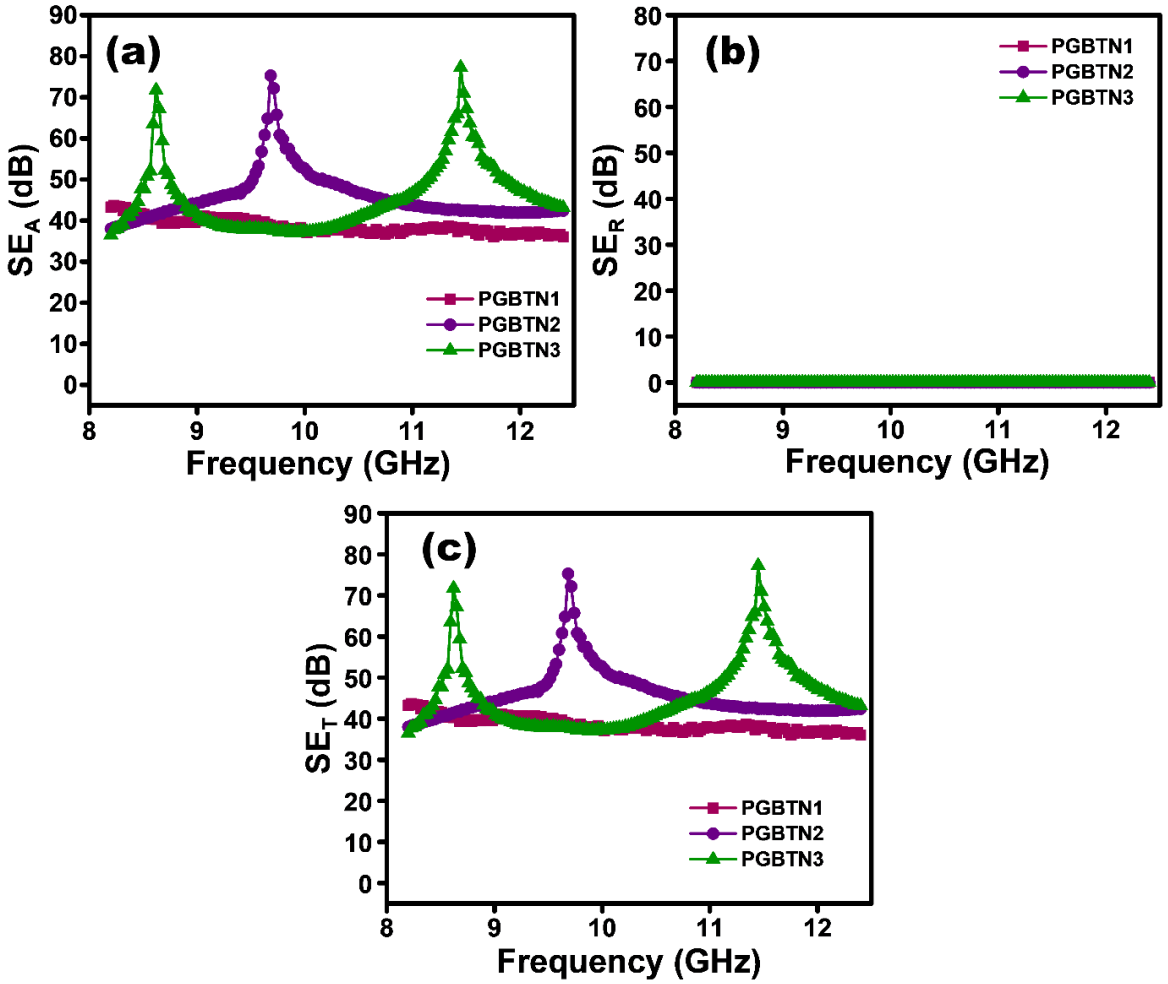

Figure 6.14 The EMI shielding efficiency of PGBTN sample with different thickness (a) Absorption (b) Reflection (c) Total shielding

The MWCNT is added to the PBTN composite and the shielding efficiency is measured. The average total shielding efficiency of PMBTN sample is 35 dB, 37 dB and 43 dB with thickness 1,1.3 and 2 mm respectively. Fig.6.15 shows shielding efficiency of PMBTN samples. It can be observed that the EMI shielding efficiency increases with thickness, this is because with increases in thickness the MWCNT is continuously distributed and conductivity increases. These two factors positively affect shielding efficiency [47] [48] [49]. Along with MWCNT, TiN also is a conducting filler that contribute to conductivity. In this case reflection is below 1dB and absorption dominant shielding mechanism is obtained, the details are given in table.6.3.

Table 6.3. Shielding efficiency of PMBTN samples

Sample code	Thickness (mm)	Shielding efficiency (dB)	Shielding efficiency (%)
PMBTN1	1	SE_{avg} - 35 dB	99.8
PMBTN2	1.3	SE_{avg} - 37 dB	99.9
PMBTN3	2	SE_{avg} - 43 dB	99.99

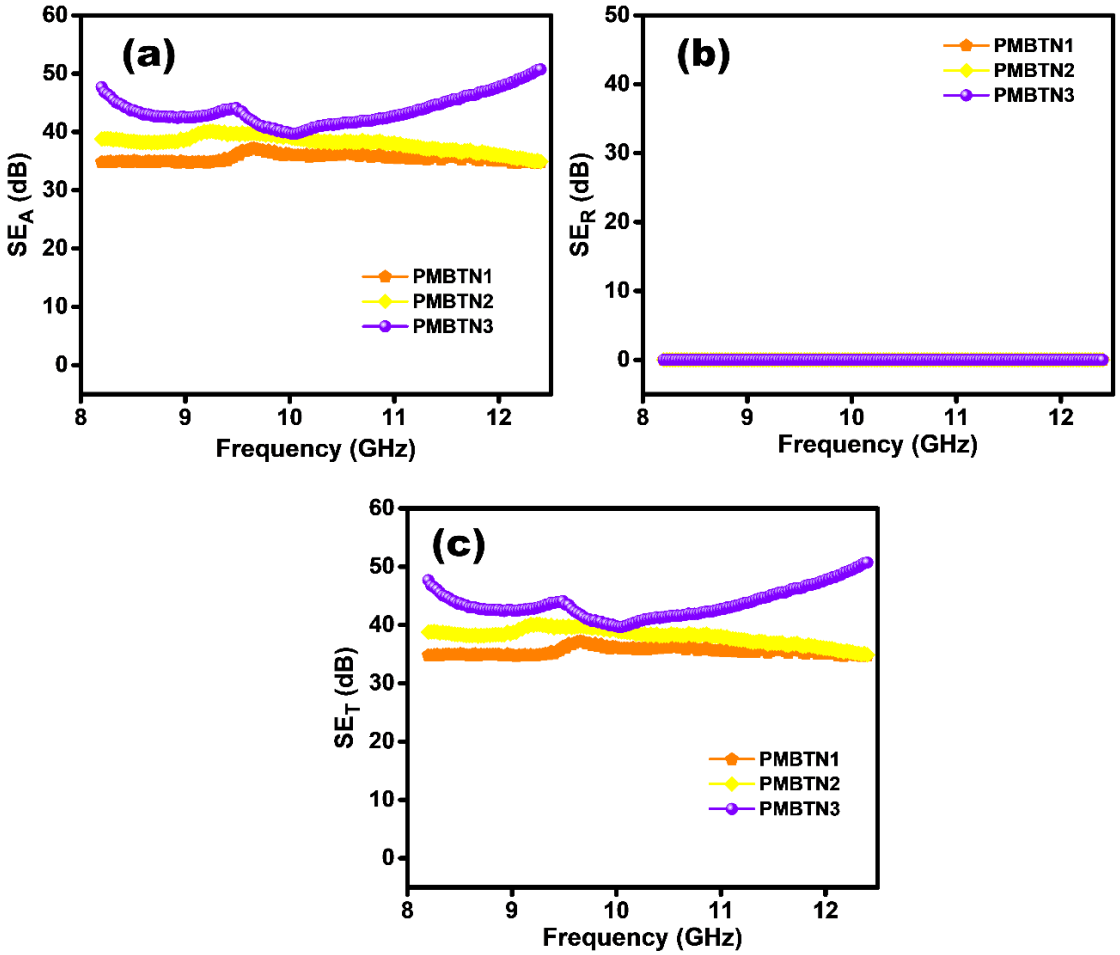

Figure 6.15 The EMI shielding efficiency of PMBTN sample with different thickness (a) Absorption (b) Reflection (c) Total shielding

Then, carbon black is added to the PBTN matrix and three samples are fabricated with different thickness and shielding efficiency is measured. Fig.6.16. shows absorption, reflection and total shielding efficiency of PCBTN samples. Compared with PGBTN and PMBTN samples, PCBTN sample shows more total shielding efficiency. Carbon black is a good conducting filler and suitable for EMI shielding applications [50] [51] [52] [53]. The average total shielding efficiency is 34 dB, 48 dB, 61 dB with thickness 0.75 mm, 1.2 mm and 1.4 mm respectively. The PCBTN3 sample shows two peaks at 9.4 GHz and 11.2 GHz and the shielding efficiency is 83 dB and 90 dB respectively.

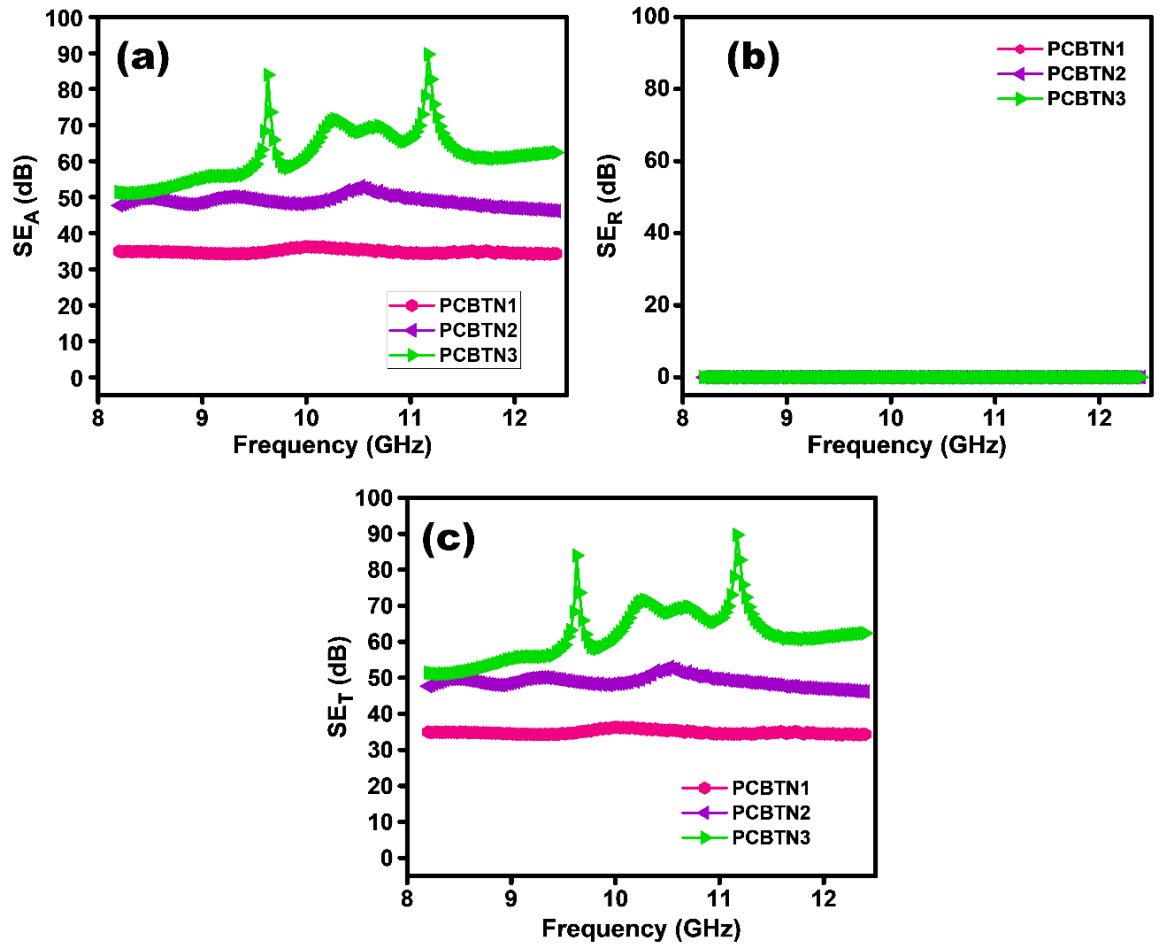

Figure 6.16 The EMI shielding efficiency of PCBTN sample with different thickness (a) Absorption (b) Reflection (c) Total shielding.

The concentration of conducting fillers is fixed and the thickness is varied. The thickness is increased its shielding also increased and PCBTN3 sample shows two absorption peaks with very high shielding efficiency. The details are given in table.6.4.

Table.6.4. Shielding efficiency of PCBTN samples

Sample code	Thickness (mm)	Shielding efficiency (dB)	Shielding efficiency (%)
PCBTN1	0.75	SEavg - 34 dB	99.9
PCBTN2	1.20	SEavg - 48dB	99.99
PCBTN3	1.40	83 dB (at 9.5 GHz) 90 dB (at 11 GHz) SEavg - 61 dB	99.999999 99.9999999 99.9999

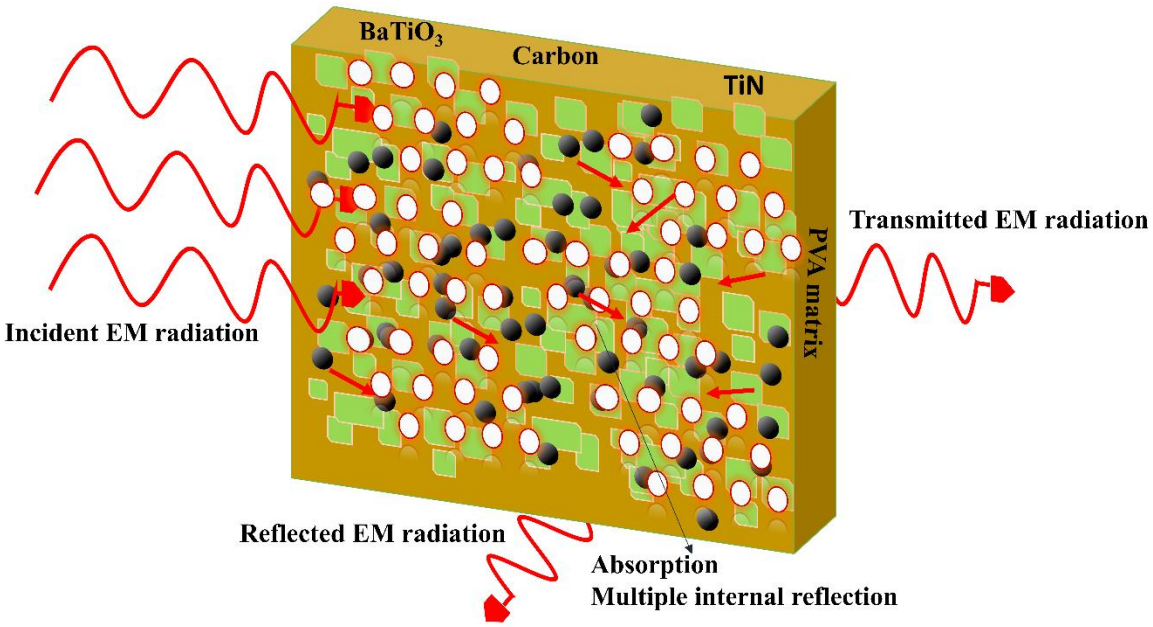

Scheme 6.4 Shielding mechanism of Polymer composite with ceramic fillers $BaTiO_3$, TiN and carbon fillers (CB, MWCNT and Graphite)

The detailed shielding mechanism is given in scheme 6.4. The polymer composites consist of three fillers (one dielectric filler and two conducting fillers) is suitable for the entry of

electromagnetic wave into the matrix. Here, dielectric filler $BaTiO_3$ is a good material for EMI shielding with high dielectric constant and shows dielectric loss peak at GHz region and a good microwave absorber [54]. The ceramic conducting filler TiN also shows remarkable properties such as low density, good electrical conductivity, corrosion and heat resistance and good absorber [55]. All carbon conducting fillers are good microwave absorbers because of its high conductivity and that can absorb or dissipates electromagnetic radiation. The huge polarization is possible with these fillers due to the interfaces between these fillers and with polymer matrix. These interfaces create multiple internal reflection and dissipate the EM waves within the material. Increasing the thickness more interfaces produce and shielding efficiency also increased. In all samples, EMI shielding efficiency fluctuates with frequency due to irregular conductive network in the composites [56] [57] .

6.6 Conclusion

In summary, $BaTiO_3$ nanoparticles synthesized through a novel solvothermal method were employed as the matrix in the fabrication of $BaTiO_3$/TiN metacomposites through blending and compression moulding technique. These metacomposites exhibit intriguing ability to achieve negative permittivity that can be finely adjusted by varying the concentration of TiN, particularly in the radio frequency range. Below the percolation threshold, positive permittivity was obtained, which subsequently decreased as the frequency increased, a phenomenon attributed to the Maxwell-Wagner-Sillars effect. However, beyond the percolation threshold, the application of Lorentz model yielded negative permittivity due to dielectric resonance. Examining the impedance property, inductive character was identified as the driving force behind negative permittivity. Consequently, the constructed epsilon-negative $BaTiO_3$/TiN metacomposites in this study hold substantial promise for practical applications in electromagnetic interference mitigation, shielding, and absorption. Simultaneously, the positive permittivity $BaTiO_3$/TiN composites generated here are well-suited for applications

demanding large dielectric permittivity. Then polymer nanocomposites of $BaTiO_3$/TiN are fabricated for electromagnetic interference shielding applications. All samples show absorption dominant shielding mechanism. The reflection is below 1 dB and $BaTiO_3$ – TiN metacomposites shows shielding efficiency of 28 dB. In order to improve the shielding efficiency of the composites, carbon nanostructures such as graphite, MWCNT and carbon black are added. When MWCNT and graphite are added to the polymer composites, its shows an average shielding efficiency of 43 dB and 45 dB. When carbon black is added its shows an average shielding efficiency of 61 dB. From the current study it is concluded that compared with other carbon compounds carbon black shows highest shielding efficiency.

****

References

[1] J. Dai, H. Luo, M. Moloney, and J. Qiu, ACS Appl. Mater. Interfaces **12**, 22019 (2020).
[2] J. Wang, Z. Shi, F. Mao, S. Chen, and X. Wang, ACS Appl. Mater. Interfaces **9**, 1793 (2017).
[3] Y. Qu, J. Lin, J. Wu, Z. Wang, K. Sun, M. Chen, B. Dong, Z. Guo, and R. Fan, J. Phys. Chem. C **124**, 23361 (2020).
[4] C. Cheng, R. Fan, Y. Ren, T. Ding, L. Qian, J. Guo, X. Li, L. An, Y. Lei, Y. Yin, and Z. Guo, Nanoscale **9**, 5779 (2017).
[5] X. T. Song, G. Shi, G. Fan, Y. Liu, and R. Fan, Ceram. Int. **48**, 832 (2022).
[6] Z. Wang, K. Sun, P. Xie, Q. Hou, Y. Liu, Q. Gu, and R. Fan, Acta Mater. **185**, 412 (2020).
[7] Z. Wang, K. Sun, P. Xie, Y. Liu, Q. Gu, R. Fan, and J. Wang, J. Materiomics **6**, 145 (2020).
[8] Z. Wang, P. Xie, G. Fan, Z. Zhang, Y. Liu, Q. Gu, and R. Fan, Ceram. Int. **46**, 9342 (2020).
[9] Z. Wang, H. Li, H. Hu, Y. Fan, R. Fan, B. Li, J. Zhang, H. Liu, J. Fan, H. Hou, F. Dang, Z. Kou, and Z. Guo, Adv. Electron. Mater. **6**, 1901005 (2020).
[10] M. Han, Z. Shi, W. Zhang, K. Zhang, H. Wang, D. Dastan, and R. Fan, Compos. Part Appl. Sci. Manuf. **149**, 106559 (2021).
[11] H. S. Bhatti, S. T. Hussain, F. A. Khan, and S. Hussain, Appl. Surf. Sci. **367**, 291 (2016).
[12] T. Kim, H. Lim, Y. Lee, and B. J. Kim, RSC Adv. **10**, 29278 (2020).
[13] H. Lu, S. Glinsek, P. Buragohain, E. Defay, J. Iñiguez, and A. Gruverman, Adv. Funct. Mater. **30**, 1 (2020).
[14] B. Szafraniak, Ł. Fuśnik, J. Xu, F. Gao, A. Brudnik, and A. Rydosz, Coatings.
[15] B. L. Phoon, C. W. Lai, J. C. Juan, P. L. Show, and W. H. Chen, Int. J. Energy Res. **43**, 5151 (2019).
[16] B. Jiang, J. Iocozzia, L. Zhao, H. Zhang, Y. W. Harn, Y. Chen, and Z. Lin, Chem. Soc. Rev. **48**, 1194 (2019).
[17] D. Morikawa and K. Tsuda, Appl. Phys. Lett. **119**, 1ENG (2021).
[18] T. Charoonsuk, S. Sriphan, C. Nawanil, N. Chanlek, W. Vittayakorn, and N. Vittayakorn, J. Mater. Chem. C **7**, 8277 (2019).
[19] M. B. Smith, K. Page, T. Siegrist, P. L. Redmond, E. C. Walter, R. Seshadri, L. E. Brus, and M. L. Steigerwald, J. Am. Chem. Soc. **130**, 6955 (2008).
[20] U. A. Joshi, S. Yoon, S. Baik, and J. S. Lee, J. Phys. Chem. B **110**, 12249 (2006).
[21] M. T. Buscaglia, M. Bassoli, V. Buscaglia, and R. Alessio, J. Am. Ceram. Soc. **88**, 2374 (2005).
[22] Y. Liu, C. Xu, H. Ren, Z. Wei, and Z. Zhang, World Sci. **13**, 2050017 (2020).
[23] Y. Qu, Y. Du, G. Fan, J. Xin, Y. Liu, P. Xie, S. You, Z. Zhang, K. Sun, and R. Fan, J. Alloys Compd. **771**, 699 (2019).
[24] Z. Wang, H. Li, H. Hu, Y. Fan, R. Fan, B. Li, J. Zhang, H. Liu, J. Fan, H. Hou, F. Dang, Z. Kou, and Z. Guo, Adv. Electron. Mater. **6**, (2020).
[25] K. Sun, P. Yang, Q. He, J. Tian, W. Duan, X. Wu, Y. Qu, and H. Du, Ceram. Int. **47**, 32297 (2021).
[26] T. Haldar, U. Kumar, B. C. Yadav, and V. V. R. K. Kumar, J. Mater. Sci. Mater. Electron. **31**, 11791 (2020).
[27] P. Patsalas, N. Kalfagiannis, and S. Kassavetis, Materials **8**, 3128 (2015).
[28] Y. Qu, Y. Li, C. Xu, G. Fan, P. Xie, Z. Wang, Y. Liu, Y. Wu, and R. Fan, J. Mater. Sci. Mater. Electron. **29**, 5853 (2018).
[29] C. Yang, Z. Shi, C. Zhang, and R. Fan, Mater. Lett. **231**, 87 (2018).
[30] Y. Liu, G. Fan, Y. Qu, P. Xie, Z. Wang, Z. Zhang, R. Fan, and X. Yin, J. Mater. Sci. Mater. Electron. **29**, 12144 (2018).
[31] M. N. Solovan, V. V. Brus, E. V. Maistruk, and P. D. Maryanchuk, Inorg. Mater. **50**, 40 (2014).
[32] S. Kappadan, T. W. Gebreab, S. Thomas, and N. Kalarikkal, Mater. Sci. Semicond. Process. **51**, 42 (2016).
[33] Y. Hakuta, H. Ura, H. Hayashi, and K. Arai, Mater. Lett. **59**, 1387 (2005).
[34] Z. C. Shi, R. H. Fan, Z. D. Zhang, H. Y. Gong, J. Ouyang, Y. J. Bai, X. H. Zhang, and L. W. Yin, Appl. Phys. Lett. **99**, 032903 (2011).
[35] Z. Wang, K. Sun, P. Xie, Y. Liu, and R. Fan, J. Phys. Condens. Matter **29**, 365703 (2017).

[36] C. Xu, Y. Qu, G. Fan, P. Xie, H. Ren, J. Chen, Y. Liu, Y. Wu, and R. Fan, J. Mater. Sci. Mater. Electron. **29**, 15994 (2018).
[37] P. Swetha, R. Aswini, M. Binesh, M. S. Muhammed, K. Sridharan, and S. Swaminathan, Mater. Today Commun. **34**, 105287 (2023).
[38] R. Singh, A. Chakravarty, S. Mishra, R. C. Prajapati, J. Dutta, I. K. Bhat, U. Pandel, S. K. Biswas, and K. Muraleedharan, ACS Appl. Mater. Interfaces **11**, 48212 (2019).
[39] T. Haldar and V. V. R. Kanth Kumar, J. Alloys Compd. **772**, 218 (2019).
[40] Y. Qu, Y. Wu, J. Wu, K. Sun, and R. Fan, J. Alloys Compd. **847**, 156526 (2020).
[41] G. H. Tabhane, S. M. Giripunje, and S. B. Kondawar, Synth. Met. **279**, 116845 (2021).
[42] J. Xu, Q. Wu, L. Lu, and J. Chen, Thin Solid Films **783**, 140056 (2023).
[43] G. K. Sharma and N. R. James, Carbon **220**, 118846 (2024).
[44] D. D. L. Chung, Carbon **216**, 118569 (2024).
[45] N. Agnihotri, K. Chakrabarti, and A. De, RSC Adv. **5**, 43765 (2015).
[46] T. Zhou, C. Xu, H. Liu, Q. Wei, H. Wang, J. Zhang, T. Zhao, Z. Liu, X. Zhang, Y. Zeng, H.-M. Cheng, and W. Ren, ACS Nano **14**, 3121 (2020).
[47] P. Gahlout and V. Choudhary, Synth. Met. **266**, 116414 (2020).
[48] S. Panda and B. Acharya, J. Mater. Sci. Mater. Electron. **32**, 16215 (2021).
[49] R. Prasad, A. R. Pai, S. O. Oyadiji, S. Thomas, and S. K. S. Parashar, J. Clean. Prod. **377**, 134290 (2022).
[50] J. Kim, G. Kim, S.-Y. Kim, S. Lee, Y. Kim, J. Lee, J. Kim, Y. C. Jung, J. Kwon, and H. Han, Compos. Part B Eng. **221**, 109010 (2021).
[51] J. Ju, T. Kuang, X. Ke, M. Zeng, Z. Chen, S. Zhang, and X. Peng, Compos. Sci. Technol. **193**, 108116 (2020).
[52] Y. Yao, S. Jin, M. Wang, F. Gao, B. Xu, X. Lv, and Q. Shu, Appl. Surf. Sci. **578**, 152007 (2022).
[53] A. G. El-Shamy, Prog. Org. Coat. **146**, 105747 (2020).
[54] G. P. Abhilash, K. Sushmita, S. Bose, and C. Shivakumara, Synth. Met. **297**, 117387 (2023).
[55] Y. Qing, L. Ma, X. Hu, F. Luo, and W. Zhou, Ceram. Int. **44**, 8706 (2018).
[56] L. Vovchenko, O. Lozitsky, L. Matzui, V. Oliynyk, V. Zagorodnii, and M. Skoryk, Mater. Chem. Phys. **240**, 122234 (2020).
[57] S. Sankaran, K. Deshmukh, M. B. Ahamed, and S. K. Khadheer Pasha, Compos. Part Appl. Sci. Manuf. **114**, 49 (2018).

CONCLUSION AND FUTURE OUTLOOK

A summary of the thesis work focuses on the fabrication of polyvinyl alcohol (PVA) metacomposites with carbon nanostructures including carbon black (CB), MWCNT and graphite. PVA metacomposites with carbon nanostructures exhibit intriguing and distinct dielectric behaviour due to their tuned physical properties. Additionally, ceramic metacomposites are prepared and PVA is added to these ceramic composites to impart flexibility. By judiciously choosing combinations of materials, dielectric parameters are modified and electromagnetic interference shielding applications in the X-band (8-12 GHz) frequency range are explored.

PVA – CB metacomposites are fabricated in section one of this thesis, and their Drude model negative permittivity is measured from 10^4 to 10^6 Hz. 1.25 wt% of CB added to PVA matrix results in percolation. As CB concentrations increase beyond percolation, negative permittivity increases greatly. PVA - CB metacomposites show weakly negative permittivity, making them ideal for impedance matching.

Another carbon nanostructure, MWCNT, was added to the PVA matrix and this metacomposite achieved percolation at 1 wt%. Drude model and Drude-Lorentz model negative permittivity is obtained for this composite in the frequency range of 10^3 to 10^7 Hz. Due to the high electron density of MWCNT composites, PVA composites based on MWCNT have high negative permittivity compared to CB composites. At 3 wt% MWCNT added to PVA matrix, it has negative permittivity throughout the whole test frequency range.

Graphite flakes were also selected as a filler for PVA-based metacomposites, achieving percolation at 1 wt%. Graphite flakes based PVA metacomposites show a large negative permittivity in the frequency range of 10^1 to 10^3 Hz compared with CB and MWCNT. An

additive of 3 wt% graphite flakes to the PVA matrix shows negative permittivity across the entire frequency range of the test.

A ceramic metacomposite (BTN) is fabricated using $BaTiO_3$ as the matrix and TiN as the filler and it shows Lorentz model huge negative permittivity in the order of 10^5 in the frequency range of 10^4 to 10^5 Hz. Here, spherical shaped $BaTiO_3$ is synthesized by solvothermal method. The ceramic metacomposite (BTN) is added to the PVA matrix for flexibility, but this polymer composite shows only positive permittivity. The permittivity can further be tuned by adding carbon nanostructures to the BTN-PVA composites. Metacomposites with tuned negative permittivity were formed by combining carbon black (CB), multiwall carbon nanotubes (MWCNT) and graphite with BTN-PVA composites. It was found that BTN-PVA with carbon black has the highest negative permittivity in the frequency range 10^1 to 10^4 Hz of these metacomposites. In Table 7.1, all the composites discussed above are compared in terms of their dielectric behavior and carbon nanostructures are identified as the best candidates for tuning negative permittivity.

Composites	**Frequency range (Hz)**	**Highest Permittivity**	**Conductivity (S/cm)**
PVA – CB	10^4 - 10^6	- 445	2.5×10^{-4}
PVA – MWCNT	10^3 - 10^7	- 3259	3.4×10^{-3}
PVA – Graphite	10^1 - 10^6	- 12985	1.0×10^{-3}
$BaTiO_3$ – TiN	10^4 - 10^5	$- 3.4 \times 10^5$	8.5×10^{-2}
PBTN	10^1 - 10^6	761	1.8×10^{-8}
PCBTN	10^1 - 10^6	$- 2.5 \times 10^5$	4.34×10^{-4}
PMBTN	10^1 - 10^5	- 9112	7.64×10^{-5}
PGBTN	10^1 - 10^2	- 1218	1.6×10^{-5}

Table 7.1 Conductivity, Permittivity and their corresponding frequency range of metacomposites

The conductivity and flexibility of polymer metacomposites make them ideal for EMI shielding applications. We tested the EMI shielding performance of all-synthesised samples. In various industries, the development of effective EMI shielding materials, particularly for the X-band frequency range, is essential to mitigate electromagnetic interference and ensure reliable operation of electronic devices. Advanced materials with superior shielding effectiveness while maintaining lightweight and durable properties are critical in this research. EMI shielding performance is measured for two-component systems, such as PVA - CB, PVA - MWCNT, and PVA - Graphite flakes. Shielding efficiency increased with increasing concentration of conducting fillers in all cases. In 2.5 wt% (0.41 mm thickness) of CB concentration, PVA – CB composite shows 23 dB EMI shielding efficiency. With MWCNT added to this PVA matrix, the efficiency is 18 dB (2.5 wt%) and the thickness is 0.48 mm. However, PVA - graphite composite has a shielding efficiency of 26 dB at 2.5 wt% concentration with thickness of 0.5 mm, but at 1 mm, the shielding efficiency reaches 34 dB and can be commercialized.

An EMI shielding system based on three components (PVA, $BaTiO_3$, and TiN) is then evaluated. At 0.2 mm thickness, this composite has a shielding efficiency of 20 dB. When the thickness is increased to 0.6 mm, its shielding efficiency increases to 28 dB, making it suitable for commercial EMI shielding applications.

To further increase shielding efficiency, a four-component system is considered. In this CB, MWCNT and Graphite are added to the three-component system mentioned above (PVA - $BaTiO_3$ - TiN), samples are made with various thicknesses, and shielding efficiency is measured. PVA - $BaTiO_3$ - TiN with MWCNT as a shielding agent has a maximum shielding efficiency of 43 dB (PMBTN) with a thickness of 2 mm. With the addition of graphite, the PVA - $BaTiO_3$ - TiN composite has a maximum shielding efficiency of 45 dB (PGBTN), an increase of 2 dB over MWCNT, and a thickness of 1.9 mm. With the addition of carbon black

to the PVA - $BaTiO_3$ - TiN matrix, it demonstrates 57 dB shielding efficiency (PCBTN) with thickness of 1.4 mm, making it well suited for commercial applications. Table 7.2 gives details of shielding efficiency shown by the PVA based metacomposites.

Composite code	**Carbon conducting Filler (wt%)**	**$BaTiO_3$ Content (wt%)**	**TiN Content (wt%)**	**Thickness (mm)**	**Average Shielding efficiency (dB)**	**Shielding efficiency (%)**
PC	Carbon black (2.5)	-	-	0.41	23	99
PM	MWCNT (2.5)	-	-	0.48	18	98
PG	Graphite flakes (2.5)	-	-	0.50	26	99
PBTN	-	1	3	0.2,0.6	20,28	99,99.8
PMBTN	MWCNT (2.5)	1	3	1.1, 1.3, 2	27, 35, 43	99, 99.9 99.99
PGBTN	Graphite flakes (2.5)	1	3	1.2,1.5 1.90	38,45,45	99, 99.99 99.99
PCBTN	Carbon black (2.5)	1	3	0.75, 1.25,1.40	26, 44, 57	99, 99.99 99.999

Table 7.2 Concentration of the fillers, thickness and their shielding efficiency (% and dB) of PVA – CB, PVA – MWCNT, PVA -Graphite, PVA – $BaTiO_3$ – TiN, PVA – $BaTiO_3$ – TiN – MWCNT, PVA – $BaTiO_3$ – TiN – Graphite flakes and PVA – $BaTiO_3$ – TiN – CB composites

Future scope of this work

By judiciously choosing the material combinations in a metacomposites, we achieved tuning of negative permittivity either in a select frequency range or across the entire test frequency range (10^1 to 10^5 Hz). However, the fillers chosen are not suitable for tuning the permeability of the metacomposites. Hence, we planned to tune both negative permittivity and negative permeability in future work to impart double negative properties to these composites. Metacomposites with double negative property are suitable for negative refractive index applications.

Due to the increased use of electronic devices and communication systems, electromagnetic radiation and interference are now major problems. Suitable shielding materials are required to solve this problem. The composites synthesized here are suitable for use in EMI shielding applications. In the future, this thesis will focus on improving shielding efficiency and commercializing shielding materials.

****

RECOMMENDATIONS

1. By judiciously choosing the material combinations in a metacomposites and we fabricated polymer metacomposites and achieved negative permittivity in the (10^1 to 10^5 Hz) frequency range.

2. The obtained metacomposites have moderate negative permittivity and suitable for impedance matching applications.

3. The fabricated composites are also suitable for X – band microwave absorption.

4. In the future, this work will focus on improving shielding efficiency and commercializing shielding materials.

5. The tuning of both negative permittivity and permeability is the future aim of my work.

6. The double negative metacomposites are suitable for negative refractive index applications.